Generation of Ultrahigh Frequency Acoustic Waves for the Characterization of Complex Materials

ARCHIVES

MASSACHUSETTS INSTITUTE
OF TECHNOLOGY
MAR 2 5 2005
LIBRARIES

By

Jaime Dawn Choi

B.A. Chemistry
Rice University, 1999

Submitted to the Department of Chemistry in partial fulfillment of the
requirements for the degree of

DOCTOR OF PHILOSOPHY IN PHYSICAL CHEMISTRY
AT THE
MASSACHUSETTS INSTITUTE OF TECHNOLOGY
[February 2005]
~~January 2005~~

© Massachusetts Institute of Technology, 2005. All rights reserved.

The author hereby grants to MIT permission to reproduce and to distribute publicly
paper and electronic copies of this thesis document in whole or in part.

Signature of Author..
Department of Chemistry
January 18, 2005

Certified by..
Keith A. Nelson
Professor of Chemistry
Thesis Supervisor

Accepted by..
Robert W. Field
Chairman, Departmental Committee on Graduate Students

This doctoral thesis has been examined by a committee of the Department of Chemistry as follows:

Professor Moungi G. Bawendi ....
Chairman

Professor Keith A. Nelson ....
Thesis Supervisor

Professor Robert. G. Griffin ....

Generation of Ultrahigh Frequency Acoustic Waves for the Characterization of Complex Materials

By

Jaime Dawn Choi

Submitted to the Department of Chemistry on January 18, 2005 in Partial Fulfillment of the Requirements for the Degree of Doctor of Philosophy in Chemistry.

ABSTRACT

A discussion of the anomalous low-temperature thermal properties of amorphous materials is first given as a theoretical framework in which the rest of the thesis is treated. The theory models the form and function of microscopic dynamical and structural features that are thought to be common to amorphous materials, which interact strongly with ultrahigh frequency acoustic waves and creating the anomalies. The model has been found to well reproduce the measured anomalous thermal conductivity of silica glass. Separately, an experiment which utilizes impulsive stimulated thermal scattering is used to measure the anomalous low-temperature thermal conductivity of a molecular glass, glycerol. The results, taken in the context of the aforementioned theory, illustrate the ambiguity of using a macroscopic measurement to quantify microscopic parameters.

However the validity of the microscopic assumptions of the theory has heretofore been difficult to test directly due to a lack of a proper experimental method. The remainder of the thesis is devoted to developing a technique of generating ultrahigh frequency acoustic waves, which can be used to directly probe the dynamics and structure believed to dominate the low-temperature thermal properties of amorphous materials. The generation of ultrahigh frequency tunable narrowband acoustic waves is accomplished with a novel retroreflection-based ultrafast pulse shaper. It generates optical pulse sequences of frequency tunable between 2-2000 GHz through movement of a single delay line. Optical to acoustic conversion by aluminum transducers yields acoustic waves with bandwidth limited by the metal temporal response to 2-500 GHz. The detection of the ultrahigh frequency acoustic waves is accomplished with a novel grating-based interferometer. The alignment, flexibility, and calibration of the interferometer is described.

Lastly the use of the technique is illustrated for the characterization of the structure and dynamics of silica glass, the prototypical amorphous material, at room temperature and at 20 K. The room temperature results are considered in terms of the only other data available in the literature, and the 20 K data are considered in terms of the theory of amorphous materials, as no other information has been published in this temperature and frequency range. Both results suggest that current models of amorphous materials be reconsidered.

Thesis Supervisor: Keith A. Nelson
Title: Professor of Chemistry

Acknowledgements

I have had the privilege of sharing my graduate experience with so many excellent scientists and good friends. I would first like to thank my advisor, Keith Nelson, who has helped me develop my scientific technique and skills in ways I would not have believed five years ago. His unwavering enthusiasm and sanity checks saw me through many a flood and broken laser.

Few people have impacted my life as tremendously as my husband Michael has. Thank you for your love, cheerfulness, and unquestioning support. You have been a source of stability and kept me smiling through trying times. I look forward to seeing where the road takes us.

I owe my parents a debt of gratitude. They taught me the importance of honesty, integrity, hard work, and education, and always loved me. They sacrificed so much to give me opportunities, and encouraged me to take chances. Thank you for everything. My "new" father I thank for teaching me about the importance of family, and of understanding.

My friends – both in and out of the lab – kept my head level. Jacob has been a true friend, unbelievably supportive and encouraging throughout the years. I am sure we will share many new adventures. Mark, Mike and Xu, Jeff and Amy, Thomas and Caroline, and Ted and Pam have made my free time in grad school well worth spending outside the basement!

In my first few years at MIT, I had the fortune of working with Christ Glorieux, who is among the most didactical scientists I know. He introduced me to the computational analysis of time-domain signals, and I use his techniques (and Matlab programs, commented in Flemish) often. I thank Rebecca Slayton, who introduced me to the world of ultrafast experimentation. I cannot thank Masashi Yamaguchi enough, who played a huge part in the success of all the experiments in this thesis, through many a long night fighting the cryostat. Kenji Katayama played a crucial role in the modeling and execution of the high frequency acoustic experiments. I am also indebted to Thomas Feurer, whose German engineering made performing many of the experiments in this thesis possible.

Among my graduate compatriots, there are so many people to thank for their friendship and generosity of time. Benjamin Paxton has been a selfless lab partner who has spent many long hours (okay, weeks…months?) writing programs to run the experiments, working on the laser, and generally responding to my panicked calls for help. David Ward has been an excellent partner in crime since day one, providing me with general cheer, name-calling, and ranting sessions. Josh Vaughan has been a great friend, source of support, and resource. Darius Torchinsky helped substantially with theoretical "issues" as well as with much-needed beers. Peter Poulin's thoughtfulness in advice and friendship is appreciated. Neal Vachhani offered much insight into the nature of complex materials, and helped get a truly challenging experiment to work nicely. Long ago Christoph Kleiber made significant contributions to the thermal conductivity experiments, and I'm so happy he's back to join us! I thank the many other current and past Nelson group members: Nikolay, Efren, Ka-Lo, Kathy, Eric, Thomas H., Cindy, Taeho, and Kevin, who have all been willing to share their time and opinion with me. I especially thank Gloria who has been incredibly friendly and taken such good care of me and the rest of the group. Thanks to all!

To Michael

And

To My Parents

Who All Have Ever Loved

And Supported Me

Table of Contents

1. **Introduction** **13**
    - 1.1 References 16

2. **The Interaction of High-Frequency Acoustic Waves with Amorphous Materials** **17**
    - 2.1 Introduction: Low-Temperature Anomalies of Glasses 17
    - 2.2 Modeling the Phonon-Structure Interaction 17
    - 2.3 Predictions for Microscopic and Macroscopic Behavior of Glasses 33
    - 2.4 References 37

3. **Low Temperature Thermal Anomalies of Glycerol** **41**
    - 3.1 Introduction 41
    - 3.2 Impulsive Stimulated Thermal Scattering: Experiment and Results 45
    - 3.3 Discussion 60
    - 3.4 Conclusions 71
    - 3.5 References 72

4. **Generation, Modeling, and Characterization of Narrowband Acoustic Waves In the GHz Regime** **75**
    - 4.1 Introduction 75
    - 4.2 Experimental Design 80
        - 4.2.1 Deathstar Pulse Shaper 80
        - 4.2.2 Sample Preparation 85
        - 4.2.3 Interferometric Detection 87
    - 4.3 Optic to Acoustic Conversion 88
    - 4.4 Model for Propagation 98
    - 4.5 High Resolution Characterization of Nanoscale Structures 107
    - 4.6 Using Narrowband Acoustic Waves to Characterize Complex Materials 119
    - 4.7 Summary 121
    - 4.8 References 122

5. Grating Interferometry 125

5.1 Introduction 125
5.2 Alignment, Calibration, and Evaluation 130
    5.2.1 Experimental Design 130
    5.2.2 Spatiotemporal Limitations 135
    5.2.3 Calibration, Resolution, and Noise Characteristics 137
5.3 Imaging Surface Acoustic Waves 139
5.4 Probing Ultrahigh Frequency Acoustic Waves 142
5.5 Probing Phonon-Polaritons 153
5.6 Conclusions 155
5.7 References 155

6. Structure and Dynamics of Amorphous Solids in the GHz Regime: Silica Glass 159

6.1 Introduction 159
6.2 Experimental Details 162
    6.2.1 Optical Setup 162
    6.2.2 Fabrication, Characterization, and Design of Samples 162
    6.2.3 Acoustic Analysis 166
6.3 Results for Silica Glass 167
    6.3.1 Room Temperature Spectrum 168
    6.3.2 Low Temperature Spectrum 194
6.4 Conclusions on the Properties of Amorphous Materials at the Microscopic Level 199
6.5 Future Directions 200
6.6 References 202

Chapter One

Introduction

The field of study of disordered materials encompasses a tremendous host of materials, including polymers; ionic, molecular, and network glasses; and their cousins, molecular, polar, and glass-forming liquids. The common feature of these materials, here labeled generally "glasses," is solely that they lack long-range structure. They are homogeneous on the bulk scale. However a glass possesses features at the molecular length scale dominated, as in the crystal, by inter- and intra- molecular forces determined by the chemical composition. It is unusual then to find the same result repeated over and over in nature: that most glasses exhibit *remarkably* similar trends in their bulk physical and thermal properties.[1] The natural, if counterintuitive, conclusion is that therefore the *lack* of structure determines key elements of the disordered material's character. A discussion of a model of the microscopic origins of this result is presented in Chapter 2.

An experiment that typifies the universal thermal behavior of glasses is described in Chapter 3. A non-contact all-optical technique, impulsive stimulated thermal scattering (ISTS) is utilized to measure the bulk thermal diffusion[2] in the temperature range 1.4-20 K in a molecular glass, glycerol, and relate the result to the thermal conductivity, κ. The same unusual behavior that has been hotly debated since the seminal work performed by Zeller and Pohl[3] decades ago is observed – with some unusual features. As the temperature is increased in the glass from 1.4 K, an increasing number of high-frequency phonon modes become available to carry heat diffusively through the glass. This results in an increase in the thermal conductivity. However near 10 K, the thermal conductivity is found to *plateau* in glycerol, as it does in nearly every other glass. That is, the additional modes populated with increasing temperature do not carry additional heat: they fail to propagate significantly. At low temperature, the ISTS measurement yields some unusual results showing a thermal conductivity which is very low, but rises with a temperature dependence more expected of a crystal. Possible origins of this observation are discussed.

The thermal conductivity experiment highlights the intriguing question that has yet to be satisfactorily answered: what happens to the heat-carrying phonons? Models have been developed which attribute the non-propagation of high-wavevector acoustic phonons to interactions with dynamical fluctuations and static structural heterogeneity,[4,5,6] and these models are used are used to reconstruct the bulk thermal conductivity, as discussed in Chapter 2. However the weakness of these models is that they have not been reliably tested by any convenient method, but instead rely on a bulk measurement to surmise the behavior of myriad multiple microscopic modes and interactions. The goal of the remainder of the thesis is to make a *direct* measurement of the microscopic modes of the glass, and to compare the result to the models which have stood for decades.

Chapter 4 describes the development and implementation of a high-frequency/high-wavevector acoustic method of probing the structure and dynamics of disordered materials. High frequency acoustic phonon properties are the key determinants of the thermal anomalies discussed in Chapters 2 and 3. In the method, a narrowband acoustic wave of a selected frequency ω is generated at the front of a sample of interest via combination of a novel ultrafast pulse shaper called the Deathstar that generates pulse sequences with widely tunable repetition rates, and a thin "transducer" aluminum film which converts the shaped optical waveforms into tunable-frequency acoustic waves that propagate into the sample. Chapter 5 describes the development, alignment, and calibration of a new interferometer[7] that is used for quantitative measurement of the transmitted acoustic amplitude at each selected frequency at the back of the sample. Taken together, the acoustic generation and detection methods enable direct examination of phonons throughout the high-frequency (GHz) range, approaching the "end of the acoustic branch."[8]

Chapter 6 presents the results of the high-frequency/high-wavevector experiment on silica glass, which was chosen because it is extremely well characterized by a broad variety of methods, including thermal conductivity, specific heat, and some high-frequency acoustic measurements, at many temperatures including the region of the thermal conductivity plateau. In this chapter reliable measurements are presented at narrowband acoustic frequencies up to 300 GHz. The frequency-dependent phonon mean free path is presented at both room temperature and 20 K, and results for both are shown to be surprising in the context of widely accepted modes and previously reported experimental results for thermal conductivity and high-frequency phonon behavior. The results demand a reconsideration of the mechanisms for reduced phonon and thermal transport in glassy materials.

The methods developed for study of high-frequency phonons are not restricted to glasses or even to solids. As an indication of future prospects, data from a polymer sample at temperatures below and above its glass transition temperature are presented. The results illustrate the possibility of direct assessment of high-frequency phonon propagation and the fast structural relaxation dynamics that mediate phonon propagation in the liquid state.

1.1 References

1. W.A. Phillips, Editor. *Amorphous Solids: Low Temperature Properties.* Springer-Verlag, Berlin, 1981.

2. Y. Yang, K.A. Nelson. Impulsive stimulated light scattering from glass-forming liquids: I. Generalized hydrodynamics approach. *Journal of Chemical Physics*, 103(18): 7722-7731, 1995.

3. R.C. Zeller, R.O. Pohl. Thermal conductivity and specific heat of noncrystalline solids. *Physical Review B*, 4(6): 2029-2041, 1971.

4. P.W. Anderson, B.I. Halperin, C. Varma. Anomalous low-temperature thermal properties of glasses and spin glasses. *Philosophical Magazine*, 25(8): 1-9, 1972.

5. W.A. Phillips. Tunneling states in amorphous solids. *Journal of Low Temperature Physics*, 7(3-4): 351-360, 1972.

6. D.A. Parshin. Soft Potential Model and Universal Properties of Glasses. *Physica Acta*, T49: 180-185, 1993.

7. C. Glorieux, J.D. Beers, E.H. Bentefour, K. Van de Rostyne, K.A. Nelson. Phase mask-based interferometer: Operation principle, performance, and application to thermo-elastic phenomena. *Review of Scientific Instruments*, 75(9): 2906-2920, 2004.

8. R. Vacher, E. Courtens, M. Foret. Are high frequency acoustic modes in glasses dominated by strong scattering or by lifetime broadening? *Philosophical Magazine B*, 79(11-12): 1763-1774, 1999.

Chapter Two

The Interaction of High-Frequency Acoustic Waves with Amorphous Materials

2.1 Introduction: Low-temperature Anomalies of Glasses

For decades, the unusual thermal properties of glasses at low temperatures have remained an unresolved and hotly debated issue in physical chemistry. Glasses, whose many classes comprise a significant subset of disordered materials, have anomalous specific heat, thermal conductivity and acoustic properties at low temperatures, compared to the crystalline forms of the same materials. An even more unusual result is that nearly every glass – network, metallic, ionic, molecular, and polymer – exhibits *quantitatively comparable* values of these anomalous properties, usually within an order of magnitude.[1,2,11] The "anomalous" properties are those related to the propagation of phonons, or acoustic waves, through the glass. Their universal observation implicates the intrinsic disorder of the glass as modifying the transport of energy by the phonons. Probing and understanding the nature of this modification is the main goal of this thesis. Understanding the relationship between the microscopic dynamical and structural features of the glass, the measurable specific heat and thermal conductivity, and the high frequency acoustic spectrum expected based on these features measurements, is the goal of this chapter.

2.2 Modeling the Phonon-Structure Interaction

The interactions of acoustic phonons with microscopic features of the glass have been strongly implicated in the anomalous macroscopic properties. For example, the bulk heat capacity C_p of a crystal increases rapidly with temperature, $C_p \sim T^3$, as more and higher energy phonon modes become available to carry heat.[3] However, at the lowest temperatures C_p of the corresponding glass is much higher than that of the crystal, due to the presence of "excess" low-frequency phonon modes, as shown in Figure 2.1. Without these modes, the graph would appear as a straight line. These modes are believed to arise from structural transitions between the numerous possible quasi-isoenergetic local configurations for particles in the glassy matrix, which can be described approximately as two-level systems. Around 10 K, an additional set of "excess" modes appear, as illustrated in Figure 2.1. These have been correlated with high-frequency modes which have been observed around 1 THz in inelastic x-ray,[4,5] inelastic neutron,[6,7] and light[8] scattering experiments as well as time-domain dielectric spectroscopy,[9] called the Boson peak. The excess heat capacity for a glass can be successfully described by:[11]

$$C(T) = a_1 T + a_3 T^3 \qquad 2.1$$

where the coefficient for the linear term is found to be remarkably similar for different classes of glasses,. indicating a similar density of "extra" modes arising from disorder. The origin of the numerous high frequency excitations is still unsatisfactorily resolved,[10] and their identification is one of the targets of this thesis. The excitations have been attributed to, e.g., the glass behaving simply like a disordered crystal wherein every atom is displaced from its lattice site,[11] from heterogeneity on extended molecular length scales affecting phonon transport on much longer length scales,[12] or from the hybridization of the heat-carrying acoustic phonons into vibrational modes at the molecular level.[13,14] At the most fundamental level, the common feature of these varied postulates is that the universally observed "extra" excitations, and the consequent macroscopic observables at low temperatures, arise from the structural, rather than chemical, character of the glass.

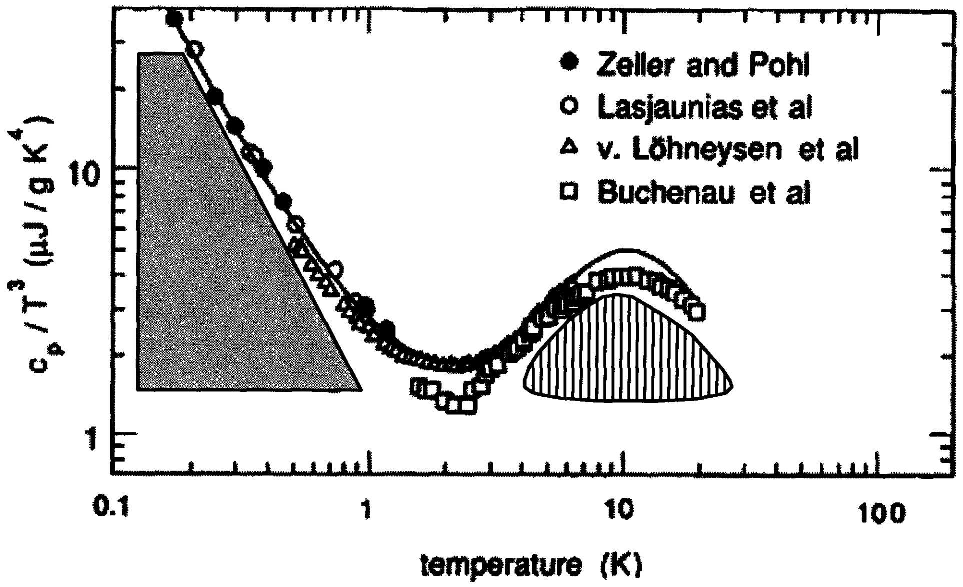

Figure 2.1. Excess low frequency (grey) and high frequency (striped) modes observed in the heat capacity of silica glass. Adapted from Reference 15.

The same microscopic properties that are implicated in the anomalies in C_p are also believed to drastically affect the values and temperature dependence of the thermal conductivity, κ. As shown in Figure 2.2, κ grows as T^3 in α-quartz, the crystalline form of SiO_2. The conductivity grows rapidly with temperature as an increasing number of unhindered system eigenmodes become thermally excited and therefore available to carry heat. In contrast, in the glassy state the conductivity is suppressed, grows more slowly as T^2, and in a temperature range near 10 K more or less ceases to increase with temperature, or "plateaus." The thermal excitation of the same distribution of acoustic phonons as exist in the crystal does not result in the same ability to transmit heat through the sample. At temperatures near the plateau, the high-energy thermally excited acoustic phonons *do not carry significant additional heat.* The appearance of excess modes in C_p at this same temperature, as shown above, implies that the thermal phonons are absorbed into these modes instead of propagating normally. These macroscopic observations[11] instigated the development of microscopic models for the interaction between high-frequency acoustic waves and the microscopic details of the glass, and to a large extent spurred the whole field of study of amorphous materials.

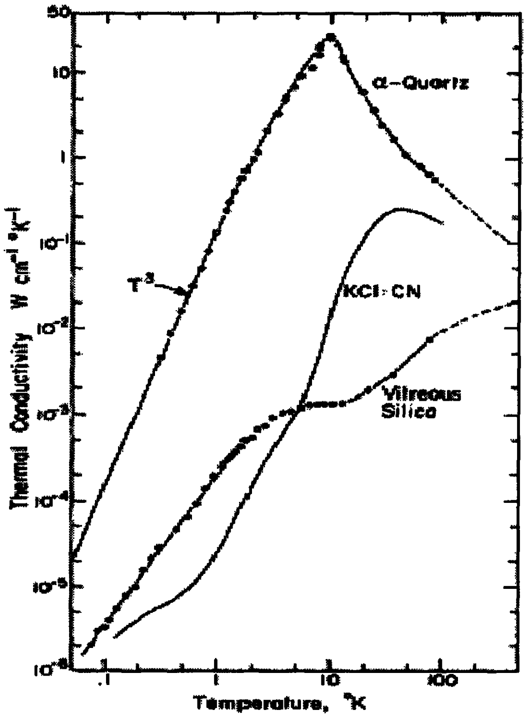

Figure 2.2. Experimentally measured thermal conductivity of crystalline and vitreous silica, as well as the mixed crystal KCl:CN. Adapted from Reference 11.

Even more remarkable than the thermal anomalies found in silica glass, are the facts that 1) that the thermal conductivity of nearly *all glasses* plateaus near 10 K, and 2) the value of the thermal conductivities of nearly *all glasses* lie within an order of magnitude of each other. Yet the anomalies do not simply arise from the presence of defects or impurities in the material (glasses possessing the maximum possible number of defects). A crystal with a high defect concentration, KCl:CN, also shown in Figure 2.2, has a lower κ value than the glass at low temperatures, and yet shows much faster growth in κ with temperature, implying good phonon propagation at high wavevectors. In the case of KCl:CN the suppression of κ has been shown to arise from resonant phonon scattering from CN quasirotational states; it is typical for a crystal bearing impurities to show anomalies that are specific to both the crystal and the defect.[38] For the amorphous case, the reduction in the thermal conductivity must arise from microscopic properties which are not very particular to the material, but instead are related to the inherent structural disorder.

This section connects the measurable bulk thermal conductivity to the microscopic processes and structures within the glass, using the "standard" tunneling model[16,17] to describe reductions in the mean free path of the heat-carrying acoustic phonons. It should be noted that this is one of several models for the glassy state.[18,19] However, its reliability for modeling anomalies in the thermal and low-frequency acoustic properties of amorphous materials at low temperatures makes it an excellent starting point for a discussion of the relation between microscopic (mostly unobservable)[20] and macroscopic (observable) properties. The thermal conductivity κ increases in a material as temperature is increased, as more and higher energy phonons become available to transport heat. This is expressed as the kinetic formula:[3]

$$\kappa(T) = \frac{1}{3}\sum_{\alpha} \int_{0}^{\tilde{\omega}_{\alpha,\max}} C_{\alpha}(\tilde{\omega},T) v_{\alpha} \lambda_{\alpha}(\tilde{\omega},T) d\tilde{\omega} \qquad 2.2$$

where the heat capacity $C(\tilde{\omega},T)$ expresses how much heat is carried by phonons of reduced frequency $\tilde{\omega} = \hbar\omega/k_B$. The phonon group velocity v gives the speed at which the phonons can move energy. It is generally not expressed as a frequency or temperature dependent quantity as experiment has shown it to be dispersionless in most measurements. This section treats it in the same manner, anticipating the direct experimental results on frequencies up to 300 GHz presented in Chapter 6, and in view of other results indicating little change in the speed of sound up to 400 GHz and over a wide temperature range.[26,21] The phonon mean free path $\lambda(\tilde{\omega},T)$ describes how far the phonons travel before being damped or scattered inside the material. The branch (phonon polarization) index is indicated for all parameters by α. The expression is integrated over all frequencies throughout the Brillouin zone, up to the Debye frequency $\tilde{\omega}_{\max}$, which is determined to be 360 K (~7.5 THz) for silica glass,[26] as compared with 552 K (~11.5 THz) for α-quartz crystal.[11] After summing over the transverse and longitudinal branch contributions, values are obtained that can be compared to the experimentally measured temperature-dependent thermal conductivity.

The quantity of primary interest for understanding the anomaly in κ is the phonon mean free path, $\lambda(\tilde{\omega},T)$, which expresses the ability of phonons to propagate through the material, and thereby to carry heat. In contrast, the heat capacity expresses the number of modes available to transport heat. The total temperature-dependent specific heat, including the density of states, of phonons of frequency $\tilde{\omega}$ is given by the Debye form:

$$C_\alpha(\tilde{\omega},T) = \frac{k_B{}^4}{2\pi^2\hbar^3 v_\alpha^3 T^2} \frac{\tilde{\omega}^4 e^{\tilde{\omega}/T}}{(e^{\tilde{\omega}/T}-1)^2} \qquad 2.3$$

Clearly the total heat capacity is dominated by the highest frequency phonons.. This implies that the strongest modifications to κ are related to these high frequency phonons. Equations 2.2 and 2.3 may be simplified somewhat by averaging the contributions from the longitudinal and transverse branches, so that $v_\alpha \rightarrow v$:

$$\frac{1}{v^2} = \frac{1}{3}\left(\frac{1}{v_l{}^2} + \frac{1}{v_t{}^2}\right) \qquad 2.4$$

Experiment indicates the validity of this approximation in a glass, though in a crystal anisotropy precludes its use..

The variations in the phonon mean free path $\lambda(\tilde{\omega},T)$ owing to microscopic details of an amorphous material, using Equation 2.2 to determine the resulting thermal conductivity, are the key feature of the tunneling model. These contributions include: phonon-mediated tunneling between minima of structural two-level systems, $\lambda_{res}(\tilde{\omega},T)$; thermally-activated relaxation processes, $\lambda_{rel}(\tilde{\omega},T)$; and the Rayleigh scattering of phonons from microscopic density fluctuations arising from structural inhomogeneities, $\lambda_{ray}(\tilde{\omega})$. Lastly, λ_{min} accounts for the fact that a propagating phonon mode with wavelength shorter than the length of a minimal structural unit cannot be supported in the material. λ_{min} is calculated using the Debye temperature from Equation 2.2, and is found to be ~0.6 nm in silicate glasses, ~1.1 nm in amorphous polymers, and ~0.4 nm in metallic glasses.. This is comparable to the size of a crystalline unit cell of the same material.[22] The total reduction in the mean free path is described by:[29]

$$\lambda(\tilde{\omega},T)=\left(\lambda_{res}^{-1}(\tilde{\omega},T)+\lambda_{rel}^{-1}(\tilde{\omega},T)+\lambda_{ray}^{-1}(\tilde{\omega})\right)^{-1}+\lambda_{min} \tag{2.5}$$

The specifics of the contributions to $\lambda(\tilde{\omega},T)$ are described individually below. Again, while there are alternate models, the tunneling model description of the microscopic features that impact the bulk thermal properties of a glass does an excellent job of duplicating most of the key observed low-temperature thermal and low-frequency acoustic anomalies.

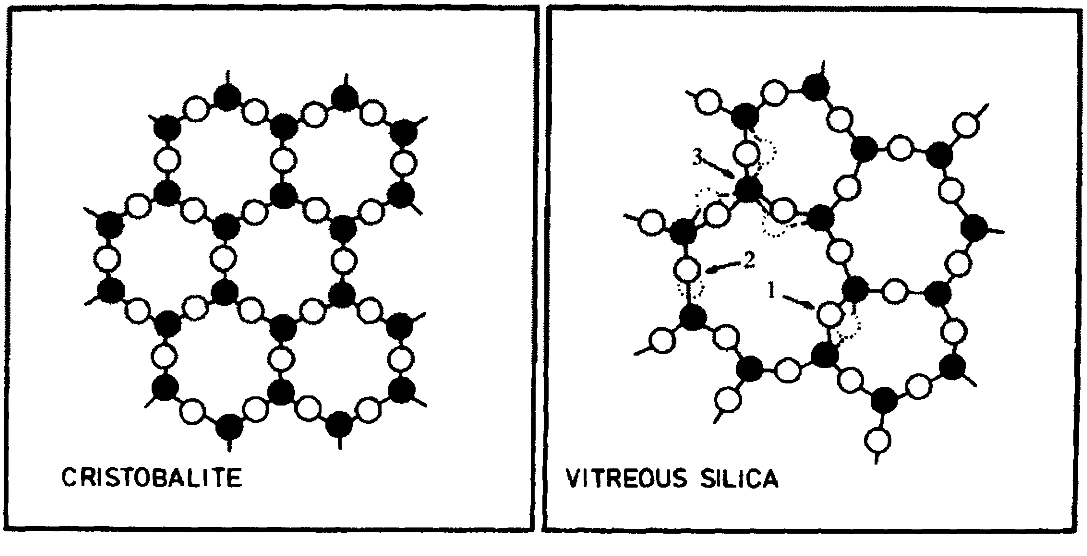

Figure 2.3. Structure of crystalline and vitreous silica, and three possible two level systems indicated by 1, 2, and 3 as described in the text. Adapted from Reference 23.

At very low temperatures, T<5 K, the thermal conductivity of the glass is suppressed by more than an order of magnitude and grows more slowly with temperature than that of the crystal, as T^2 instead T^3. A large amount of experimental evidence[24] suggests that a wide distribution of structural two-level systems (TLS) interacts with thermal phonons, reducing $\lambda(\tilde{\omega},T)$. While the true identity of the TLS remains to be conclusively proven, the means by which they arise from disorder are illustrated in Figure 2.3, which contrasts the structures of cristobalite, a crystalline form of SiO_2, and vitreous silica. Full circles indicate silicon atoms and open circles oxygen atoms. While the crystal has only a single state, the disorder in vitreous silica makes possible a number of "defect modes" marked by the numbers 1, 2, and 3, which are examples of possible TLS. The motion indicated by "1" is the transverse motion of an oxygen atom in a double-well potential. "2" is motion between two other minima, but in the bond direction. "3" shows the rotation of an SiO_4 tetrahedron..

All of these motions can approximately be described as occurring within double-well potentials, as shown in Figure 2.4. The states are nearly isoenergetic, but are separated by a small energy difference Δ and barrier height V. At temperatures low enough that the dominant thermal phonon energies are much smaller than the barrier between the states, $V \gg 3k_BT$, only the ground states of the wells are occupied, described by energy $\hbar\Omega/2$. The two states have a small population difference ΔN. Phonons of energy $\Delta_0=\hbar\Omega e^{-\mu}$ resonantly mediate tunneling between the two states. The overlap μ between the two states[24] is related to the separation d between the wells, the mass m of the tunneling "particle," and the barrier height, $\mu=d(2mV/\hbar)^{1/2}$. The resulting reduction in the phonon mean free path is expressed by:

$$\lambda_{res}^{-1}(\tilde{\omega},T) = A\tilde{\omega}\tanh\left(\frac{\tilde{\omega}}{2T}\right) \tag{2.6}$$

where the constant A describes the coupling between the TLS and acoustic phonons. This can be expressed as:

$$A = \frac{\pi k_B \bar{n}_0 \gamma^2}{\hbar \rho v^3} \tag{2.7}$$

where ρ is the material density, $\bar{n}_0$ is the average density of states (DOS) of TLS, and γ describes the TLS-phonon coupling constant..

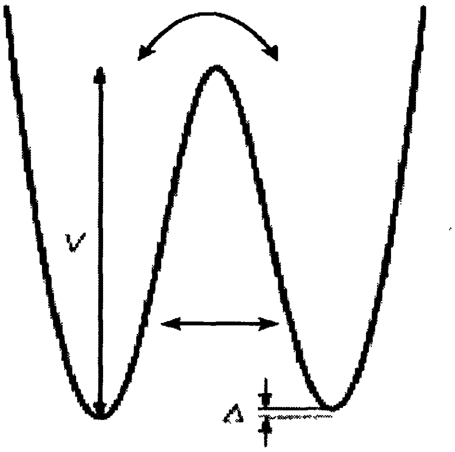

Figure 2.4. Asymmetric double-well potential with barrier height V and minima energy difference Δ. Tunneling through barrier and transitions over barrier are shown. Adapted from Reference 25.

A key feature of the tunneling model is the assumption of a wide and flat distribution of TLS states. These arise from a constant (but unrelated) distribution of energy differences Δ and also of tunneling overlap terms λ between the states, which arise from a broad density of barriers V. These simple assumptions reproduce low-temperature thermal and low-frequency acoustic data remarkably well. However the physical basis of the assumption is debatable. The development of a model for the TLS distribution is limited by the lack of understanding of their origins. The value of A is usually determined phenomenologically by fitting the low-temperature part of the thermal conductivity curve, where this effect dominates.[26] The value of $\lambda_{res}(\tilde{\omega},T)$

described by Equation 2.6 is shown in Figure 2.5 at several temperatures. Frequency is given in Hz as well as in Kelvin. As the temperature is increased, $\lambda_{res}(\tilde{\omega},T)$ actually *increases* since the equilibrium population difference ΔN → 0, and while tunneling transitions between the states continue, phonon absorption due to this effect becomes negligible.[27]

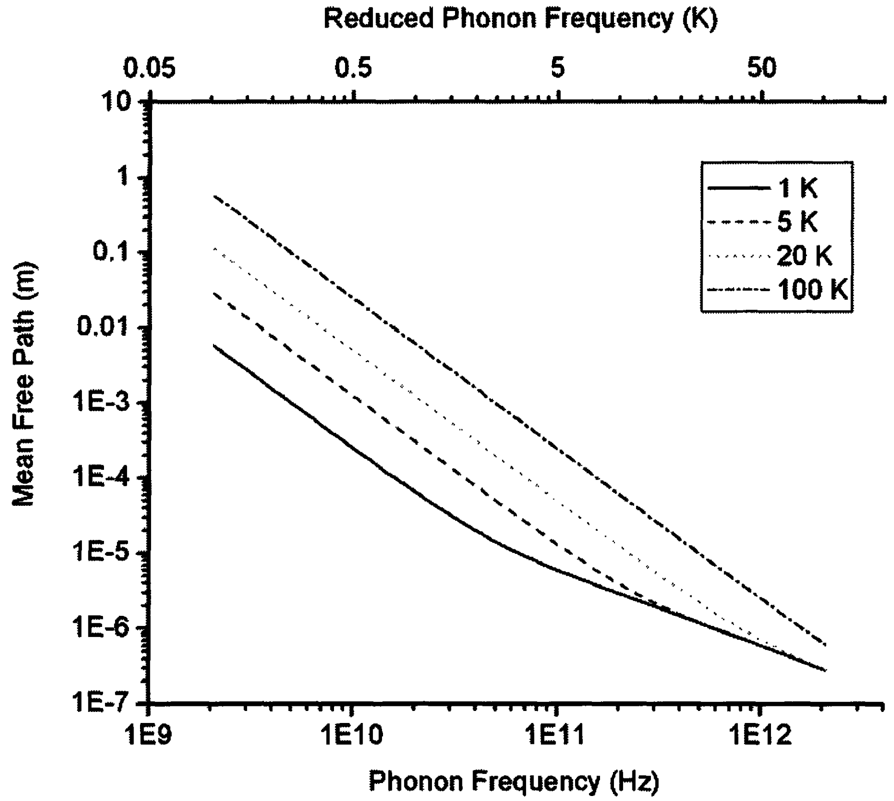

Figure 2.5. Phonon mean free path in glass due to resonant interactions with a flat distribution of structural two-level systems. Parameters used for SiO_2 from Reference 26: A=3.5x10^4 m^{-1}K^{-1}.

At higher temperatures where the energies of the dominant thermal phonons exceed the barrier height V illustrated in Figure 2.4, e.g. when $V \leq 3k_BT$, phonons induce thermally-assisted "hopping" transitions between the TLS minima. Because there are many different kinds of motion in a glass, and the thermal motion of the surrounding atoms disrupts coherent transitions of the two-level system,[25] there is a much more complicated distribution of activated processes than would be expected for a thermally activated Arrhenius-type process, which would yield

$\tau_{th}^{-1} = \tau_0^{-1}\exp\left(-V/k_B T\right)$. Because the tunneling model assumes a broad distribution of TLS asymmetries and energy splittings, their relaxations occur with a wide variety of characteristic time constants, described by:[24]

$$t_1^{-1} = \frac{\gamma^2 E^3}{2\pi\hbar^4\rho v^5}\coth\frac{E}{2k_B T} \qquad 2.8$$

where $E=(\Delta+\Delta_0^2)^{1/2}$ is the energy of the transition and the constants are the same as those for Equation 2.7. It should be noted that this relaxation time has an important impact on measurements of quantities that interact with the TLS. Depending on the experimental time scale, possibly only a subset of the TLS distribution would be probed, which can lead to some conflicting results for the same parameters measured by different techniques.. Implications of this effect are discussed in Chapter 3. The resulting attenuation of phonons interacting with this relaxation is given by:

$$\lambda_{rel}^{-1}(\tilde{\omega},T) = \frac{\overline{n}_0\gamma^2}{2k_B T\rho v^3}\int_0^{\infty} dE\,\mathrm{sech}^2\left(\frac{k_B E}{2\hbar^2 T}\right)\int_{t_{min}}^{\infty} dt\left(1-\frac{t_{min}}{t}\right)^{\frac{1}{2}}\left(\frac{k_B^2\hbar^{-2}\tilde{\omega}^2 t_1}{1+k_B^2\hbar^{-2}\tilde{\omega}^2 t_1^2}\right) \qquad 2.9$$

where the temporal dependence comes from the relaxation of TLS as in Equation 2.8, $t_{\min}$ is the shortest timescale of TLS motion, when $E=\Delta_0$, e.g. there is no asymmetry between the wells (but still overlap) and the longest relaxation time has been measured to be at least 10^4 seconds in silica glass (e.g., infinite for the current experimental methods.)[28] The delayed response of the TLS to the acoustic wave results in energy dissipation, and due to the non-resonant character of the interaction the relaxation absorption cannot be saturated.[24] The solutions of the integration in the high and low frequency or temperature limits of the phonon-relaxation interaction are considered separately. When the temperature is high, or the frequency is low, ωt_1 □ 1 and:

$$\lambda_{rel}^{-1}(\tilde{\omega},T)=\frac{A}{2}\tilde{\omega} \qquad 2.10$$

Here the coefficient A is the same as in Equation 2.7, and reflects the density of states as well as transition probability between the TLS. When the temperature is low, or the frequency is high, $\tilde{\omega}t_1$ □ 1 and:

$$\lambda_{rel}^{-1}(\tilde{\omega},T)=\frac{A}{2}BT^3 \qquad 2.11$$

Here the phonon mean free path experiences a strong reduction with increasing temperature. The coefficient B is, like A, related to the phonon-system coupling and the speed of sound in the material:

$$B=\frac{\pi k_B^2\gamma^2}{12\rho\hbar^3v^5} \qquad 2.12$$

The value of B can be somewhat more ambiguous to determine than A, because its contribution to the thermal conductivity curve is never isolated. It is typically found by fitting the curve above ~2 K and through the plateau region, where it overlaps with the structural term described below by Equation 2.14. The high and low temperature limits of Equation 2.9 may be combined with the interpolation formula:[29]

$$\lambda_{rel}^{-1}(\tilde{\omega},T)=\frac{A}{2}\left(\frac{1}{\tilde{\omega}}+\frac{1}{BT^3}\right)^{-1} \qquad 2.13$$

The reduction in $\lambda(\tilde{\omega},T)$ from the interactions in Equation 2.13 is shown in Figure 2.6.

As shown in Figure 2.2, the thermal conductivity is suppressed at low temperatures, and this is described well by the interactions summarized in Equations 2.6 and 2.13. However the *plateau* is totally unexplained by these. In order for κ to cease growing with increasing temperature, phonons of increasing energy that dominate the heat capacity near 10 K, in

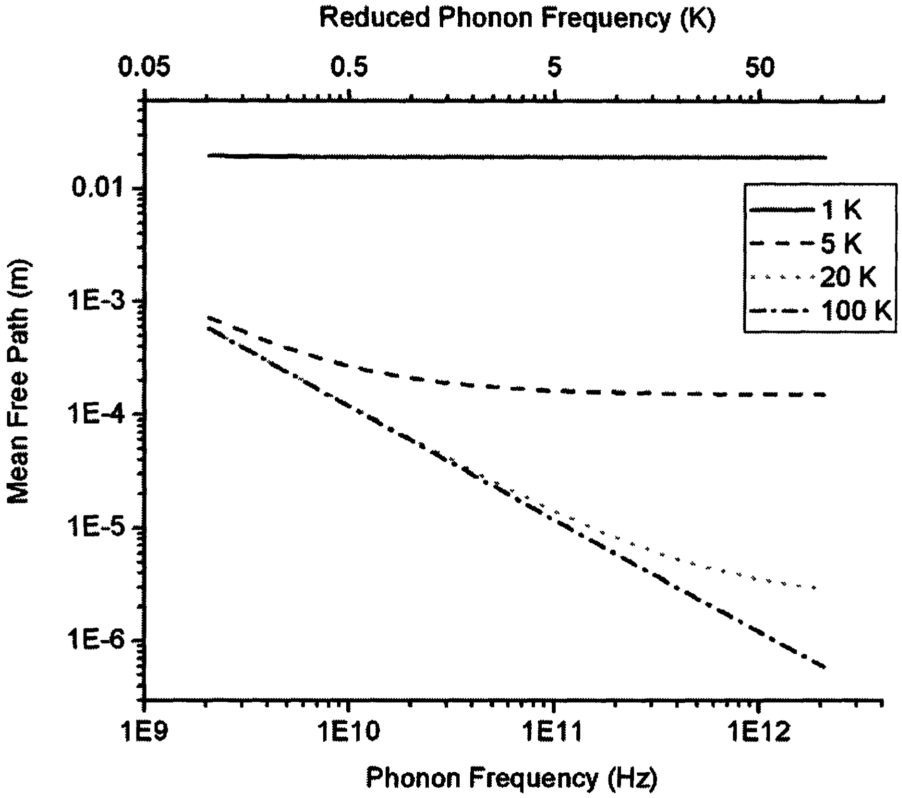

Figure 2.6. Phonon mean free path in glass due to relaxational interactions with a flat distribution of structural two-level systems. Parameters used for SiO_2 from Reference 26: A=3.5x10^4 $m^{-1}K^{-1}$, B=3x10^{-3} K^{-2}.

Equation 2.3, must stop propagating. Because glasses have in common that they 1) possess a large amount of disorder, and 2) exhibit quantitatively similar anomalies in properties mediated by phonon transmission, their heterogeneity is a likely source of interference with propagation. When a material appears homogeneous on the length scale of the acoustic wavelength, phonons propagates in the elastic limit, with minimal scattering. But as illustrated in Figure 2.3, disorder in the glass yields static density fluctuations at a molecular as well as an "extended" scale,. where clearly the elastic limit does not hold. Phonons with wavelengths of comparable scale to these heterogeneities will experience strong scattering in this limit, and will be "damped" rapidly (i.e. will have reduced mean free path) rather than propagate. The frequency Ω_{co} above which propagation stops is known as the Ioffe-Regel crossover, and has been demonstrated with inelastic x-ray scattering (IXS) to occur at a around 1 THz in SiO_2[30] and around 2 THz in *densified* SiO_2,[4,31] where the length scale of the heterogeneities is reduced via the densification process. These frequencies coincide with the frequencies of the phonons which dominate the thermal conductivity at the onset of the plateau, at ~10 K for SiO_2 as shown in Figure 2.2, and ~20 K for densified SiO_2. At these high acoustic frequencies, no periodic structure exists to support a propagating wave with a well defined wavevector. This has been called "the end of the acoustic branch."[32] Below Ω_{co} the elastic limit still is not entirely appropriate, and there is strong interaction between the phonons and the "extended" structure of the glass.[4] Between the elastic limit and the crossover, the tunneling model postulates Rayleigh scattering of phonons from the heterogeneous microscopic structure of the glass:

$$\lambda_{ray}^{-1}(\tilde{\omega}) = D\tilde{\omega}^4 \qquad 2.14$$

The interaction is with static structural variations, and is therefore temperature independent. The functional form expressed by Equation 2.14 is shown in Figure 2.7.

The Rayleigh scattering strength D is related to the magnitude of the density variations that cause scattering:

$$D = 8\left\langle\left(\frac{\Delta v}{v}\right)^2\right\rangle \frac{\bar{a}^3}{v_0^4}\left(\frac{k_B}{\hbar}\right)^4 \qquad 2.15$$

where $\left\langle(\Delta v/v)^2\right\rangle$ is the mean squared variation in the acoustic velocity due to heterogeneities, and ā is the average spatial extent of structural correlations in the glass.. The value of D can be though of as a first-order description of the "structure" of the glass. There has been heated debate on the physical significance of the phenomenologically determined magnitude of D, 120 $m^{-1}K^{-4}$, required to suppress κ to its typical value.:"[33] If one assumes an extremely disordered material, with correlation lengths on the order of the bond lengths, such as the Si-O bond

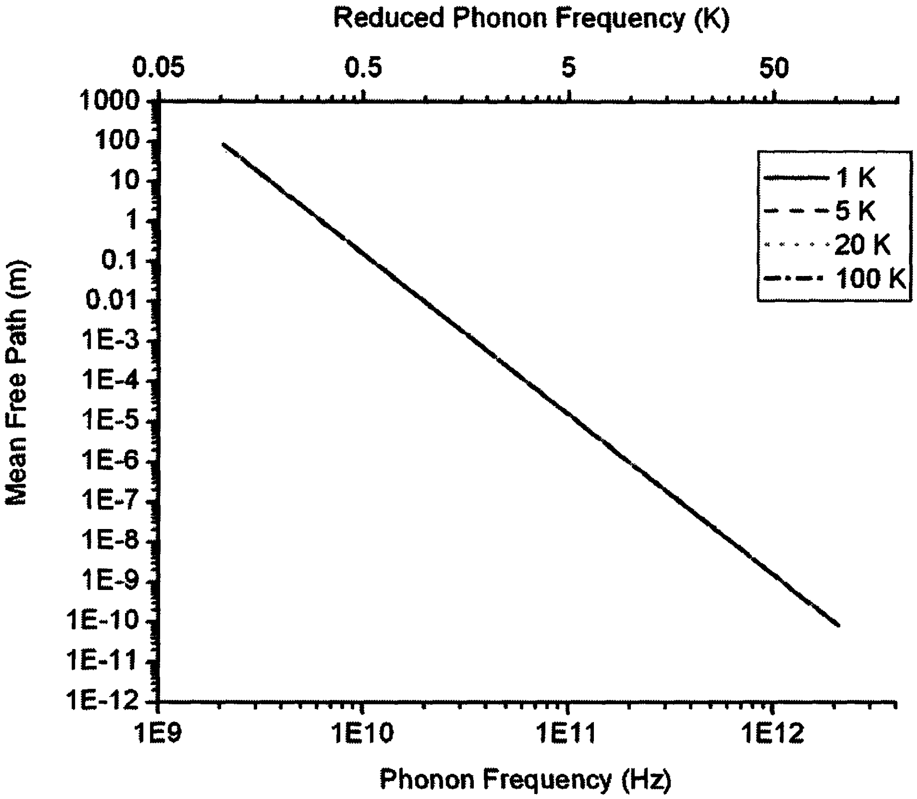

Figure 2.7. Phonon mean free path in glass due to phonon scattering from density fluctuations arising from heterogeneity. Parameters used for SiO_2 from Reference 12: D=120 $m^{-1}K^{-4}$

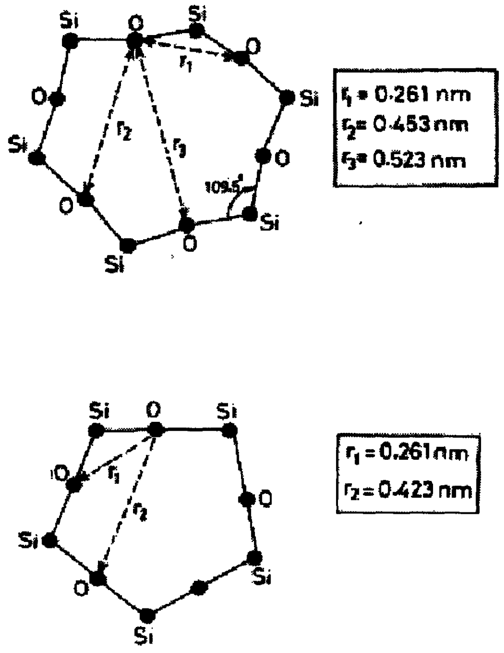
Si
O
Si
O
Si
O
Si
O
Si
O
Si
O
r_1
r_2
r_3
109.5°
r_1 = 0.261 nm
r_2 = 0.453 nm
r_3 = 0.523 nm
Si
O
Si
O
O
Si
O
Si
Si
r_1
r_2
r_1 = 0.261 nm
r_2 = 0.423 nm

Figure 2.8. Correlations within molecular rings containing five or six silicon atoms. Adapted from Reference 12.

distance 0.16 nm in silica glass, D is calculated to be an order of magnitude too low. But as shown in Figure 2.8, the local structure is correlated through the glassy network over a distance of several bond lengths, estimated in SiO_2 glass to be 0.45 nm. The variation in density owing to static heterogeneity on this length scale yields a contribution to D of 4 $m^{-1}K^{-4}$, underestimating D by a factor of 30. The remainder of the strong scattering can be estimated to result from a wide distribution of Si-O-Si bond angles, yielding strong variations in resistance to local shear or compression, reflected in a variation in Si-O-Si bending frequencies, that can yield the additional velocity fluctuation required to make D physical, $\left\langle (\Delta v/v)^2 \right\rangle = 0.1$.. However this value seems extremely large, so it is unclear whether this description is accurate. The dynamics in this picture, like those for the TLS, arise directly from the presence of disorder. Note that this particular explanation for the network glass would require translation to the microscopic picture of an ionic or molecular glass in order to yield quantitatively similar results for the bulk observable anomalies. The details of each material must be considered, but the general result is an intrinsic consequence of structural heterogeneity in the amorphous material.

The net effect of the interactions between heat-carrying acoustic phonons and the microscopic details of the glass, using Equations 2.6, 2.13, and 2.14 as described by the tunneling model, with a term for the minimum mean free path included as discussed above, is:

$$\lambda(\tilde{\omega},T) = \left(A\omega \tanh\left(\frac{\tilde{\omega}}{2T}\right) + \frac{A}{2}\left(\frac{1}{\tilde{\omega}} + \frac{1}{BT^3}\right)^{-1} + D\tilde{\omega}^4 \right)^{-1} + \lambda_{min} \qquad 2.16$$

The total phonon mean free path expressed by Equation 2.16 is shown in Figure 2.9 at several temperatures, in the "high frequency" range in which structural correlations and two level systems strongly mediate the propagation of acoustic waves. At low frequencies, there is some modest temperature dependence in $\lambda(\tilde{\omega},T)$ owing to TLS interactions, but all frequencies above

100 GHz are dominated by the Rayleigh scattering described by Equation 2.14, up to a cutoff around 1 THz above which propagation ceases entirely. Figure 2.9 shows the temperature variation of the mean free path for different frequency phonons. Again, frequencies above around 100 GHz have no temperature dependence, as the dominant phonon-material interaction is Rayleigh scattering arising from static structural variations.

2.3 Predictions for Macroscopic and Microscopic Behavior of Glasses

The greatest strength of the tunneling model is that despite its simplicity, it does an excellent job of reproducing most thermal and spectroscopic data obtained from many different classes of amorphous materials. However, it is disconcerting that different classes of measurements which purport to yield the same information on a particular material frequently give *conflicting* evidence for the validity of the tunneling model.[34] For example, broadband acoustic measurements[35] performed in silica glass up to frequencies of 440 GHz suggest that the phonon mean free path goes as ω^2, as opposed to ω^4 as indicated by the tunneling model and its agreement with thermal conductivity measurements. Phonon spectroscopy measurements in a similar range, using the superconducting tunnel junction technique, indicate a phonon mean free path at 1 K varying as ω^3 *or* as ω^6, a striking difference.[36,37] Somewhat worrisome also is the recent discovery of an amorphous solid, $CdGeAs_2$, that appears to completely *lack* structural two-level systems. In the same study it was also found that the gradual increase of defects in a crystal caused the development of glass-like thermal anomalies, despite the crystallinity.[38] These results imply that TLS do not naturally or necessarily arise from amorphous structure.

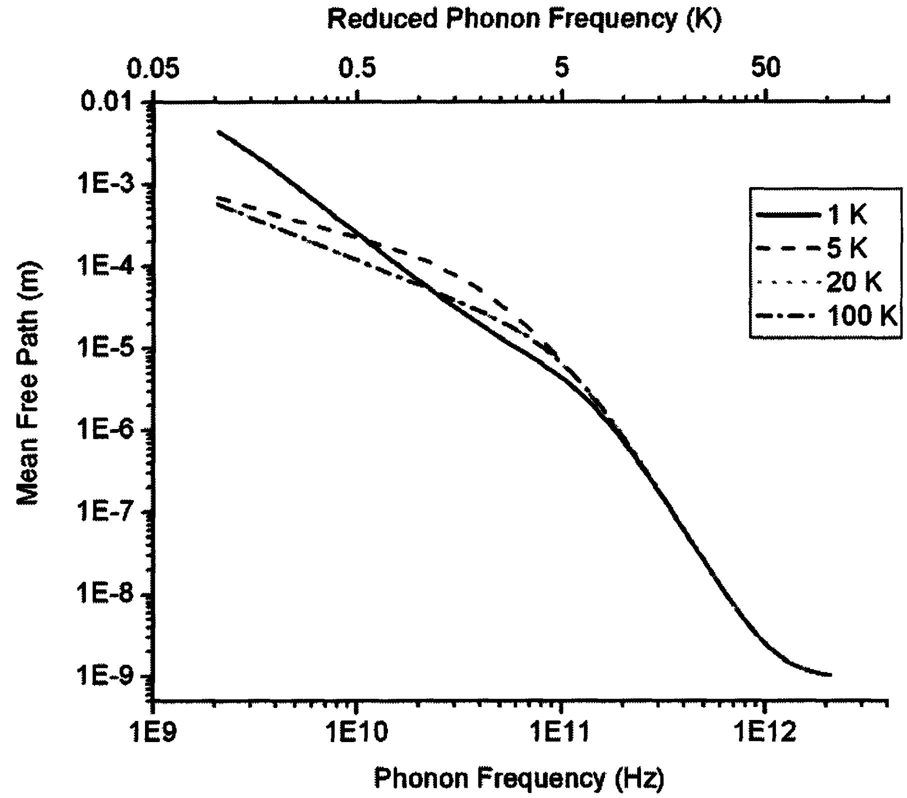

Figure 2.9. Frequency dependence of the phonon mean free path in glass, described by the tunneling model, using parameters for silica glass as described in the text.

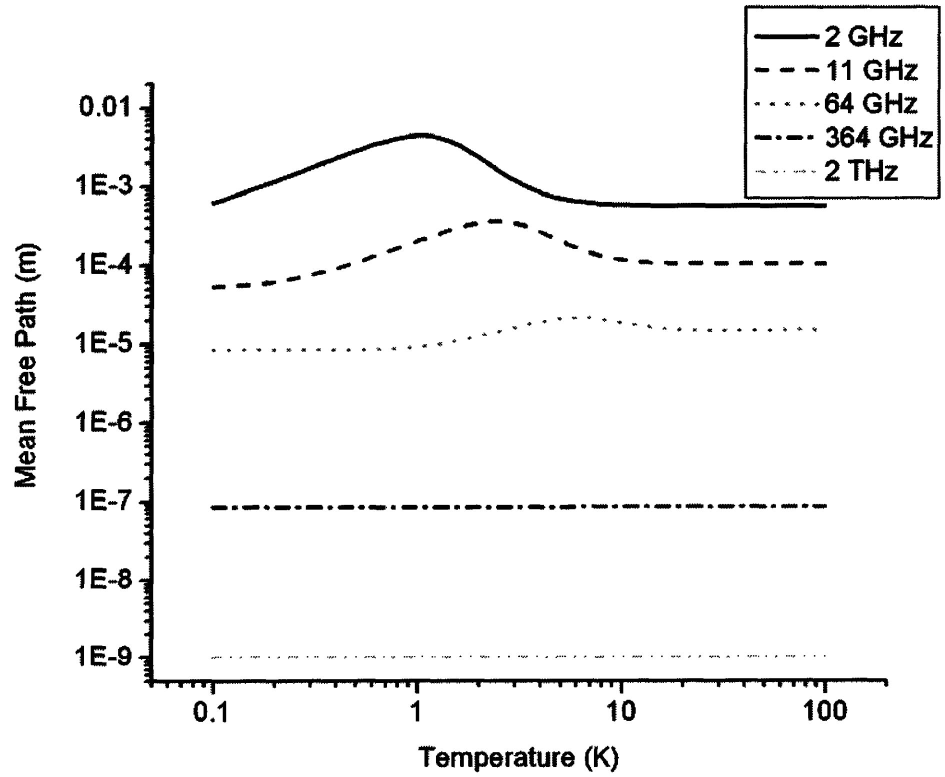

Figure 2.10. Temperature dependence of the phonon mean free path in glass, described by the tunneling model, using parameters for silica glass as described in the text.

Despite the inconsistencies, the tunneling model does reproduce the temperature dependence of the thermal conductivity very well, using Equations 2.2 and 2.3 with parameters described throughout the text, as shown in Figure 2.11. Data taken from Reference 12 are included in order to illustrate the excellent quantitative and qualitative agreement between the tunneling model and the measured conductivity. The small offset between the model and the data is an artifact resulting from the digitization of the data. An additional line showing the calculated conductivity without a contribution from Rayleigh scattering is included for comparison. This illustrates clearly that the testing of the tunneling model, or any model of low-temperature amorphous solids, and determination of model parameters through measurement of thermal conductivity is insufficiently stringent to give confidence in the model's validity or in the physically meaningful interpretation of its parameters.

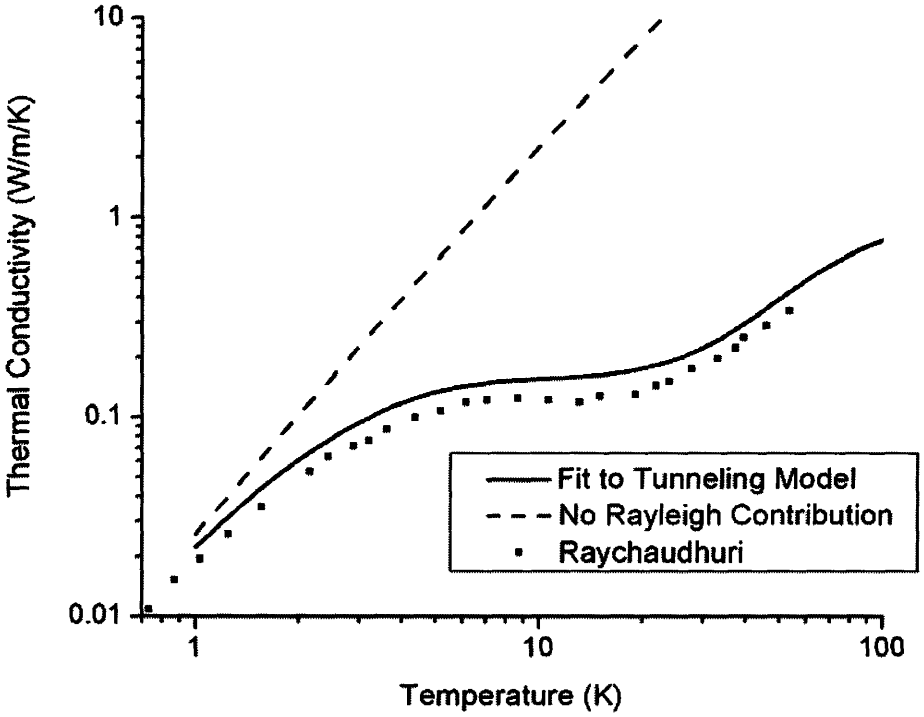

Figure 2.11. Thermal conductivity of a glass, calculated with the tunneling model using parameters for silica glass as described in the text. Data were adapted from Reference 12. The dashed line shows the conductivity of a material with no Rayleigh scattering contribution as described by Equation 2.14.

It is clear that accurate measurements of both bulk thermal conductivity and frequency-dependent phonon behavior are necessary for reliable understanding of glassy behavior. While the subsequent chapters of this thesis present a novel approach to the important problem of frequency-dependent phonon characterization, reliable measurement of thermal conductivity also presents significant challenges. Quantitative measurements have not been reported for most glass-forming materials. Given the similarities in behavior among glasses with widely varying microscopic structures, measurements are needed a wide range of samples. In Chapter 3, measurements are presented for a common organic glass former, glycerol, and the results are compared to the model described in this chapter. As will be illustrated, the most notable weakness of the tunneling model and the conventional determination of its parameters is that they rely upon bulk measurement of very few macroscopic parameters to characterize the results of several processes, each of which is the result of a weighted average of microscopic parameters and phonon characteristics. A direct measurement of the phonon properties as a function of frequency and temperature would far more incisively reveal the phonon-material interactions; as mentioned before, attempts to date of such measurements have frequently given conflicting results with each other and with the tunneling model. The development of a novel technique to directly generate the acoustic phonons in the crucial frequency range presented in Figure 2.9 is the subject of Chapter 4, and new data on their interactions with microscopic processes in silica glass is presented in Chapter 6.

2.4 References

---

1. R.O. Pohl, X. Liu, E. Thompson. Low-temperature thermal conductivity and acoustic attenuation in amorphous solids. *Reviews in Modern Physics*, 74(4): 991-1013, 2002.

2. J.J. Freeman, A.C. Anderson. Thermal conductivity of amorphous solids. *Physical Review B*, 34(8): 5684-5690, 1986.

3. N.W. Ashcroft, N.D Mermin, *Solid State Physics*. Saunders College, Fort Worth, 1976.

4. B. Rufflé, M. Foret, E. Courtens, R. Vacher, G. Monaco. Observation of the onset of strong scattering on high frequency acoustic phonons in densified silica glass. *Physical Review Letters*, 90(9): 095502, 2003.

5. G. Ruocco, F. Sette, R. Di Leonardo, D. Fioretto, M. Krisch, M. Lorenzen, C. Masciovecchio, G. Monaco, F. Pignon, T. Scopigno. Nondynamic origin of the high-frequency acoustic attenuation in glasses. *Physical Review Letters*, 83(26): 5583-5586, 1999.

6. D. Engberg, A. Wishnewski, U. Buchenau, L. Börjesson, A.J. Dianoux, A.P. Sololov, L.M. Torrell. Origin of the boson peak in a network glass B_2O_3. *Physical Review B*, 59(6): 4053-4057, 1999.

7. A. Wischnewski, U. Buchenau, A.J. Dianoux, W.A. Kamitakahara, J.L. Zaretsky. Sound-wave scattering in silica. *Physical Review B*, 57(5): 2663-2666, 1998.

8. N.V. Surovtsev, J.A.H. Wiedersich, V.N. Novikov, E. Rossler, A.P. Sokolov. Light scattering spectra of fast relaxation in glasses. *Physical Review B*, 58(22): 14888-14891,1998.

9. S. Kojima, M. Wada Takeda, S. Nishizawa. Terahertz time domain spectroscopy of complex dielectric constants of boson peaks. *Journal of Molecular Structure*, 651-653: 285-288, 2003.

10. W.A. Phillips, Editor. *Amorphous Solids: Low Temperature Properties.* Springer-Verlag, Berlin, 1981.

11. R.C. Zeller, R.O. Pohl. Thermal conductivity and specific heat of noncrystalline solids. *Physical Review B*, 4(6): 2029-2041, 1971.

12. A.K. Raychaudhuri. Origin of the plateau in the low-temperature thermal conductivity of silica. *Physical Review B*, 39(3): 1927-1931, 1989.

13. A. Jagannathan, R. Orbach, O. Entin-Wohlman. Thermal conductivity of amorphous materials above the plateau. *Physical Review B*, 39(18): 13465-13477, 1989.

14. M. Foret, R. Vacher, E. Courtens, G. Monaco. Merging of the acoustic branch with the boson peak in densified silica glass. *Physical Review B*, 66(2): 024204, 2002.

15. J.C. Lasjaunias, A. Ravex, M. Vandorpe, S. Hunklinger. Density of low-energy states in vitreous silica – Specific heat and thermal conductivity down to 25 mK. *Solid State Communications*, 17(9): 1045-1049, 1975.

16. P.W. Anderson, B.I. Halperin, C. Varma. Anomalous low-temperature thermal properties of glasses and spin glasses. *Philosophical Magazine*, 25(8): 1-9, 1972.

17. W.A. Phillips. Tunneling states in amorphous solids. *Journal of Low Temperature Physics*, 7(3-4): 351-360, 1972.

18. D.A. Parshin. Soft Potential Model and Universal Properties of Glasses. *Physica Acta*, T49: 180-185, 1993.

19. U. Buchenau. Dynamics of glasses. *Journal of Physics: Condensed Matter*, 13: 7827-7846, 2001.

20. Please refer to Chapter 6 for a discussion on the observable microscopic properties of glasses.

21. B. Golding, J.E. Graebner, R.J. Schutz. Intrinsic decay lengths of quasimonochromatic phonons in a glass below 1 K. *Physical Review B*, 14(4): 1660-1662, 1976.

22. C. Kittel. Interpretation of the thermal conductivity of glasses. *Physical Review*, 75(6): 972-974,1949.

23. S. Hunklinger, W. Arnold. *Physical Acoustics, Principles and Methods, Volume XII.* W.P. Mason, R.N. Thurston, Editors. Academic Press, New York, 1976.

24. S. Hunklinger, A.K. Raychaudhuri. *Progress in Low Temperature Physics, Volume IX.* D.F. Brewer, Editor. Elsevier, Amsterdam, 1986.

25. S. Rau, C. Enss, S. Hunklinger, P. Neu, A. Würger. Acoustic properties of oxide glasses at low temperatures. *Physical Review B*, 52(10): 7179-7194, 1995.

26. D.P. Jones, W.A. Phillips. Thermal conductivity of vitreous silica. *Physical Review B*, 27(6): 3891-3894, 1983.

27. R.B. Kummer, R.C. Dynes, V. Narayanamurti. Fast-time heat capacity in amorphous SiO_2 using heat-pulse propagation. *Physical Review Letters*, 40(18): 1187-1190, 1978.

28. J. Zimmermann, G. Weber. Thermal relaxation of low-energy excitations in vitreous silica. *Physical Review Letters*, 46(10): 661-664, 1981.

29. J. Jäckle. G.H. Frischat, Editor. *The Physics of Non-Crystalline Solids, Fourth International Conference.* Trans Tech Publications, Rockport, 1976.

30. M. Foret, E. Courtens, R. Vacher, J.-B. Suck. Scattering investigation of acoustic localization in fused silica. *Physical Review Letters,* 77(18): 3831-3834, 1996.

31. E. Rat, M. Foret, E. Courtens, R. Vacher, M. Arai. Observation of the crossover to strong scattering of acoustic phonons in densified silica. *Physical Review Letters,* 83(7): 1355-1358, 1999.

32. E. Courtens, M. Foret, B. Hehlen, R. Vacher. The vibrational modes of glasses. *Solid State Communications,* 117(3): 187-200, 2001.

33. M. Dutta, H.E. Jackson. Low-temperature thermal conductivity of amorphous silica. *Physical Review B,* 24(4): 2139-2146, 1981.

34. For a survey of conflicting experimental results, please see: T. Nakayama. Boson peak and terahertz frequency dynamics of vitreous silica. *Reports on Progress in Physics,* 65(8): 1195-1242, 2002.

35. T.C. Zhu, H.J. Maris, J. Tauc. Attenuation of longitudinal-acoustic phonons in amorphous SiO_2 at frequencies up to 440 GHz. *Physical Review B,* 44(9): 4281-4289, 1991.

36. W. Dietsche, H. Kinder. Spectroscopy of phonon scattering in glass. *Physical Review Letters,* 43(19): 1413-1417, 1979.

37. A.R. Long, A.C. Hanna, A.M. MacLeod. The scattering of phonons in thin films of amorphous silica. *Journal of Physics C: Solid State Physics,* 19: 467-485, 1986.

38. R.O. Pohl, X. Liu, R.S. Crandall. Lattice vibrations of disordered solids. *Current Opinion in Solid State and Materials Science,* 4: 281-287, 1999.

Chapter Three

Low Temperature Thermal Anomalies of Glycerol

3.1 Introduction

The subject of this chapter is the anomalous low-temperature thermal conductivity of the molecular glass glycerol, which is an extremely well characterized material above its glass transition temperature T_g=180 K. The thermal conductivity is of particular interest because it provides an indirect measurement of the underlying structure and dynamical processes in the glass, as described in detail in Chapter 2. The phonons that carry heat through a glass are absorbed and scattered by dynamical processes and static heterogeneities within the material, resulting in a sharp reduction in the thermal conductivity of the glass relative to that of its corresponding crystal. By modeling the possible microscopic phonon-material interactions, one can hope to understand the anomalous bulk conductivity. However, conventional determination of the thermal conductivity can present many challenges. It usually involves some variation of preparing a bulk sample, heating one end of it, and measuring the time-dependent temperature rise at the other end.[1,2] To quantify the conductivity, the contribution from any sample holder must be independently measured and subtracted, any radiative (photon) heat transfer contribution eliminated, and then the non-exponential time-dependent temperature rise at thermometers placed at different locations in the sample must be modeled.

Here a different class of conductivity measurements, based on the well-established impulsive stimulated thermal scattering (ISTS)[3,4] technique, is exploited. ISTS is a non-contact method wherein the sample is gently heated by absorption of crossed laser pulses, and the resulting spatially periodic thermal expansion gives rise to changes in the material's density and refractive index that form a bulk transient grating pattern. These changes are monitored via coherent scattering of probe laser light from this pattern. As the deposited heat is transported from grating peaks to (unheated) nulls by thermal diffusion processes, the scattered signal varies measurably in time. In this configuration, a well-defined wavevector magnitude q is determined by the spatial period of the excitation interference pattern, and therefore a simple single-exponential decay, directly related to the thermal diffusion constant, describes the time-dependent signal $I(t)$:

$$I(t) \sim e^{t/\tau_{th}} \tag{3.1}$$

The decay constant τ_{th} can be used directly to calculate the thermal diffusion constant D (unrelated to the Rayleigh scattering parameter discussed in Chapter 2) and the thermal conductivity κ, by:

$$\tau_{th}^{-1} = Dq^2 = \frac{\kappa q^2}{\rho C_p} \tag{3.2}$$

where the wavevector q, along which the diffusion constant is measured, may be varied by changing the experimental geometry in order to test for the expected q^{-2} dependence of τ_{th} and to reliably determine the value of κ. The density ρ and the heat capacity C_p are bulk values of the glass that may be obtained from independent measurements,[5] or from models. The relative simplicity of the ISTS measurement and its analysis permit versatile and reliable determination of κ in bulk and thin film samples.[6],[7] However, most ISTS measurements to date have been conducted on samples at relatively high temperatures, i.e. 77 K and above. Since the thermal expansion coefficients of materials are strongly reduced at low temperatures, so are ISTS signal levels. ISTS measurements at low temperatures therefore can be more difficult than those at elevated temperatures.

The class of molecular glasses is significantly underrepresented among studies of amorphous materials. The subject of the experiments presented in this chapter is the thermal conductivity of the molecular glass glycerol, $C_3H_5(OH)_3$. Glycerol is thoroughly studied above its glass transition temperature T_g~180 K, where it exhibits the two-step dynamics typical of a glass-forming liquid – a fast "β-relaxation" process that is often interpreted in terms of motions that do not disrupt intermolecular networks, i.e. the motions of a particle inside its cage, and a slow and strongly temperature-dependent "α-relaxation" process corresponding to the correlated motions of many particles.[8,9] The dynamics above T_g of a network (e.g., silicate) glass are characterized by an activation energy that is temperature independent and by Arrhenius-like behavior, which arise from the relative simplicity of the intermolecular interactions determined by the covalent network. In particular, we expect in such "strong" glasses a relatively small number of deep local potential energy minima that control local structural arrangements. However the dynamics of a molecular liquid, shown in Figure 3.1, are complicated by the lack

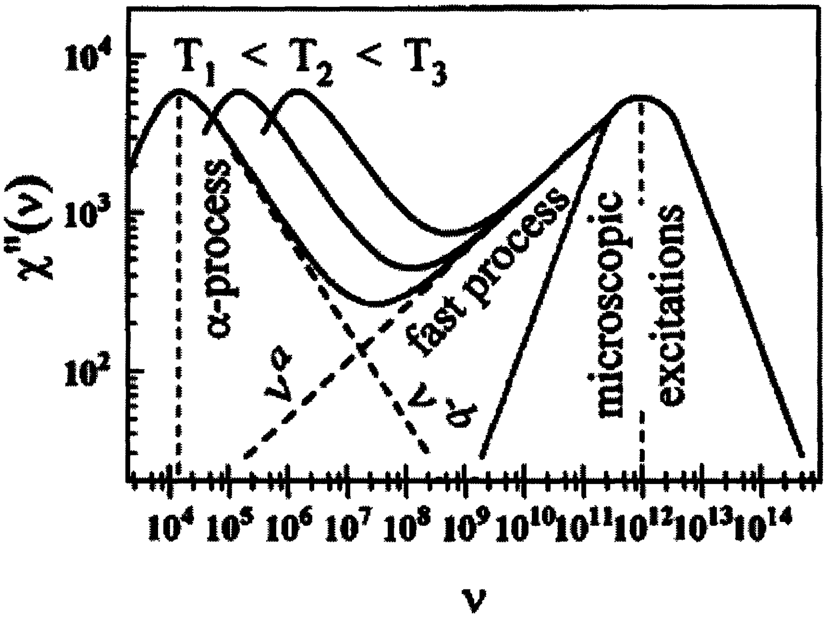

Figure 3.1. Dynamical ranges of temperature-dependent slow and fast processes in glass-forming liquids. Adapted from Reference 10

of a strong intermolecular potential, instead determined typically by weak van der Waals interactions. While the spectrum of a network glass above T_g would certainly be characterized by "fast" and "slow" dynamics, the temperature-dependent interrelationship is far less interesting and can be explained by simulations which describe the dynamics as transitions between two minima, separated by a barrier of energy E. More "fragile" glasses are expected to have energy landscapes with many shallow local minima of comparable energies, with a broad distribution of activation energies. Glycerol, with its hydrogen-bonded network, is intermediate between these two limiting cases.

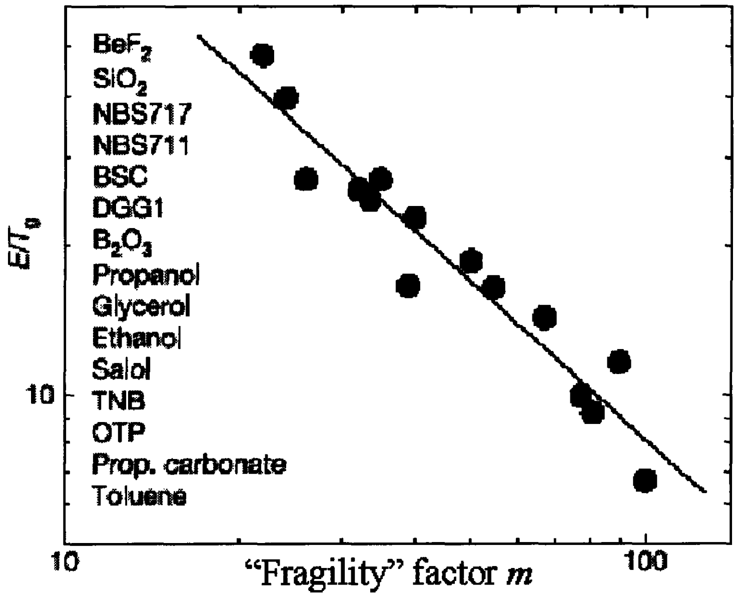

Figure 3.2. Relationship between high temperature activation energy E for correlated motion in the liquid state, the glass transition temperature T_g, and the "fragility" or weakness of interaction m between the particles. Adapted from Reference 11.

Like the tunneling model for glasses discussed in Chapter 2, the main theory[12] which describes these dynamics is hotly debated. The typical frequencies of these dynamics, along with the "microscopic excitations" described in Chapter 2 can be well-separated in time – by up to 12 orders of magnitude difference – but are still believed to couple to each other. Also debated is the connection between these complex liquid-state dynamics and the presence of the aforementioned thermal and acoustic anomalies in the glassy state.[13,14,15] For example, the onset of the glass transition T_g, where dynamics are dominated by high-frequency motion, has been found to be directly related to the activation energy E of correlated motion at high temperatures, similar to the barrier to motion between structural two-level systems in the glassy state, and to the "fragility" m, or weakness of intermolecular interaction, as shown in Figure 3.2. Because of their unusual properties and rich behavior, molecular glasses are in a sense the "quintessential" glass-formers.

However the nature of the microscopic excitations in a molecular glass has not been studied extensively. A recent and extremely thorough review of the acoustic and thermal properties of disordered solids[16] by one of the founders of the field was remarkably unable to locate a sound velocity for glycerol below T_g. A single measurement of its low-temperature thermal conductivity and heat capacity is found in the literature. This chapter describes the new use of an all-optical method to determine the low-temperature thermal conductivity of glycerol, as a representative of a wide class of hydrogen-bonded molecular glasses. The current result differs markedly from that of a more traditional experimental method.[17] The possible reasons for this difference are addressed experimentally and also in the framework of the model described in Section 2.2. The low temperature acoustic dispersion is also addressed in the 50-250 MHz range.

3.2 Impulsive Stimulated Thermal Scattering: Experiment and Results

Impulsive stimulated thermal scattering (ISTS) is a well established method of probing thermo-elastic phenomena in a wide variety of samples, on multiple timescales. Generally the technique involves heating of the sample in a spatially periodic pattern, by crossing two laser pulses inside the sample where they interfere and are partially absorbed. The resulting changes in the refractive index induced by the material response are probed by diffraction of variably delayed laser pulses, or, as in our case, of a continuous wave (cw) laser beam. The experimental layout is shown in Figure 3.3. A phase mask is used to diffract the short excitation laser pulse indicated in black (200 ps, λ=1064 nm, 500 μJ, from a home-modified Spectron Nd:YAG laser which is Q-switched, mode-locked, and cavity-dumped) into multiple orders. The phase mask (Pm) was designed[18] in order to maximize energy in the ±1 orders of diffraction, which are spatially filtered and crossed inside the sample by a two-lens imaging system. For this experiment L1 was a horizontally mounted cylindrical lens, f=15 cm, and L2 was a spherical lens, also f=15 cm. This resulted in an excitation spot which imaged the horizontal features of the phase mask with a roughly 1:1 ratio, and was vertically focused, with a total spot size of 2.5 mm x 100 μm.

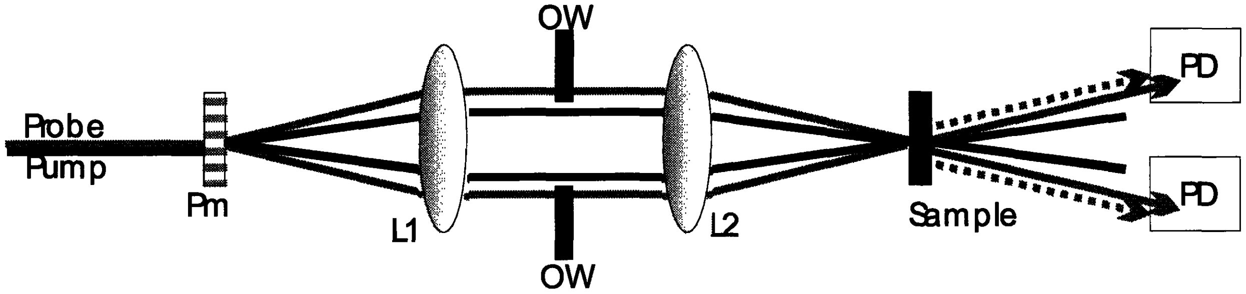

Figure 3.3. Transient grating experiment with differential optically heterodyned detection. Excitation beam is shown in black, probe beam in grey, and diffracted signal in dotted line. OW: optical window; Pm: phase mask of variable periodicity; L1 cylindrical lens, f=15 cm; L2 spherical lens, f=15 cm; PD: photodiode.

The grating spacing of the phase mask (1-100 μm) and the imaging ratio of the telescope define the angle Θ at which the two excitation beams cross, and determines the wavelength Λ of the interference pattern inside the sample:

$$\Lambda = \frac{\lambda}{2\sin\left(\Theta/2\right)} \qquad 3.3$$

The excitation wavevector is given by $q = 2\pi/\Lambda$, and can be easily varied between $6.3\text{x}10^4$ m^{-1} and $6.3\text{x}10^6$ m^{-1} by translating the phase mask to different etched patterns. The 1064 nm light is very weakly absorbed by the glycerol sample in the 2nd overtone of the OH stretch. The sudden heating causes rapid thermal expansion, which launches counter-propagating acoustic waves of wavelength Λ and frequency $f = v/\Lambda$. On a longer timescale, the deposited heat slowly diffuses from the heated peaks to the unheated nulls of the temperature grating. The thermal and acoustic responses modulate the refractive index of the glycerol, resulting a transient grating of wavevector magnitude q.

To monitor the time-dependent material response, a cw probe laser beam indicated in grey (532 nm, 30 mW, Coherent Verdi) is introduced to its own optimized phase mask collinearly and directly above that of the excitation beam. Likewise it is diffracted into many orders and the ±1 diffracted orders are selected and crossed inside the sample by a two-lens telescope, generating a second grating which is spatially overlapped with the excitation grating. The spatial phase of the probe grating may be varied relative to that of the excitation grating with the optical windows OW. The geometry ensures that the probe beams arrive at the Bragg angle of the transient grating inside the sample,[19] where a small amount of their light ($\sim 10^{-4}$-10^{-5}) is diffracted, as indicated by the dotted lines. The transmitted part of each probe beam is collinear with and phase-coherent with the diffracted signal from the other probe beam, for optically heterodyned detection of the signal. The signal in each beam is focused into one of two diodes in a custom-built differential detector (Cummings Electronics Labs, North Andover, MA). The two diodes have the same gain but are biased oppositely to each other, and the two signals are combined electronically. The signal intensity I_S^+ observed at the positively biased diode is given by the heterodyne equation:

$$I_S^+ = (\sqrt{I_R} + \sqrt{I_D})^2 = I_R + I_D + 2\sqrt{I_R I_D} \cos\Phi \qquad 3.4$$

where I_D is the intensity of the beam diffracted from the transient grating, I_R is the "reference" intensity of the undiffracted probe beam $(I_R - I_D \approx I_R)$, and Φ is the total optical phase difference between the diffracted and reference beams. The optical phase of the field in the (+) direction experiences a $\pi/2$ phase shift due to the static phase mask, and the field in the (-) direction experiences a $-\pi/2$ phase shift. Then they both experience an additional shift resulting from the spatial phase of the excitation grating pattern relative to the probe grating, which may be varied with the optical windows inserted in the probe beams. The signal intensity I_S^- observed at the negatively biased diode is given by:

$$I_S^- = -I_R - I_D - 2\sqrt{I_R I_D} \cos(\pi - \Phi) \qquad 3.5$$

The total phase difference may be optimized by rotating the optical windows to yield maximum differential signal when $\Phi = 0, \pi, 2\pi$, etc.:

$$I_S = I_S^+ + I_S^- = 4\sqrt{I_R I_D} \qquad 3.6$$

A traditional heterodyne detection scheme is described by Equation 3.4, where the reference beam intensity I_R adds to the signal an unavoidable background. In that case, I_R must usually be significantly attenuated in order to limit the amount of light (and the accompanying laser noise) that reaches the photodiode, and also to limit the electrical signal (and the accompanying electrical noise) that is then amplified (to a level that must be kept below the saturation or damage level) in a digitizing oscilloscope. However this requisite attenuation also reduces the heterodyne signal level, $2\sqrt{I_R I_D}$. In the differential detection geometry, far higher light levels of I_R ~10 mW could be introduced to both diodes, whose electrical outputs are added prior to processing by an on-board high-bandwidth (3 GHz) amplifier. The amplified signal is acquired and averaged by a fast digitizing oscilloscope (Tektronix TDS6000 series, 4GHz).

The optical geometry of ISTS is extremely well-suited to temperature-controlled measurements because it is non-contact and it allows an almost arbitrarily large distance between the final lens L2 and the sample. After alignment of the experiment on an unenclosed sample, a cryostat (Janis SVT-200, Wilmington, MA) with windows for optical access on four sides was inserted in the beam path, with the glycerol sample inside and in the plane of focus of L2. The cryostat was of a "sample-in-vapor" style, with the sample immersed in helium gas that had been heated to a desired temperature at a vaporizer. This eliminated any stringent requirements for thermal contact between the sample and coldfinger or temperature sensor. The temperature at both the sample and the vaporizer was monitored with silicon diodes (Lakeshore Cryotronics DT-670, Westerville, OH) and the heater output was controlled by a Lakeshore 331 temperature controller. The temperature at the sample was taken below 4.2 K by filling the sample chamber with liquid helium, sealing it, and then reducing the pressure above the liquid with a standard rotary pump. The glycerol sample cell was assembled by placing a ¼" thick 1" outside diameter rubber o-ring on a ¼" thick 1" diameter sapphire window, and filling it with anhydrous glycerol. A second sapphire window was placed on top of the o-ring, and the sandwiched assembly was held together with two metal plates and 4-40 screws. A new sample was made at the beginning of each cool-down cycle to avoid water contamination which occasionally resulted from condensation during the previous warm-up cycle because the sample is not kept under vacuum in this sort of cryostat.

Measurements requiring the sample to be submerged in liquid helium were problematic and required modification of the experiment. One of the benefits of ISTS is that the phase fronts of the excitation pulses arrive parallel to each other at the sample, resulting in a volume grating which can extend for several millimeters through the depth of the sample, especially if large excitation spots and small crossing angles are used.[18] It was found that this volume grating extended outside of the glycerol sample and generated low-frequency acoustic modes in the helium, as shown in Figure 3.7, which temporally overlapped with the thermal diffusion processes in the glycerol. In order to avoid signal contributions from the beams crossing inside the liquid, two additional modifications to the experiment had to be made to confine the excitation region inside the glycerol. First, an additional lens was included in the setup prior to the phase mask, which adjusted the horizontal size of the pump and probe spots in order to minimize the depth of overlap. A horizontally mounted cylindrical lens which focused the beams *into* the phase mask resulted in an excitation region at the sample which was roughly 150 μm x 100 μm. This introduced the added complication that as the phase mask was translated to smaller grating spacings, i.e. larger crossing angles, spherical aberrations as well as dichroic effects in L2 resulted in systematically poorer overlap between the pump and probe beams. Choice of a very large diameter lens L2 (3") reduced this effect somewhat. Alignment was carefully optimized by inserting a CCD camera in the sample plane, and ensuring that all beams overlapped over a wide range of grating spacings. As an additional precaution against beam overlap inside the liquid helium, sapphire windows of 3/8" thickness were glued to the outside of the sample cell. Despite this, some helium contribution to signal was observed at the lowest temperatures, and is presented slightly later in this section. Generally by careful data acquisition and analysis, the effect was minimized. It should be noted that the signal from liquid helium is not due to ISTS, since the excitation wavelength is not absorbed even weakly by the liquid helium. Instead, acoustic wave generation occurs due to impulsive stimulated Brillouin scattering (ISBS). This effect is normally considerably weaker than ISTS, but in the present case the ISTS signal is weaker than normal because of the weak absorption of 1.06 μm excitation light by the glycerol and the low thermal expansion constant of the sample at low temperatures. It is clear from the difficulty of avoiding the effect that ISBS signal is unusually strong in liquid helium, indicating a particularly strong electrostriction constant, or Brillouin scattering cross-section, in helium.[20]

The goal of this experiment is to measure the thermal conductivity, but the ISTS data also yield the acoustic velocity and (generally) attenuation rate as well. The time dependent signal is given by:.

$$I_S(t) = (A+B)e^{-t/\tau_{th}} - Ae^{-t/\tau_{ac}}\cos(2\pi ft) \qquad 3.7$$

Here A and B are the strengths of the thermal and acoustic parts of the signal, and are unrelated to the parameters of the tunneling model described in the previous chapter. The thermal diffusion time is given by τ_{th}, from which the thermal conductivity will be calculated, and the *apparent* acoustic damping rate is approximated by τ_{ac}. In the present case the apparent damping is a convolution of the actual damping rate α, which is exponential, and the loss of signal due to the propagation of the acoustic waves away from the probe region, which is Gaussian.. This effect can be seen below in Figure 3.15, which includes a fit of Equation 3.7 to the signal data. Signal from glycerol held inside a cryostat at 5.0 K is shown in Figure 3.4 on a linear scale to emphasize the single-exponential thermal decay, in Figure 3.5 on an expanded linear scale to

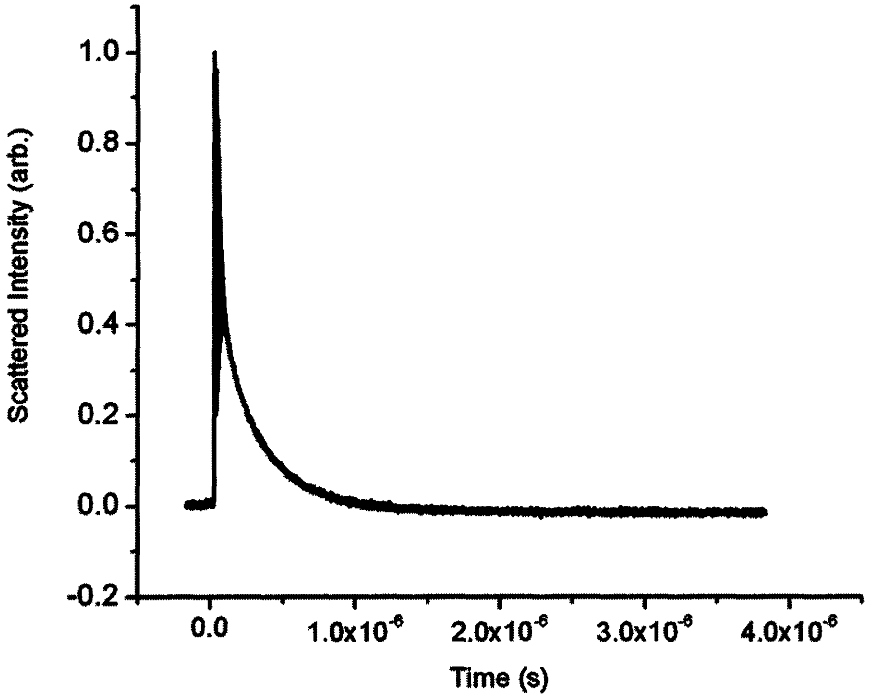

Figure 3.4. ISTS signal in glycerol at 5 K, 15 micron grating spacing, plotted on a linear scale to emphasize the single-exponential thermal decay.

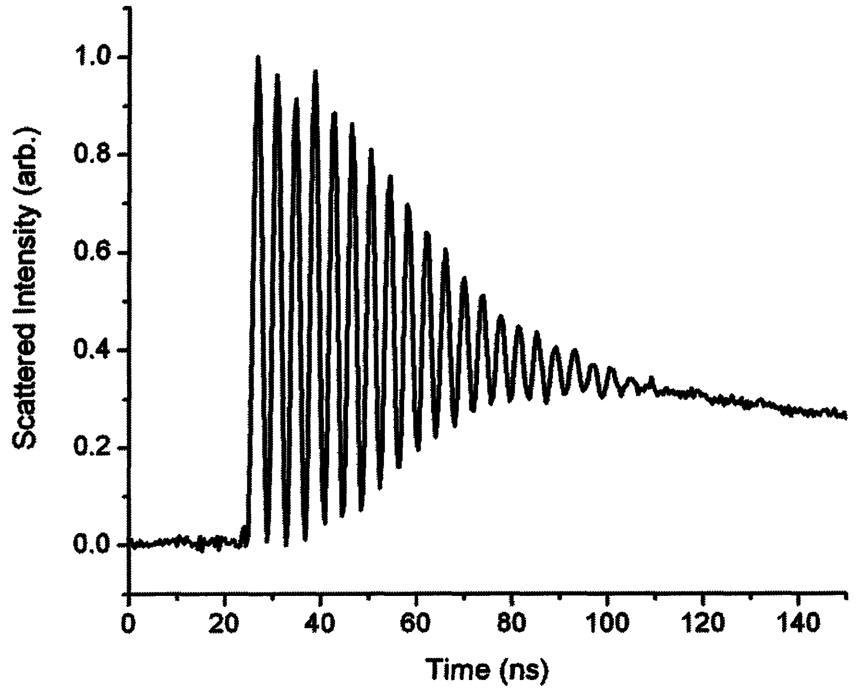

Figure 3.5. ISTS signal in glycerol at 5 K, 15 micron grating spacing, plotted on an expanded linear scale to emphasize the acoustic contribution to signal.

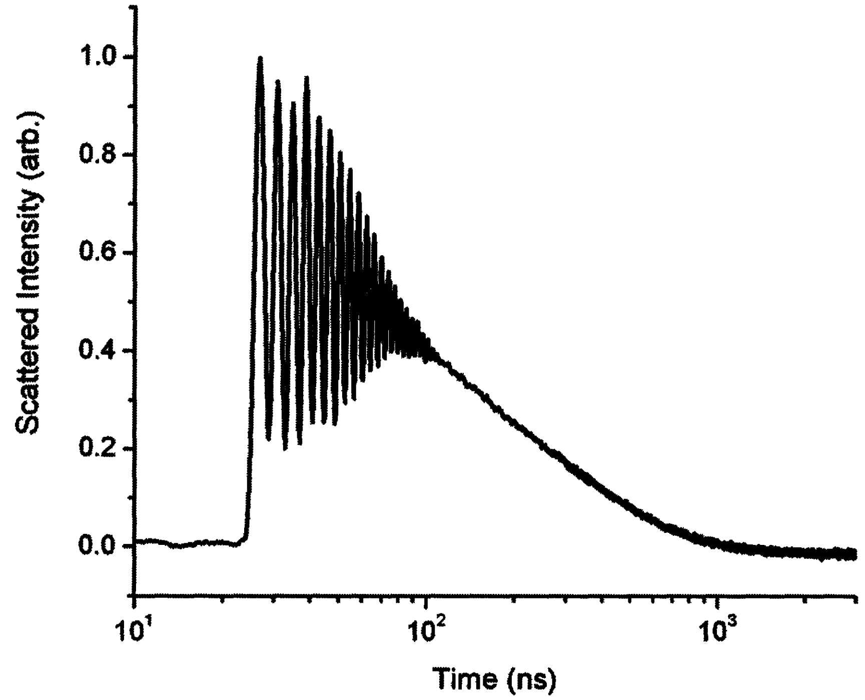

Figure 3.6. ISTS signal in glycerol at 5 K, 15 micron grating spacing, plotted on a logarithmic scale to emphasize the linearity of the single-exponential thermal diffusion contribution to signal.

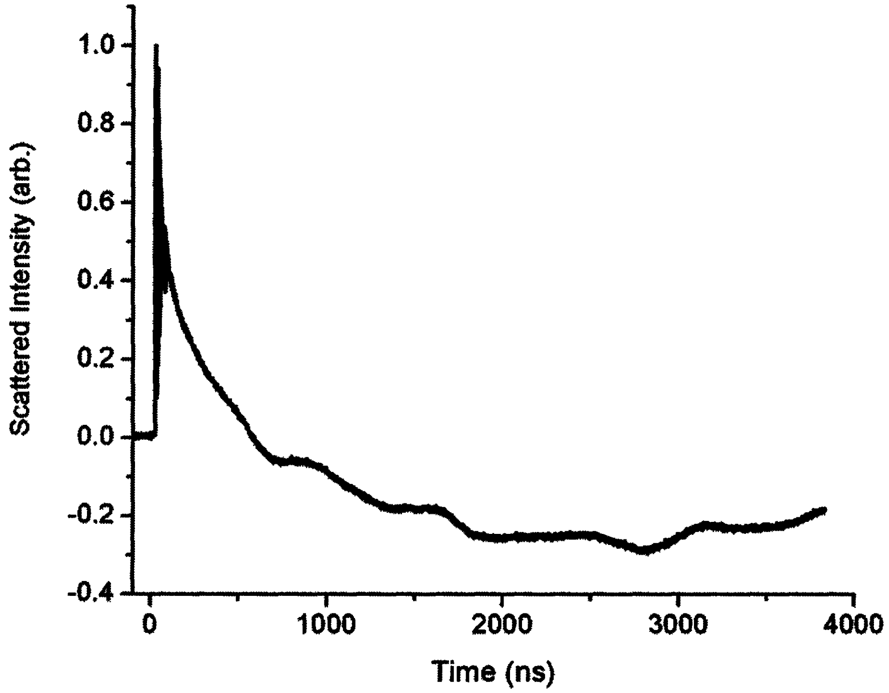

Figure 3.7. ISTS signal in glycerol at 1.8 K, 15 micron grating spacing, with strong contribution from liquid helium signal.

emphasize the acoustic oscillations, and in Figure 3.6, on a logarithmic scale to emphasize the linearity of the single-exponential thermal diffusion contribution to signal. As discussed previously, at very low temperatures strong signal contributions arise from excitation beam overlap inside of the liquid helium in which the sample is immersed; this effect is demonstrated in Figure 3.7.

The transient grating wavelength was carefully calibrated to within 1% accuracy prior to the experiment, by making the same ISTS measurement in ethylene glycol at 294 K (room temperature), but inside the cryostat with the same geometry as the low-temperature glycerol experiment. Ethylene glycol has a temperature-dependent acoustic velocity v_0 near room temperature given by:[21]

$$v_0 = \left(1.658\frac{km}{s}\right) - \left(2.1\times10^{-3}\frac{km}{sK}\times\left(T - 298\,K\right)\right) \tag{3.8}$$

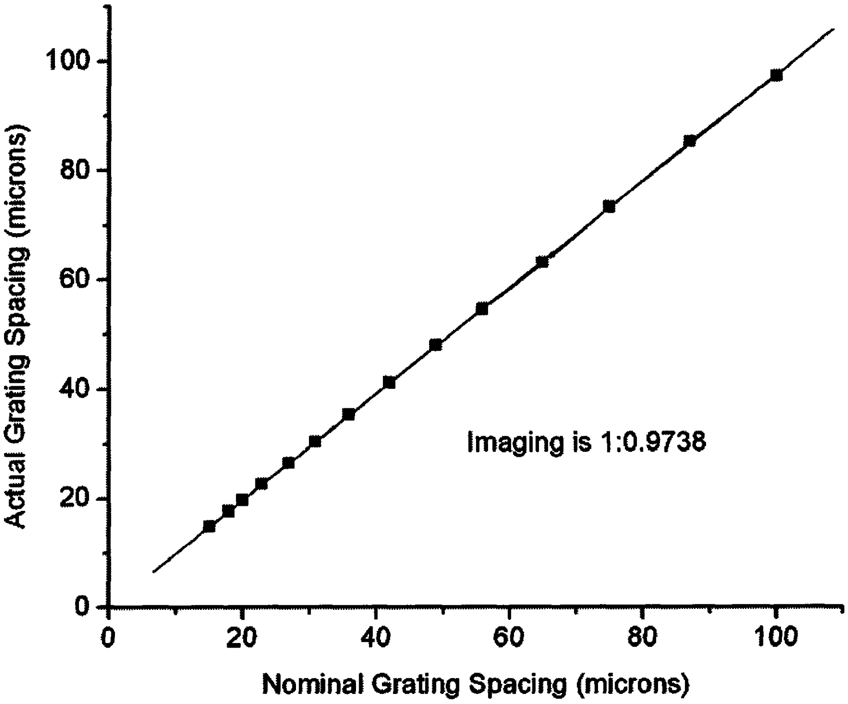

Figure 3.8. Calibration of transient grating spacing in ethylene glycol using a series of phase masks with different spatial periods *d*. The nominal grating spacings are given by $\Lambda = d/2$, calculated assuming the two-lens telescope had a 1:1 imaging ratio.

By taking the Fourier transform of the acoustic part of the ISTS signal, and using the resulting acoustic frequency f_0 with the calculated velocity v_0=1666 m/s, the grating wavelength Λ could be determined via $\Lambda = v_0/f_0$. The periodicity of the etched phase mask, versus the acoustic wavelength inside the material determined in this manner, is shown in Figure 3.8. The phase mask to transient grating imaging ratio was found to be 1:0.97.

With the wavevector $q = 2\pi/L$ of the measurement well characterized as described above, the thermal conductivity is obtained in glycerol by first determining the time constant τ_{th} of the exponential decay of the signal, by fitting the data numerically to Equation 3.7. The results of this fit are shown in Figure 3.9 for three different grating wavelengths (wavevectors). The variation with wavelength is quite apparent, and naturally arises from the difference in length scales along which heat must diffuse from the heated peaks of the transient grating to the unheated nulls. It should be noted that if the mean-free path of the dominant phonons responsible for thermal diffusion is longer than the experimental grating wavelength, then the transport will be characterized by ballistic rather than diffusive dynamics.[22] The possibility of this case is experimentally addressed later on in this section. The thermal diffusion constant D can be easily obtained from the τ_{th} signal fits via the relation:

$$D(T) = \frac{1}{\tau_{th}(T)q^2} \qquad 3.9$$

The value of $D(T)$ is shown in Figure 3.10 for the grating wavelengths/wavevectors shown in Figure 3.9, as well as for a 36.0 micron grating spacing, which was obtained in a measurement made months earlier. Excellent agreement between values of $D(T)$ from the different grating wavelengths is found at higher temperatures. At lower temperatures the scatter is within the error of the wavevector calibration, but appears systematic enough to warrant further study.

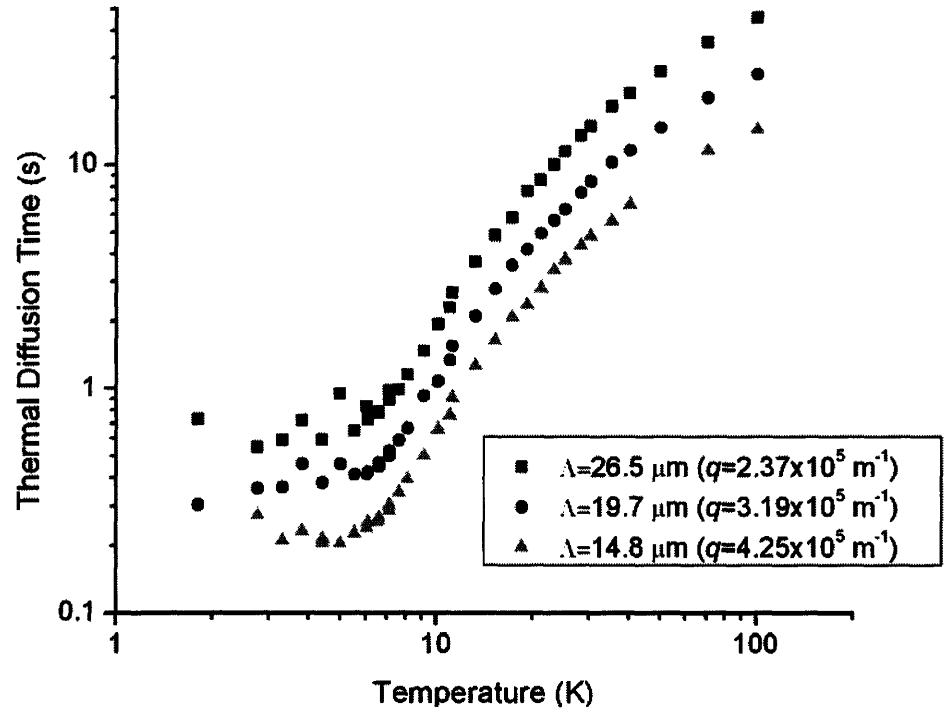

Figure 3.9. Temperature dependence of thermal diffusion time for three different grating wavelengths/wavevectors in glycerol.

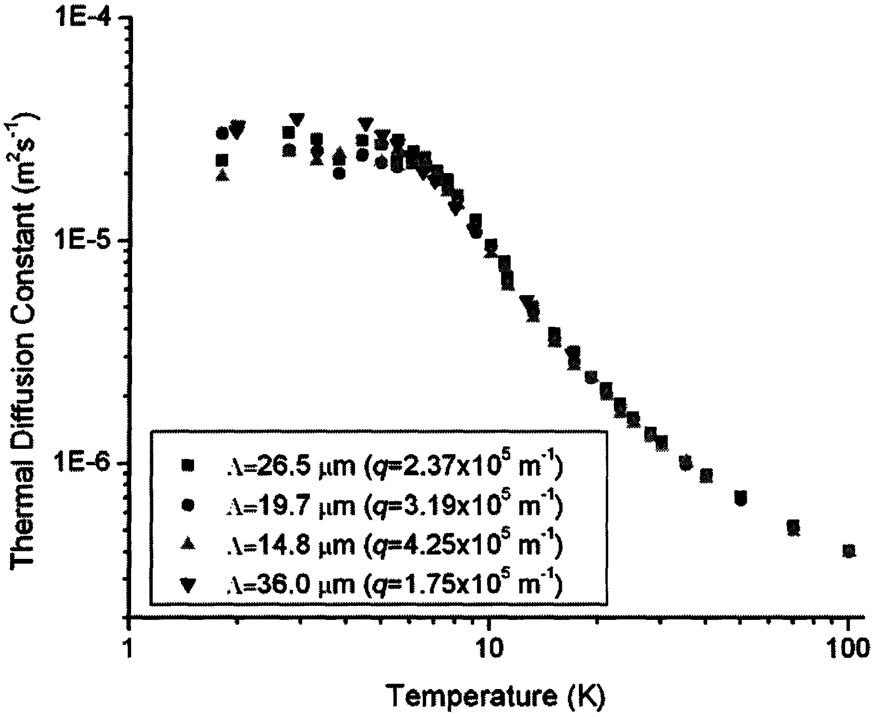

Figure 3.10. Thermal diffusion constant of glycerol determined by ISTS, at four different grating wavelengths/wavevectors.

The calculation of the thermal conductivity κ from $D(T)$ is extremely straightforward, and is given by the relation:

$$\kappa(T) = \frac{D(T)}{\rho C_p(T)} \qquad 3.10$$

where ρ and $C_p(T)$ are the density and bulk heat capacity, respectively. The heat capacity data and density data generously provided by Professor Miguel A. Ramos (Universidad Autonoma de Madrid) obtained as described in References 5 and 17 are presented in Figure 3.11 on a linear scale, and in Figure 3.12 divided by T^3 in order to illustrate the extra modes present in the glass, over the T^3 dependence predicted for the crystal, as discussed in Section 2.2 and shown in Figure 2.1 for silica glass. Ramos' data were found to be in good agreement with values found elsewhere at temperatures above 2 K.[23]

Using the values of $D(T)$ obtained through ISTS in Equation 3.10 with values of ρ and of C_p from Ramos, the thermal conductivity was calculated. The result is presented along with Ramos' results obtained by a more conventional method in Figure 3.13, also provided by Professor Ramos. Also shown is the conductivity of silica glass calculated using the tunneling model and associated parameters, as described in Section 2.2 and shown in Figure 2.11. The ISTS data are extremely consistent across the different grating spacing measurements, and show a strikingly different behavior than Ramos'. Generally, the ISTS values are roughly 0.2 $\mathrm{Wm^{-1}K^{-1}}$ lower than that measured by the standard approach, and show an unexpected temperature dependence below 10 K. Possible origins of the large difference are discussed in Section 3.3.

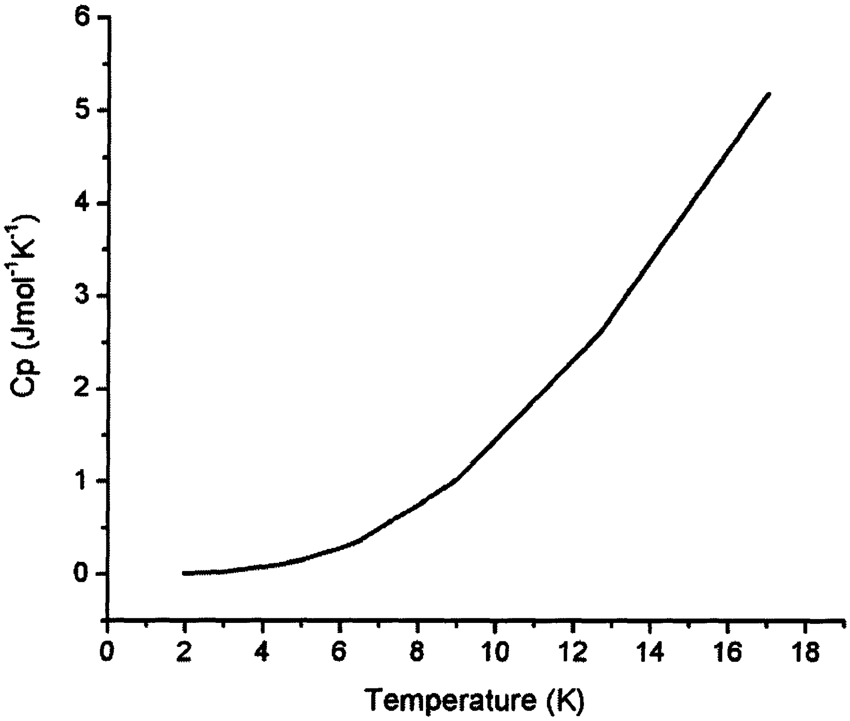

Figure 3.11. Heat capacity of glycerol at low temperatures. Generously provided by Professor Miguel A. Ramos (Universidad Autonoma de Madrid).

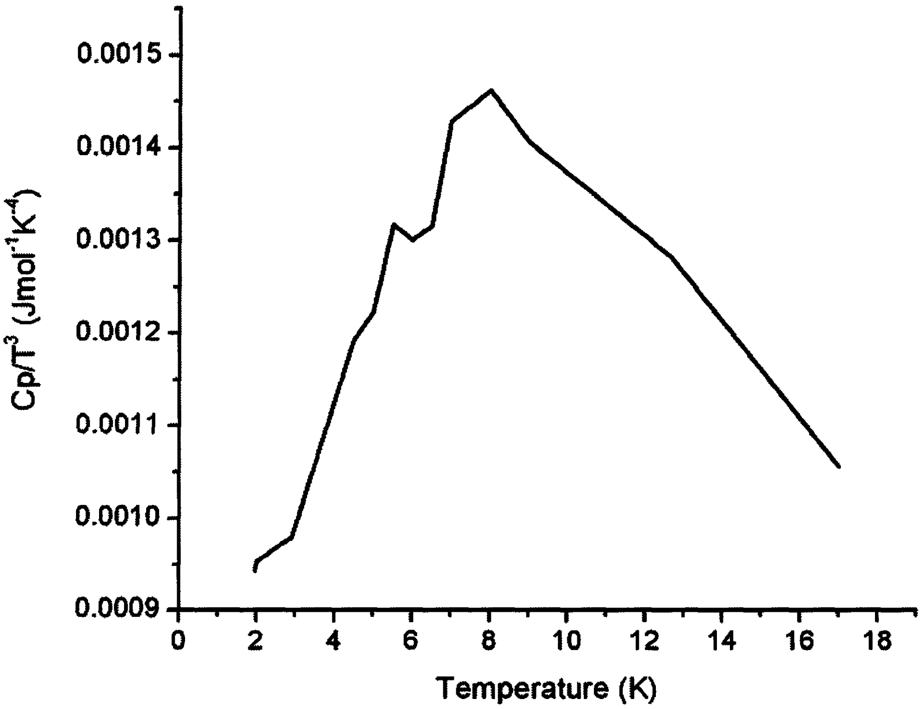

Figure 3.12. Heat capacity of glycerol at low temperatures, divided by T^3 in order to illustrate excess of modes near 10 K. Generously provided by Professor Miguel A. Ramos (Universidad Autonoma de Madrid).

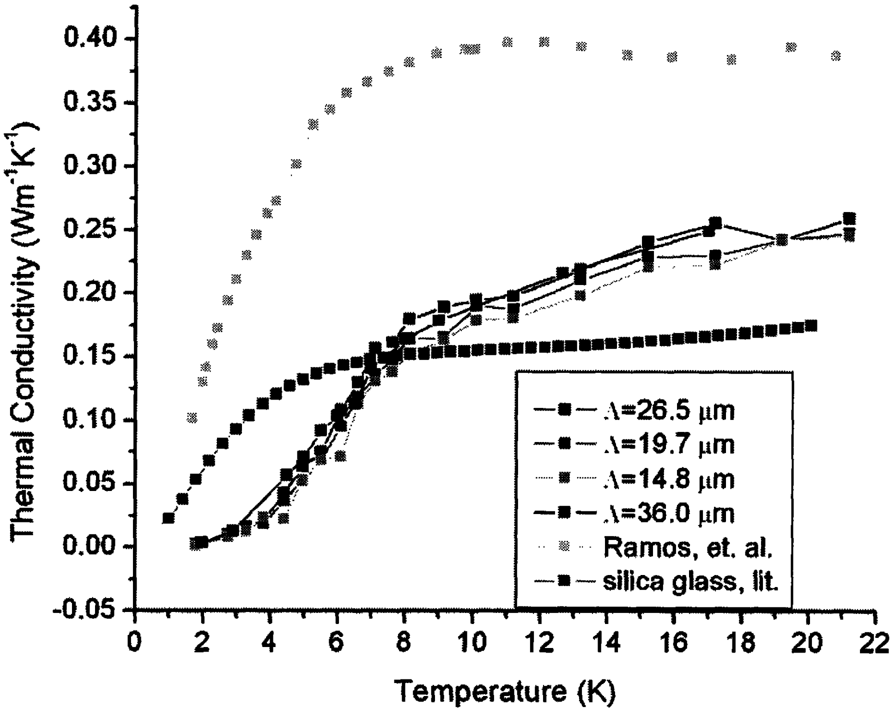

Figure 3.13. Thermal conductivity measured at several grating wavelengths/wavevectors by ISTS, compared to that measured by the more conventional method used by Ramos, et. al., as in Reference 2. Also included is silica glass conductivity as discussed in Chapter 2.

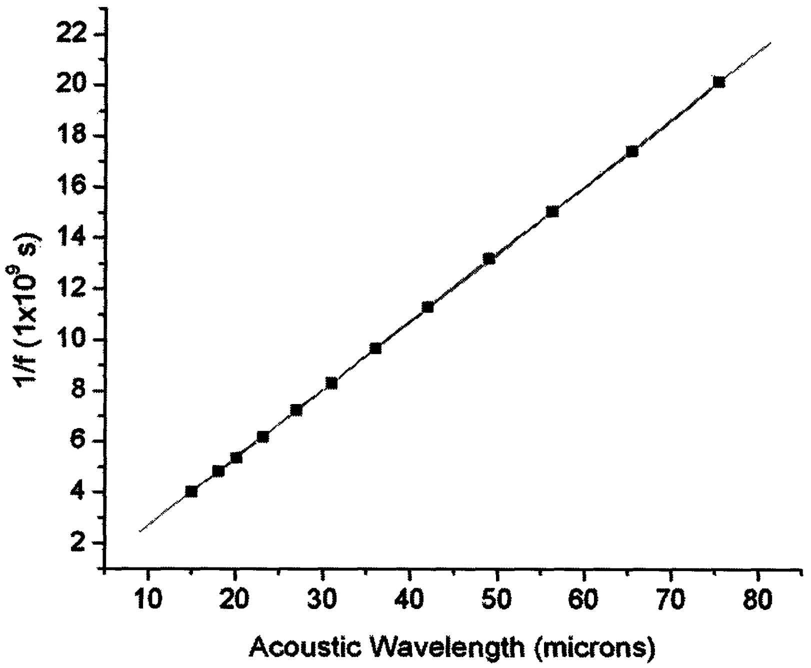

Figure 3.14. Acoustic wavelength vs. inverse frequency at 5 K, with linear fit yielding acoustic speed of 3750 m/s.

Values of the acoustic velocity at the wavelengths described above were measured concurrently with the diffusion data. The peak frequency of the acoustic wave at each calibrated grating spacing in Figure 3.8 was obtained by Fourier transformations of the data, and the result is presented in Figure 3.14. A linear fit to the data allows precise determination of the acoustic velocity, which is found to be 3750 m/s at 5 K.

3.3 Discussion

The large discrepancy between the result of ISTS and of the conventional method for the thermal conductivity of glycerol raises many concerns regarding the experiment. As shown in Figure 3.13, the ISTS results are consistent across multiple measurements. The fits of Equation 3.7 to the raw data are excellent, as shown in Figure 3.15. The acoustic part of the fit appears less than optimal, and this is due to propagation out of the probing region as mentioned in Section 3.2. First the general characteristics of the conventional and ISTS results are addressed, and later the possible sources of the difference will be discussed in terms of the theoretical framework of Chapter 2 and tested experimentally.

At the lowest temperatures, T<2 K, thermal phonons are modeled to induce tunneling between quasi-isoenergetic states of structural two-level systems (TLS), as described by Equation 2.6. This typically yields the power law $\kappa \sim T^2$ for the bulk conductivity of the glass, as compared with the Debye result $\kappa \sim T^3$ for the crystal. This difference is one of the main "results" discussed regarding thermal anomalies of glasses. However both the conventional and ISTS experiments discussed here have a low-temperature limit of ~1.7 K, limiting discussion of this feature. At higher temperatures, above 2 K, the thermal conductivity data are not usually described in terms of a "characteristic" power law, and instead the focus shifts to the onset of the plateau near 10 K.

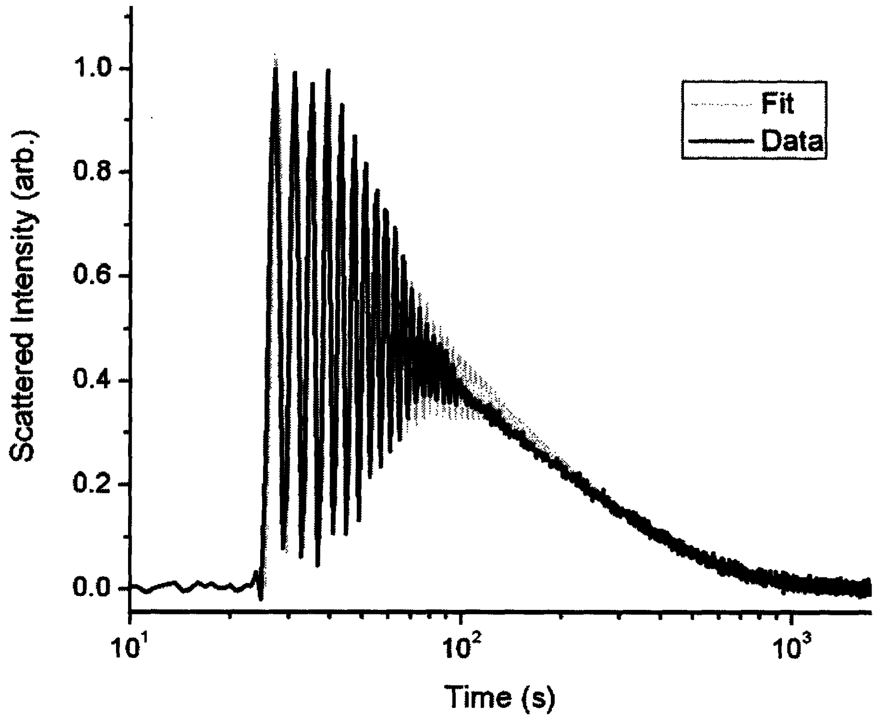

Figure 3.15. ISTS data at 3.30 K, 15 μm grating spacing, and fit using Equation 3.7

However it is apparent that the conventional and the ISTS data have remarkably different temperature dependence below the plateau. A fitting program (OriginPro 7.0) was used to determine the power laws of different temperature regions of the thermal conductivities, $\kappa \sim T^m$, from the two glycerol measurements, as well as from the silica glass calculation performed in Section 2.2 which reproduces the literature measurements at all temperatures of interest as shown in Figure 2.11. The results are presented in Table 3.1. The different temperature regions were chosen by examining the temperatures where the trends in the conductivity curves from the various materials and measurements show a distinct change, such as shown in Figure 3.17. For the silica glass, the numerical integration of Equation 2.2 (performed in Matlab) has a low-temperature limit of 0.6 K, so the temperature range considered here does not contain the "pure" TLS resonant contribution, resulting in a power law somewhat lower than $\kappa \sim T^2$. Between 1.6-3.9 K, where the thermal conductivity is determined by resonant as well as relaxational TLS-

Temperature (K)	*m*, Silica	*M*, Glycerol (Ramos)	*m*, Glycerol (ISTS)
0.6-1.6	1.57	N/A	N/A
1.7-3.9	0.95	1.04	2.87
1.7-7.1	0.64	0.80	2.85
7.1-12	0.086	0.14	0.59
12-21	0.13	-0.032	0.42

Table 3.1. Fits of the thermal conductivity to a power law, $\kappa \sim T^m$, in various temperature ranges for silica glass as calculated in Chapter 2, and for glycerol, from traditional measurement as from Reference , and from ISTS measurement. Errors were less than 10% in all fits.

phonon interactions, the curve for silica becomes nearly linear with temperature, $\kappa \sim T^1$, as does Ramos' data. In stark comparison, the ISTS measurement yields a power law that nearly duplicates that expected of a crystal, $\kappa \sim T^3$. However the magnitude is much lower than that of the crystal, as well as that of Ramos' data, indicating that this phonon-material interaction is extremely strong, but deviates from that described by Equation.2.16. This behavior persists all the way up to 7.1 K, as shown in Figure 3.16. Above this temperature, the behavior crosses over to a different power law, described roughly by $\kappa \sim T^{1/2}$. The silica glass and Ramos' data cross over to a nearly temperature-independent value, $\kappa \sim T^0$.

By looking at the slopes of the different thermal conductivity data sets, the temperature ranges over which different behavioral regimes occur can be distinguished more easily. As shown in Figure 3.17, the silica and Ramos' data behave qualitatively in the same manner, with a gradual reduction in slope that flattens around 10 K. Around and above 10 K, the ISTS data follow a qualitatively similar trend. However at low temperatures the ISTS data exhibit an *increasing* instead of decreasing slope, reaching a maximum near 7 K before crossing over to a more expected behavior. The increasing slope, and in particular the T^3 dependence reminiscent of that observed in crystalline solids suggest that the mean free paths of low to moderate frequency phonons (those thermally excited at temperatures below 7 K) have a frequency dependence more closely resembling that of crystalline solids than that of most glasses. Yet the low absolute values of the thermal conductivity strongly suggest that the acoustic phonons are interacting strongly with structural rearrangement dynamics (i.e. with TLS) in glycerol. Taken together, the results may point to an unusual distribution of TLS splittings and/or energy barriers, such that although phonons at all frequencies are strongly damped, the transport of higher frequency phonons relative to those at low frequencies is better than in other low-temperature glasses. Thus as the temperature is raised, the thermal conductivity increases at a higher rate than in other glasses.

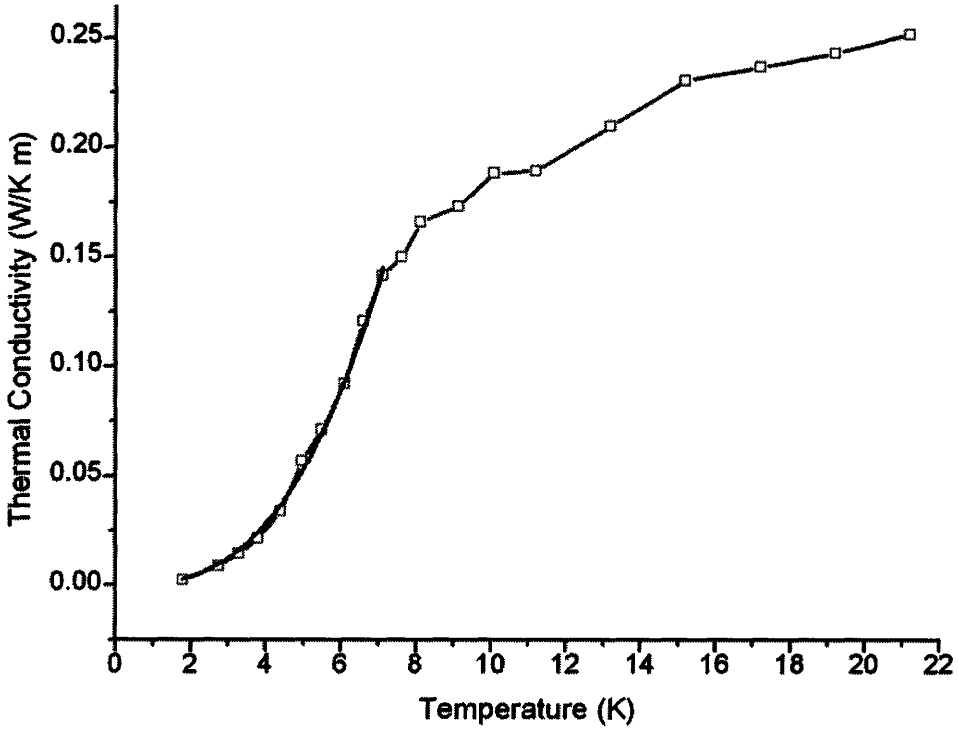

Figure 3.16. Fit of the power law $\kappa \sim T^{2.85}$ to the thermal conductivity of glycerol measured by ISTS. A linear dependence is expected, $\kappa \sim T^{1}$.

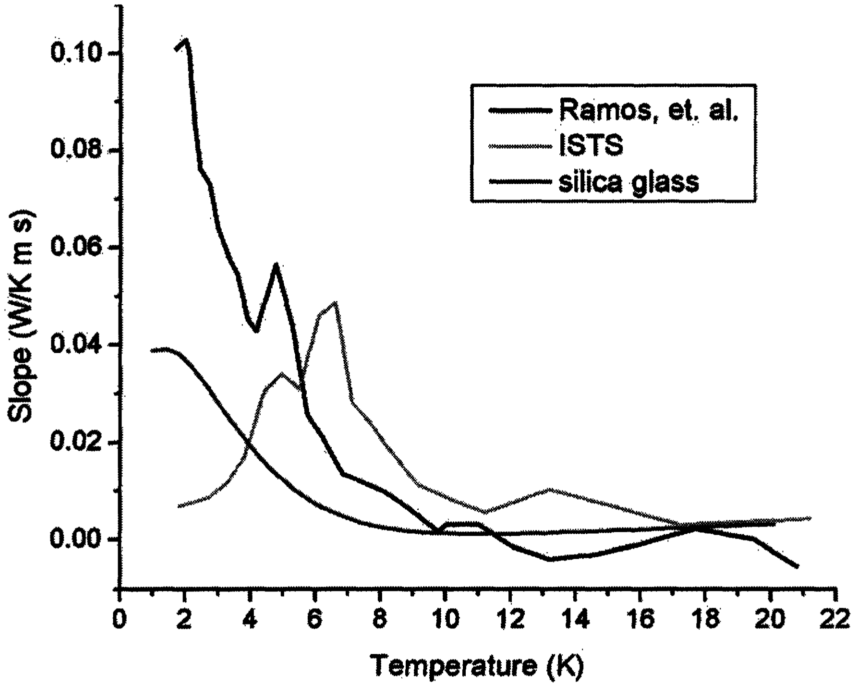

Figure 3.17. Derivative of thermal conductivity data for silica glass as calculated in Chapter 2, and for glycerol, from traditional measurement as from Reference 17, and from ISTS.

The strengths of the various phonon-material interactions posited by the tunneling model are usually phenomenologically determined by fitting different temperature regimes of the measured thermal conductivity curve to the curve calculated by integrating Equation 2.2 while varying the magnitudes of different terms in Equation 2.16. The strength of the phonon-TLS interaction is normally determined independently by varying the parameter A described by Equation 2.6 to match the slope of the thermal conductivity below 2 K. As neither data from Ramos, et. al. or from the ISTS measurement extends into this temperature range, the value of A cannot be independently determined and so here is determined simultaneously with the other interaction strengths described by B and D by fitting the full curve of Equation 2.16. It should be emphasized that the tunneling TLS still contribute to the reduction of the thermal conductivity even at higher temperatures. The value of the acoustic velocity v was obtained from the literature[24] for silica, and from the acoustic measurement described in Section 3.2 for glycerol, assuming the shear velocity is one-half the longitudinal velocity and using Equation 2.4. The results of the fits are presented in Table 3.2. The fitted curves can be seen in Figure 3.18. The low-temperature part of the ISTS curve is very poorly fitted by the tunneling model. The difficulty of fitting the ISTS data lies in its extremely low magnitude, which is not predicted by the tunneling model.

Parameter	Silica	Glycerol (Ramos)	Glycerol (ISTS)
A, $\mathrm{m^{-1}K^{-1}}$	$3.5\text{x}10^4$	$2.6\text{x}10^4$	$2.7\text{x}10^5$
B, $\mathrm{K^{-2}}$	$3.0\text{x}10^{-3}$	$1.3\text{x}10^{-4}$	$8.7\text{x}10^{-6}$
$AB/2$, $\mathrm{m^{-1}K^{-3}}$	53	1.69	1.17
D, $\mathrm{m^{-1}K^{-4}}$	120	190	137
V, $\mathrm{ms^{-1}}$	4100	2905	2905

Table 3.2. Strengths of the various microscopic parameters described by Equation 2.16, fitted by comparing the measured thermal conductivity to that calculated by numerical integration of Equation 2.2.

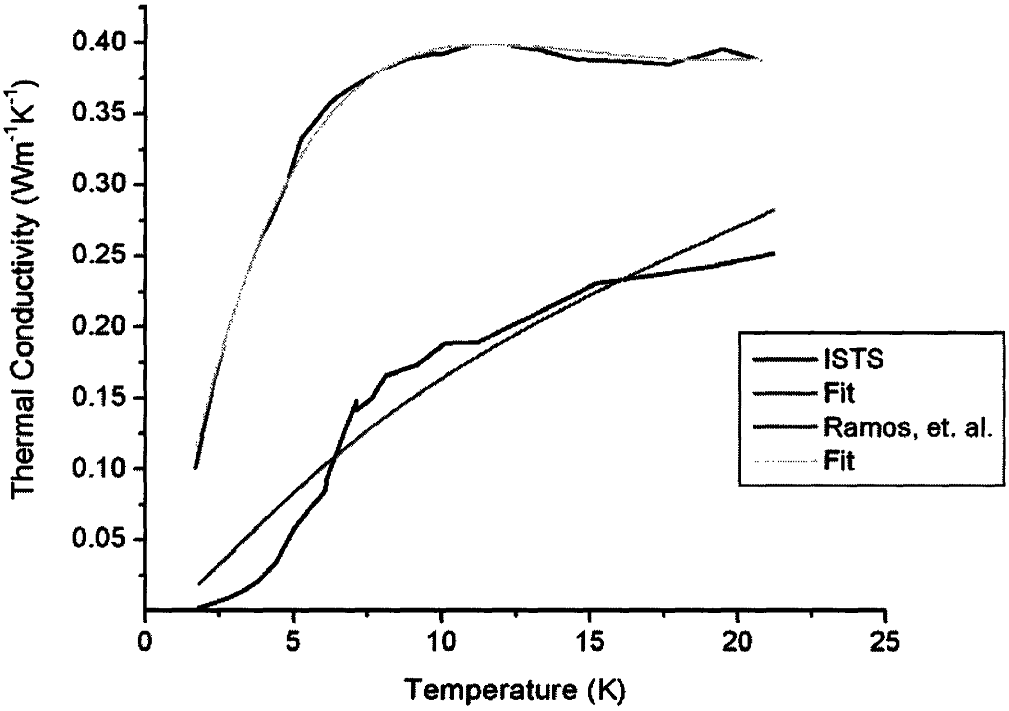

Figure 3.18. Fits of ISTS and Ramos' data to the tunneling model, Chapter 2. Fit parameters are given in Table 3.2.

The silica glass and Ramos' glycerol data have comparable magnitudes of parameters that describe the TLS resonant and low-frequency/high-temperature relaxational interaction, *A* in Equations 2.6 and 2.10, while the ISTS result is an order of magnitude higher. The larger value is necessary, within the context of this model, in order to give the very low thermal conductivity values determined from ISTS measurements at the lowest temperatures. The value of the Rayleigh scattering term, *D*, is fairly comparable for all the measurements. The product *AB*/2, in Equation 2.11, describes the strength of the high-frequency/low temperature limit of the TLS relaxational interaction, which is much smaller than for silica and is comparable for the two glycerol measurements. The far lower value of *B* determined from the present results is necessary, again in the context of this model, in order to yield the rapid, $\sim T^3$ increase in thermal conductivity with temperature. To summarize, the net phonon interactions (within the description of the tunneling model) with structural TLS are enhanced in glycerol as compared with silica glass for resonant and low-frequency/high-temperature relaxational dynamics, but are significantly reduced for the high-frequency/low temperature relaxations. It should be also noted that the fit of the bulk ISTS thermal conductivity curve was adequate near the plateau, but that the actual conductivity was significantly overestimated by the tunneling model at low temperatures. This strongly implies that there is a dynamical process which is observed in this particular measurement, but not accounted for by the form of the model expressed by Equation 2.16.

Lastly the differences between the ISTS results and the more conventional measurement are explored to try to understand the nature of the discrepancy. For example if the difference $\Delta\kappa$ is taken between the two measurements, as shown in Figure 3.19, the difference increases rapidly with temperature to a peak near 4 K, before gradually decreasing. The shape of the curve is qualitatively reminiscent of Figure 3.12, which illustrates the number of excess modes available to hold heat in the glass, and is reproduced here. The temperatures of the maxima are within ~3 K of each other, but it is unclear whether the similarity is coincidental. The presence of additional modes near this temperature could certainly explain the plateau in the conductivity. If the ratio κ/T is taken, as shown in Figure 3.20, a qualitative change in the behavior can be seen in the data from each technique. However it appears that the change in the ISTS data fall very close to the temperature at which the excess of modes appears in the heat capacity, strongly pointing to a similar origin of both behaviors.

In trying to understand the difference between the ISTS and more traditional measurement of the thermal conductivity, two issues are of initial concern. First is the possibility that the bulk specific heat used in Equation 3.10 is not valid in this experiment. This could be due to a temporal overlap of the thermal diffusion with a dynamical process in the glass. For example a time-dependent heat capacity was observed recently in supercooled liquid glycerol.[25] When the time scale of the α-relaxation process described in Section 3.1 overlaps with the time scale of the thermal diffusion, the modes are observed to interact very strongly. The thermal diffusion becomes reduced and non-exponential as thermal energy flows into collective motions of the network, rather than propagating normally. In the current experiment there is concern that at low temperatures, the transitions of some subset of the two level systems described by Equations 2.6 and 2.9 occur on the same timescale as thermal diffusion. As mentioned before, the TLS relax with a characteristic time t_1 described by Equation 2.8. This yields a time dependence in the linear part of the heat capacity:[26]

$$C(t,T) = \frac{\pi^2}{12}\bar{n}_0 k_B^2 T \ln\frac{4t}{t_1} \qquad 3.11$$

The interaction with a distribution of two-level systems would be seen as nonexponential

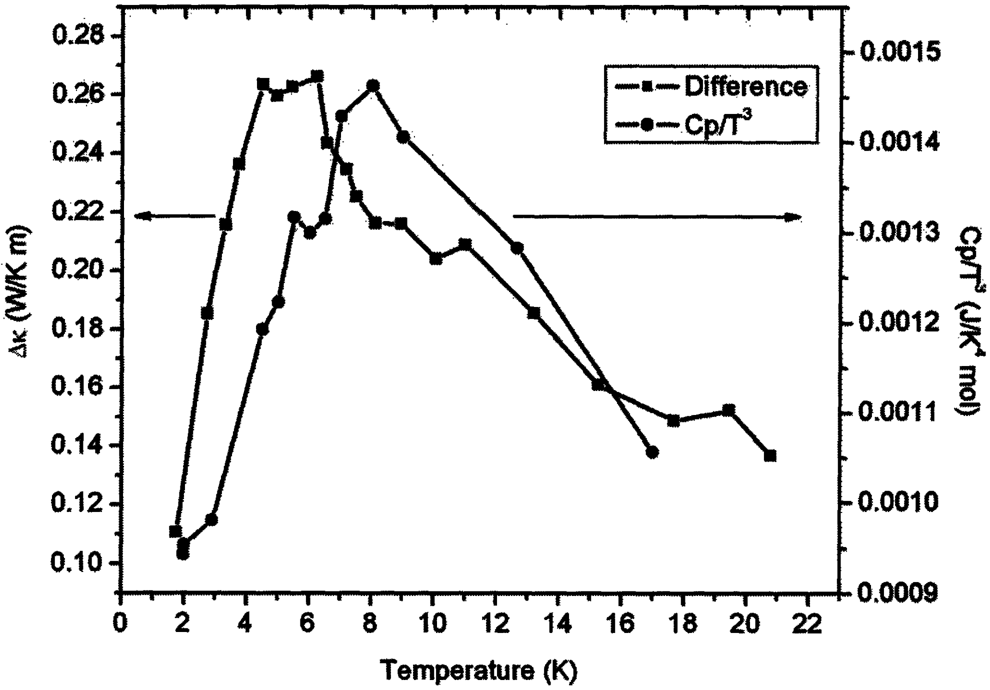

Figure 3.19. Difference Δκ between thermal conductivity measured by ISTS and by Ramos, et. al., plotted with *Cp*/*T*³ which shows qualitative similarities.

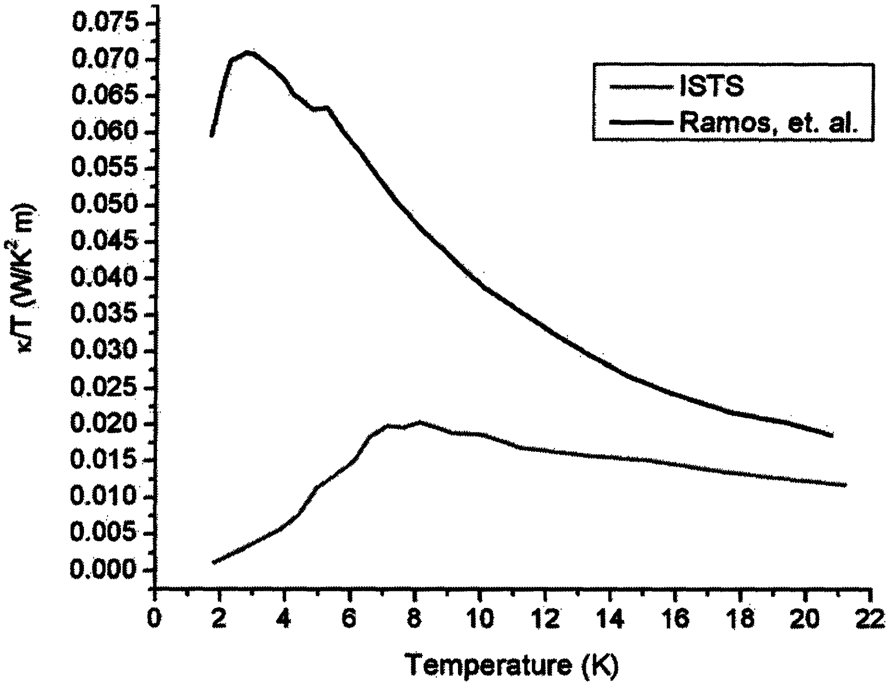

Figure 3.20. Glycerol thermal conductivity divided by temperature for conventional and ISTS measurements.

thermal diffusion that could not be fit to a single time constant τ_{th},[27] and a deviation from the relationship expressed by Equation 3.9 i.e., τ_{th} would not go as q^{-2}.

A second issue is the possibility that the mean free paths of the dominant thermal phonons involved in heat transport are longer than the grating spacing along which the diffusion constant is measured. For spacings of many microns, this is implausible at higher temperatures where heat transport is dominated by phonons of very high frequencies and low mean free paths. However, at 1.8 K, thermal excitation extends to acoustic modes only scarcely above 30 GHz frequencies, and their mean free paths could well be in the micron range. Both of these effects on the signal were tested by measuring τ_{th} while varying the wavevector and holding the temperature constant. The grating spacing was varied between 15-85 μm. The effect of varying the grating spacing over this range was to smoothly change the thermal diffusion time by nearly two orders of magnitude, from 0.2 μs – 10 μs. The results at 6.1 K and 1.8 K are shown in Figure 3.21 and Figure 3.22, respectively. With the exception of some data scatter there appears to be no discernable wavevector dependence of the thermal diffusion in this temperature and frequency range. The notable scatter in Figure 3.22 is attributed to a small signal contribution from helium, as shown previously in Figure 3.7. This yields an extremely low- frequency component to the signal (~2 MHz) which oscillates on a similar time scale to the thermal decay, and is therefore difficult to subtract out completely. It appears that within the constraints of our experiment, the bulk C_p used in Equation 3.10 is appropriate. The slope of the linear fit to each data set yields the diffusion constant at that temperature. Here the value D=2.12x10^{-5} m^{2}s^{-1} is found at 6.1 K, and D=4.08x10^{-5} m^{2}s^{-1} at 1.8 K. This is in good agreement with the values in Figure 3.10.

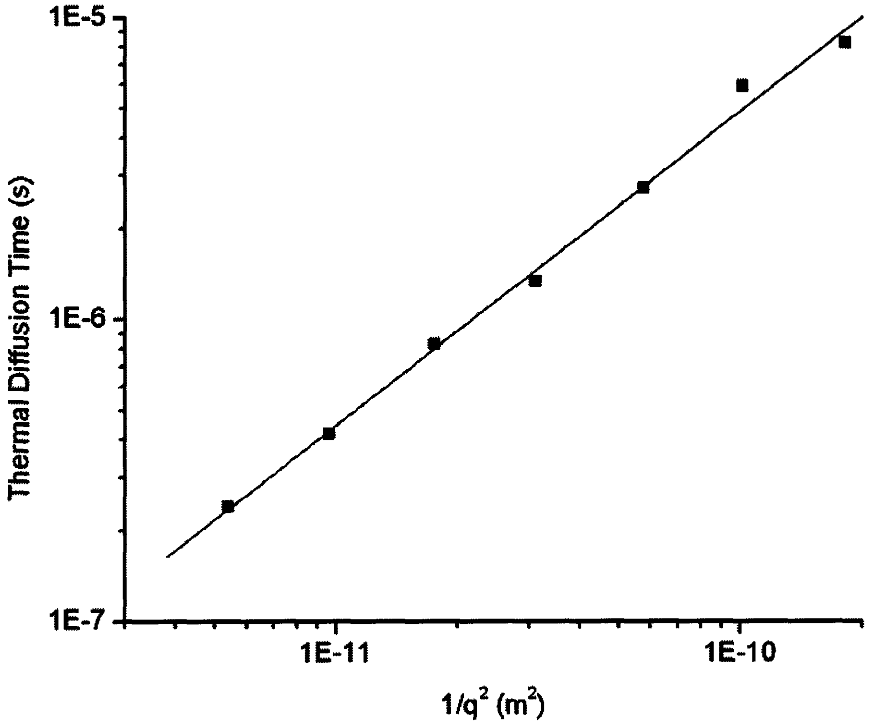

Figure 3.21. Wavevector dependence of thermal diffusion at 6.1 K.

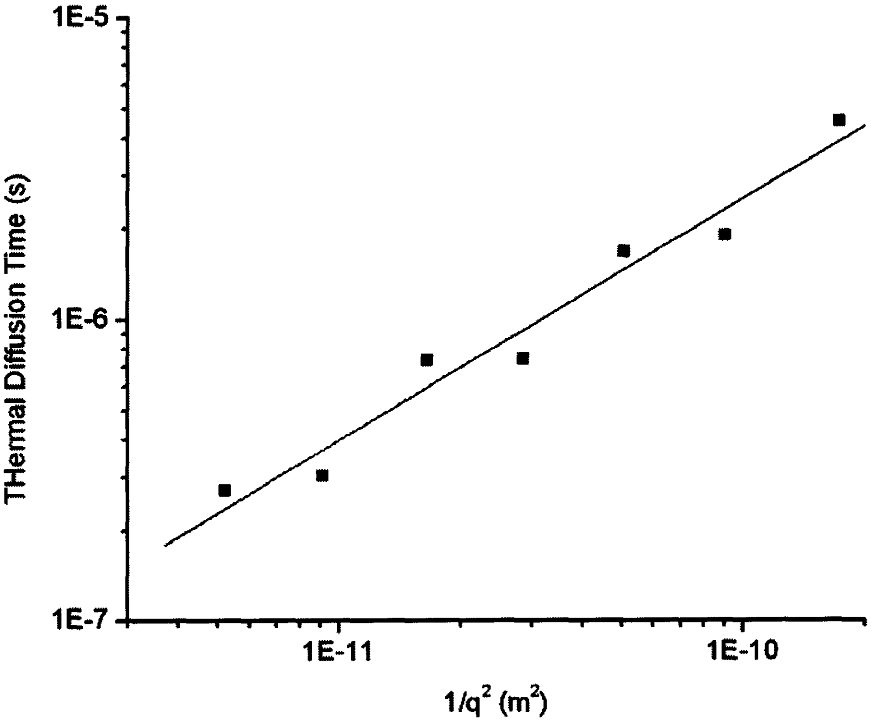

Figure 3.22. Wavevector dependence of thermal diffusion at 1.8 K.

3.4 Conclusions

The low-temperature thermal conductivity values obtained by ISTS and presented here represent a departure from the values obtained by a more traditional heater/thermometer based measurement. The ISTS measurement appears to be quite robust, in that it a) yields a single-exponential decay, requiring a single fitting parameter for data extraction, b) allows for optical access to the sample, such that the quality of the supercooled glass (including cracking that may occur upon cooling and that may influence thermal transport measurements) can be assessed, c) may be used to determine the thermal diffusivity across a wide variety of wavevectors, and d) allows the extraction of the acoustic velocity as a concurrent, and relevant, measurement. A weakness of the measurement is that it is not possible to make independent measurements of κ and C_p, so the use of outside data is required to separate the contributions of the two variables to the diffusion constant. Despite this, the addition of ISTS thermal conductivity measurements to the library of techniques for study of low-temperature glasses can substantially benefit the field. The present results illustrate the value that it can play in providing reliable quantitative results in a versatile, non-contact manner.

The present results, showing a temperature dependence of the thermal conductivity at temperatures below the plateau region that is substantially different from that expected of glasses, strongly call for further study of thermal conductivity in molecular glasses including both hydrogen bonded and van der Waals materials. The question is raised as to whether the TLS distribution in molecular glasses might be systematically different from that in ionic glasses, leading to consistently different temperature-dependent behavior as observed in the one case reported here.

3.5 References

1. L. van der Tempel, G.P. Melis, T.C. Brandsma. Thermal conductivity of a glass: I. Measurement by the glass-metal contact. *Glass Physics and Chemistry*, 26(6): 606-611, 2000.

2. S. Vieira, M.A. Ramos, Q.W. Zou, C. Talón. Low-temperature properties of molecular glasses and crystals. *Phase Transitions*, 64(1-2): 87-102, 1997.

3. Y.-X. Yan, K.A. Nelson. Impulsive stimulated light scattering. I. General theory. *Journal of Chemical Physics*, 87(11): 6240-6256, 1987.

4. Y.-X. Yan, K.A. Nelson. Impulsive stimulated light scattering. II. Comparison to frequency-domain light scattering spectroscopy. *Journal of Chemical Physics*, 87(11): 6257-6265, 1987.

5. For example, in this thesis C_p was obtained from Professor Miguel A. Ramos, as published in: M.A. Ramos, C. Talón, S. Vieira. The Boson peak in structural and orientational glasses of simple alcohols: specific heat at low temperatures. *Journal of Non-Crystalline Solids*, 307-310: 80-86, 2002.

6. J.K. Cocson, C.S. Hau, P.M. Lee, C.C. Poon, A.H. Zhong, J.A. Rogers, K.A. Nelson. Transverse isotropic elastic-moduli and inplane thermal-diffusivity in silicon-supported thin-films of a photosensitive polyimide measured using impulsive stimulated thermal scattering. *Polymer* 36(21): 4049-4075, 1995.

7. Y.W. Yang, K.A. Nelson, F. Adibi. Optical measurement of the elastic-moduli and thermal-diffusivity of a C-N film. *Journal of Materials Research*, 10(1): 41-48, 1995.

8. T. Franosch, W. Gotze, M.R. Mayr, A.P. Singh. Evolution of structural relaxation spectra of glycerol within the gigahertz band. *Physical Review E*, 55(3): 3183-3190, 1997.

9. C.A. Angell. Relaxation in liquids, polymers and plastic crystals – strong/fragile patterns and problems. *Journal of Non-Crystalline Solids*, 131-133(1): 13-31, 1991.

10. A. Brodin, L. Börjesson, D. Engberg, L.M. Torell, A.P. Sokolov. Relaxational and vibrational dynamics in the glass-transition range of a strong glass former B_2O_3. *Physical Review B*, 53(17): 11511-11520, 1996.

11. V.N. Novikov, A.P. Sokolov. Poisson's ratio and the fragility of glass-forming liquids. *Nature*, 431(7011): 961-963, 2004.

12. T. Franosch, W. Gotze, M.R. Mayr, A.P. Singh. Structure and structure relaxation. *Journal of Non-Crystalline Solids*. 235-237: 71-85, 1998.

13. A.P. Sokolov, R. Calemczuk, B. Salce, A. Kisliuk, D. Quitmann, E. Duval. Low-temperature anomalies in strong and fragile glass formers. *Physical Review Letters*, 78(12): 2405-2408, 1997

14. V.N. Novikov, A.P. Sokolov. Poisson's ratio and the fragility of glass-forming liquids. *Nature*, 431(7011): 961-963, 2004.

15. J.C. Dyre. Glasses – Heirs of liquid treasures. *Nature Materials*, 3(11): 749-750.

16. R.O. Pohl, X. Liu, E. Thompson. Low-temperature thermal conductivity and acoustic attenuation in amorphous solids. *Reviews in Modern Physics*, 74(4): 991-1013, 2002.

17. C. Talón, Q.W. Zou, M.A. Ramos, R. Villar, S. Vieira. Low-temperature specific heat and thermal conductivity of glycerol. *Physical Review B*, 65(1): 012203.

18. T.F. Crimmins. *Ultrahigh frequency characterization of complex materials using transient grating techniques*. Ph.D. Thesis, Massachusetts Institute of Technology, Department of Chemistry, June 2000.

19. A.A. Maznev, K.A. Nelson, J. Rogers. Optical heterodyne detection of laser-induced gratings. *Optics Letters*, 23(16): 1319-1321, 1998.

20. K.D. Bonin, M.A. Kadarkallen. Linear electric-dipole polarizabilities. *International Journal of Modern Physics B*, 8(24): 3313-3370, 1994.

21. S. Silence. *Time-resolved light scattering studies of structural rearrangements in disordered condensed phase systems*. Ph.D. Thesis, Massachusetts Institute of Technology, Department of Chemistry, 1991.

22. G. Chen. Ballistic-diffusive equations for transient heat conduction from nano to macroscales. *Journal of Heat Transport - Transactions of the American Society of Mechanical Engineers*, 124(2): 320-328, 2002.

23. A.J. Leadbetter, K.E. Wycherley. A calorimeter for the range 1 to 30 K the heat capacity of copper and glycerol glass. *Journal of Chemical Thermodynamics*, 2(6): 855-866, 1970.

24. T.C. Zhu, H.J. Maris, J. Tauc. Attenuation of longitudinal-acoustic phonons in amorphous SiO_2 at frequencies up to 440 GHz. *Physical Review B*, 44(9): 4281-4289, 1991.

25. R. Di Leonardo, A. Taschin, R. Torre, M. Sampolini, G. Ruocco. Structural and entropic modes in supercooled liquids: experimental and theoretical investigation. *Journal of Physics: Condensed Matter*, 15(11): S1181-S1192, 2003.

26. S. Hunklinger, A.K. Raychaudhuri. *Progress in Low Temperature Physics, Volume IX*. D.F. Brewer, Editor. Elsevier, Amsterdam, 1986.

27. M.T. Loponen, R.C. Dynes, V. Narayanamurti, J.P. Garno. Thermal relaxation in *a*-As_2S_3 and *a*-As. *Physical Review B*, 25(6): 4310-4312, 1982.

Chapter Four

Generation, Modeling, and Characterization of Narrowband Acoustic Waves in the GHz Regime

4.1 Introduction

This chapter describes a novel method of generating high-frequency and high-wavevector acoustic waves for the characterization of complex materials. When acoustic waves propagate with velocity v_s within a material, they interact with density variations which may be static or dynamic in nature. If the inverse of the acoustic frequency ω is on the order of a characteristic relaxation time τ_c $(\omega\tau_c \sim 1)$, of if the inverse of the acoustic wavevector $q=\omega/v_s$ approaches the order of a structural element with size d $(qd \sim 1)$, the acoustic velocity and attenuation rate change in a detectable way, enabling the experimentalist to probe the dynamical process or structural element characteristics. Thus, the higher the frequency, the smaller or faster the feature of the material that may be probed. A versatile method for optical generation and detection of *tunable, narrowband* acoustic waves throughout the GHz range has not been reported to date. Here for the first time the generation of coherent narrowband acoustic waves throughout the ultra-high frequency range 1-1000 GHz is demonstrated, using a conceptually simple but novel ultrafast pulse shaper called the "Deathstar." This frequency window, which has been difficult to access by other methods, now enables the robust measurement of structural features with sizes on order of 10 μm to 10 nm, and dynamical processes with characteristic times of 1 ns to 1 ps. The high end of this frequency range is particularly important for the study of disordered materials, because it includes the range within which structural heterogeneity causes acoustic waves to cease propagating entirely, e.g., "the end of the acoustic branch."[1] The generation of high frequency optical waveforms and their conversion into acoustic waves, their modeling, and their use for the characterization of nanoscale structures such as thin films and heterogeneity in amorphous materials are demonstrated.

Photoacoustic spectroscopy has been used for many years to understand the properties of complex materials – for example to characterize mesoscopic structures, which may behave differently than their bulk counterparts,[2] to probe subsurface elements or defects[3], and to characterize electronic properties of nanocrystals.[4] Optical acoustic spectroscopy is particularly well-suited for the study of materials because it allows static or dynamic density fluctuations to be probed in a non-contact manner, in a wide range of frequencies (especially high frequencies) and in many sample and experimental configurations. Generation and detection of tunable, narrowband acoustic waves through optical means has long been possible in the MHz frequency range, with impulsive stimulated thermal scattering, or ISTS.[5] The technique consists of crossing two short (~100 ps) laser pulses inside the material of interest, where they interfere with a wavelength that depends on the angle at which they cross and on the optical wavelength. Absorption heats the material, and concurrent rapid expansion launches counter-propagating acoustic waves with a wavelength that matches that of the laser interference pattern. The experimental geometry has been extensively refined and simplified in recent years,[6] allowing easy tuning of the acoustic wavelength. This approach has permitted generation of acoustic waves with wavelengths as long as a few hundred μm (typical frequencies of tens of MHz), and as short as 1 μm (typical frequencies up to a few GHz).[7] The time-dependent change in refractive index resulting from the propagating acoustic wave is typically probed with a third laser beam. A detailed description of the use of ISTS to probe the low-temperature MHz acoustic and thermal properties of a disordered material is given in Chapter 3.

A number of methods for optical generation and detection of acoustic waves of micron through nanometer wavelengths have emerged in recent years,[8,9,10] enabling the characterization of ever smaller and faster features of materials. A technique known as picosecond ultrasonics is used to reach acoustic frequencies in the GHz range.[11,12] Broadband acoustic wavepackets (i.e. single-cycle pulses) with frequency components up to 440 GHz [8] have been generated through optical irradiation of a thin metal film by a subpicosecond laser pulse. As in ISTS, the concurrent rapid expansion of the material launches an acoustic wave, in this case longitudinally through the plane of the film. The frequency content and initial amplitude of the acoustic pulse are limited by several factors, which will be discussed in more detail in Section 4.3. The acoustic wave may propagate out of the film in which it was generated and into and through underlying layers for broadband study of their material properties. Typically, partial reflections of the wave at interfaces within the sample are detected as "echoes" upon their return to the excitation film surface, usually via time-resolved measurement of strain-induced changes in reflectivity of the initial excitation film, or "transducer".[8,9, 27] In some cases the acoustic waves are instead detected through coherent scattering[12] or interferometry.[13,14] Fourier analysis of the reflected or transmitted waves allows study of the frequency-dependent material response. The broadband approach of picosecond ultrasonics is complicated by both the low signal-to-noise ratios typical at the highest frequencies of interest and the difficulty of unambiguous extraction of both the frequency-dependent velocities and damping rates from the detailed form of the reflected acoustic wavepackets, although in some cases it has been accomplished.[15]

Acoustic spectroscopy would benefit tremendously from a narrowband approach, which would reduce the experimental information content to be extracted from a single measurement at a given frequency to simply the acoustic velocity v_s and damping coefficient α. Then by tuning the frequency, variations in v_s and α resulting from structural and dynamical interactions would be obtained to shed light on the material properties. Narrowband acoustic waves in the 1 GHz - 1 THz range have been generated by a few methods, but with difficulty or without versatile tunability of the frequency. Femtosecond optical irradiation of multiple quantum well (MQW) structures has been used to generate acoustic waves in the ~700 GHz range. Here, the spatial periodicity of the wells determines the frequency of the acoustic wave; this has the unfortunate consequence that a different structure must be used to generate each different frequency.[16] Despite this limitation the upper frequency range is impressive. The broadband picosecond ultrasonics technique described above also has a narrowband analog. After the thin metal film is irradiated, the resulting acoustic wave may resonate inside it with a frequency that depends on the film's thickness and acoustic velocity, and an intensity that depends on the film's interface reflection coefficients (described in Section 4.3).[17] Each time the echo completes an additional round trip inside the film, partial transmission into the sample yields an additional "cycle" of a narrowband acoustic pulse. Frequencies up to 320 GHz have been generated by this method.[17] A limitation of this particular technique is, as above, that a new transducer must be fabricated to generate each frequency of interest. Further, if the transducer and the sample have similar acoustic impedances, then the echo amplitude will be very weak, leading to frequency-broadened acoustic waves with few cycles.

A more flexible method of generating acoustic waves between the frequencies 1-1000 GHz would have myriad applications in the study of mesoscopic structures and picosecond dynamics. Concentration of all the acoustic energy into a narrow frequency range offers enhanced signal/noise levels at the selected frequency, and as mentioned above, simplifies data analysis tremendously. The cost of this simplified analysis is that many separate measurements at different frequencies must be made in order to deduce the full frequency-dependent material response. A suitably robust and versatile approach to tunable narrowband acoustic wave generation would make thorough characterization of materials in this crucial frequency range possible. This thesis chapter reports a novel method for the optical generation and detection of tunable, narrowband acoustic waves throughout the GHz regime. The method is based on an ultrafast pulse shaper called the "Deathstar," which uses a multiple retro-reflection technique to generate optical pulse sequences which are then converted into longitudinal acoustic waves using a thin metal transducer, as in picosecond ultrasonics. This yields an acoustic waveform which is a convolution of the metal response and the optical input.[18] The principle and alignment of the pulse shaper are described, and the resulting optical waveforms characterized, in Section 4.2.1. The details of sample preparation are discussed in Section 4.2.2. The detection scheme is briefly described in Section 4.2.3, and in much more detail in Chapter 5. In Section 4.3 the conversion of the optically shaped pulses into acoustic waves is quantified and experimentally demonstrated at extremely high frequencies. Although the narrowband acoustic waves could be detected upon their return to the same film surface after partial reflections at interfaces, as is the usual case,[8,13] detection at the opposite side of the film was used in order to reduce time-dependent signal contributions due to electronic and thermal responses of the irradiated film, better isolating the signal due to the propagating acoustic wave. In Section 4.4 implementation of the widely used acoustic mismatch model for calculating acoustic waveforms at these frequencies in multilayer samples is demonstrated. Results of the model are compared to data. Sections 4.5 and 4.6 illustrate the information about complex materials that can be obtained from this technique. The resonant excitation of nanoscale structures with narrowband acoustic waves, as a method of determining their thickness, is demonstrated in Section 4.5. In Section 4.6 the effects on ultrahigh frequency acoustic wave speeds and attenuation rates upon propagation through a disordered material is demonstrated. The use of a sample design which simplifies extraction of absolute damping rates while requiring no assumptions regarding the material of interest, is demonstrated. Preliminary data from silica glass are shown, and the results are compared to those of other measurements. Lastly in Section 4.7, conclusions on the effectiveness of the experimental method for probing the structure and dynamics of complex materials are drawn.

4.2 Experimental Design

4.2.1 Deathstar Pulse Shaper

The "Deathstar" is an ultrafast pulse shaper which generates optical pulse trains with frequencies tunable between 1-1000 GHz. The field of pulse shaping is replete with schemes to generate ever more complicated sequences of pulses,[19,20] and with experiments that formerly required a table full of optics.[21] However, these widely used methods are most suitable for generation of pulse sequences in the 1-100 THz frequency range,[22] due to their inherently limited temporal window. In order to access lower frequencies, with as wide a dynamic range as possible, the Deathstar pulse shaper was designed. It is shown in the upper part of Figure 4.1 along with the rest of the experimental setup. The laser (not shown) is an amplified Ti:sapphire system consisting of an Innova-400 argon pump laser, Mira-900 oscillator, and RegA-9000 amplifier (Coherent, Inc., Santa Clara CA) whose output is a 200 fs pulse with 6 μJ energy, centered at 800 nm. The repetition rate was set to 75 kHz in order to provide enough time for complete thermal diffusion from the sample between laser pulses. A single laser pulse is introduced to the system of retro-reflectors in the pulse shaper, where it completes a series of round trips as shown. Each time the pulse passes the custom designed variable reflector (O.I.B. GmbH, Jena Germany), part of the pulse is transmitted. The reflection coefficients of the different parts of the variable reflector, the design of which is shown in Figure 4.2, were chosen so that temporal envelope of energies of pulses leaving the pulse shaper is roughly Gaussian. The system of mirrors following the pulse shaper compensates for the ~20 cm round trip that each subsequent pulse traverses, to temporally re-overlap the pulses when the delay line is fully forward (to the right in the figure).

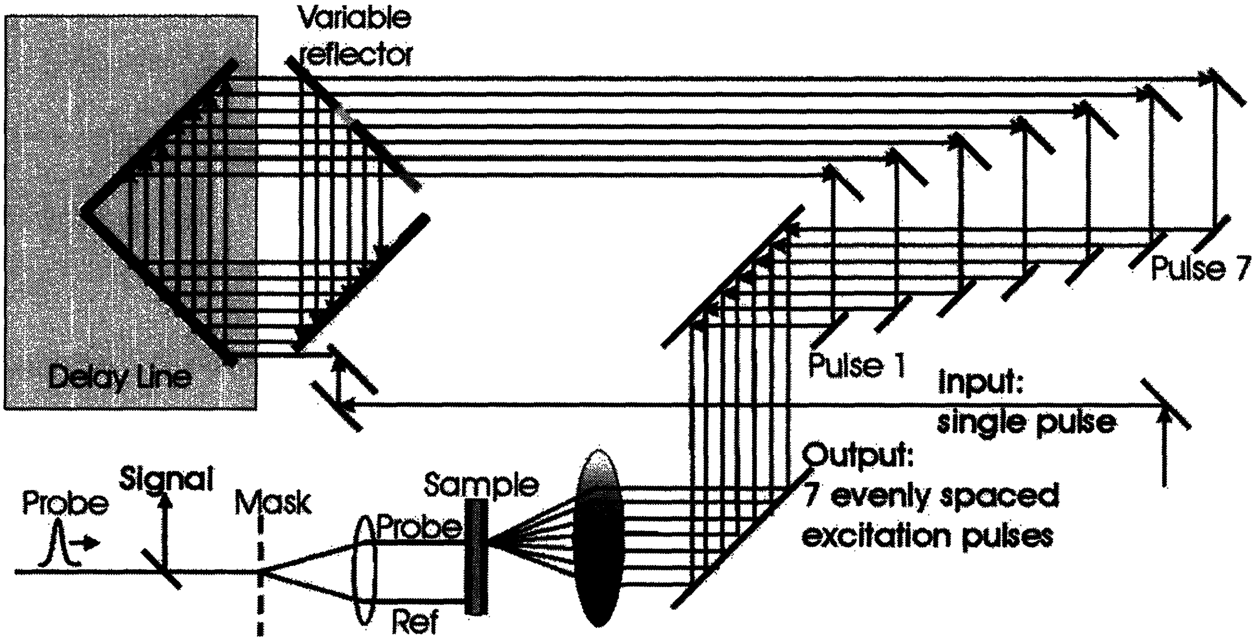
Variable reflector
Delay Line
Pulse 7
Pulse 1
Input: single pulse
Output: 7 evenly spaced excitation pulses
Probe
Signal
Mask
Sample
Probe
Ref

Figure 4.1. Deathstar pulse shaper, sample, and interferometric detection.

6.4%	13.8%	24.5%	37.3%	51.7%	70.4%	100%

Figure 4.2. Design of variable reflector. Substrate is fused silica 2.5 cm high by 7 cm wide. The backside of the optic has an antireflective coating for 800 nm light.

By adjusting the position of the delay line (Owis, Staufen Germany) in the pulse shaper (towards the left in Figure 4.1) the spatial, and therefore temporal, separation between all of the pulses is increased evenly. When the delay line is at its maximum extension to the left, the pulses are separated by 500 ps, resulting in a 2 GHz pulse train. This limit could easily be lowered through use of a longer delay line. Here the limit was chosen to overlap with the highest frequencies accessible by ISTS, as described in Section 4.1. The upper frequency limit of the pulse shaper is roughly 2 THz, and is constrained here by the laser pulse duration. It should be noted that the acoustic bandwidth, being a function of the transducer performance, is limited to roughly 500 GHz as described below in Section 4.3. An additional component of the pulse shaper is an ultrafast pulse stretcher (not shown) which is used to modify the duration of the incoming single pulse to any arbitrary length between 200 fs and 200 ps. This stretcher is external to the laser, and is comprised of two parallel holographic gratings (1800 lines/mm, Spectrogon US, Parsippany NJ) separated by a distance tunable by an additional delay line (Owis, Staufen Germany). It was designed to tune the duty cycle of the optical pulse train in order to narrow or broaden the frequency content of the waveform. In most cases it was found that using the shortest possible pulses generated the optimal acoustic response, and so the stretcher is not used routinely. With different sample and metal transducer parameters from those typically usually used in this chapter, in particular for considerably thicker metal films, the stretcher could play a useful role. After the optical waveform is optimized for the experiment, the pulses are focused through a common lens to a single spot of 120 μm diameter at the sample. Their conversion to acoustic waves is described in the following section.

The pulse shaper was aligned in two stages. First, the retroreflector assembly on the delay line was optimized so that its translation on the stage did not result in motion of the outgoing beam. Then, the angle of the variable reflector and its partner optic (just below it in Figure 4.1) were adjusted to make all of the pulses from the shaper parallel in both near field and far field. Lastly the partner optic was translated along a path perpendicular to its orientation, horizontally in the figure, to adjust the inter-pulse distance so that one pulse was transmitted through each unique part of the variable reflector. The second stage of alignment involved optimizing the positions of the series of mirrors following the pulse shaper in order to precisely re-overlap all seven pulses temporally when the delay line at or near its minimum extension, to the right in the figure. The round trip distance (i.e. timing) of consecutive pulses was measured, and this was first roughly corrected by placing the sets of mirrors after the shaper to approximately make up the difference. The sample was replaced with a thin BBO crystal, and the positions of the mirrors were adjusted until temporal overlap was found between every pulse inside of the crystal. A single "probe" laser pulse could be mixed with the shaped waveform inside the BBO to yield a cross-correlation to ensure optimal overlap.

Once the pulse shaper was aligned, the frequency of its output pulse sequence was adjusted simply by moving the delay line. Here the ease with which a variety of optical waveforms is demonstrated. Covering nearly 3 decades of frequency, the waveforms are generated with an arbitrary duty cycle by simply moving this delay line and, if desired, the one in the pulse stretcher. Cross-correlations for high frequencies, between 1 THz and 250 GHz, without the use of the external pulse stretcher are shown in Figure 4.3. Cross-correlations for lower frequencies, 50 GHz and 5 GHz, with the pulse stretcher adjusted to yield a 50% sine-like duty cycle to the waveform are shown in Figure 4.4. The intensity envelope in all scans appears somewhat rougher than the actual pseudo-Gaussian profile of the pulse intensities; this results

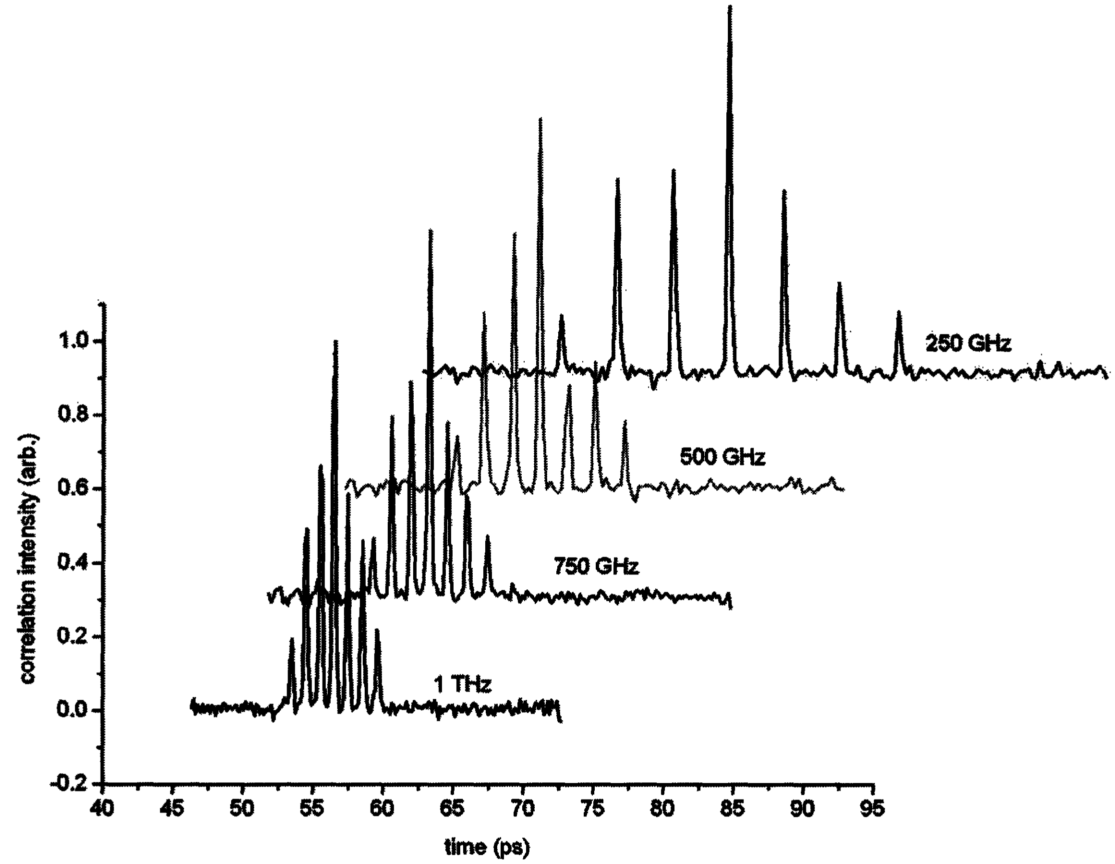

Figure 4.3. Cross-correlations of shaped pulse train with a single pulse, at high frequencies: 1 THz, 750 GHz, 500 GHz, 250 GHz, without use of additional pulse stretcher.

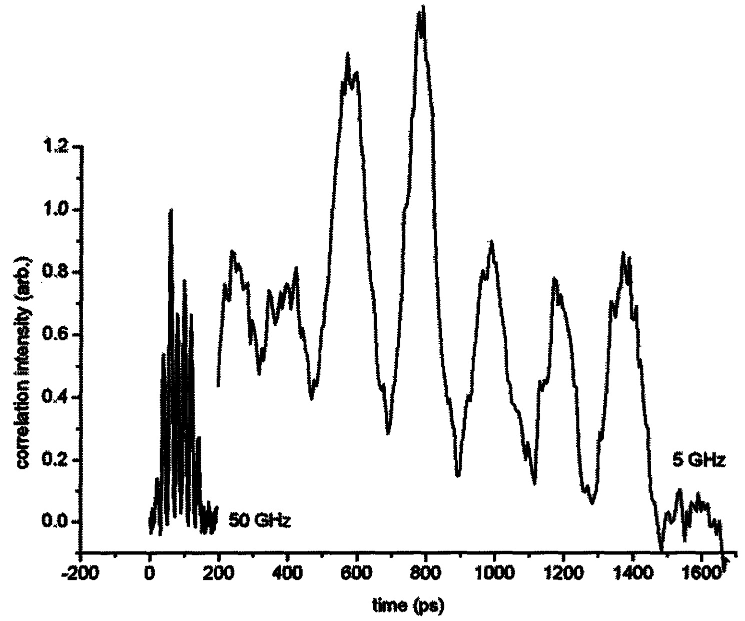

Figure 4.4. Cross-correlations of shaped pulse train with a single pulse, at "low" frequencies: 50 GHz and 5 GHz, with use of additional pulse stretcher to yield a 50% duty cycle.

from the fact that the shaped pulses arrive at slightly different angles at the BBO crystal, therefore experiencing slightly different conversion efficiencies into blue light when overlapped temporally with the reference pulse for the cross-correlation. Acoustic wave generation is not affected in a significant way by the angular variation of the beams, as will be demonstrated by the measured acoustic wave packet profiles in Section 4.3.

4.2.2 Sample Preparation

The sample is a "sandwich" structure which consists of 1) a thin metal film for the excitation of acoustic waves, in this case aluminum; 2) the sample of interest, in this case silica glass; and 3) a second aluminum film which allows the time-dependent displacement resulting from the arrival of the acoustic waves to be detected by a reflection-mode interferometer. The "excitation" aluminum film transducer was deposited in-house onto a sapphire substrate by electron-beam assisted evaporation at a pressure of 10^{-6} torr. High-resolution profilometry was used to determine the aluminum film thickness, which was found to be 17.6 nm. The amorphous silica glass (SiO_2) was hard-coated on top of the aluminum film by plasma-enhanced chemical vapor deposition (PECVD). This deposition technique was chosen in favor of sputtering or evaporation because the PECVD film characteristics more closely match those of bulk SiO_2, which is well characterized.[8] Different thicknesses of glass were coated on top of different parts of the excitation film, so that by translating the sample in the beam path, the propagation length of acoustic waves in the glass could be varied, simplifying extraction of absolute damping rates and velocities from the raw data as demonstrated below in Section 4.6. The sample was fabricated by first coating a thin layer of silica glass onto the entire substrate with aluminum film, then masking roughly ¼ of the structure with a microscope slide. An additional thin layer of silica glass was coated over the remaining exposed structure, then an additional ¼ of the substrate was masked; this procedure was continued across the sample so that there were four distinct thicknesses of glass on top of the aluminum film. The thicknesses of SiO_2 were 135, 210, 480, and 1010 nm, and were determined by a combination of 1) ellipsometry and 2) profilometry. They were also later characterized acoustically, using the technique described in Section 4.5. In order to accurately determine acoustic damping through the glass, thicker films (e.g., longer propagation lengths) were used for acoustic frequencies with low damping rates, and thinner films were used for frequencies with higher damping rates, in order to maintain a detectable signal but still have strong enough attenuation to measure reliably. A second aluminum film, identical to the first, was deposited on top of the various silica glass regions. This film "receives" the acoustic waves after propagation through the sample, and is displaced at the air-aluminum interface in a time-dependent manner which is detected interferometrically. The final sandwich structure is illustrated in Figure 4.5. In all measurements the acoustic waves were excited at the aluminum-sapphire interface, at which rapid diffusion of heat away from the excitation region was possible.

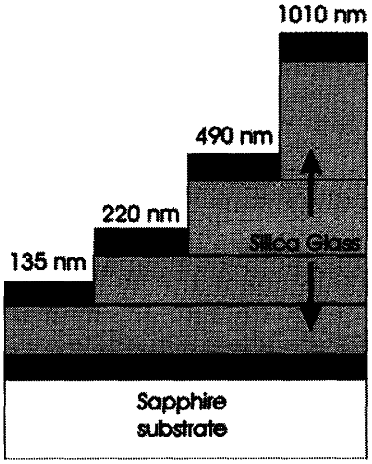

Figure 4.5. Sandwich structure for measuring acoustic properties of silica glass. The substrate has a 1" lateral dimension and is ¼" thick.

4.2.3 Interferometric Detection

The traveling acoustic wave was detected with a variably delayed probe pulse at the air-aluminum interface using a novel "grating" interferometer, which is described in greater detail in Chapter 4, and shown above in the lower left of Figure 4.1. The benefits of the interferometer are that the probe and reference arms travel on a common path, significantly reducing noise due to air currents and table vibrations; and that the interferometer is quite compact, consisting of only two optics. Briefly the interferometer works as follows: the two arms of the interferometer are generated by diffraction from a binary phase mask pattern, which has an etch depth chosen to maximize energy in the ±1 orders of diffraction for the optical wavelength[23] (Digital Optics Corp., Charlotte NC). These are called the "probe" and "reference" based on which one is used to monitor the time-dependent sample response, although they are entirely symmetrical in the interferometer. For interferometric detection, 390 nm light obtained by frequency doubling a small part of the unshaped pump beam was determined to be much preferable to use of ~800 nm light, which has been experimentally observed to experience a much more significant signal contribution from acoustic and thermal strain-induced reflectivity changes. The ~400 nm wavelength used here has only a minor reflectivity contribution, and also gives twice the interferometric sensitivity to displacements. The comparison between ~400 and ~800 nm light for interferometric measurement in this material system is demonstrated in Section 5.3, and the difference in reflectivity signal contribution is given. The reflectivity change for 800 nm light[11] is typically used in other experiments as the only source of signal,[8,9] and does not allow for calibration of displacement.

The periodicity of the phase mask could be varied between 2-100 μm, depending on the experimental requirements for spacing between the two interferometer arms. Generally the larger the spacing, the smaller the inter-arm separation and the more stable the interferometer. Here a 50 μm grating was used, yielding a roughly 1.5 mm interbeam spacing at the sample. A lens, *f*=18 cm, is used to focus the two beams onto the sample plane, where one of them (the probe) is overlapped with the excitation beam inside a pinhole which the two beams approach from opposite sides. The pinhole is then replaced by the sample. The probe beam experiences a time-dependent change in path length (on the order of $\lambda/1000$) due to the traveling acoustic wave that is launched by the excitation pulse at the front of the sample. The probe and reference beams are reflected at the air-aluminum interface at the back of the sample, recollimated by the same lens, and recrossed onto the phase mask, where they diffract and the different orders interfere with each other. The +1 order of the probe diffracts collinearly and phase-coherently with the -1 order of the reference, approximately in the direction opposite to that of the incident probe beam on the phase mask, and this yields the signal beam which is picked off with a thin beamsplitter. The interferometric signal level varies with time as a function of the acoustically induced displacement at the probe spot, and is detected with a lock-in amplifier. Signals from bare transducers are shown in Section 4.3 and from the full sandwiched sample in Section 4.6.

4.3 Optic to acoustic conversion

Here the mechanism for converting shaped optical pulses into acoustic waves via thin aluminum films, or transducers, is discussed. The numerical calculations in this section were performed by K. Katayama. The generation of ultrasonic pulses via ultrafast irradiation of thin metal films has been extensively studied and is fairly well understood.[18,24,25,26,27] At the simplest level, when a laser pulse of energy Q irradiates an area A of a metal film, it penetrates some distance described by ζ = 1/e intensity attenuation. The resulting temperature rise on the length scale z into the film is given by:[18]

$$\Delta T(z) = \frac{(1-R)Q}{CA\zeta}\exp\left(\frac{-z}{\zeta}\right) \qquad 4.1$$

where R is the optical reflectivity of the film and C the heat capacity. For aluminum the value of ζ at 800 nm is 8.3 nm, and the temporal duration of the laser pulse is unimportant so long as it is sub-picosecond. The temperature rise is then expected to be reflected in the temporal and spatial shape of the acoustic strain pulse $\eta(z,t)$ launched in the plane of the film by:

$$\eta(z,t) = \frac{-3(1-R)Q\beta B}{2AC\zeta\rho v_s^2}\exp\left[\frac{-(z-v_s t)}{\zeta}\right]\operatorname{sgn}(z-v_s t) \qquad 4.2$$

Here β is the linear thermal expansion coefficient, B is the bulk modulus, and v_s is the longitudinal acoustic velocity in the material. The strain pulse is related to the displacement of the film (e.g., the observable signal) by:

$$\eta(z,t) = \frac{\partial u}{\partial z} = \frac{1}{v_s}\frac{\partial u}{\partial t} \qquad 4.3$$

A problem in these expressions arises if thermal diffusion out of the excitation region occurs more quickly than the acoustic wave can propagate away, e.g. in the case:

$$D \geq \zeta v_s \qquad 4.4$$

where D is the diffusion constant. In metals D and ζv_s are of the same order, so this effect does broaden the acoustic strain pulse. However, this is not the only additional effect that must be considered. In order to understand the true strain profile, the macroscopic picture described above must be revised because it does not reflect the true dynamics which significantly broaden the strain profile and limit the acoustic bandwidth. In particular, the dynamics of the "hot" electrons produced through light absorption in the thin front region of the sample must be treated. Excited electrons travel at supersonic speeds through the material, much more quickly than normal thermal transport, $D_e \sim 100D$,[18] yielding the dominant broadening effect beyond what is contained in Equation 4.2. An illustration of the broadening of the temperature distribution in an aluminum film is shown in Figure 4.6.

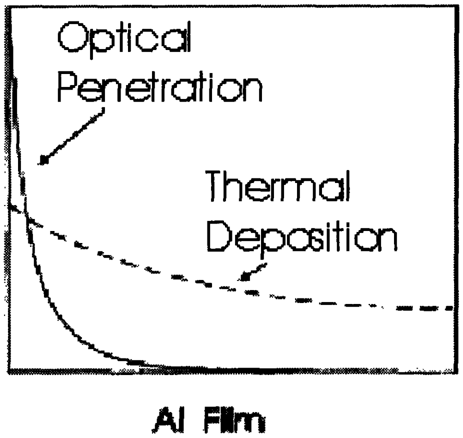

Figure 4.6. Temperature profiles in aluminum film expected from optical penetration depth into the film (solid curve) and broadening of the response by rapid thermal and electron diffusion through the film (dashed curve). Adapted from Reference 18.

A two-temperature model (TTM)[18,25,28] describes the dynamical processes which determine the actual profile of the acoustic strain pulse, which is required here for understanding the modifications to the pulse upon propagation through a complex sample. When a light pulse with energy Q irradiates the metal film, it excites the electrons and raises them to a temperature T_e which is different from the lattice temperature. Over a few picoseconds, this energy is then transferred into the acoustic phonon modes of the lattice, which have a temperature T_{ph}. Eventually the entire lattice cools to its equilibrium temperature. The equations of motion which describe the two coupled temperatures of the system are:

$$\gamma T_e \frac{\partial T_e}{\partial t} = \kappa(T_e)\frac{\partial^2 T_e}{\partial z^2} - G(T_e - T_{ph}) + S(z,t) \qquad 4.5$$

$$\rho C \frac{\partial T_{ph}}{\partial t} = G(T_e - T_{ph}) \qquad 4.6$$

where γ is the electronic specific heat, ρ is the material density, and κ is the electronic conductivity, which is a temperature dependent quantity, simplified by the approximation:[18]

$$\kappa(T_e) = \frac{\kappa_e T_e}{T_{ph}} \qquad 4.7$$

through which it is related to the bulk conductivity κ_e. $S(z,t)$ expresses the source term, which is here a single ultrafast laser pulse penetrating into the film, similar to that of Equation 4.1 but including the temporal dependence of the pulse:[29]

$$S(z,t) = \frac{(1-R)Q}{\zeta A} \exp\left(\frac{-z}{\zeta} - 2.77\left(\frac{t}{\tau_p} \right)^2 \right) \qquad 4.8$$

The value τ_p=0.2 ps describes the optical pulse duration. Lastly, G in Equation 4.5 describes the transfer of energy from electrons to phonons. It is related to the electron-phonon coupling constant λ by:[18]

$$G = \frac{3\hbar\lambda\left\langle \omega^2 \right\rangle \gamma}{\pi k_B} \qquad 4.9$$

where $\left\langle \omega^2 \right\rangle$ is the average of the square of the phonon frequency. The value of G is difficult to obtain theoretically, and here is simply treated as an empirical value 1x10^{17} Wm^{-3}K^{-1} obtained from electron diffusion experiments reported in the literature.[30]

The temperature rise is calculated numerically with the system of Equations 4.5 and 4.6 for a single laser pulse as a function of depth into the film. The optical, electronic, and thermal parameters used for the calculation are listed in Table 4.1. The mechanical parameters such as density are listed later on in Table 4.2**Table 4.2. M** with those of other materials in the system. From the

Parameter	Description	Value
Q	Pulse energy	100 nJ
A	Beam diameter	400 μm
τ_p	Pulse duration	200 fs
Z	Optical penetration depth	8.3 nm
C	Specific heat	$0.9\text{x}10^{3}$ J kg^{-1} K^{-1}
R	Optical reflectivity	0.88
B	Linear expansion coefficient	$26\text{x}10^{-6}$ K^{-1}
B	Bulk modulus	$75.2\text{x}10^{9}$ Pa
Γ	Electronic heat capacity	30.5 J $\text{K}^{-2}\text{m}^{-3}$ x T
G	Electron-phonon coupling constant	$1\text{x}10^{17}$ W K^{-1} m^{-3}

Table 4.1. Optical, thermal, and electronic parameters used in two-temperature model to calculate acoustic waveforms resulting from optical excitation of aluminum films. Electronic heat capacity requires multiplication by temperature to obtain the value.

solution to the equations the "effective" optical penetration depth, illustrated by the dashed line in Figure 4.6, is determined to be roughly 18 nm. If the input to Equation 4.5 is the actual optical waveform from the Deathstar pulse shaper, as shown in Figure 4.7, then the result may be used in the thermo-elastic equation of motion to calculate, at the value of z corresponding to the back of the sample, the displacement $u(z,t)$ and strain $\partial u(z,t)/\partial t$, using Equation 4.3:

$$\frac{\partial^2 u(z,t)}{\partial t^2} = v_s^2 \frac{\partial^2 u(z,t)}{\partial z^2} - \frac{3\beta B}{\rho} \frac{\partial T_{ph}(z,t)}{\partial z} \tag{4.10}$$

The calculated excitation transducer response is shown in Figure 4.8 for the "sandwich" sample described above, with the aluminum film between sapphire and silica glass. Clearly the film's response is much slower than the ultrafast input pulse duration, roughly 2.5 ps vs. 200 fs FWHM, and ultimately this limits the maximum acoustic bandwidth to ~500 GHz with the current materials.

For the experiment, aluminum thickness values of approximately 15 nm were selected in order to maximize the absorption of light by the transducer while at the same time keeping the

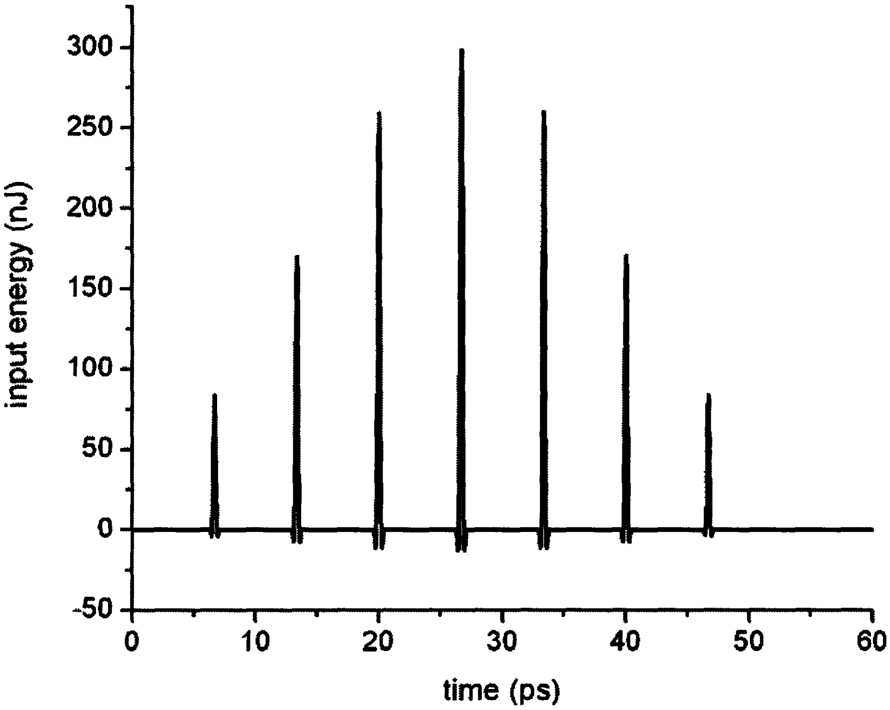

Figure 4.7. Input to numerical calculation of acoustic transducer response (approximate pulse shaper output at 150 GHz, with 200 fs unbroadened pulses).

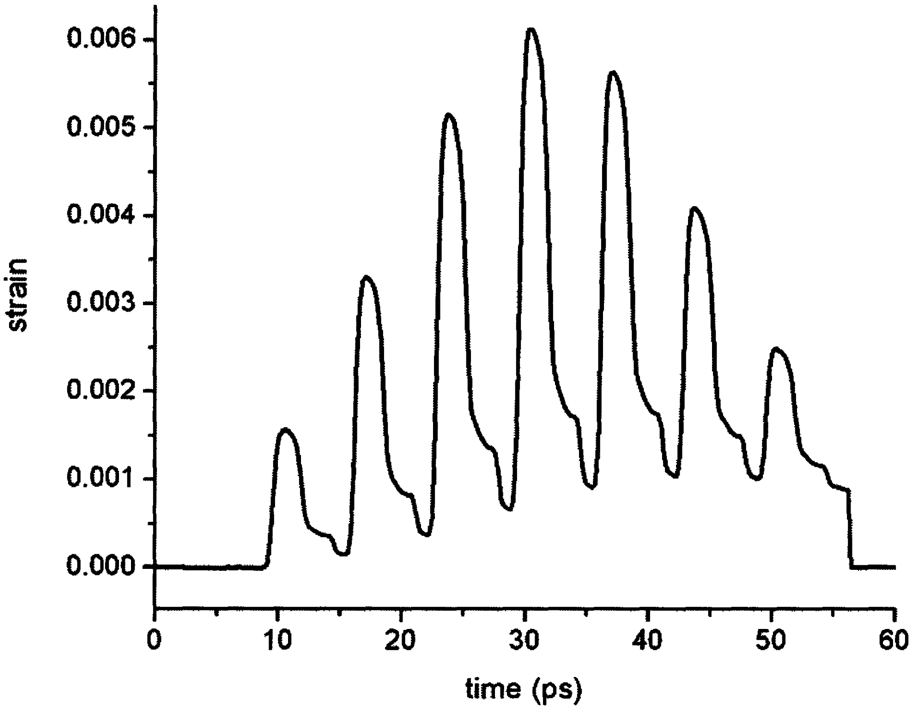

Figure 4.8. Strain at the back of the excitation transducer from numerical calculation of thermo-elastic equation of motion 4.10 using a two-temperature model to calculate the temperature profile with Equation 4.5, with pulse shaper output at 150 GHz with 200 fs pulses. The sharp edge at the end of the waveform is an artifact from the numerical calculation.

acoustic bandwidth fairly high. Use of a thinner transducer would yield a higher bandwidth but reduced signal. The measured response of a "bare" excitation transducer film, coated onto a sapphire substrate but lacking the silica glass sandwich, to the shaped pulse train is demonstrated here. In all cases the film was excited at the sapphire-aluminum interface and the acoustic wave detected at the aluminum-air interface. This scheme was chosen instead of probing at the aluminum-silica interface, because a strong signal contribution from the acoustic wave propagating through the glass masks the aluminum signal. However the aluminum response is directly proportional to that calculated above, differing only by a constant factor of the acoustic reflection coefficient $\tilde{r}_{Al-SiO_2}$ at the interface. Figure 4.9 (a) and (b) show the displacement and strain (calculated from the raw data using Equation 4.3) in a ~15 nm aluminum film excited at 95 GHz. Figure 4.10 (a) and (b) show the displacement and strain at 190 GHz, and Figure 4.11 (a) and (b) show the displacement and strain at 415 GHz, near the bandwidth limit of the film. The strain was calculated by applying Equation 4.3 to the raw data.

The first notable feature of the three figures is a steady increase in the displacement as each acoustic pulse, appearing as a "step," arrives at the probing region. This is a result of the strain pulse having a nearly unipolar temporal profile, due to the large acoustic impedance mismatch between aluminum and sapphire, where the pulse is generated.[12] Typically in photoacoustic experiments, strain is generated at the air-aluminum interface,[8] resulting in a bipolar strain pulse; in that case the signal returns to its baseline value after the pulse propagates out of the probing region. Here sapphire is used because it rapidly conducts heat away from the excitation region, allowing the sample to essentially fully cool between laser pulses. This substrate effect has little consequence to the current experiment, contributing a quasi-dc component to the signal, and can be avoided by choice of a different substrate with a somewhat

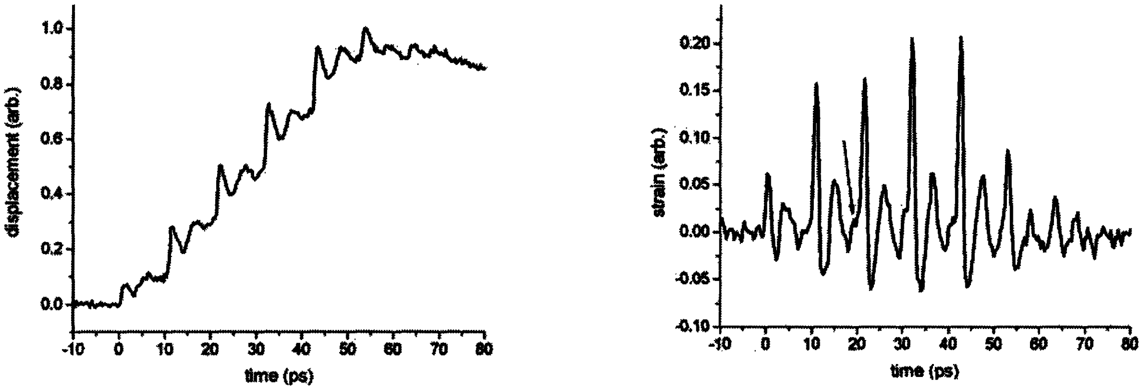

Figure 4.9. (a) Displacement of 15 nm aluminum film resulting from shaped excitation at 95 GHz. (b) Strain in film. The arrow indicates the arrival of an acoustic "echo".

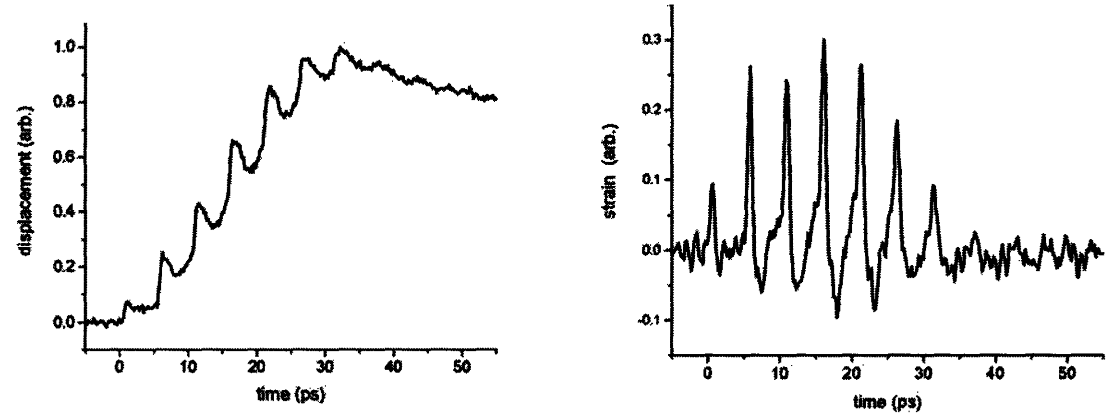

Figure 4.10. (a) Displacement of 15 nm aluminum film resulting from shaped excitation at 190 GHz. (b) Strain in film.

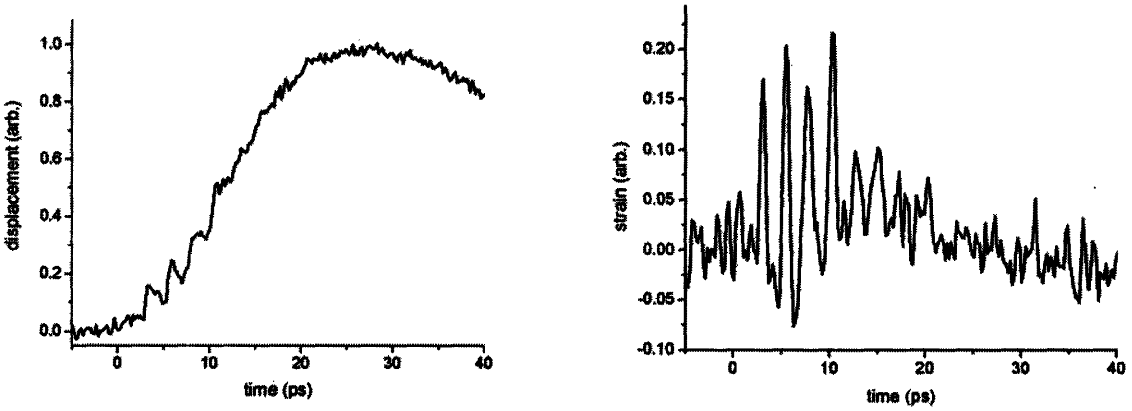

Figure 4.11. (a) Displacement of 15 nm aluminum film resulting from shaped excitation at 415 GHz. (b) Strain in film.

lower acoustic impedance than aluminum.[15] The shape of the acoustic features may be understood more readily by examining the strain induced by the material response, and can be seen to look as one might expect.

The conversion to acoustic energy may be observed readily with excitation at 95 GHz, shown in Figure 4.9 (b). The arrival times of the seven pulses are apparent as sharp "peaks" in the strain roughly 10 picoseconds apart. A notable difference from the TTM is that the peaks appear somewhat sharper than expected from Figure 4.8. This results from a signal contribution not only from acoustic displacement, but also from the presence of excited electrons that are present during and shortly after the optical excitation pulse is interacting with the metal. This is observable because the probe spot is separated from the excitation region by only the thickness of the film, roughly 15 nm. Some probe light penetrates into the film to "see" the arrival of the excitation pulses, and perhaps more importantly, the hot electrons rapidly (within the excitation pulse duration) traverse the film as discussed above. In the short time during which the hot electrons relax, the generated acoustic wave traverses the thin film with a single-time trip ~2.3 ps, and so is not independently observable except as a broad tail to the electronic peak. Following each excitation pulse at a time ~4.6 ps corresponding to the acoustic round-trip traversal time in the film, a distinct signal can be observed in both the displacement and strain traces, corresponding to the arrival of an "echo" of the excited acoustic wave. Because its frequency content is limited by the bandwidth of the transducer, and because the signal contribution is purely acoustic, the wave appears rounded compared to the peaks resulting directly from optically excited electrons. Then the next excitation pulse arrives at a time corresponding roughly to twice the round trip time of the acoustic wave in the film, ~9.2 ps. The slightly earlier arrival of a second "echo" at this time is noted with an arrow in the figure.

For excitation at 195 GHz, Figure 4.10 (b), the round trip time of the echoes so apparent in Figure 4.9 (b) overlaps with the temporal spacing of the excitation pulses, and so the echoes are not observed. However an additional "ringing" of the film subsequent to the last excitation pulse arrival, which can be clearly seen at a time around 35 ps, is an indication that the acoustic echoes experienced some constructive interference due to their temporal overlap. At 415 GHz, Figure 4.11 (b), the time between electronic peaks is less than the acoustic traversal time through the film, and it is not possible to independently assess the presence of acoustic waves in the signal. Note that this does not rule out the presence of an acoustic response in the film. Figure 4.12 shows the expected weak generation of acoustic phonons at 400 GHz, calculated from the TTM.

The generation of tunable, narrowband acoustic waves has been demonstrated, noting that while the optical pulse shaping technique allows frequencies up to 1 THz, the use of metal transducers limits the acoustic frequencies to a somewhat lower region.

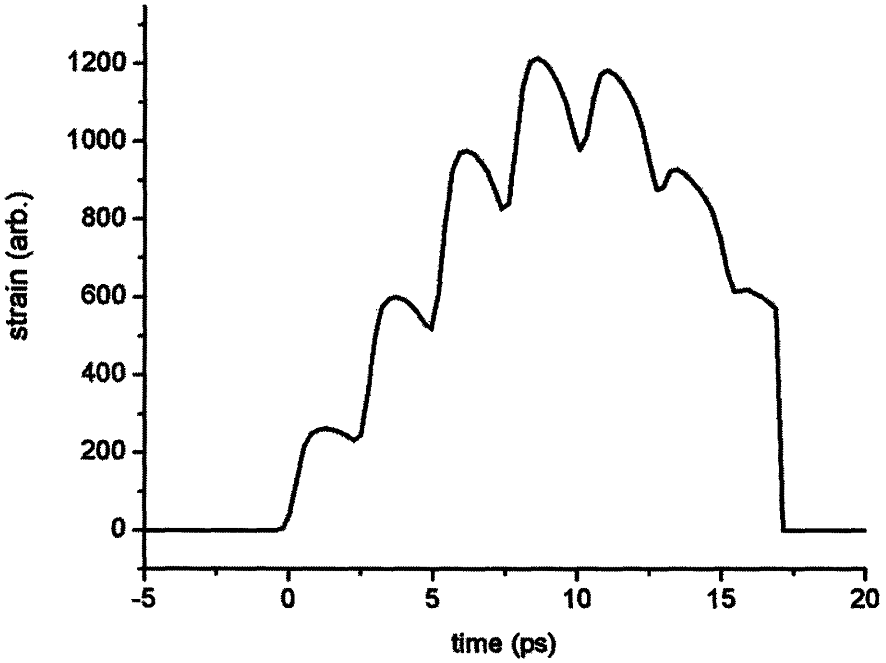

Figure 4.12. Generation of acoustic waves at 400 GHz calculated with TTM.

4.4 Model for Propagation

Next the interaction of high frequency acoustic waves with the multilayer structures to be used for spectroscopy is modeled as a way of understanding the actual signals obtained from the measurement. The model is referred to as "acoustic mismatch theory," after Reference 8, and is widely known and used without reference to a unique source. Quantifying the propagation of acoustic waves through multilayer structures requires careful analysis of reflection and transmission coefficients at each interface, as well as frequency-dependent acoustic velocities and damping rates. The amplitude of the transmitted acoustic wave $u_{sig}(z,\omega)$, i.e., the signal detected at the end of the sample, depends upon the reflection and transmission coefficients at all boundaries, as well as the temporal delay collected by propagation through the various layers. The analysis method is taken from References 3 and 23, here for a multilayer sample consisting of five materials: the sapphire substrate, excitation transducer, silica glass, receiver transducer, and air, from left to right as shown in Figure 4.13.

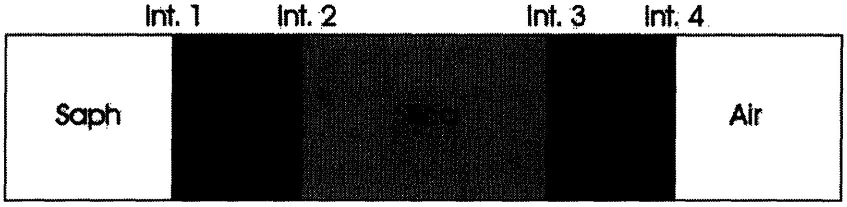

Figure 4.13. Multilayer system to be modeled.

The calculation is performed in the frequency domain, allowing frequency-dependent dispersion and damping to be easily treated, and then Fourier-transformed into the time domain to yield the expected signal. A longitudinal acoustic wave of arbitrary shape $u_{exc}(z,t)$ is launched through the plane of the excitation aluminum transducer film, as calculated above in Equation 4.10, and it is assumed that no further modifications to the shape occur during propagation within the aluminum. Though acoustic broadening upon propagation through hundreds of nm of aluminum has been observed,[31] the film thicknesses here should exhibit a comparatively negligible effect. This assumption is not made for propagation through the silica layer, for which the frequency dependent acoustic properties are of interest. The frequency content of the wave after generation in the aluminum is then given by the Fourier transform:

$$u_{exc}(z,\omega)=\frac{1}{2\pi}\int_{-\infty}^{\infty}u_{exc}(z,t)e^{i\omega t}dt \qquad 4.11$$

When the wave travels through the aluminum layer and into the silica glass layer, it undergoes partial transmission and reflection at the boundary which is determined by the mismatch of the acoustic impedance $Z=v\rho$ of the two materials:

$$\vec{r}_{Al-SiO_2}=\frac{v_{Al}\rho_{Al}-v_{SiO_2}\rho_{SiO_2}}{v_{Al}\rho_{Al}+v_{SiO_2}\rho_{SiO_2}} \qquad 4.12$$

$$\vec{t}_{Al-SiO_2}=\frac{2v_{Al}\rho_{Al}}{v_{Al}\rho_{Al}+v_{SiO_2}\rho_{SiO_2}} \qquad 4.13$$

Where the notation $\vec{r}$ and $\vec{t}$ indicates the reflection and transmission coefficients for a wave traveling from left to right, as compared to $\overleftarrow{r}$ and $\overleftarrow{t}$ to be used in the case of a wave traveling right to left. The coefficients satisfy the boundary condition:

$$\vec{t}=\vec{r}+1 \qquad 4.14$$

After partial transmission the wave propagates in silica glass with amplitude and phase given by:

$$u_{SiO_2}(z,\omega)=\vec{t}_{Al-SiO_2}\exp\left(\frac{i\omega z}{v_{SiO_2}}\right) \qquad 4.15$$

Here the wave travels for a distance $z=d_{SiO2}$, where d is the thickness (determined experimentally as described above in Section 4.2), before it experiences partial reflection at the silica-aluminum boundary, which can be described by Equations 4.12 and 4.13 with the appropriate values for material properties.

The velocity with which the wave propagates through the silica layer is a frequency-dependent complex quantity, related to the experimentally defined (i.e. real) frequency and the complex wavevector by:

$$\tilde{v}(\omega) = \frac{\omega}{\tilde{q}(\omega)} = \frac{\omega}{q'(\omega) + iq''(\omega)} \approx \frac{\omega}{q'(\omega)} - i\frac{\omega q''(\omega)}{q'(\omega)^2} = v'(\omega) - iv''(\omega) \qquad 4.16$$

For the discussion here the phase velocity $v'(\omega) = \omega / q'(\omega)$ is assumed to be frequency-independent, $v'(\omega) \approx v_0$. This based on the results of previous experiments which show no acoustic dispersion at high frequencies in glasses at low temperatures,[32] and on the basis of indirect observation via the thermal conductivity[33] (see Section 2.2 for further discussion). The imaginary part of the velocity is related to the observed damping coefficient $\alpha(\omega) \equiv q''(\omega)$ in the material by the phase velocity:

$$v''(\omega) = \frac{\alpha(\omega)\omega}{q'(\omega)^2} = \frac{\alpha(\omega)v'(\omega)^2}{\omega} \approx \frac{\alpha(\omega)v_0^2}{\omega} \qquad 4.17$$

The damping coefficient $\alpha(\omega)$ varies strongly with frequency, and its experimental determination across a wider and higher frequency spectrum than previously possible is one of the goals of this thesis. In Chapter 2 its expected behavior at low temperature is calculated based on a well-known model which relates the bulk thermal conductivity to microscopic interactions of the acoustic wave with the glass. A shortcoming of this technique is that the interactions are observed indirectly. In Chapter 6 the techniques described in the current chapter are used obtain a preliminary acoustic spectrum $\alpha(\omega)$ for silica glass, which is compared to the results of previous measurements at room temperature, and to the model from Chapter 2 at low temperature where no other literature results are available. For the simulations performed here based on the acoustic mismatch theory, the value of the damping coefficient may be fit phenomenologically to the narrowband measurement at a particular frequency ω_0.

To calculate the signal $u_{sig}(z,\omega)$, a system of coupled equations must be solved which incorporates the optical input to the sample (which is a waveform of arbitrary shape) and the response of each coupled layer, which are related to each other by reflection coefficients and propagation times. A diagram of the system is shown in Figure 4.14. Here A and C are aluminum, B is silica glass, and the interfaces are numbered 1, 2, 3, and 4, as in the schematic Figure 4.13. Because the acoustic propagation through sapphire and air is uncoupled from the rest of the system, only their interfaces with the other layers are treated. The coefficients a_n describe the inputs to the various layers and interfaces, and b_n describe the output of each layer or interface, as in Reference 23. The values at the interface b_n come from the reflection and transmission coefficients $\vec{r}$ and $\vec{t}$ or $\overleftarrow{r}$ and $\overleftarrow{t}$ as shown above in Equations 4.12 and 4.13. The values of the outputs b_n come from the propagation of the acoustic wave, as in Equation 4.15, here using frequency-independent velocities v_n for aluminum, air, and sapphire, and for silica glass a constant phase velocity and a phenomenological damping coefficient, $v_B = v_0 - i\alpha(\omega_0)v_0^2/\omega$. The values of the mechanical properties of the materials modeled in this chapter and Chapter 6 are listed in Table 4.2.

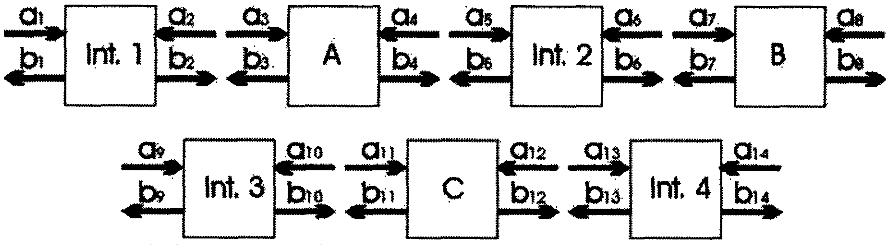

Figure 4.14. Multilayer model system with inputs a_n and outputs b_n from each interface and layer. The system at upper right continues at lower left.

Material	Thickness d (m)	Density ρ (kg m^{-3})	Velocity v (ms^{-1})	Impedance Z (kg m^{-2} s^{-1})
Sapphire	N/A	3990	11100	44.3x10^{6}
Aluminum	18x10^{-9}	2700	6420	17.3x10^{6}
Silica glass	Varied	2200	5900	13.0x10^{6}
PMMA	Varied	1190	2830	3.37x10^{6}
Air	N/A	1.29x10^{-3}	331.5	0.428

Table 4.2. Mechanical properties of various materials discussed and modeled in this chapter, and in Chapter 6.

The optical excitation of the system occurs at the boundary between sapphire and aluminum, a_1. However the conversion into acoustic waves occurs inside the aluminum, and if the numerically calculated TTM response of the aluminum is used for the optical input, then the acoustic input to the system must be placed at a_5. The signal $u_{sig}(z,\omega)$ will be measured at the air-aluminum interface *4*, as the output b_{14}. The system of coupled equations can then be written as:

$$\begin{gathered}
b_2 = b_3 \overleftarrow{r}_1 \\
b_3 = \exp\left(i\omega d_A v_A^{-1}\right) b_5 \\
b_4 = \exp\left(i\omega d_A v_A^{-1}\right) b_2 \\
b_5 = b_4 \overrightarrow{r}_2 + b_7 \overleftarrow{t}_2 \\
a_5 = b_4 \overrightarrow{t}_2 + b_7 \overleftarrow{r}_2 - b_6 \\
b_7 = \exp\left(i\omega d_B v_B^{-1}\right) b_9 \\
b_8 = \exp\left(i\omega d_B v_B^{-1}\right) b_6 \\
b_9 = b_8 \overrightarrow{r}_3 + b_{11} \overleftarrow{t}_3 \\
b_{10} = b_8 \overrightarrow{t}_3 + b_{11} \overleftarrow{r}_3 \\
b_{11} = \exp\left(i\omega d_C v_C^{-1}\right) b_{13} \\
b_{12} = \exp\left(i\omega d_C v_C^{-1}\right) b_{10} \\
b_{13} = b_{12} \overleftarrow{r}_4 \\
b_{14} = b_{12} \overrightarrow{t}_4
\end{gathered}$$

In order to obtain the signal output b_{14}, the system of equations must be solved computationally, which was performed here by converting them into matrix form and solving in

MATLAB as otherwise reported in Reference 23. This was then back-transformed into the time domain to obtain the displacement signal $u_{sig}(z,t)$ and strain $\eta_{sig}(z,t)$:

$$u_{sig}(z,\omega) = b_{14}(z,\omega) \qquad 4.18$$

$$u_{sig}(z,t) = 2\pi \int_{-\infty}^{\infty} b_{14}(z,\omega) e^{-i\omega t} d\omega \qquad 4.19$$

$$\frac{\partial u_{sig}(z,t)}{\partial t} = \eta_{sig}(z,t) \qquad 4.20$$

The calculated displacement resulting from excitation at 150 GHz and propagation through 210 nm of SiO_2 is plotted in Figure 4.15, and the calculated strain is shown in Figure 4.16. The input a_5 to the simulation the result of the two-temperature model discussed in Section 4.3. The damping coefficient $\alpha(\omega_0)$=1.1x10^6 at 150 GHz was determined experimentally using the techniques described in Section 4.6, and can also determined by varying its value to improve the fit to the data with somewhat less reliability, due to the dependence then on the initial assumptions. For example as shown in Chapter 6 a fit to a different set of data from the same sample yields a different fitted constant. The difference likely comes from some modeling parameter which is more sensitive to the particulars of the sample or even the alignment than expected. Also included is experimentally measured signal, which has a maximum displacement of 0.48 nm as calibrated using the techniques described in Chapter 5. This displacement is typical for experiments with various materials inside the sandwich structure, because the total displacement comes from the thermal expansion following optical excitation.

Using Equation 4.3 the maximum strain is found to be 0.0041, which is comparable to that calculated by the TTM for the strain after the first aluminum film, as shown in Figure 4.8. It should be noted that the use of Equation 4.3 connects displacements only to the *dynamical* strain. For example, the steady-state displacements seen near 175 or 275 ps in Figure 4.15 yield zero

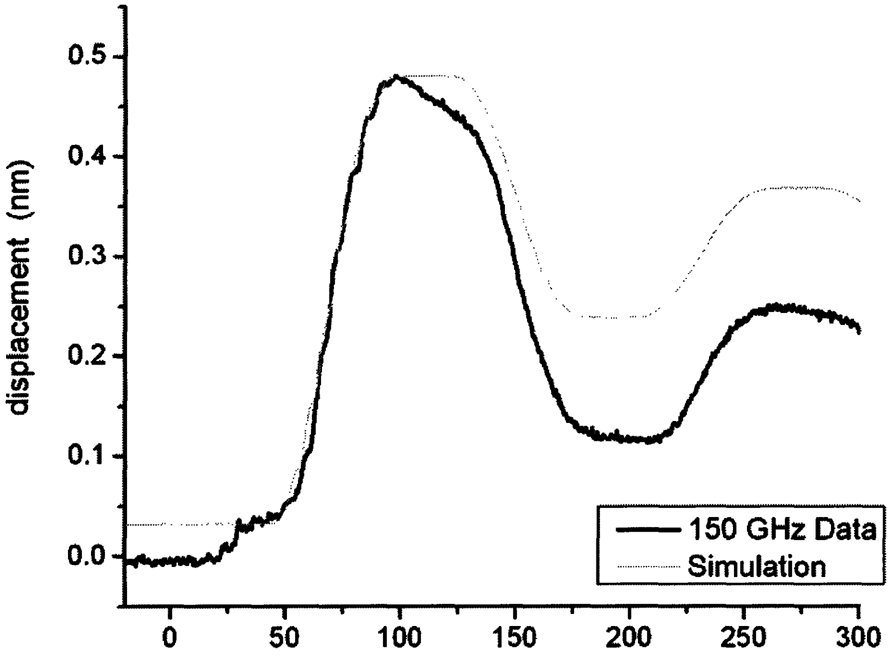

Figure 4.15. Calibrated displacement resulting from propagation of 150 GHz acoustic wave through 210 nm silica glass, plotted with acoustic mismatch simulation using α(150 GHz)=1.1x10^6 m^{-1} and the parameters listed Table 4.2.

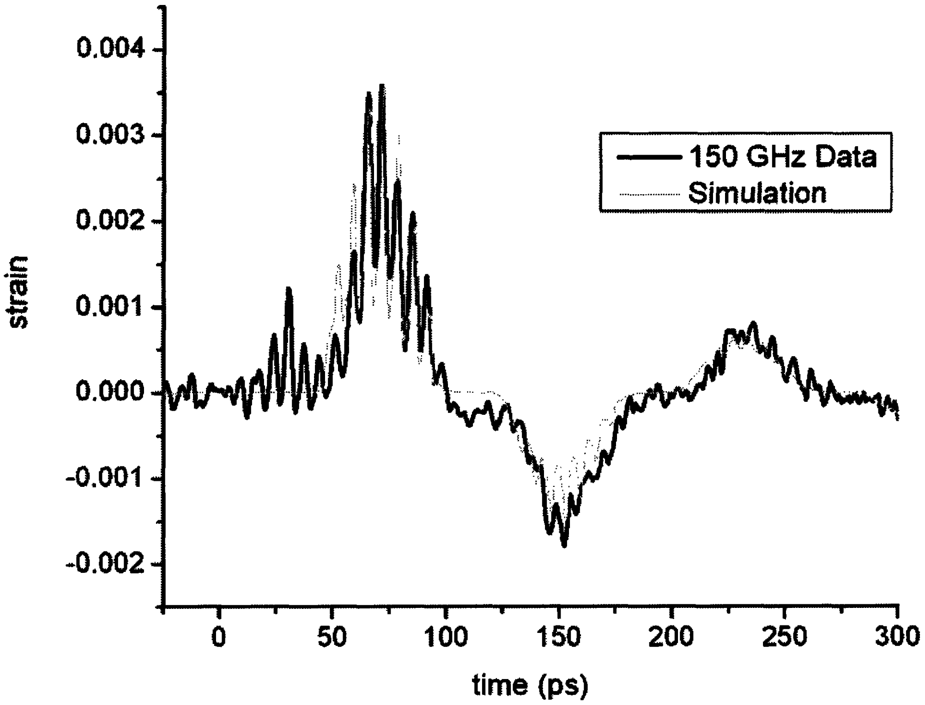

Figure 4.16. Calibrated strain resulting from propagation of 150 GHz acoustic wave through 210 nm silica glass, plotted with acoustic mismatch simulation using α(150 GHz)=1.1x10^6 m^{-1} and the parameters listed in Table 4.2.

strain in Figure 4.16. However, propagations traveling at speed v_s do produce a strain. The typical value of the dynamical strain at the back of the sample following propagation through multiple layers varies from sample to sample (and frequency to frequency) as the damping rate of the acoustic wave is very sensitive to the microscopic parameters of the material, as shown in Chapter 6 for the frequency-dependent acoustic damping in silica glass. However the magnitude of the displacement is usually comparable from sample to sample, as it is related to the low-frequency part of the acoustic envelope, arising from the deposition of heat into the sample. In Figure 4.16 the simulation is normalized to the measured strain. However the modeling method described in this section does yield an absolute magnitude of the expected transmitted strain of 0.0032 for the shaped optical input shown in Figure 4.7, which is comparable to that of the measurement.

Mechanical engineers frequently describe the strain in terms of a steady state displacement of the film relative to the thickness of the film, which in this case is much larger, 0.032. This large value can be rationalized because the film is not very thick, and the acoustic envelope is at least as large so the dynamic strain across the acoustic response extends throughout the film. Strains of this magnitude would not be likely without damage in larger (macroscopic) samples. The steady state strain predicted by the two-temperature model described in Section 4.3, based on thermal expansion, fall in line with the measured values. For a spot size of 100 μm (within 20% of the actual value) and a total excitation energy of 1.3 μJ, the temperature is calculated to rise to ~1600 K. This yields a strain of 0.041, which is on the order but somewhat larger than the steady-state strain measured in the film. However the melting point of aluminum is 923 K, and it was indeed found that frequently the excitation energy had to be significantly attenuated to ~600 nJ avoid burning holes in the sample. With the variation of all the experimental parameters considered, the value of the steady-state strain is within about 40% of that expected from the models.

At a time of zero picoseconds in the experimental displacement shown in Figure 4.15, a small rise in the displacement is observed, and in the experimental strain shown in Figure 4.16 a series of small peaks can be clearly seen. The timing and shape of these features are strongly reminiscent of those seen in Figure 4.10 (a) and (b), respectively. They result from the small amount of probe light which leaks through the optically thin aluminum receiver film and is modulated at the excitation region. This leakage may be incorporated into the simulation by including a signal contribution just after interface 2 of Figure 4.14,

$$u_{sig}(z,\omega) = b_{14}(z,\omega) + Cb_6(z,\omega) - Cb_7(z,\omega) \qquad 4.21$$

where C is a coefficient which describes the intensity of the signal contribution from the excitation region, and is related to the transmission of probe light through the receiver film. Typically C~0.3, and is determined experimentally.

After roughly 50 ps a sharp increase in the displacement is observed in Figure 4.15 as the phonons generated at zero ps arrive at the back of the receiving film following propagation through the silica layer and both aluminum layers. The narrowband character of the wavepacket can be seen as a weak oscillation superimposed on the rise. After roughly another 80 ps, a sharp decrease in the displacement is observed, which correlates to the arrival of the first echo of the wavepacket at the receiver transducer, following reflections first at the aluminum-air interface and then the aluminum-sapphire interface. This echo has an inverted phase relative to the initial displacement, e.g., is expansive rather than compressive, due to the large impedance mismatch at the aluminum-air interface which yields a negative reflection coefficient via Equation 4.12 replaced with the proper material values, $\bar{r}_{air-Al} = -1.00$. When the negative-going echo reaches the aluminum-sapphire interface it experiences loss, but not a second inversion, $\vec{r}_{saph-Al} = 0.43$, and so is still expansive when it returns to the probe spot. The difference in amplitude between the displacement simulation and data can be attributed to the absence of two signal contributions from the acoustic mismatch model – first, the leakage of the probe light through the sample, and second, the relatively slow diffusion of heat away from the excitation region into the sapphire, which returns the material to its original (unexcited) state after a few nanoseconds as can be seen in Figure 5.7.

The narrowband character of the waves is better revealed in the strain plot of Figure 4.16, where the wave transmitted beginning around 50 ps has lost some of its modulation, due to damping. The inverted echo beginning ~80 ps later has reduced amplitude due to loss upon reflection at the sapphire-aluminum interface, but also is damped relative to the initial wave. Though the magnitude of the measured acoustic echo is somewhat larger than expected from the calculated reflection and transmission coefficients at the various interfaces, the acoustic mismatch model simulates the data quite well, even at later times with later echoes.

4.5 High Resolution Characterization of Nanoscale Structures

The coherent nature of the narrowband acoustic waves discussed in this chapter may be employed for the high-resolution determination of the size of nanoscale structures, in a way that has been not been previously possible. In this section the established use of broadband acoustic waves to determine film thickness is illustrated, as an introduction to the technique. Then the coherent superposition of narrowband acoustic waves is shown by tuning the Deathstar frequency to cause constructive or destructive interference in a film, which either enhances or suppresses the material response. Lastly, the use of constructive interference between multiple cycles of the narrowband acoustic waves inside a thin film to determine its thickness to angstrom precision is illustrated. In all cases the measurement of film thickness is made by determining the round-trip time of an acoustic wave inside the structure,

$$\tau_{RT} = \frac{2d}{v_s} \tag{4.22}$$

where d is the structure size or film thickness, and v_s is the longitudinal speed of sound taken from the literature.[8] Here it is noted that the accuracy of this technique is limited to the accuracy of the acoustic velocity value, which may be frequency dependent or may vary due to the film having different properties from the bulk. Measurements on a sample of known thickness, determined independently through profilometric or ellipsometric measurements for example, can be used to determine the sound speed in the film material and then enable further measurements of film thickness for newly fabricated films of the same material.

For the broadband picosecond ultrasonics approach to film thickness determination, the sandwich structure described in Section 4.2 was excited at the sapphire-aluminum interface with a single optical pulse. The wave traveled through the aluminum film, into the silica glass, and was detected interferometrically on the other side of the sample, as shown in Figure 4.17 (a) and (b) along with a simulation of the data performed with the acoustic mismatch model described in Section 4.4. Echoes at later times were also detected, allowing the round trip time of the acoustic wave within the sample to be determined. The excited acoustic wave is dominated by a relatively low frequency component,[12] and so it was assumed that it propagates through silica glass with the bulk low-frequency speed of sound, 5900 m/s.[8] A good agreement between the simulation and the data can be seen. The excitation strain pulse observed at t=0 in (b) is much sharper than expected from the simulation, and is due to a signal contribution from excited electrons, as discussed previously. The width of the wave after propagation is due to acoustic damping, which was not treated in the simulation. The oscillatory component between the two pulses can be attributed to an artifact arising from a small amount of probe light reflecting from the acoustic wave while it is traveling inside the silica glass, and interfering with the probe light which reflects from the fixed back surface of the sample. [15] The period of this oscillation depends on the sound speed and refractive index of the material, and the probe wavelength; if the refractive index is known then the acoustic velocity may be measured using this information.[9]

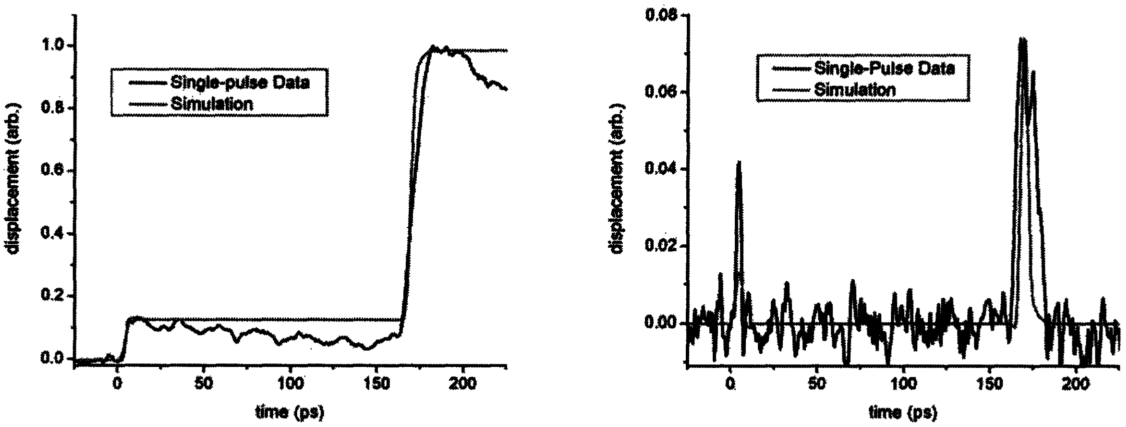

Figure 4.17. (a) Displacement resulting from single-pulse excitation of 1000 nm region of silica glass sandwich structure described in Section 4.2.2 (b) Resulting strain in sample.

Figure 4.18 shows the single trip propagation time ($\tau_{RT}/2$) for the different thickness regions of the sample on the right axis, and the calculated acoustically determined thickness on the left vertical axis, as a function of the measured location on the sample. The somewhat smooth variation in thickness between the different regions is a result of the masking process used to deposit the glass. For the thicker sections of the sample, good agreement was found between the ellipsometric, profilometric, and acoustically determined thicknesses. However for the thinnest section the ellipsometric measurement yielded a much lower value (95 nm) than that determined by the other two methods. A discussion of the discrepancies between thickness

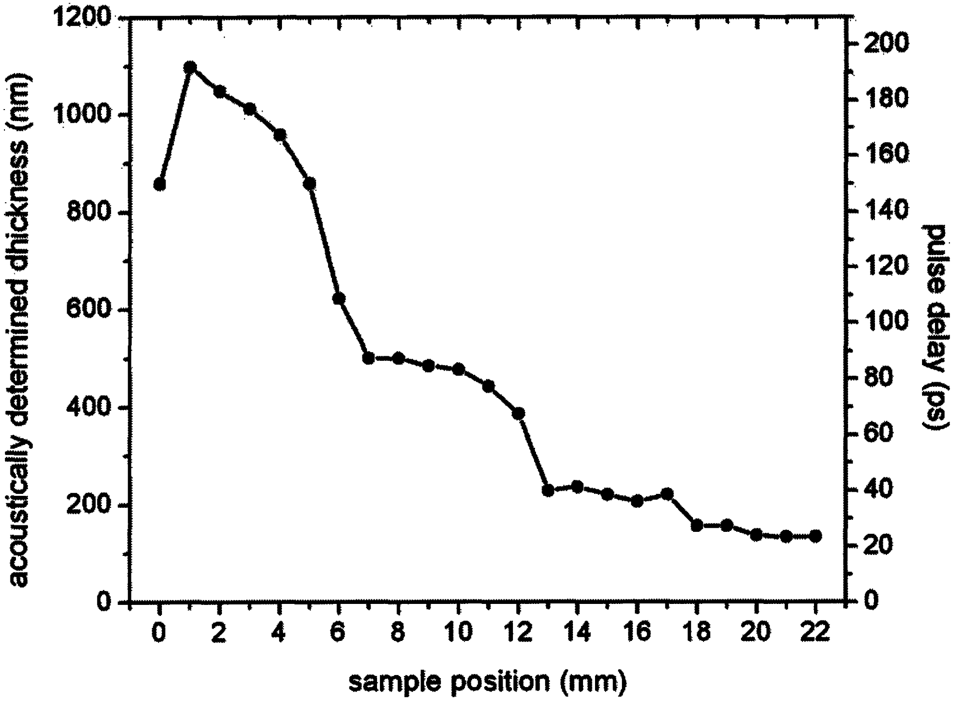

Figure 4.18. Acoustically measured thickness of silica glass based on the single trip time of a broadband acoustic wave in the sample.

measured by different methods is presented in Section 6.2.2, for an assortment of materials which all show growing discrepancies between ellipsometrically and acoustically measured thicknesses for extremely thin samples.

If the film is excited by a single pulse, echoes of the resulting acoustic wave resonate inside it with a natural frequency

$$f_{res} = \frac{v_s}{2d}. \qquad 4.23$$

For the samples discussed in this chapter, the *observed* resonance frequency occasionally varies from this, due to the different boundary conditions at the two surfaces of the aluminum. For the case of a relatively thick aluminum film, $d > \zeta_{eff}$, the acoustic wave may be thought of as propagating in a "bulk-like" medium. When the wave propagates from the sapphire-aluminum interface where it is excited, and reflects from the aluminum-air interface, it experiences an inversion due to the acoustic impedance mismatch, as discussed in Section 4.4. When this echo subsequently reflects from the sapphire-aluminum interface it does not experience a second inversion, so when it returns again to the aluminum-air interface (i.e., the probing region) it has a negative phase relative to the previous trip. Thus, it takes two round trips for the echo to be re-inverted to its original phase,

$$f_{res,d>\zeta_{eff}} = \frac{v_s}{4d} \qquad 4.24$$

In the case of the very thin aluminum films discussed in Section 4.3, $d \leq \zeta_{eff}$ and the acoustic wave can no longer be thought of as "propagating" inside the film. In this non-propagative case the mode does not experience inversion at the air-sapphire interface, and Equation 4.23 expresses the resonant frequency. The thickness was gradually varied between "thick" and "thin," and the crossover between the behavior limits has been observed to occur somewhere between 25 and 50 nm. This is an unusual result and could be the subject of further study. A very few selected results are presented subsequently.

If, after excitation with an optical pulse, the film is excited by a second pulse at time $\tau = f_{res}^{-1}$, the second incoming pulse overlaps temporally with the acoustic echo of the first pulse, and the acoustic responses constructively interfere. By exciting with a *sequence* of pulses at the frequency f_{res}, the acoustic response of the material can be greatly enhanced due to constructive interference. The response of a 60 nm aluminum film ($d>\zeta_{eff}$) driven at its resonant frequency by a sequence of pulses from the Deathstar pulse shaper at 25 GHz is shown in Figure 4.19 (a). The response is quite similar to that of the thinner film at higher frequencies, such as in Figure 4.10 (a). Also shown in Figure 4.19 (b) is the response of the film to excitation at twice its resonant frequency, 50 GHz. Here the excitation pulses which generate acoustic waves at the sapphire-

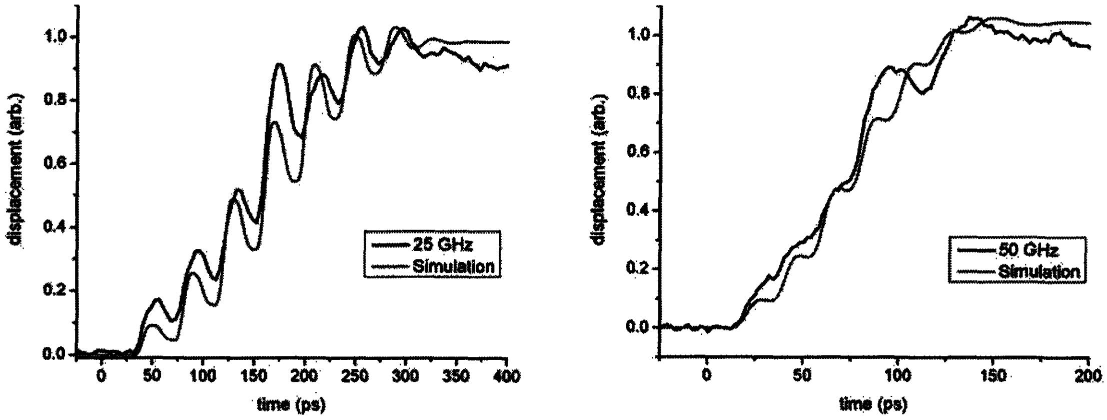

Figure 4.19. Displacement resulting from excitation of 60 nm aluminum film at (a) once and (b) twice its resonant frequency, given by Equation 4.24, along with simulations described in Section 4.4

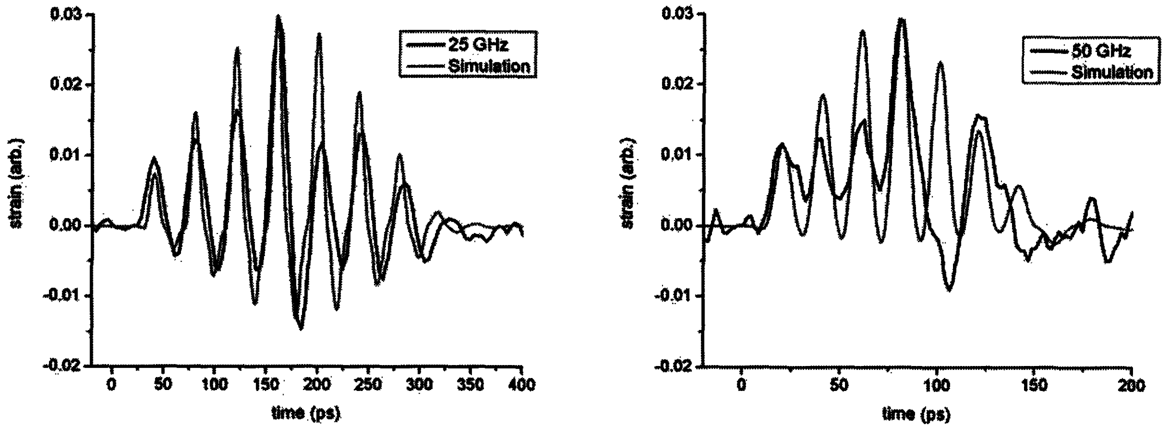

Figure 4.20. Strain resulting from excitation of 60 nm aluminum film at (a) once and (b) twice its resonant frequency, given by Equation 4.24, along with simulations described in Section 4.4.

aluminum interface arrive at exactly the same time as the negative-going acoustic echo of the previous pulse, and the two pulses interfere destructively. The acoustic response can be seen to be significantly suppressed, and nearly cancelled except for the large pulse in the middle of the scan, which is much larger than the acoustic echo of the previous pulse and is not fully cancelled. The scale of each plot is determined directly from the raw uncalibrated data (coincidence places their magnitudes near one) and is the same for both scans; for example the first pulse in both plots can be seen to be the same magnitude as it has not yet experienced interference effects, and the total signal level is determined by the amount of heat deposited, which is the same for both frequencies.

The resulting strain is shown in Figure 4.20 (a) for the 25 GHz excitation, and (b) for the 50 GHz excitation, along with simulations using the acoustic mismatch theory described in Section 4.4. For the 25 GHz excitation, between the positive-going excitation pulses at ~20 ps, 60 ps, 100 ps, etc., strongly negative-going echoes are observed at ~40 ps, 80 ps, 120 ps, etc. In the 50 GHz scan such strong features are not observed, and the series of small peaks at early times, as well as the large peak around 60 ps, are due to the variation in the pulse energies across the pulse shaping envelope. The interference appears slightly stronger in the 50 GHz scan than the simulation would suggest; this may be an effect of a misalignment such that the energies of the 2nd, 3rd, and especially 5th pulses in the sequence give reduced signal intensities. These reduced responses can also be seen in the 25 GHz data.

As shown in Figure 4.21, excitation of a ~23 nm aluminum film at 140 GHz, i.e. at its f_{res} given by Equation 4.23, yields a characteristic amplification of the response even after excitation is complete. Excitation at one half f_{res} is also shown, and acoustic echoes in between excitation pulses are clearly resolved. The film thickness was otherwise characterized by ellipsometry and by a quartz microbalance in the deposition chamber where it was fabricated, to be approximately 15 nm, which agrees fairly well with what is expected.

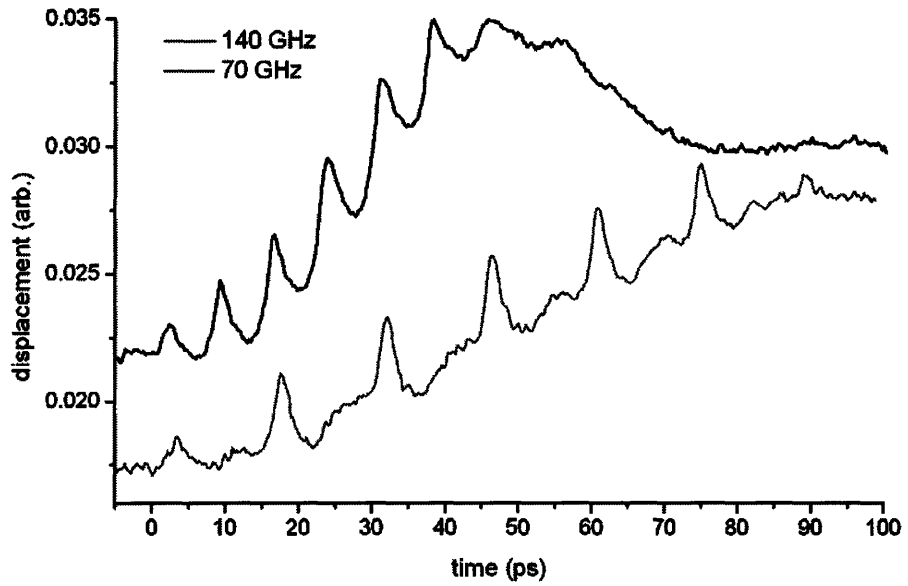

Figure 4.21. Excitation of 23 nm aluminum film at once and at one-half its resonant frequency.

Lastly the resonant excitation of a film is demonstrated as a method of determining its thickness to excellent precision (again noting that the assumption of a literature speed of sound limits the absolute accuracy). After the optical excitation of a film near its resonant frequency (described by either Equation 4.23 or Equation 4.24 depending on the thickness) is complete, the constructively enhanced response is manifested as acoustic "ringing" which persists for many picoseconds. This can be clearly seen in the displacement, Figure 4.22, and in the strain, Figure 4.23, of scans where the ~18 nm aluminum film described in Section 4.2.2 was driven below (125 GHz), near (190 GHz), and above (225) its resonant frequency. The resulting enhanced response near resonance is noted with an arrow. A few cycles of the constructive oscillation can be seen by eye in the strain plot at 190 GHz.

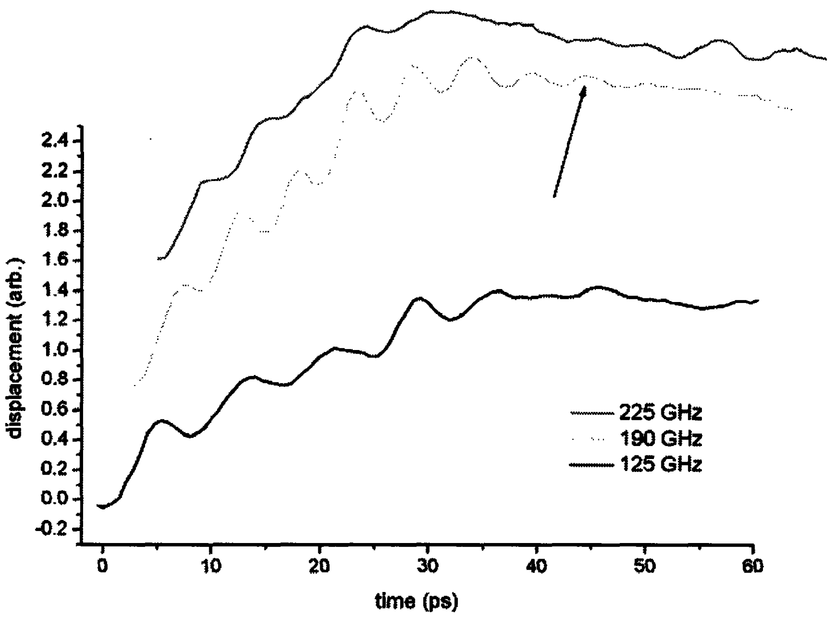

Figure 4.22. Displacement due to response of ~18 nm aluminum film to excitation below, near, and above its resonant frequency, described by Equation 4.23. Persistence of the film response following after the arrival of the last (7th) optical pulse is apparent in the 190 GHz scan, noted with arrow.

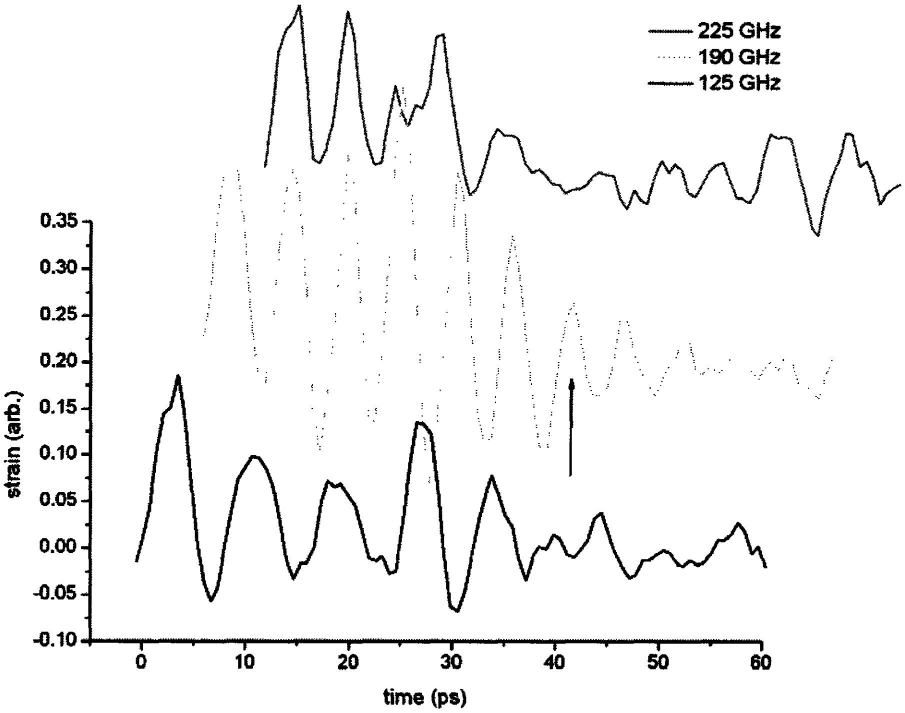

Figure 4.23. Strain due to response of ~18 nm aluminum film to excitation below, near, and above its resonant frequency, described by Equation 4.23. Persistence of the film response after the arrival of the last (7th) optical pulse is apparent in the 190 GHz scan, noted with arrow.

By Fourier transforming the signals *after* excitation is complete, the presence of a resonance condition may be evaluated. As shown in Figure 4.24, a 200% enhancement is found in the Fourier amplitude of the film response *after* excitation at 190 GHz is completed, as compared to that following excitation at 125 or 225 GHz. By varying the driving frequency of the excitation in small steps using the Deathstar pulse shaper, and observing the frequencies and amplitudes of enhancements in the acoustic response, the resonant frequency of the film could be determined. In Figure 4.25 the driving frequency is tuned and the frequency of the largest peak in the signal's Fourier spectrum is shown. Clearly when the driving frequency is within ±10 GHz of the resonance, the film responds at its resonant frequency. Where the driving and response frequencies are the same the resonant condition is met, here at 188 GHz which corresponds to a film thickness of 17.1 nm via Equation 4.23, in very good agreement with the 17.6 nm value found by high-resolution profilometry, which had an error of ~10% (1.5 nm).

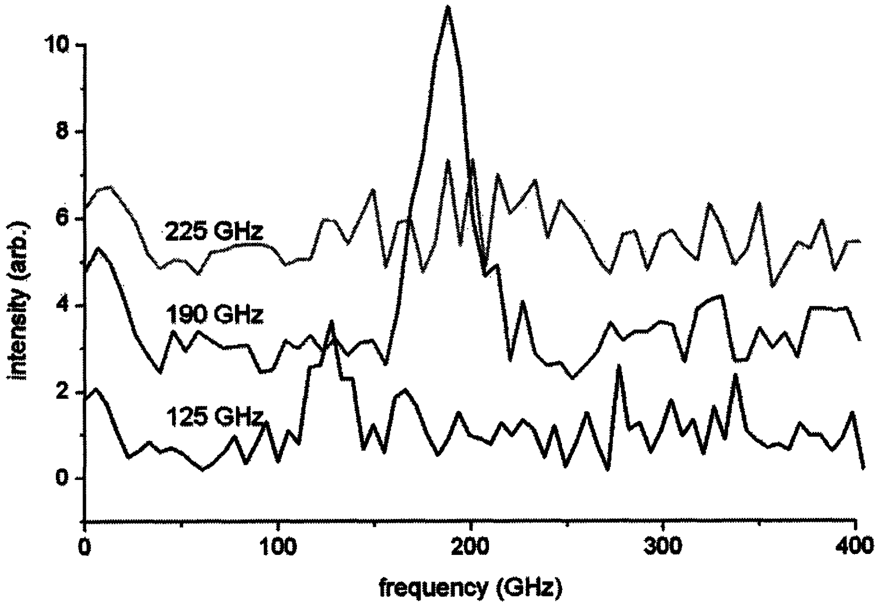

Figure 4.24. Fourier amplitude of signal from an aluminum film following pulse shaped excitation near and far from its resonant frequency.

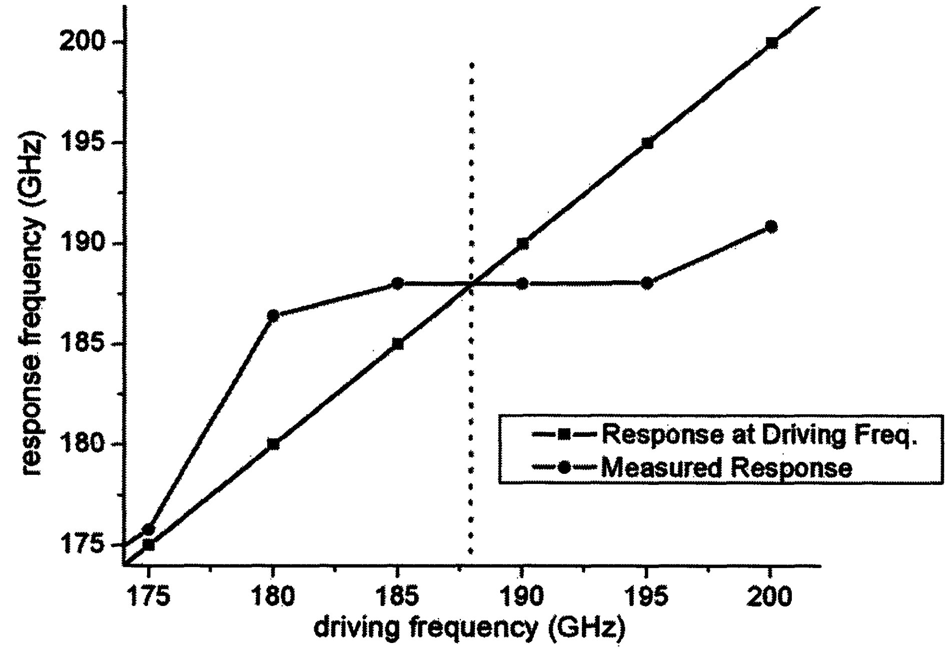

Figure 4.25. Response frequency of aluminum film as a function of driving frequency. Also shown is a calculated response with no resonant interaction. Where the driving and response frequencies match, the resonant condition is met (188 GHz).

Similar results are found by varying the driving frequency and observing the Fourier amplitude of the signal at 1) the driving frequency, and 2) the resonant frequency of the film. The results, shown in Figure 4.26, show an unmistakable enhancement in the film response near 188 GHz. Of particular interest is the enhancement at 188 GHz when the driving frequency is 100 GHz; this corresponds to driving the film near the first overtone of its resonance. This effect can be seen also above in Figure 4.9, when the film is driven at 95 GHz and the film echoes once between excitation pulses. It should be noted that the raw data have an inherent spectral resolution of 3 GHz, which is limited by the short temporal window during which the data are acquired. This limits the measurement accuracy to 17.1 ± 0.3 nm, which is comparable to commonly used methods such as high-resolution profilometry, or ellipsometry. Zero-padding could be used to further enhance the spectral resolution, by expanding the temporal window of the raw data with "zeroes" (e.g., with constant values that correspond to the beginning or end of the data) but is not done here, as the accuracy of the measurement is on the order of one or two molecular layers for the entire film. The variation between the resonant acoustic measurement and the high-resolution profilometry determination is about 3%, an excellent agreement within the resolution of both measurements.

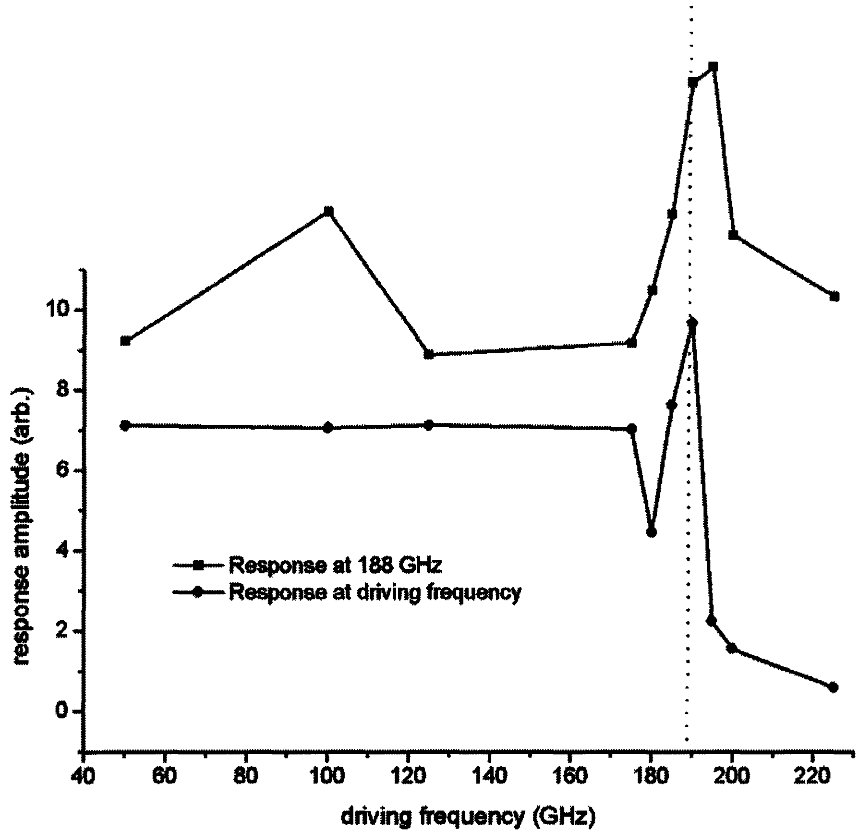

Figure 4.26. Response amplitude of aluminum transducer at driving frequency and at resonant frequency (190 GHz) as a function of driving frequency. Plots are vertically offset as an aid to the eye.

In summary, the coherent constructive and destructive interferences within a narrowband acoustic wave, and their use for the determination of film thickness with sub-nanometer accuracy, have been demonstrated. This approach might have particular value in characterization of subsurface layers of unknown thickness, whose presence might not be apparent at all until driven on resonance to produce a detectable acoustic response.

4.6 Using Narrowband Acoustic Waves to Characterize Complex Materials

This section illustrates the measurement of frequency-dependent damping and dispersion of a complex disordered material using the Deathstar pulse shaper, in this important frequency range that has been otherwise difficult to access. In the broadband picosecond ultrasonics method, the acoustic damping rate is extracted from the spectra resulting from Fourier transformation of broadband data which have frequency components ranging from quasi-dc up to ~440 GHz. Either the magnitude of the excited strain is modeled and compared to the transmitted strain,[15] as was done in Section 4.4, or the magnitudes of echoes resulting from multiple round trips inside the sample are compared to each other.[8] The success of these methods is limited by the ability to obtain adequate signal/nose ratios at the highest frequencies, which comprises a modest part of the total spectrum, as well as by the ability to resolve the contributions to the broadened transmitted wave from the modulation of different frequency components. To a lesser extent the success is limited by the accuracy of the assumption of either the excited strain, or of the material parameters ρ and v which determine the transmission and reflection coefficients at each of the interfaces with which the wave interacts.

The Deathstar pulse shaping technique described in the sections of this chapter avoids these problems by focusing much of the spectral energy of the acoustic waves into a very narrow region. Then instead of attempting to acquire the entire spectrum in a single long sweep, the damping coefficient and acoustic velocity may be obtained quickly and with high accuracy at any desired frequency in the range 2-500 GHz. An additional simplification to the experiment (which could also be employed in other techniques) is the use of a clever sample design, which is described in Section 4.2.2 and illustrated in Figure 4.5. By allowing phonons of a given frequency to travel through two different propagation lengths, e.g. 210 nm and 480 nm of silica glass, but with the excitation and detection films (and therefore conditions) otherwise identical, the damping constant and velocity may be easily determined. The only difference in the sample response comes from the difference in silica glass thicknesses Δd_{SiO2}. The difference in transmitted amplitude as well as time of flight for a 150 GHz acoustic wave through the two sample thicknesses can be seen in Figure 4.27.

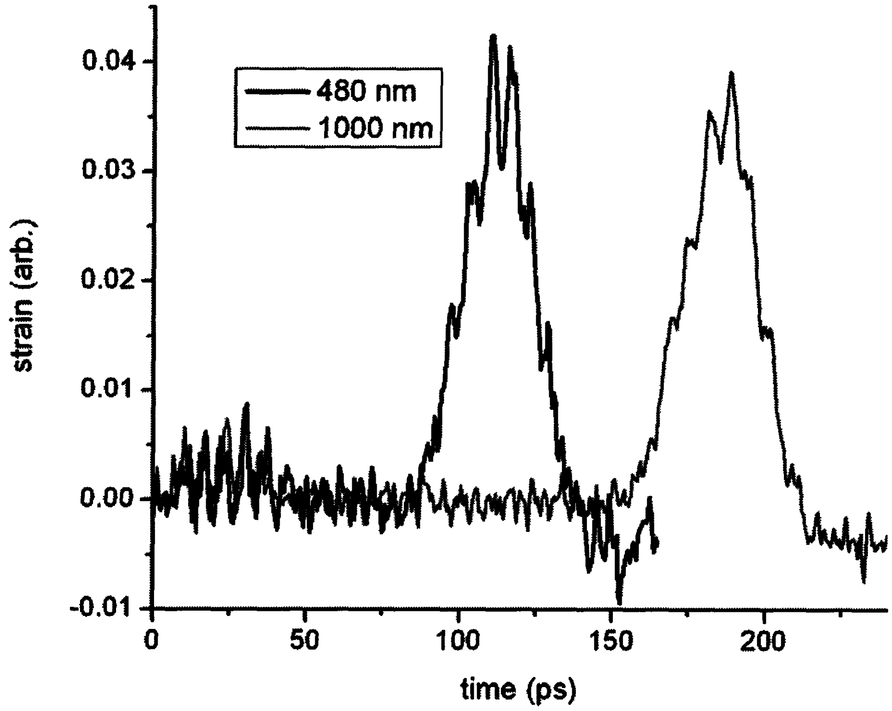

Figure 4.27. 150 GHz acoustic wave transmitted through 480 and 1000 nm of silica glass.

By taking the Fourier transforms of the transmitted acoustic waves and comparing their spectral amplitude I at the driving frequency $\omega_0 = 150GHz$ for each sample, the damping rate may be determined:

$$\alpha(\omega_0) = \frac{1}{\Delta d_{SiO_2}} \ln \left| \frac{I_{210nm}(\omega_0)}{I_{480nm}(\omega_0)} \right| \qquad 4.25$$

The careful processing of data to compensate for variation in experimental parameters such as laser intensity is discussed thoroughly in Section 6.3.1. Similarly the acoustic velocity may be determined by the difference in time of flight τ of the acoustic wave through each film:

$$v_{SiO_2}(\omega_0) = \frac{\Delta d_{SiO_2}}{\left[\tau_{480nm}(\omega_0) - \tau_{210nm}(\omega_0)\right]} \qquad 4.26$$

The results of the experiment at 150 GHz are shown in Table 4.3, and are compared to literature values from the picosecond ultrasonics method..

	Damping Coefficient, m^{-1}	**Sound Speed, ms^{-1}**
Deathstar Technique	1.1×10^6	5790
Picosecond Ultrasonics, Ref. 8	5.7×10^6	5900

Table 4.3. Damping rate and sound speed in silica glass at 150 GHz for the technique described in this chapter, and literature values.

4.7 Summary

A new technique for the optical generation and detection of tunable, high frequency acoustic waves based on a simple but novel femtosecond pulse shaping method has been demonstrated. Further the resulting capabilities for location of acoustic resonances in nanometer-scale structures and for frequency-by-frequency determination of GHz acoustic parameters of complex materials have been illustrated. These capabilities permit the determination of film thickness and other properties, and permit narrowband spectroscopy of ultrahigh-frequency acoustic responses. Further study of the properties of multilayer film stacks, amorphous solids such as glasses, polymers and block co-polymers, and liquids under variable temperature and pressure conditions to reveal nanometer structural elements and picosecond dynamics are under way, and some of these studies are described in Chapter 6.

4.8 References

---

1. R. Vacher, E. Courtens, M. Foret. Are high frequency acoustic modes in glasses dominated by strong scattering or by lifetime broadening? *Philosophical Magazine B*, 79(11-12): 1763-1774, 1999.

2. T. Saito, O. Matsuda, O.B. Wright. Picosecond acoustic phonon pulse generation in nickel and chromium. *Physiscal Review B*, 67(20): 205421, 2003.

3. R.M. Slayton, K.A. Nelson, A.A. Maznev. Transient grating measurements of film thickness in multilayer metal films. *Journal of Applied Physics*, 90(9): 4392-4402, 2001.

4. A.V. Bragas, C. Aku-Leh, S. Constantino, A. Ingale, J. Zhao, R. Merlin. Ultrafast optical generation of coherent phonons in Cd-$Te_{1-x}Se_x$ quantum dots. *Physical Review B*, 69(20): 205306, 2004.

5. K.A. Nelson, D.R. Lutz, M.D. Fayer, L. Madison. Laser-induced phonon spectroscopy. Optical generation of ultrasonic waves and investigation of electronic excited-state interactions in solids. *Physical Review B*, 24(6): 3261-3275, 1981.

6. A.A. Maznev, K.A. Nelson, J.A. Rogers. Optical heterodyne detection of laser-induced gratings. *Optics Letters*, 23(16): 1319-1321, 1998.

7. G.A. Antonelli, P. Zannitto, H.J. Maris. New method for the generation of surface acoustic waves of high frequency. *Physica B*, 316-317: 377-379, 2002.

8. T.C. Zhu, H.J. Maris, J. Tauc. Attenuation of longitudinal-acoustic phonons in amorphous SiO_2 at frequencies up to 440 GHz. *Physical Review B*, 44(9): 4281-4289, 1991.

9. O.B. Wright. Thickness and sound velocity measurement in thin transparent films with laser picosecond acoustics. *Journal of Applied Physics*, 71(4): 1617-1629, 1992.

10. J.A. Rogers, A.A. Maznev, M.J. Banet, K.A. Nelson. Optical generation and characterization of acoustic waves in thin films: Fundamentals and applications. *Annual Review of Materials Science*, 30: 117-157, 2000.

11. C. Thomsen, H.T. Grahn, H.J. Maris, J. Tauc. Surface generation and detection of phonons by picosecond light pulses. *Physical Review B*, 34(6); 4129-4138, 1986.

12. R.M. Slayton, K.A. Nelson. Picosecond acoustic transmission measurements. I. Transient grating generation and detection of acoustic responses in thin metal films. *Journal of Chemical Physics*, 120(8): 3908-3918, 2004.

13. D.H. Hurley, O.B. Wright. Detection of ultrafast phenomena by use of a modified Sagnac interferometer. *Optics Letters*, 24(18): 1305-1307, 1999.

14. M. Nikoonahad, S. Lee, H. Wang. Picosecond photoacoustics using common-path interferometry. *Applied Physics Letters*, 76(4): 514-516, 2000.

15. R.M. Slayton, K.A. Nelson. Picosecond acoustic transmission measurements. II. Probing high frequency structural relaxation in supercooled glycerol. *Journal of Chemical Physics*, 120(8): 3919-3930, 2004.

16. Ü. Özgür, C.-W. Lee, H.O. Everitt. Control of coherent acoustic phonons in semiconductor quantum wells. *Physical Review Letters*, 86(24): 5604-5607, 2001.

17. C.J. Morath, H.J. Maris. Phonon attenuation in amorphous solids studied by picosecond ultrasonics. *Physical Review B*, 54(1): 203-213, 1996.

18. G. Tas, H.J. Maris. Electron diffusion in metals studied by picosecond ultrasonics. *Physical Review B*, 49(21): 15046-15054, 1994.

19. A.M. Weiner. Femtosecond optical pulse shaping using spatial light modulators. *Review of Scientific Instruments,* 71(5): 1929-1960, 2000.

20. T. Feurer, J.C. Vaughan, K.A. Nelson. Spatiotemporal coherent control of lattice vibrational waves. *Science*, 299(5605): 374-377, 2003.

21. T. Hornung, J.C. Vaughan, T. Feurer, K.A. Nelson. Degenerate four-wave mixing spectroscopy based on two dimensional pulse shaping. *Ultrafast Phenomena XIV Proceedings*, in press, 2004.

22. H. Kawashima, M.M. Wefers, K.A. Nelson. Femtosecond pulse shaping, multiple-pulse spectroscopy, and optical control. Annual Review of Physical Chemistry, 46: 627-656, 1995.

23. T.F. Crimmins, *Ultrahigh Frequency Characterization of Complex Materials Using Transient Grating Techniques*. Ph.D. Thesis, Massachusetts Institute of Technology, Department of Chemistry, June 2000.

24. O.B. Wright, V.E. Gusev. Ultrafast acoustic phonon generation in gold. *Physica B*, 219-220: 770-772, 1996.

25. K. Katayama, Y. Inagaki, T. Sawada. Ultrafast two-step thermalization processes of photoexcited electrons at a gold surface: Application of a wavelength-selective transient reflecting grating method. *Physical Review B*, 61(11): 7332-7335, 2000.

26. G.L. Eesley, B.M. Clemens, C.A. Paddock. Generation and detection of picosecond acoustic pulses in thin metal films. Applied Physics Letters, 50(12): 717-719, 1987.

27. J. Hohlfield, J.G. Muller, S.-S. Wellershoff, E. Matthias. Time-resolved thermoreflectivity of thin gold films and its dependence on film thickness. *Applied Physics B*, 64(3): 387-390 1997.

28. O.B. Wright. Ultrafast nonequilibrium stress generation in gold and silver. *Physical Review B*, 49(14): 9985-9988, 1994.

29. P.M. Norris, A.P. Caffrey, R.J. Stevens, J.M. Klopf, J.T. McLeskey, A.N. Smith. Femtosecond pump-probe nondestructive examination of materials (Invited). *Review of Scientific Instruments*, 74(1): 400-406, 2003.

30. K. Dou, J. Wu, R.L. Parkhill, E.T. Knobbe. Femtosecond studies of highly excited electrons in metals. *Journal of Luminescence*, 94-95: 617-621, 2001.

31. R.M. Slayton. *Developing a Transient Grating Technique to Probe Fast Acoustic Dynamics in Liquids*. Ph.D. Thesis, Harvard University, Department of Chemistry and Chemical Biology, May 2002.

32. B. Golding, J.E. Graebner, R.J. Schutz. Intrinsic decay lengths of quasimonochromatic phonons in a glass below 1 K. *Physical Review B*, 14(4): 1660-1662, 1976.

33. D.P. Jones, W.A. Phillips. Thermal conductivity of vitreous silica. *Physical Review B*, 27(6): 3891-3894, 1983.

Chapter Five:

Grating Interferometry for the Detection of Thermoelastic Phenomena

5.1 Introduction

The broad applicability of optical interferometry to the analysis of surfaces and bulk materials is reflected in the growing library of available techniques. Laser interferometers are highly sensitive, non-destructive probes that can be readily adapted to numerous applications. Topics of recent interferometric studies have included, e.g., the topology of surfaces,[1,2] small motions of surfaces;[3] electrostrictive displacements in low-k dielectrics;[4] and time-resolved travel of bulk[5] as well as surface[6,7,8,9] acoustic waves. The current work demonstrates a novel diffractive-optic based interferometer that is simple, stable, and compact. Use of a novel grating-based interferometer for the purposes of imaging in-plane surface acoustic waves, as well as point-detection of traveling through-plane acoustic waves and in-plane coherent lattice vibrations, or phonon-polaritons, is illustrated in this chapter. The versatility of the interferometer for different geometrical and temporal measurements is demonstrated, as is its ease of alignment and use for sensitive quantification of displacements.

Ordinarily, laser interferometry is conducted by splitting a spatially coherent light beam into probe and reference beams through partial reflection. The probe beam is sent through or reflected off of the sample of interest, and the reference beam (sometimes referred to as a local oscillator) is sent along a path of almost equal length (within the coherence length or spatial extent of the laser beam). Again through partial reflection the two beams are recombined, and small differences in their optical path lengths cause intensity changes in the interferometrically recombined beam. These can be observed as spatial variations in a fringe pattern, for determination of topology, or as time-dependent fluctuations in intensity, to yield mechanical dynamics. In both cases, resolution of displacements or phase shifts with sub-angstrom accuracy is possible.[10]

To optimize resolution and signal/noise ratio, the relative path lengths of the measurement and reference beams must be held constant to within a small fraction of the light wavelength. Vibrations of the optical elements in either beam path, air currents, and laser pointing instability cause interferometric fluctuations which can be compensated via a wide range of methods. For example, active feedback based on automated tracking of fringe intensities and piezoelectric modulation of the reference beam phase was recently shown to yield $\lambda/100$ accuracy in a Michelson interferometer,[11] which is currently less than other methods due to piezoelectric limitations, but is quite good. A good overview of sensitivity and signal-to-noise issues of Michelson interferometers is also given in Reference [12]. A common approach used in numerous other designs is phase-shifting interferometry, in which five interferograms that are piezoelectrically phase-shifted by $\pi/2$ are acquired sequentially, and the phase data are reconstructed computationally.[13] This results in high accuracy measurements but requires extremely stable beam intensity during the sequential measurements and an extremely noise-free environment.[14,15] A passive compensation method was recently introduced which uses a custom grating mask in a modified Michelson interferometer to *simultaneously* obtain four interferograms shifted by $\pi/2$ from each other, which can be subsequently analyzed to subtract noise contributions from phase drift and laser fluctuations. A potential and simple adaptation of this technique to the current design is discussed in Section 5.2. Another technique uses single-frame acquisition of interferograms with a Twyman-Green interferometer on a time scale (0.1-20 ms) much shorter than that of the mechanical vibrations (~100 ms) that cause noise.

Sophisticated fringe analysis compensates for the lack of phase-shifting and averaging. A general common feature of the above compensation techniques is the use of computational algorithms (sometimes intensive) to control input beams or, alternatively, to analyze the output interferograms. An interesting and very performant stroboscopic speckle-shearing interferometer design was proposed in Reference 16.

An alternate approach to interferometry uses diffractive rather than reflective optics for separation and recombination of the beams. Several designs for diffraction-based interferometry have been developed over the years, and generally have the common features of a low number of optical elements and a common-path for probe and reference beams, resulting in enhanced stability even in noisy environments. One advantage of splitting probe and reference beams through diffraction rather than partial reflection is that the phase fronts of the probe and reference beam propagate parallel to each other, enabling retrieval of a centrosymmetric interferogram which greatly eases analysis. A lateral shearing interferometer[17] uses a double transmission-grating design. The first grating diffracts light into many orders, and the +1 and –1 orders are selected and made parallel by diffraction off of the second grating which is spaced a few millimeters away. The two first orders interfere and the pattern can be analyzed for phase modulation of the wavefront. Tuning the inter-grating distance varies the shear ratio, and phase-stepping is achieved by piezo-translation of the second grating. Performance has been directly compared to a traditional Twyman-Green interferometer and found to be similar, but with much less sensitivity to noise.

A reflective grating interferometer[18,19] has an extremely compact two-optic design that folds the +1 and –1 orders of diffraction interferometrically onto each other. It can easily be used in either a symmetric mode, which is sensitive to asymmetric errors in wavefront like coma, or in an asymmetric shearing mode to which can be used to study symmetric aberrations. A three-grating Mach-Zehnder interferometer[20] uses transmission gratings instead of mirrors to split, direct, and recombine the probe and reference beams, so that a sample can be inserted for analysis of, e.g., index of refraction. Non-diffractive common path designs have also been found to be highly successful. Hurley and Wright[21] developed a modified time-division Sagnac interferometer, in which polarizing beam splitters are used to generate probe and reference beams that follow the same path, but are delayed in time relative to each other. The reference samples the excitation region before t=0, and the probe at a variable time after t=0, then the two beams are recombined by use of waveplate-beamsplitter combination. The interference pattern reflects the time derivative of the sample displacement. Nikoonahad et al.[22] developed a similar common-path time-division interferometer and demonstrated its use for the study of picosecond photoacoustics in multilayer metal-insulator assemblies.

Here a modified and extremely compact diffractive interferometer design is introduced. Its sensitivity, stability and versatility through several examples in which thermoelastic responses of materials are measured, is demonstrated. The applications involve fixed-point detection of acoustic waves as well as lattice vibrations, or phonon-polaritons, as well as spatially resolved imaging of thermally and acoustically induced strain. The material response is detectable due to time-dependant changes in bulk refractive index or surface displacements caused by laser excitation.

In terms of general design, the grating interferometer compares to those described above in that it gives the probe and reference arms a common path, and it is comprised of a small number of interferometric optics. Like the lateral shearing and three-grating Mach-Zehnder interferometers, the independent probe and references are generated by transmission diffraction into multiple orders. In this case, only the +1 and –1 orders are selected, and their amplitude is maximized by optimizing the etch depth of the binary grating. Like the reflective grating interferometer, the current design is comprised of two optical elements (four for transmission mode). The current design also has no crucial dimensions of alignment, in contrast with the above which require the separate phase masks to be extremely parallel in the case of transmission designs.’’. or the mirror and grating to be at precisely 90 degrees to each other in the case of the reflection design.. The current scheme allows for flexibility in the size of the region sampled, is easily adaptable to reflection measurements of displacement or transmission measurements of refractive index, and has utility for various time domains as well as static applications. Lastly, robust data can be extracted directly from the recovered interferograms without sophisticated computational analysis.

In Section 5.2, the alignment of the interferometer is described and its response is systematically evaluated. Procedures for calibration are described. In Section 5.3, images of time-resolved measurements of surface thermoelastic responses are presented. In Section 5.4, the measurement of the time-dependent evolution of through-plane acoustic waves is demonstrated, and is compared to the usual method, a change in probe reflectivity, by which they are detected. Section 5.5 briefly describes the use of this technique to monitor the ultrafast changes in refractive index resulting from coherent lattice vibrations, or phonon-polaritons, traveling through a ferroelectric crystal. The performance of this novel interferometer is summarized in Section 5.6.

5.2 Alignment, Calibration, and Evaluation

5.2.1 Experimental Design

The diffraction-based interferometer is based closely on the robust diffraction-based time-resolved transient grating, or four-wave mixing, experimental design[23,24,25,26] which was described in Section 3.2, and is illustrated in Figure 3.3. In that setup, the interference patterns formed by the interference of the +1 and -1 orders of diffraction of both the pump and probe have been found to be extremely phase stable for hours with no external stabilization.[27] Based on this result, its adaptation to interferometry suggested itself. The current interferometer design is shown in Figure 5.1 for transmission mode and reflection mode respectively, is based on this result. The design is reminiscent of Figure 3.3.

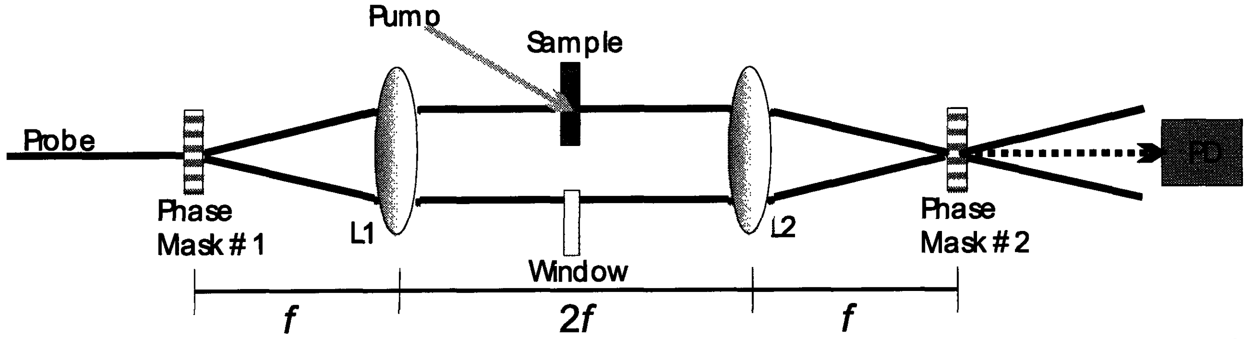

Figure 5.1. Grating interferometer, transmission mode. Probe and reference arms are generated at phase mask #1 and recombined interferometrically at phase mask #2. For adjustment of static phase the window may be rotated. Pump may be introduced to sample in one of many ways as discussed in text. Interferometric signal is indicated with dashed line. Distances relative to lenses L1 and L2 focal length *f* are indicated.

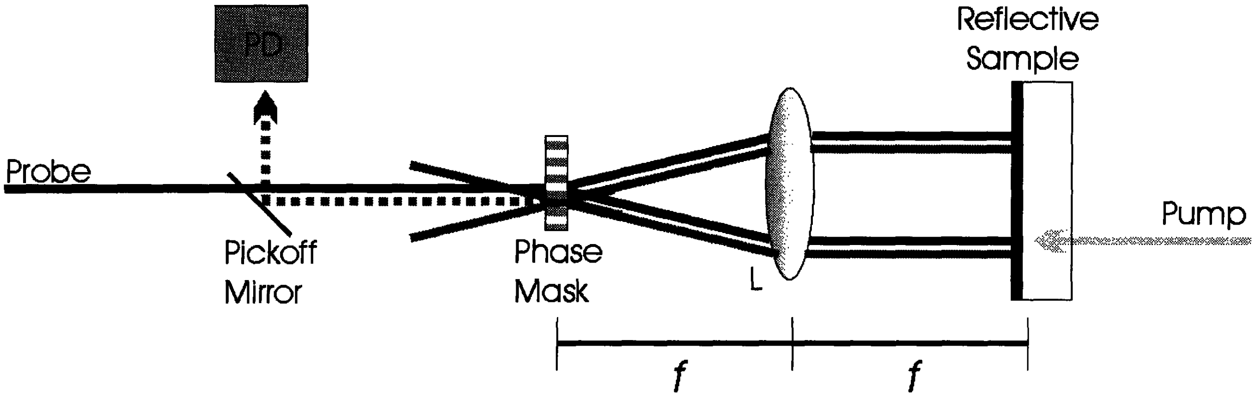

Figure 5.2. Grating interferometer, reflection mode. Probe and reference arms are generated and recombined at same phase mask. Beams reflected from sample are indicated in medium grey to aid the eye. The sample is tilted slightly downward so that the reflected interferometric beam may be picked off with a mirror, without loss of interferometric quality. Distances are indicated.

A single beam is incident on the first phase mask and split into ±1 diffraction orders to produce the probe and reference beams. In transmission mode, a second phase mask is placed in the image plane of a two-lens telescope, e.g. in the sample position of the transient grating measurement. The sample is placed in the Fourier plane of the first lens. Since the first phase mask is in the focal plane of the lens, the probe and reference beams arrive at the sample parallel and focused. The choice of the lens focal length f determines the desired spot size, and the phase mask period Λ and optical wavelength λ determine the probe/reference inter-beam spacing D. Using the diffraction formula, Equation 3.1, the spacing may be determined by:

$$D = 2f\tan\left(\frac{\Theta}{2}\right) = 2f\frac{\frac{\lambda}{\Lambda}}{\sqrt{1-\left(\frac{\lambda}{\Lambda}\right)^{2}}} \qquad 5.1$$

where Θ is the diffraction angle from the phase mask. The spacing should be minimized to optimize the stability of the interferometer and is typically 0.5-5 mm in the experiments presented here.

In the case of reflection mode, the first lens recollimates the probe and reference beams and recrosses them onto the phase mask. For transmission mode, a second lens spaced its focal length away from the sample performs this function. In both cases, on the second pass through a phase mask the probe and reference beams are diffracted into many orders. The newly diffracted +1 order of probe and −1 order of reference are collinear, and recombine interferometrically. In reflection mode, the interferometric signal beam is collinear with the original beam, but can be deflected slightly downward by tilting the sample, and can be picked off with a mirror without loss of signal integrity. The alignment requires no special care taken with the intra-optic distances, though for transmission mode it is important to carefully match the first and second sets of lenses and phase masks, since otherwise the beams are recrossed at the wrong angle and do not interfere centrosymmetrically. Further, the first and second phase masks need to be approximately vertically parallel to each other, which can be accomplished by placing the second mask on a standard tilt stage and optimizing the outgoing interference pattern.

As shown in Figure 5.3, the interferometer can also be adapted to an imaging configuration with the addition of a lens which focuses the laser beam onto the phase mask. The probe and reference beams then arrive at the sample collimated, collect information about the sample, and are interferometrically recombined at a second phase mask. The entire illuminated region is imaged onto a CCD with an additional lens.

In all cases, the sample is perturbed by an excitation pulse or waveform that initiates time-dependent changes in either bulk refractive index (transmission mode) or surface position (transmission or reflection mode) which modulate the intensity of the interferogram as recorded by a photodetector. The static phase difference of the probe and reference beams determines the sensitivity of the interferometer, as described in Section 5.2.3. The static phase can be

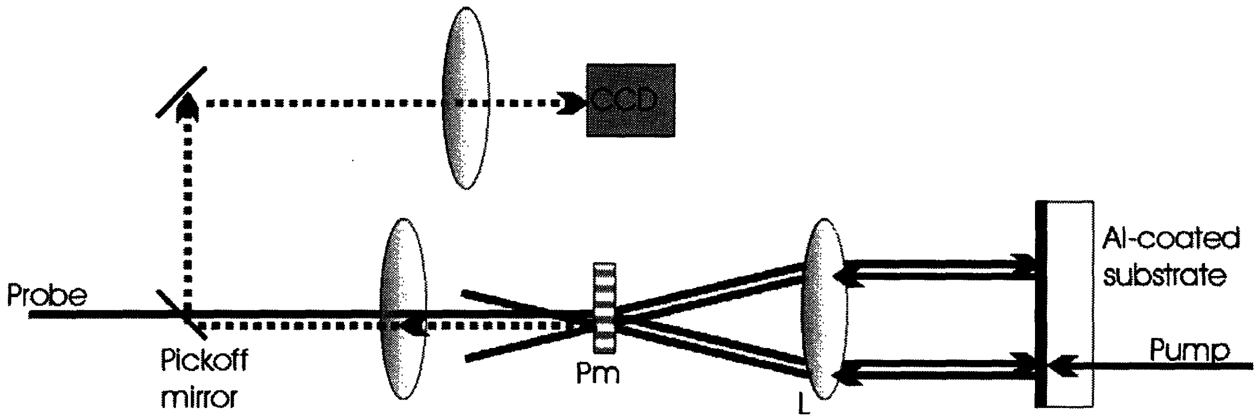

Figure 5.3. Grating interferometer, imaging mode. Same as in Figure 5.2, but including an additional lens L1 to focus the probe at the phase mask, and lens L3 to image the interferometric signal onto the CCD. The magnification of the used imaging system (ratio of image size and size of probed sample area) is around 5 times.

independently controlled by rotating an optical window inserted in the reference beam, as shown in Figure 5.1, or by shifting the phase mask slightly on a sensitive translation stage, perpendicular to the beam direction. Potentially, phase stepping interferometry could be implemented by adding a piezotranslator to the phase mask as in Leibbrandt, et. al.[15] to enhance the accuracy and reduce the noise of the measurement. Rather than serially acquiring data for later processing, a simpler adaptation would be similar to that of Ho, et. al.[5] This method uses simultaneous acquisition of phase-shifted interferograms to eliminate noise caused by beam intensity fluctuations or air currents. At the second phase mask in our design, the most intense signal beam contains the +1 probe order and -1 reference order and is diffracted collinearly with the original beam. However, all other diffraction orders from the phase mask have a static phase shifted by π from that of the signal beam, so collectively any change in signal intensity must be offset by an equal and opposite change in intensity of the other orders, thereby conserving the total energy of the light that reaches the second phase mask. By collecting the intensity of these additional orders with a large lens into a second photodetector, and subtracting it from that of the signal beam, fluctuations in the interferometer phase could be suppressed. For present demonstration purposes, the signal/noise and data acquisition times were found to be adequate without such measures.

For the imaging of surface acoustic waves, the time-dependent material responses were excited with a home-modified Nd:YAG laser (1 mJ, 200 ps, 1064 nm, Spectron Laser Systems, Warwickshire, England). The response was monitored with nanosecond time resolution via a pulsed diode laser (4 μJ, 15 ns, 905 nm, Power Technology, Little Rock AR), which was attenuated to 800 nJ/pulse by selecting only one of 5 diode outputs for improved mode quality. The pulses were synchronously triggered and delayed relative to the pump (DG535, Stanford Research Systems, Sunnyvale CA). For the measurement of ultrahigh frequency acoustic waves and phonon-polaritons, femtosecond time resolution was obtained through the use of a femtosecond laser to generate short pulses (6 μJ, 200 fs, 800 nm, Coherent Inc., Santa Clara CA). A beamsplitter was used to separate the excitation and probe pulses, and the relative timing was adjusted with a variable delay line. In some cases the probe was converted to 400 nm light in a non-linear crystal; the benefits of this are discussed in the appropriate sections. The excitation pulses were used to irradiate both thin metal films, generating very high-frequency acoustic waves that propagate through rather than in the plane of a thin film sample[28] as described in Section 3.2.2; and ferroelectric crystals such as $LiNbO_3$, generating phonon-polaritons, which are admixtures of optic phonons and electromagnetic waves in the terahertz (THz) frequency range via impulsive stimulated Raman scattering.[29] In both of these cases the excitation beam was asynchronously chopped, and the small change in interferometric intensity ($\sim 10^{-3}$-10^{-4}) was detected by lock-in amplification at the chopping frequency. The interferometric detection of these phenomena are described in Sections 5.4 and 5.5, respectively.

This interferometer design is simple and compact, in its most basic form involving only the sample and two optical elements, a phase mask and a lens, which interact with the separated reference and probe beams whose relative optical path length is critical. None of the optical components needs to be aligned with more than ordinary precision, and it is routinely operated without more than ordinary isolation from vibrations or air currents (e.g. on a laser table without hydraulic legs, and without a cover or other separation from room air). Its phase stability and robustness against vibrations are enhanced by the symmetry of the probe and reference optical paths. The only asymmetry is the refractive index change or displacement induced by the pump laser in the region where the probe beam interacts with the sample. In contrast, most other interferometer geometries include reflections of separated probe and reference beams that result in high sensitivity to vibrations of the reflecting elements. Quantitative characterization of the phase stability of this interferometer will be presented with the different applications discussed in further sections.

5.2.2 Spatiotemporal Limitations

The placement of the sample in the Fourier plane of a diffraction grating-lens pair, as shown in Figure 5.1, introduces potential limitations in the combined temporal and spatial resolution of the interferometer, particularly on femtosecond time scales. Because ultrafast pulses have a frequency bandwidth which is more or less wide depending on the pulse duration (~8 nm FWHM in the current case), the orders diffracted from the phase mask, e.g., the probe and reference beams, will be also be spectrally dispersed in the plane of the sample. Their shorter wavelength components will be diffracted by the phase mask at smaller angles and their longer wavelength components will be diffracted at larger angles. If the excitation spot size and the sample response to it at any given time cover a large sample area compared to the broadened probe and reference spot sizes, then this dispersion does not introduce an additional temporal resolution beyond the pulse duration. However, if the excitation beam and the sample response to it are small compared to the resulting probe and reference spot sizes, in particular along the direction between the probe and reference beams, then the material response will only be monitored by a subset of the probe spectral components at a given time. The time resolution will be given approximately by the probe pulse duration multiplied by the ratio of probe to excitation spatial dimensions. For longer pulses (with less bandwidth) monitoring slower phenomena, a noticeable compromise of temporal resolution would not be observed. In the case of the through-plane high-frequency acoustic waves, the probe and reference spot sizes are made much smaller than the excitation spot, avoiding this problem.

However, in the case of a phonon-polariton wavepacket propagating at light-like speed in the plane of the sample, the measurement could be "blurred" significantly by the limitation in temporal resolution. Note that if the excitation pulse were cylindrically oriented in the perpendicular direction, so that at any time the propagating response cut across all of the dispersed spectral components simultaneously, then the temporal resolution would not be compromised. The presence of temporal blurring in the case of the phonon-polariton measurements presented in Section 5.5 was not observed, perhaps due to the relatively limited optical bandwidth of the laser used for this particular experiment. All of the other results reported are on sufficiently slow time scales so there is no significant limitation in temporal resolution due to dispersion of the probe spectral components.

5.2.3 Calibration, Resolution, and Noise Characteristics

A first feasibility test of the grating interferometer concerned its calibration, sensitivity and stability. In each of these three aspects, the adjustability of the static phase plays a crucial role in determining the optical path length (or phase) delay ξ between the probe and reference beams. The calibration of the output signal V_{sig} from the illuminated photodiode or CCD, i.e., the assessment of the sensitivity $dV_{sig}/d\xi$, can be easily done. $V_{sig}(\xi)$ may be expressed as:

$$V_{sig}(\xi) = \frac{V_{max} + V_{min}}{2} + \frac{V_{max} - V_{min}}{2} \cos(2\pi\xi / \lambda) \qquad 5.2$$

V_{max} is obtained in the case of total constructive interference between the probe and reference beams, i.e., when $\xi = 0, \lambda, \ldots$ V_{min} is obtained in the case of total destructive interference between the beams, i.e., when $\xi = \lambda/2, 3\lambda/2, \ldots$ These values of the static phase can be achieved by adjusting either an optical window or by translating the phase mask, as discussed in Section 5.2.1. The sensitivity of the interferometer as the phase delay is varied, $(dV_{sig}/d\xi)$ is then equal to:

$$\frac{\partial V_{sig}}{\partial \xi} = -(V_{max} - V_{min})\frac{\pi}{\lambda}\sin(2\pi\xi / \lambda) \qquad 5.3$$

The maximum sensitivity is therefore reached when the optical path delay is $\xi = \lambda/4, 3\lambda/4, \ldots$ Here the voltage level on the detector will be midway between V_{max} and V_{min}:

$$\left|\frac{dV_{sig}}{d\xi}\right|_{max} = (V_{max} - V_{min})\frac{\pi}{\lambda} \qquad 5.4$$

In practice, the maximum sensitivity for experimental operation can be achieved by finding the V_{max} and V_{min} values, such as by viewing the output from the photodiode on an oscilloscope, and then rotating the static optical phase so that the voltage level is midway between them.

The calibration is routinely performed for the experimental schemes shown in Figure 5.1 and Figure 5.2, which are used for detection of the phonon-polaritons and through-plane ultrahigh frequency acoustic waves described in subsequent sections. The chopper and lock-in amplifier used in the experiment as described in Section 5.2.1 are employed in two ways. First, the lock-in signal corresponding to the maximum amplitude of material response, at maximum interferometer sensitivity, is noted. The chopper is then removed from the excitation beam and placed in the probe beam prior to the diffraction grating. Then the amplified signals resulting from chopping the probe with complete constructive and destructive interference are noted; these are $V_{\max}$ and $V_{\min}$ respectively. These values are then used to compute the sensitivity via Equation 5.4, and the signal resulting from the material response may be determined from this.

Typical fluctuations in the static interferometric intensity are on the order of 0.5%, due to laser fluctuations and interferometric disturbances. Because this noise is larger than the signal level (~ 0.1%) the scans must be averaged for about 1 hour to achieve an adequate signal to noise ratio. With this level of averaging, interferometric features as small as 0.01 nm are clearly distinguishable, as shown in the following sections. As this corresponds to a size smaller than a molecule, it is certainly adequate for most applications.

Note that the probe and reference beams as they are generated at the phase mask, and again as they recombine at the phase mask, form an interference pattern whose period is half that of the phase mask. The relative optical path delay values $\xi = 0, \lambda/4, \lambda/2, \ldots$ correspond to a spatial phase shift ϕ between the original and regenerated interference patterns with values $\phi = 0, \pi/2, \pi, \ldots$, i.e. the peaks and nulls of the two interference patterns exactly overlapping, shifted by one-fourth the period, shifted by one-half the period, etc. Note also that the signal level midway between $V_{\max}$ and $V_{\min}$ can be set to zero if desired, in which case $V_{\min} = -V_{\max}$ and the expressions above are somewhat simplified.

5.3 Imaging Surface Acoustic Waves

The demonstrations described in Sections 5.4 and 5.5 involve making individual high-sensitivity measurements at localized regions of a sample, with no significant variation of the sample response across a single measurement region. However stroboscopic imaging schemes are a much more efficient way of characterizing responses which vary in space as well as time.[16,30] The interferometer design can be easily converted to an imaging scheme, as shown in Figure 5.3, retaining all of its advantages as described previously. In this section images of traveling surface acoustic waves are presented. Provided the pump and probe laser offer sufficient time resolution and can be synchronized to the camera as described in the following paragraph, this imaging interferometer can be implemented for any experimental time scale and for any kind of displacements, in both transmission and reflection geometries.

An important non-optical experimental detail arises from the use of a CCD camera, which has refresh and readout events which must be properly syncronized with the excitation and probing events. Because the laser repetition rate was not greater than the CCD refresh rate by more than an order of magnitude, the laser and the camera needed to be synchonized in order to avoid having uneven numbers of laser shots being collected between readouts, which would introduce >10% variations in image intensity from frame to frame. For the 60 Hz CCD camera that was used, signal could not arrive at the camera at a rate exceeding 30 Hz due to the interlacing of the even and odd pixel lines, which are read out alternately at a total rate of 60 Hz. To minimize noise resulting from slow mechanical vibrations and air currents, it is useful to work in a differential mode, blocking every alternate excitation pulse in order to create a background image which may be immediately subtracted from each image collected following excitation. Due to the alternate interlacing of the CCD readout, requiring the even lines of background to be subtracted from even lines of the signal image, the maximum possible effective image averaging rate was 7.5 Hz. Use of a much faster-refreshing CCD, or increasing the repetition rate of the pump and probe pulses to well above the 30 Hz refresh rate so the number of laser shots per image would be the same, would eliminate the need for such slow synchronization.

To excite surface acoustic waves, a 200 ps, 1064 nm laser pulse was used to irradiate the backside of a Plexiglass sample which was coated with a very thin (100 nm) layer of chromium. Optical absorption by the chromium resulted in rapid thermal expansion, launching counterpropagating acoustic waves in the plane of the sample. For this demonstration, a short focal length lens was displaced from the center of the pump beam path, inducing an 'arc' aberration to the excitation region which was approximately 75 microns high and 500 microns across. The surface displacements resulting from the excitation were approximately 1 nm in magnitude. The acquisition of each frame, averaged over 400 shots, took about 1 minute. Signal from a single probe pulse was recorded at each CCD readout, and at each alternate readout the pump pulse was suppressed in order to produce a background image.

At the top of the first frame of Figure 5.4 the thermally induced surface displacements at the excitation region, caused by absorption in the chromium layer and heating of the adjacent Plexiglass, can clearly be seen as a white arc. This image, recorded at t=320 ns following excitation, also shows an acoustic wave that has begun focusing and propagating toward the center of the image, seen as a dark arc. The second frame at t=1.44 μs shows the acoustic wave

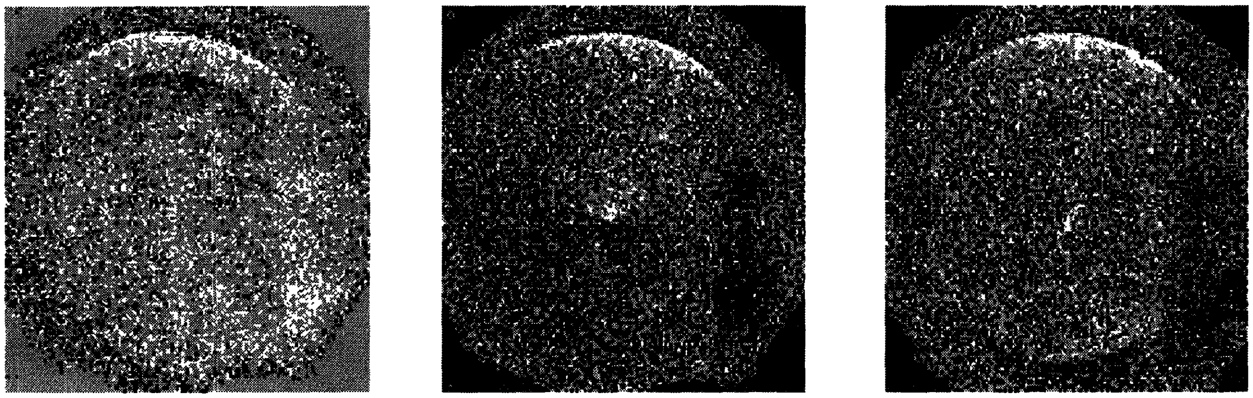

Figure 5.4. Images of time-resolved surface acoustic propagation and focusing on Cr-coated plexiglass. Images are 1.12 μs apart. Thermally induced displacements persist at the excitation region. Area is approximately 500 μm square.

which is now focused at the center of the image, about 500 microns from the excitation region. The third frame at *t*=2.40 μs shows the acoustic wave after further propagation and expansion out of the central region of the sample. For all three frames, the thermally induced displacement appears to have a roughly identical intensity and spatial profile, and this is due to the relatively slow process of thermal diffusion which will eventually return the material to its original (unexcited) state. In the latter two frames the acoustic wave can be seen to have a dark leading edge, and a lighter following edge; this is because the excited wave is bipolar, with a compressive part followed by an expansive part. This can be seen more clearly in Figure 5.5, which shows corresponding cross sections of the intensities along a vertical line (averaged across a width of 20 pixels) bisecting the images shown in Figure 5.4.

The high-intensity response on the left of each cross-section in Figure 5.5 results from the thermally induced displacement, which is essentially static on the timescale of this measurement. The right-propagating surface acoustic wave has an extremely sharp leading edge, and nearly triples in amplitude between the first frame at *t*=320 ns and the second frame at *t*=1.44 μs, before decreasing again in the third frame, at *t*=2.40 μs. This is due to the focusing

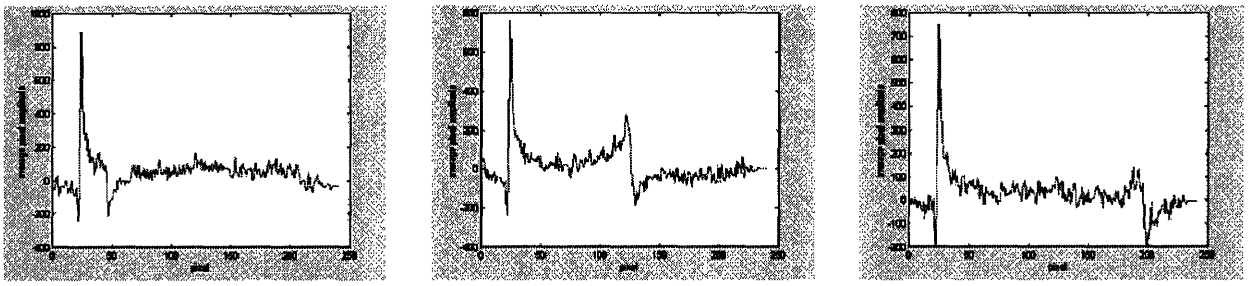

Figure 5.5. Cross-section of thermal and acoustic material responses imaged in Figure 5.4, at the same times, averaged across central 20 pixels of image.

revealed in Figure 5.4, and is a result of the spatial pattern of the initial material excitation. It is noted that even though optical excitation at the sample edge was below the damage threshold and there was no direct photoexcitation of the center of the sample, the focused acoustic energy was sufficient to tear the chromium film. This suggests that nonlinear acoustic responses may be observed in this fashion.

5.4 Probing Ultrahigh Frequency Acoustic Waves

To investigate the high-frequency acoustic responses of materials, i.e. at frequencies higher than those accessible by crossed-beam material excitation with impulsive stimulated thermal scattering as described in Section 3.2, shorter pulse durations and smaller excitation and probe dimensions need to be used. In crossed-pulse techniques, the smallest excitation region, and hence the shortest acoustic wavelength, is limited by geometry to ~2 microns. The use of thin metal films as high frequency acoustic transducers is well-understood,[28,31] and is described in Section 4.3. In this technique, sub-picosecond light pulses are used to heat a thin metal film, launching through-plane acoustic waves via the photoacoustic effect. In moderately thin films (sub-micron) the acoustic wavelength is determined by a convolution of the optical penetration depth of light into the metal, typically ~15 nm, and of the distance that hot electrons diffuse into the film before coupling into lattice phonons, ~150 nm.[31,32] Films can also be fabricated which are much thinner than either of these depths, in which case the acoustic wavelength is given by the thickness of the film itself. By this excitation method, broadband acoustic wavepackets containing frequencies over 400 GHz, and more recently narrowband acoustic wavepackets in the same frequency range have been generated, as described in Chapter 4.[33,34] In both cases, rapid expansion of the heated region of the film launches through-plane acoustic waves which can be observed, along with their echoes, in the film. Typically these changes are observed via strain-induced reflectivity changes in a delayed probe pulse at 800 nm.[31,33,35] As discussed in Section 5.1, picosecond acoustics are less frequently detected with interferometry.[21,22]

The interferometer setup is as shown in Figure 5.2. The rest of the optical setup as well as sample design, which are used together to generate ultrahigh frequency acoustic waves, are discussed in Section 4.2. Many uncalibrated examples of signals obtained with the interferometer are given in Sections 4.3-4.6 and 6.3-6.4. Data calibrated using the procedure described above are presented in Figure 4.15, which show a displacement of 0.48 nm, with much smaller features easily resolvable. A tremendous benefit of using interferometry is the accessability to a quantitiative measure of the displacements and steady-state as well as dynamical strains generated in the material, as illustrated in Section 4.4. In the initial iteration of the ultrahigh frequency acoustic wave experiment described in Chapters 4 and 6 of this thesis, 800 nm light was used as the interferometric probe. However this generated some unexpected signal contributions, which are presented here.

The response of the sample described in Section 4.2.2 with 1000 nm of silica glass to a single excitation pulse, with interferometric detection at 800 nm, is shown in Figure 5.6. At zero picoseconds, the signal jumps sharply when the pump pulse excites the sample as described

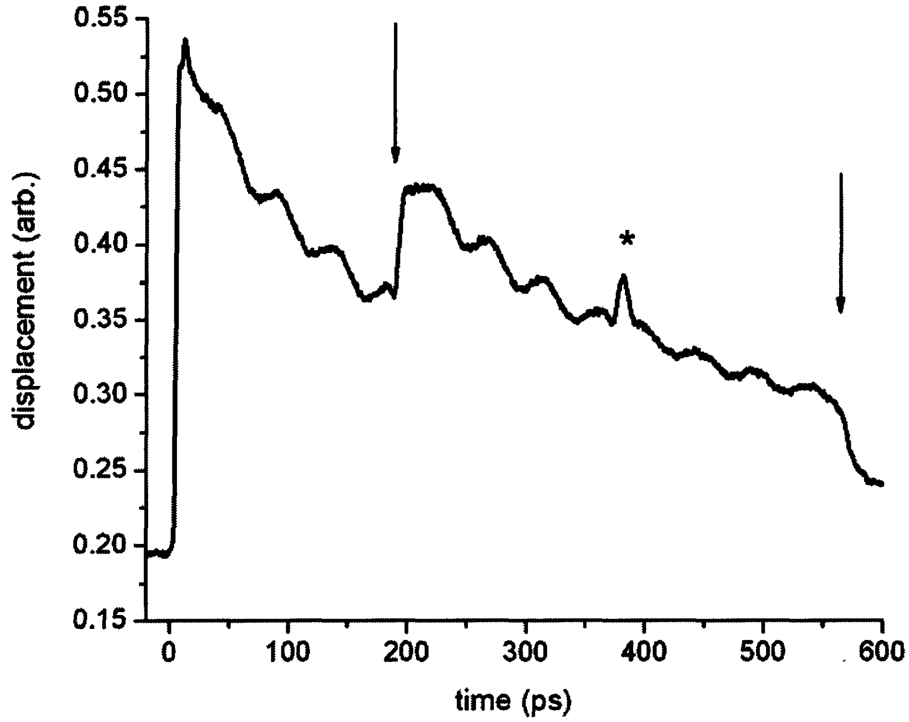

Figure 5.6. Single-pulse excitation of acoustic wave in 1000 nm silica sample described in Section 4.2.2. Expanded scale to show detail.

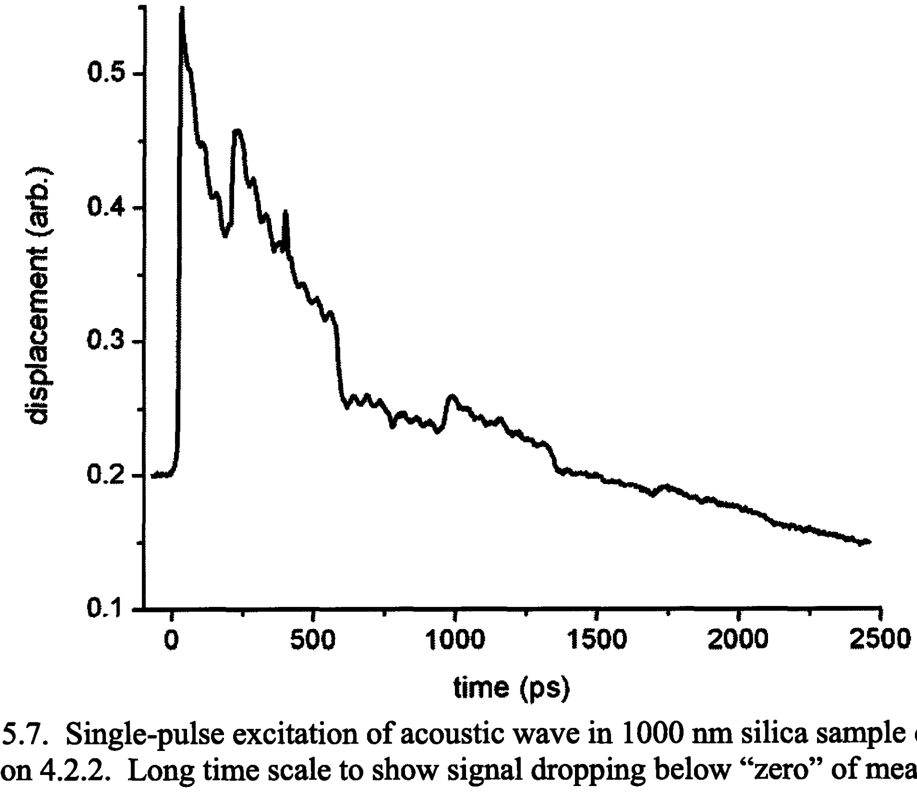

Figure 5.7. Single-pulse excitation of acoustic wave in 1000 nm silica sample described in Section 4.2.2. Long time scale to show signal dropping below "zero" of measurement.

in Section 4.3. This launches an acoustic wave through the plane of the film, but two strong signal contributions can also be seen, which indicate that the probe beam "sees" through the entire sample. First is a strong oscillation with a period of roughly 50 ps, which results from an interference between the phase of the probe reflected from the sample, and a tiny amount of light which is reflected from the acoustic wave as it travels through the silica glass. The frequency of the oscillation depends on the optical wavelength, refractive index, and sound speed in the material.[36] Another strong signal contribution is a large quasi-static background, which arises from the presence of thermally-induced strain, which modulates the reflectivity of the aluminum.[33] The acoustic signals, marked with arrows and "*," are tiny compared to this. In contrast, as shown in Figure 4.15, probing with 400 nm light does not yield a large thermal background.

After excitation at zero picoseconds, the acoustic wave propagates through the multilayer sample until it arrives roughly 200 ps later at the backside of the sample assembly. This event is marked by the rightmost arrow in the figure. Here (the air-aluminum interface), it reflects with inversion due to the low acoustic impedance of air, as described in Section 4.4, and travels back to the excitation region 200 ps later. This event is marked by "*" in Figure 5.6, and can only be seen because the probe beam optically penetrates the whole sample. The acoustic wave subsequently wave reflects from this region (the aluminum-sapphire interface) and returns again to the backside of the sample 200 ps later, as marked by the leftmost arrow. The thermal plus acoustic signal overall looks fairly comparable shown in Figure 6.23, which represents the "typical" reflectivity signal that is usually exploited to probe high-frequency acoustic waves. The unusual result came upon examination of signal at longer times, as shown in Figure 5.7. The signal can be clearly seen to drop below the "zero" level of the signal, corresponding to the level prior to excitation. Signal contributions like this are possible with interferometry because the dynamical signal makes oscillates about a static phase (i.e., unchanging light level) which may optimized for sensitivity of the interferometer, as in Equation 5.3. If there is a small increase in the optical phase delay ζ of the probe beam, then there is a small increase in the amount of light relative to that determined by the static phase. If there is a small decrease in ζ, then the light level decreases. However the signal resulting diffusion of thermal energy would be expected to be seen as an expansion of the material which decays back to the initial state, as demonstrated for the signals in Chapter 3, not to a contraction of the material.

To investigate this unusual result, the static phase of the interferometer was varied. As can be seen from Equation 5.3, a rotation of the interferometer phase by a factor of π (i.e. introducing a relative $\lambda/2$ phase delay between the probe and reference beams) results in a signal of equal strength and opposite amplitude. A "negative" going signal is possible, again because the changes in the interferometric intensity are relative to the large static phase which determines the sensitivity. As shown in Figure 5.8, rotation of the interferometer phase by π yields an unusual result – a nearly nonexistent signal. The oscillations corresponding to interference between the static reflection and the dynamic reflection from the traveling acoustic wave can still be clearly seen to begin immediately after zero picoseconds. At times corresponding to the arrival of the acoustic wave at the backside of the sample, at the excitation region, and back again at the backside of the sample, sharp fluctuations in the phase of this oscillatory signal can be seen. As in Figure 5.6, these events occur at times separated by the single-trip time of the acoustic wave in 1000 nm of glass, 200 ps, and are marked by arrows and "*" as before. As seen in Figure 5.9, at long times the signal level drops below zero again as was observed in Figure 5.7. Otherwise there is very little indication of the other signal contributions observed at the

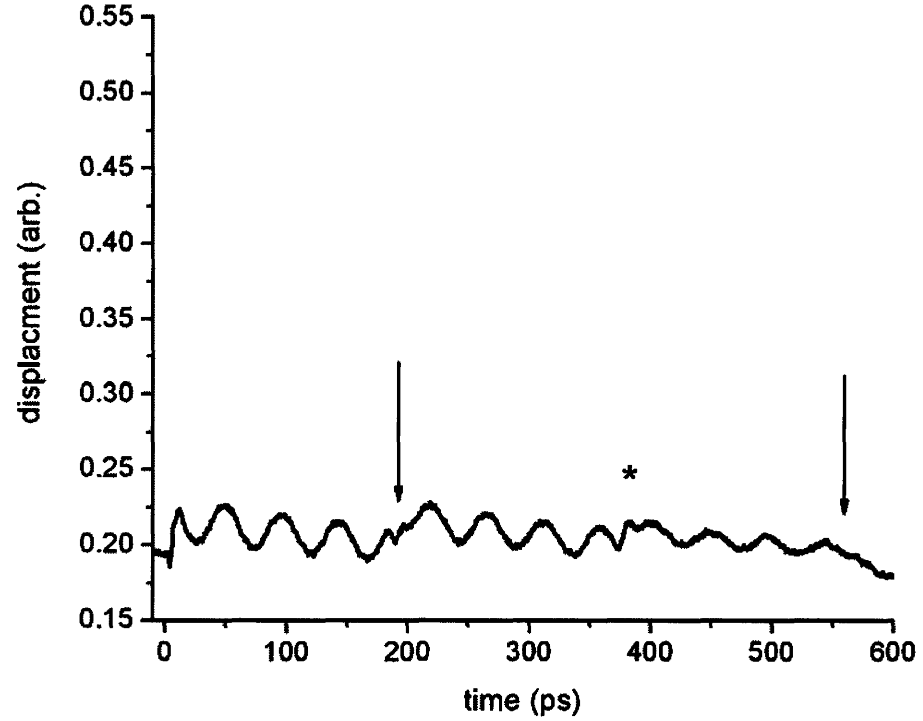

Figure 5.8. Single-pulse excitation of acoustic wave in 1000 nm silica sample described in Section 4.2.2. Interferometer phase was rotated π degrees relative to that in Figure 5.6. Expanded scale to show detail.

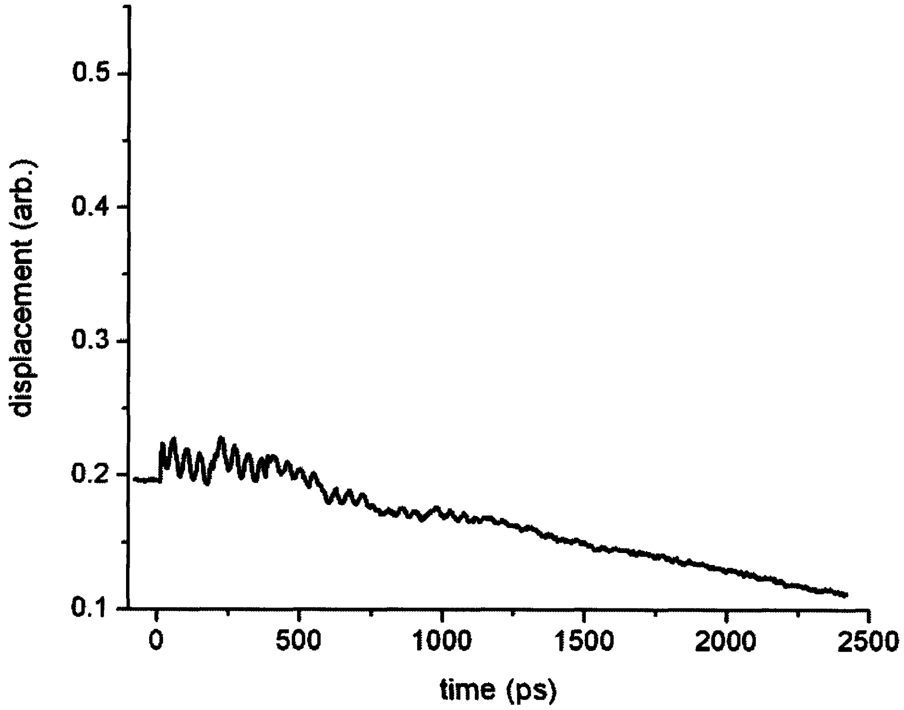

Figure 5.9. Single-pulse excitation of acoustic wave in 1000 nm silica sample described in Section 4.2.2. Interferometer phase was rotated π degrees relative to that in Figure 5.7. Long time scale to show signal dropping below "zero" of measurement.

opposite interferometer phase.

If there are signal contributions resulting from not only a tiny interferometric phase shift of the probe beam relative to the pump as had been assumed, but also from a tiny change in reflectivity of the sample as in Figure 6.23, then the nearly perfect cancellation of the signal upon rotation of the interferometer phase indicates that the strength of these two signal contributions is nearly identical. The total change in signal intensity I_S from both contributions can be expressed as the sum of the small changes in the photodiode voltage, about the static voltage (V_{max}-V_{min}) corresponding to maximal interferometric sensitivity, where the experiment is performed:

$$I_{sig} = \delta V_{ref} + \delta V_{int} \qquad 5.5$$

The reflectivity contribution is not related to the optical phase, only to the absorption of the probe light by the aluminum. For a more detailed form of the signal intensity, the interested reader is referred to Reference 28. Here it suffices to express the total reflectivity signal as related to the small change in sample reflectivity δR as modulating the total light level on the photodiode:

$$\delta V_{ref} = \delta R(V_{max} - V_{min}) \qquad 5.6$$

The interferometric contribution is related to the small change in optical phase (e.g. path length) induced by the material response $\delta\zeta$ as in Equation 5.3:

$$\delta V_{int} = -\delta\zeta(V_{max} - V_{min})\frac{\pi}{\lambda}\sin\left(\frac{2\pi\zeta}{\lambda}\right) \qquad 5.7$$

where the total phase (path length) is much larger than the small fluctuation, $\zeta + \delta\zeta \approx \zeta$. When ζ=0, π, 2π …, i.e. at the maximum sensitivity, then the total signal intensity is given by:

$$I_{sig} = \delta R(V_{\max} - V_{\min}) \pm \delta\zeta(V_{\max} - V_{\min})\frac{\pi}{\lambda} \qquad 5.8$$

As the static phase of the interferometer is rotated by factors of π, the intensity of the total signal goes from a sum to a subtraction depending on whether the total phase is given by an odd or even number cycles.

As shown in Figure 5.8 and Figure 5.9, clearly upon rotation of the interferometer phase by a factor of π relative to that shown in Figure 5.6 and Figure 5.7, the signal level due to the sum of interferometric and reflectivity signals nearly disappears. The oscillatory signal which has other origins is unaffected. The total signal level described by Equation 5.8 is close to zero, and therefore:

$$\delta R \approx \delta\zeta \frac{\pi}{\lambda} \qquad 5.9$$

This is a very useful result, because typically the measurements using a strain-induced change in reflectivity of the probe as the signal have to make estimates of the magnitude of the strains based on optical, electronic, and mechanical properties of the material.[32] Typically it is simply noted that $\Delta R/R \sim 10^{-3}$ or smaller. Because the total displacement and therefore strain may be easily calibrated interferometrically as described in Section 5.2.3, then the previous strain estimates may be quantitatively evaluated.

In contrast to the results with an 800 nm probe, the signal obtained from an interferometer with 400 light is shown in Figure 5.10. The sample is somewhat thinner, with 210 nm silica glass instead of 1000 nm, and is excited with an optically shaped 250 GHz pulsetrain as described in Chapter 4, but otherwise the experiment is nearly identical. Qualitatively, the acoustic signal contributions in the figures can be seen to be fairly comparable to those in Figure 5.6. At a time of zero picoseconds, a small feature can be seen which corresponds to the excitation of the sample; the large rise at this time is not seen because the probe is modulated only by the acoustic intensity, not by the presence of heat and excited electrons. At a time of

~35 picoseconds, the acoustic wave arrives at the back of the sample, and is marked by an arrow as in Figure 5.6. After another ~70 ps, a negative-going echo returns, which is marked with a second arrow. The signal in general shows no large background or oscillations, which is due to the reduced reflectivity and transmission of the probe beam through the sample, respectively. Shown in Figure 5.11 is the signal following rotation of the interferometer phase by a relative factor of π. It is nearly identical to that with the unrotated phase, but has the expected negative amplitude via Equation 5.8 for small ΔR. The difference between the two interferometric signals rotated by π degrees relative to each other yields the pure reflectivity signal via this equation, and the results are shown in Figures 5.12-5.14. The reflectivity contribution can be seen to be quite small for the 400 nm probe, on average roughly 20% of the total signal amplitude, whereas at 800 nm it makes up the bulk of the signal.

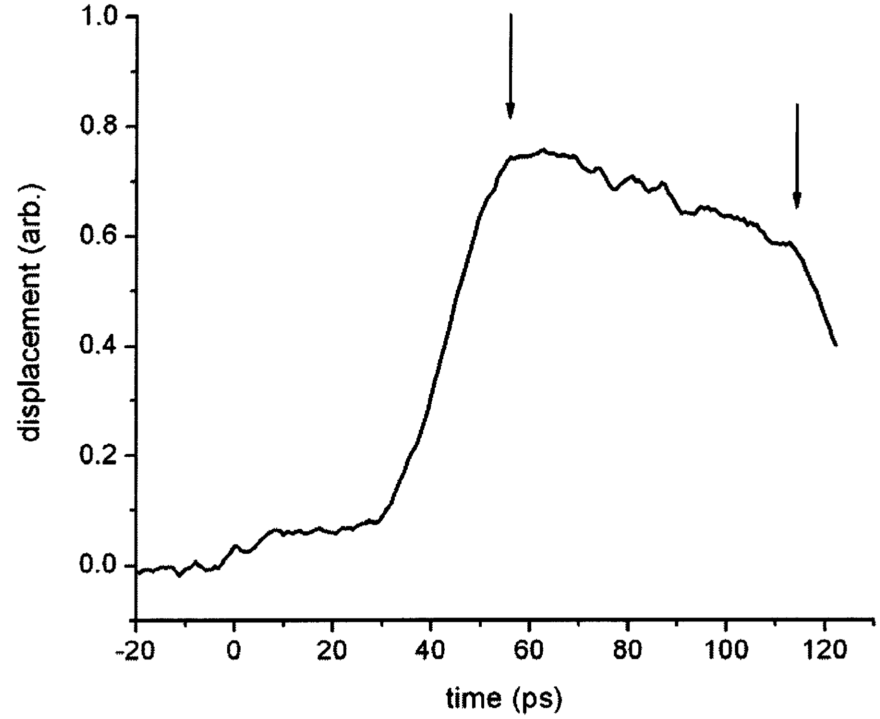

Figure 5.10. 250 GHz excitation of acoustic wave in 415 nm silica sample, probed with 400 nm light.

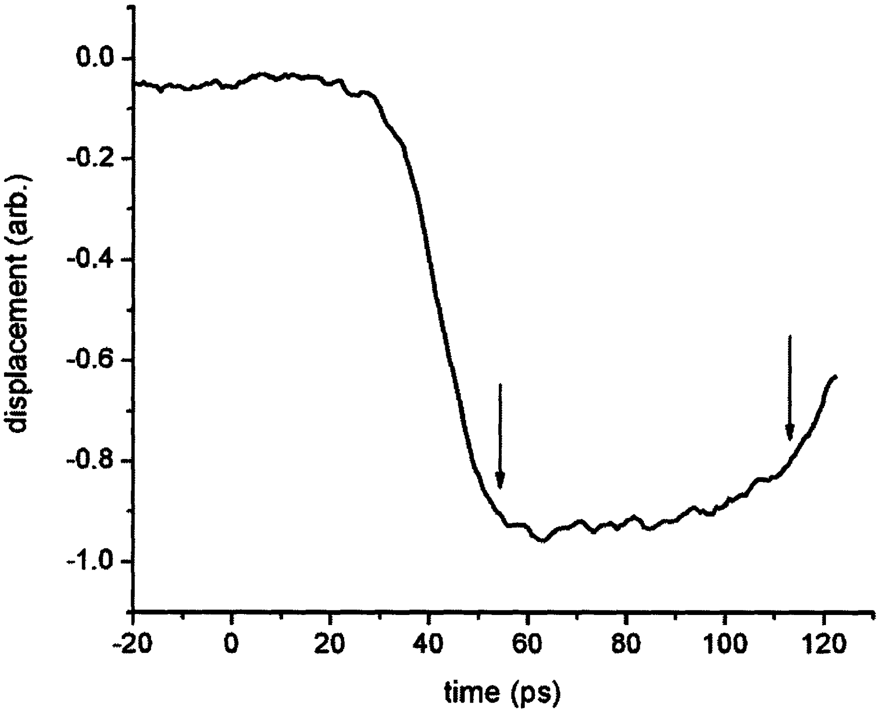

Figure 5.11. 250 GHz excitation of acoustic wave in 415 nm silica sample, probed with 400 nm light. Interferometer phase was rotated π degrees relative to that in Figure 5.10.

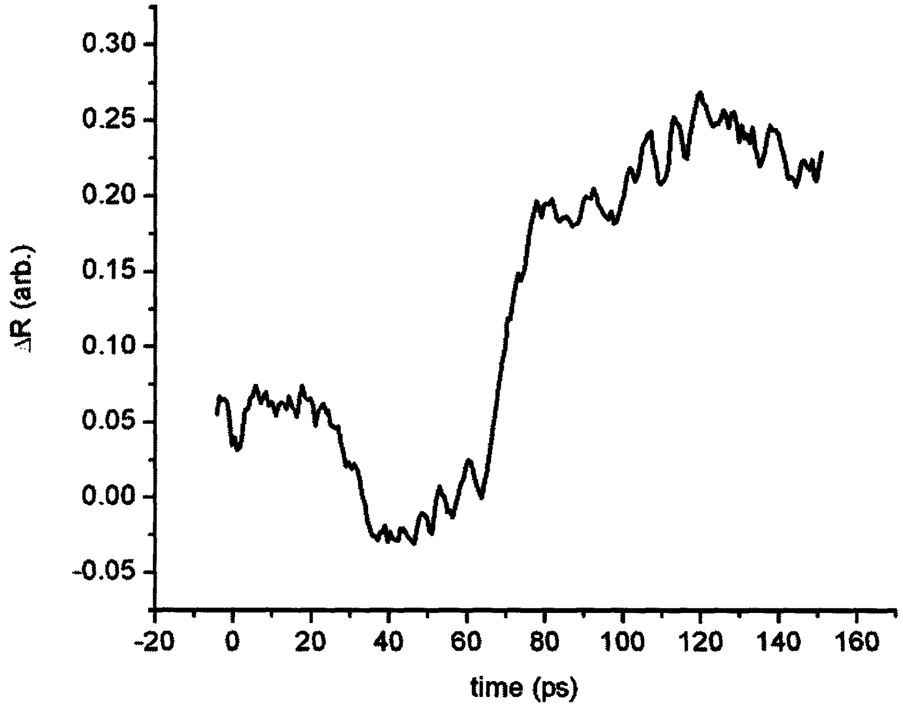

Figure 5.12. "Pure" change in reflectivity for 400 nm probe obtained from difference between signals at interferometer phases rotated by a factor of π from each other.

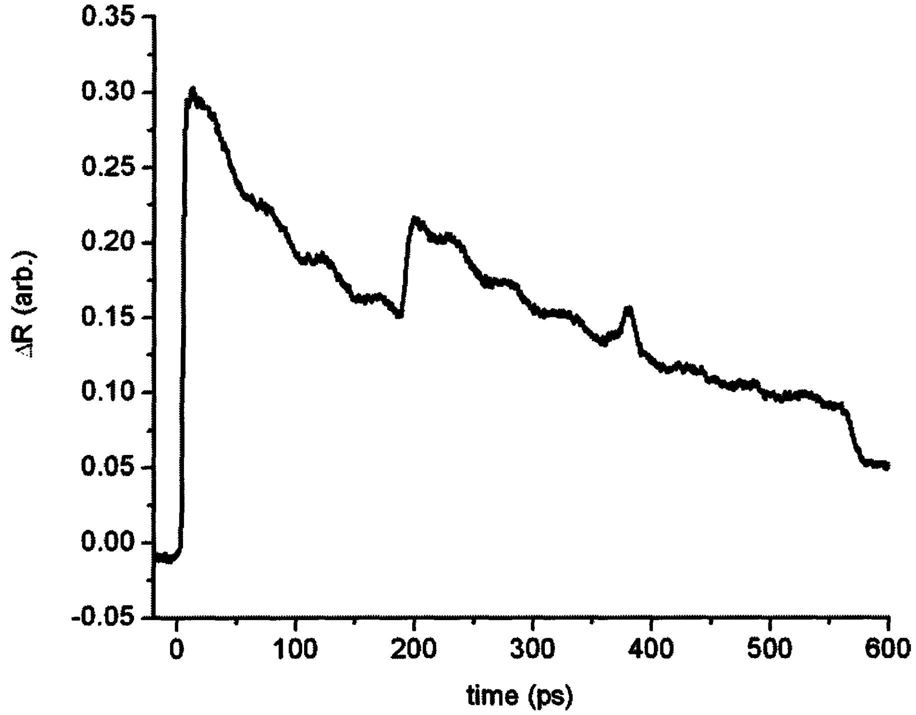

Figure 5.13. "Pure" change in reflectivity for 800 nm probe obtained from difference between signals at interferometer phases rotated by a factor of π from each other.

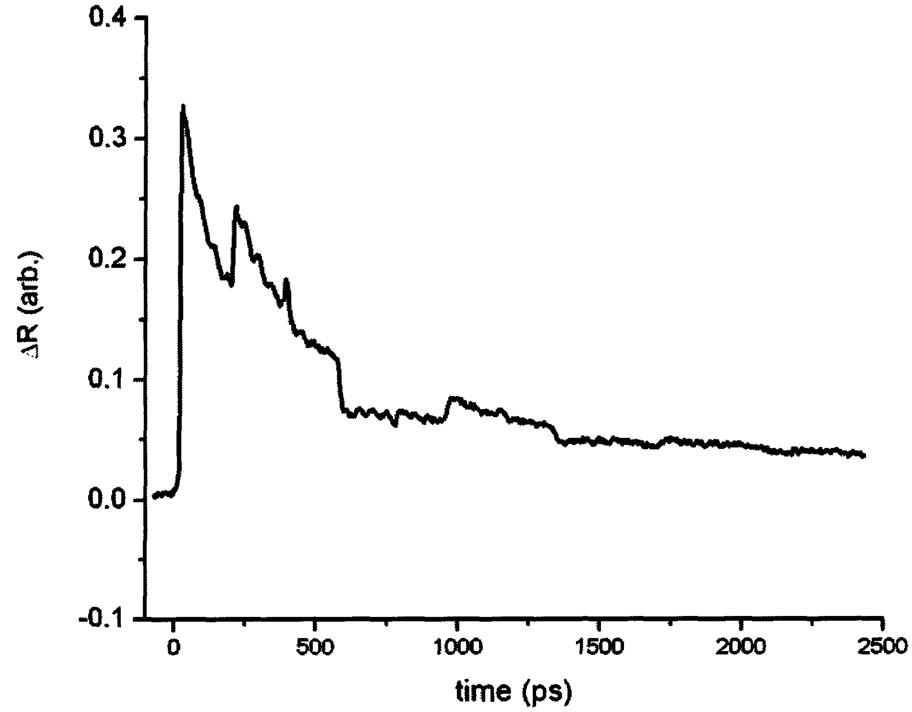

Figure 5.14. "Pure" change in reflectivity for 800 nm probe obtained from difference between signals at interferometer phases rotated by a factor of π from each other.

5.5 Probing Lattice Vibrations: Phonon-Polaritons

Via the well-established technique of impulsive stimulated Raman scattering (ISRS), 800 nm excitation of a ferroelectric crystal such as $LiNbO_3$ or $LiTaO_3$ generates ionic displacements, or optical lattice vibrations, which act like tiny antennas.[27,29,30] The radiation generated by the displacements inside the crystal simulates displacive motions in adjacent unit cells, which in turn re-radiate. This admixture of ionic displacement and electromagnetic radiation is referred to as a "phonon-polariton" (or more briefly, polariton) and it propagates at roughly 1/6 the speed of light. For an exposition on the characteristics, control, and applications of polaritons, the interested reader is referred to the thesis of David Ward, *Polaritonics: An intermediate regime between electronics and photonics*.[37]

The detection of phonon-polaritons via interferometry is illustrated in this section. A transmission-mode interferometer, as shown in Figure 5.15. The probe wavelength chosen was 400 nm, which made it very easy to exclude scatter from the 800 nm pump pulse from the photodiode, as shown in Figure 5.15. The excitation beam was from the Deathstar pulse shaper described in Chapter 4, but here it was used to generate polaritons of tunable frequency, in this case at 330 GHz.[38] The sample was a thin film of $LiNbO_3$. As shown in Figure 5.16 the polariton is generated at the probe arm of the interferometer, and can be seen as a series of sharp peaks corresponding to electronic excitation. Roughly 80 ps later, the polariton can be seen to have traveled laterally (v = 60 μm/ps) in the sample, and is detected in the reference arm of the interferometer.

Here the relative probe-reference displacement which generates interferometric signal arises from a change in refractive index in the crystal. As described in Section 5.2.3, the interferometer may be calibrated, and the results are shown in Figure 5.16. The typical maximum displacement due to electronic signal was found to be on the order of 50 nm, and due to polaritons to be on the order of 0.5 nm. This information can be used to calculate the net displacement of the ions within in the crystalline lattice due to modulation by polaritons, which in turn yields a measurement of the differential polarizability of the crystal.[39]

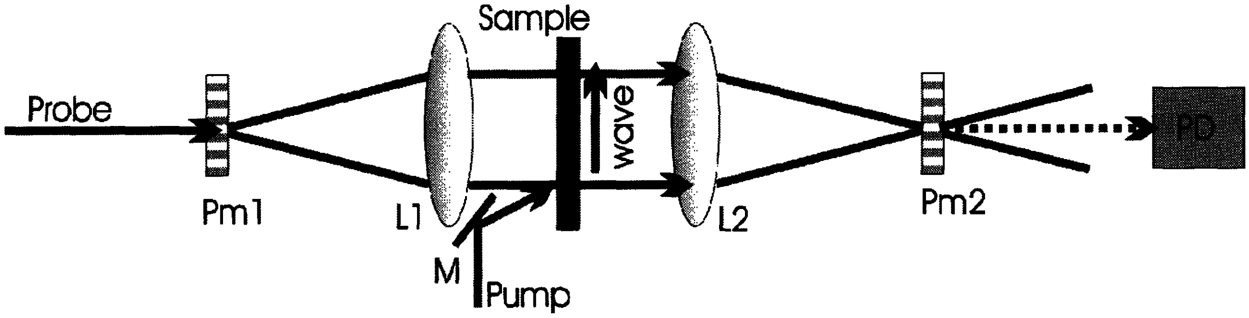

Figure 5.15. Transmission mode interferometer, indicating introduction of excitation pulse to sample, and in-plane motion of the polariton.

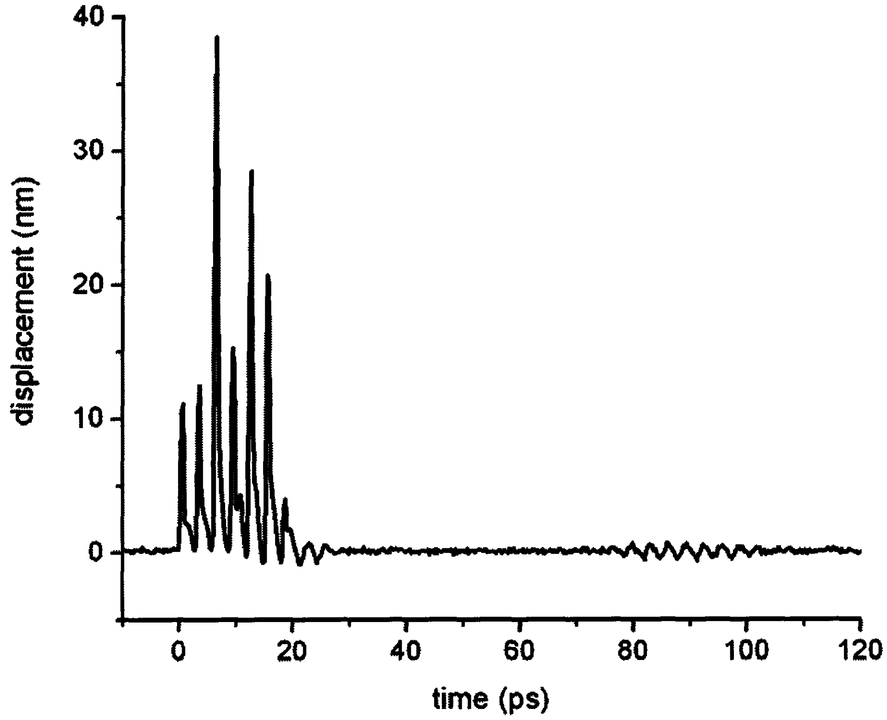

Figure 5.16. Generation of polariton at probe interferometer arm, and detection at reference interferometer arm, following propagation through ~5 mm of $LiNbO_3$.

5.6 Conclusions

In summary, a new diffraction grating-based interferometer has been developed which is simple to align and use, as well as calibrate. Its robust use for the imaging and point detection of thermoelastic phenomena on multiple timescales and in various geometries has been demonstrated.

5.7 References

---

1. D. Malacara. *Optical Shop Testing*. Wiley-Interscience, New York, 1992.
2. R. Baltazar, C. Solano, G. Martinez-Ponce, A. Camacho. Optical heterodyne profilometer to scan irregularities in reflective objects. *Optics Communications*, 204(1-6): 33-43, 2002.
3. K.M. Abedin, M. Wahadoszamen, A.F.M.Y. Haider. Measurement of in-plane motions and rotations using a simple electronic speckle pattern interferometer. *Optics and Laser Technology*, 34(4): 293-298, 2002.
4. V. Sundar, J-F. Li, D. Viehland, R.E. Newnham, "Interferometric evaluation of electrostriction coefficients." *Materials Research Bulletin*, 31(5): 555-563, 1996.
5. H.P. Ho, K.C. Lo, Y. Chan, R.K.Y. Li, C.M.L. Wu. Application of passive quadrature phase demodulation for the detection of laser ultrasound. *Optics and Lasers in Engineering*, 38(6): 549-556, 2002.
6. T. S. Jang, J. J. Lee, D. J. Yoon, S. S. Lee. Non-contact detection of laser-generated surface acoustic waves using fiber-optic Sagnac interferometer. *Ultrasonics*, 40(1-8): 803-807, 2002.
7. Y. Sugawara, O.B. Wright, O. Matsuda, V.E. Gusev. Spatiotemporal mapping of surface acoustic waves in isotropic and anisotropic materials. *Ultrasonics*, 40(1-8): 55-59, 2002.
8. D. Hurley, K.L. Telschow, D. Cottle. Probing acoustic nonlinearity on length scales comparable to material grain dimensions. *Ultrasonics*, 40(1-8): 617-620, 2002.
9. B. Köhler, F. Schubert. Optical detection of elastodynamic fields of ultrasonic transducers. *Ultrasonics*, 40(1-8): 741-745, 2002.

---

10. C.B. Scruby, L.E. Drain. *Laser Ultrasonics – Techniques and Applications*. Adam Hilger, Bristol, 1990.

11. T.H. Barnes, T. Eiju, D.C.L. Cheung, C.Y. Wu. Phase measurement accuracy of feedback interferometers. *Optics and Lasers in Engineering*, 38(6): 387-404, 2002.

12. J.W. Wagner, J.B. Spicer. Theoretical noise-limited sensitivity of classical interferometry. *Journal of the Optical Society of America B*, 4(8): 1316-1326, 1987.

13. K. Creath. Phase measurement interferometry techniques. *Progress in Optics*, 26: 349-383, 1988.

14. M. Melozzi, L. Pezzati, A. Mazzoni. Vibration-insensitive interferometer for on-line measurements. *Applied Optics*, 34(25): 5595-5601, 1995.

15. G.W.R. Leibbrandt, G. Harbers, P. J. Kunst. Wave-front analysis with high accuracy by use of a double-grating lateral shearing interferometer. *Applied Optics*, 35(31): 6151-6161, 1996.

16. P.D. Ruiz, A. Davila, G. Mendiola, G. H. Kaufmann. Measurement of the temporal evolution of periodic induced displacement derivatives using stroboscopic electronic speckle-shearing interferometry. *Optical Engineering*, 40(2): 318-324, 2001.

17. J.-P. Bétend-Bon, L. Wosinski, M. Briedne. Double grating phase stepping interferometry for testing aspherics. *Pure and Applied Optics: Journal of the European Optical Society Part A*, 1(1): 55-69, 1992.

18. M. de Angelis, S. de Nicola, P. Ferraro, A. Finizio, G. Pierattini. A reflective grating interferometer for measuring the refractive index of liquids. *Pure and Applied Optics: Journal of the European Optical Society Part A*, 5(6): 761-765, 1996.

19. S. de Nicola, P. Ferraro, A. Finizio, G. Perattini. Reflective grating interferometer: a folded reversal wave-front interferometer. *Applied Optics*, 38(22): 4845-4849, 1999.

20. A. Miffre, R. Delhuille, B.V. de Lesegno, M. Büchner, C. Rizzo, J. Vigué. The three-grating Mach-Zehnder optical interferometer: A tutorial approach using particle optics. *European Journal of Physics*, 23(6): 623-635, 2002.

21. D.H. Hurley, O.B. Wright. Detection of ultrafast phenomena using a modified Sagnac interferometer. *Optics Letters*, 24(18): 1305-1307, 1999.

22. M. Nikoonahad, S. Lee, H. Wang. Picosecond photoacoustics using common-path interferometry. *Applied Physics Letters*, 76(4): 514-516, 2000.

23. J.A. Rogers, A.A. Maznev, M.J. Banet, K.A. Nelson. Optical generation and characterization of acoustic waves in thin films: Fundamentals and applications. *Annual Review of Materials Science*, 30: 117-157, 2000.

24. J.A. Rogers, M. Fuchs, M.J. Banet, J.B. Hanselman, R. Logan, K.A. Nelson. Optical system for materials characterization with the transient grating technique: Application to nondestructive evaluation of thin films used in microelectronics. *Applied Physics Letters*, 71(2): 225-227, 1997.

25. A.A. Maznev, K.A. Nelson, J.A. Rogers. Optical heterodyne detection of laser-induced gratings. *Optics Letters*, 23(16): 1319-1321, 1998.

26. R.M. Slayton, K.A. Nelson, A.A. Maznev. Transient grating measurements of film thickness in multilayer metal films. *Journal of Applied Physics*, 90(9): 4392-4402, 2001.

27. T.F. Crimmins. *Ultrahigh Frequency Characterization of Complex Materials Using Transient Grating Techniques*. Ph.D. Thesis, Massachusetts Institute of Technology, Department of Chemistry, June 2000.

28. C. Thomsen, H.T. Grahn, H.J. Maris, J. Tauc. Surface generation and detection of phonons by picosecond light pulses. *Physical Review B*, 34(6); 4129-4138, 1986.

29. T.F. Crimmins, N.S. Stoyanov, K.A. Nelson. Heterodyned impulsive stimulated Raman scattering of phonon-polaritons in LiTaO3 and LiNbO3. *Journal of Chemical Physics*, 117(6): 2882-2896, 2002.

30. N.S. Stoyanov, D.W. Ward, T. Feurer, K.A. Nelson. Direct visualization of phonon-polariton focusing and amplitude enhancement. *Journal of Chemical Physics*, 117(6): 2897-2901, 2002.

31. O.B. Wright. Ultrafast nonequilibrium stress generation in gold and silver. *Physical Review B*, 49(14): 9985-9988, 1994.

32. G. Tas, H.J. Maris. Electron diffusion in metals studied by picosecond ultrasonics. *Physical Review B*, 49(21): 15046-15054, 1994.

33. T.C. Zhu, H.J. Maris, J. Tauc. Attenuation of longitudinal-acoustic phonons in amorphous SiO2 at frequencies up to 440 GHz. *Physical Review B*, 44(9): 4281-4289, 1991.

34. J.D. Choi, T. Feurer, M. Yamaguchi, B. Paxton, K.A. Nelson. Generation of ultrahigh frequency tunable acoustic waves. *Applied Physics Letters*, submitted, 2004.

35. J. Hohlfield, J.G. Muller, S.-S. Wellershoff, E. Matthias. Time-resolved thermoreflectivity of thin gold films and its dependence on film thickness. *Applied Physics B*, 64(3): 387-390 1997.

36. O.B. Wright. Thickness and sound velocity measurement in thin transparent films with laser picosecond acoustics. *Journal of Applied Physics*, 71(4): 1617-1629, 1992.

37. D.W. Ward. *Polaritonics: An intermediate regime between electronics and photonics.* Ph.D. Thesis, Massachusetts Institute of Technology, Department of Chemistry, January 2005.

38. D.W. Ward, J.D. Beers, T. Feurer, E.R. Statz, N.S. Stoyanov, K.A. Nelson. Coherent control of phonon-polaritons in a terahertz resonator fabricated with femtosecond laser machining. *Optics Letters*, 29(22): 2671-2673, 2004.

39. D.W. Ward, J.D. Choi, K.A. Nelson. Measurement of the differential polarizability for phonon-polaritons in the A1 mode of $LiNbO_3$ by impulsive stimulated Raman scattering. *Applied Optics*, submitted (2004)

Chapter Six

Structure and Dynamics of Amorphous Solids in the GHz Acoustic Regime: Silica Glass

6.1 Introduction

This chapter presents results obtained using a novel experimental technique to elucidate the microscopic details of disordered solids. A femtosecond optical pulse shaper called the "Deathstar" is used to generate acoustic waves in the frequency region 1-1000 GHz which has heretofore been difficult to access, and yet holds a wealth of information on the nature of disordered materials. A serious effort has been undertaken by many researchers in the last few years to obtain detailed structural and dynamical information at a material's "extended" scale, corresponding to the large-wavevector and high-frequency range where it can no longer be described as isotropic or homogeneous, but rather as a complex structurally heterogeneous network with unique dynamics arising from the numerous quasi-energetic states in its potential energy surface. The effort to develop a theory which adequately describes the universal behavior of disordered solids has been recently called the "solid state paradigm of complex systems."[1] Understanding the common microscopic features of the different classes of disordered materials is crucial to understanding the common macroscopic properties.

Several spectroscopic techniques have been applied in recent years to the problem of determining the microscopic structure and dynamics of glasses, which probe different frequency ranges of interest. These include: quasielastic light scattering (LS);[2] Brillouin scattering (BS);[3] superconducting tunnel junction techniques (TJ) which can be used to generate both longitudinal (L) and transverse (T) acoustic phonons but only at very low temperatures;[4] picosecond ultrasonics[5,6] which is discussed in more detail in Chapter 4; and inelastic X-Ray[7,8] and neutron[9] scattering (IXS, INS). Frequently these techniques give conflicting information about the material, as shown in Figure 6.1., Also presented is the acoustic damping spectrum which has long been predicted on the basis of thermal conductivity measurements, which give an indirect measure of the phonon-material interactions as discussed in Chapter 2. The conflicts between the theory and the measurements, and the measurements with each other, have demonstrated the complexity of the nature of disordered materials.

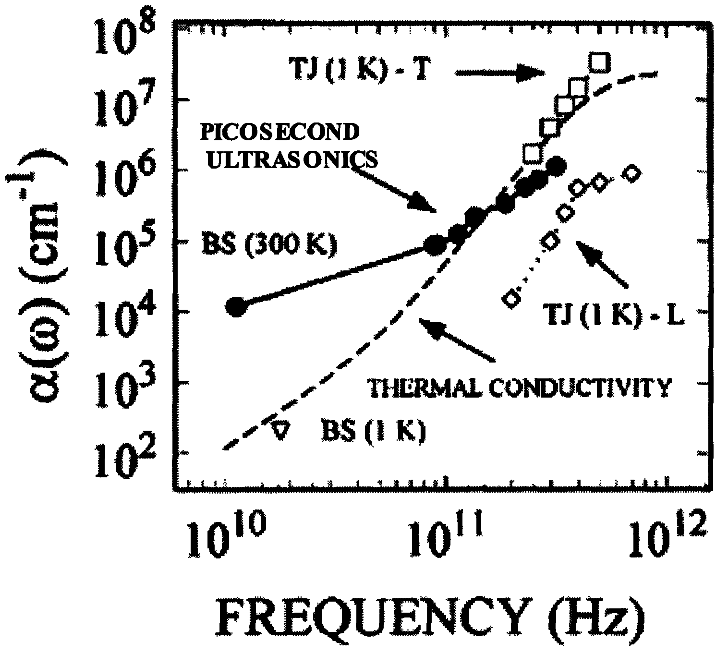

Figure 6.1. Phonon damping spectrum in PMMA obtained by various experimental techniques described in the text. Adapted from Reference 6.

This chapter presents a novel spectroscopic technique which directly and robustly gives new information in the crucial "extended" wavevector and frequency range believed to give rise to the unique bulk properties of the entire class of amorphous materials. This is done with the hope of resolving some of the conflicting results obtained in previous years, and testing the validity of the tunneling model, which is described in Chapter 2. Section 6.2 outlines many of the experimental details of the setup and samples. The optical setup, very briefly described in Section 6.2.1, is comprised of the novel ultrafast "Deathstar" pulse shaper used to generate narrowband acoustic waves of tunable frequency throughout the range 1-1000 GHz, which is discussed in much greater detail in Chapter 4, and the "grating interferometer" detection scheme, described in Chapter 5. Section 6.2.2 specifically addresses non-optical experimental considerations, such as the design, fabrication, and characterization of the sample, which influence the experimental results (and the ability to obtain results at all) in important ways. A discussion of the method of data analysis is presented in Section 6.2.3.

In Section 6.3 new spectroscopic details in the "extended" range of silica glass, obtained with this technique, are presented. This material is chosen as a starting point for the study of disordered materials in general, as it has been studied more extensively than any other since the field's inception.[10] The availability of literature data on its thermal and elastic properties makes it easy to evaluate the effectiveness of the Deathstar technique relative to others, and to compare with the results of long-standing models. Data between 50 and 300 GHz, between high (300 K) and low (20 K) temperatures, are presented in an attempt to separate the dynamical and structural contributions to the acoustic spectrum as much as possible within the current experimental constraints. The 294 K spectrum is compared to the only other spectrum available in the literature, and the 20 K spectrum is compared to the results of the tunneling model described in Chapter 2, as no data in this frequency range at low temperatures is available in the literature. Lastly, in Section 6.4 the results are summarized, and some new directions of the research are briefly discussed.

6.2 *Experimental Details*

6.2.1 *Optical Setup*

The generation of acoustic waves in the 1-1000 GHz range is accomplished by way of a novel ultrafast pulse shaper called the "Deathstar," which is described in detail in Chapter 4. Optical pulse trains of tunable frequency are used to irradiate thin aluminum films, which rapidly expand, generating acoustic waves through the plane of the film. The acoustic wave travels out of this film and into the material of interest, here a thin film of either silica glass or a polymer, where it propagates with damping rate $\alpha(\omega,T)$ and velocity $v_s(\omega,T)$. The values of these parameters are modulated by interactions within the material, and the identification of these interactions is the goal of this Chapter. After propagation through the sample, the acoustic wave propagates into a second aluminum film, where it is detected by a reflection mode grating interferometer as described in Chapter 5. By varying the Deathstar frequency, the acoustic spectrum may be determined for a material one frequency at a time.

6.2.2 *Fabrication, Characterization, and Design of Samples*

Several samples were employed in order to demonstrate both the wide applicability of the Deathstar narrowband acoustic technique, as well as to explore the common microscopic features of different classes of disordered solids. For a particular material, several samples of different thicknesses were fabricated in order to greatly simplify data analysis. For the study of silica glass, a single sample, with multiple thicknesses of the glass sandwiched between 18 nm aluminum films, was fabricated and characterized using the techniques described in Section 4.2.2, and as shown in Figure 4.5. Neal Vachhani of the Materials Science Department at MIT fabricated the polymer samples, whose preliminary results are presented in Section 6.4. His Master's thesis, *Using Narrowband Pulse-Shaping to Characterize Polymer Dynamics*, may be referred to for a more detailed discussion of the results obtained thus far, and for the considerations of fabricating ultrathin polymer samples.[11] For the study of PMMA, a number of identical sapphire substrates were simultaneously coated with a first (excitation) aluminum film via thermal evaporation. PMMA (540,000 g/mol from Scientific Polymer Products, Inc., Ontario NY, or 500,000 g/mol from Polymer Laboratories, Amherst MA), was dissolved in toluene and spin cast on top of the aluminum film. The concentration and spin rate parameters were varied as reported in Table 5.1, to obtain different thicknesses of the polymers on different substrates. After deposition the samples were annealed overnight at a temperature of 360 K. Lastly the entire set of polymer-coated substrates was coated with second (detection) aluminum film, again via thermal evaporation. The thicknesses of the aluminum, silica glass, and polymer films were measured with ellipsometry, as well as with either the single-pulse or resonant acoustic techniques described in Section 4.5, using the literature acoustic velocities for thin films of PMMA (2830 m/s), silica glass (5900 m/s), and aluminum (6420 m/s).[6] All of the material parameters used are presented in Table 4.2. The results are presented in Table 6.1. In many cases the results of the two measurement techniques were surprisingly different, as shown in the rightmost column of Table 6.1. The consistency of the difference for a given material, with a decreasing effect for thicker films, implies that ellipsometry may be relatively unreliable for the determination of very thin film thicknesses.

Material	Mol. Wt. (g/mol)	Conc. (% by wt.)	Spin Rate (rev/sec.)	Ellips. (nm)	Acoust. (nm)	% Difference
PMMA (A)	500,000	0.5	3000	15	19	27
PMMA (B)	540,000	0.5	2000	20	32	60
PMMA (C)	540,000	1.0	2000	50	77	54
PMMA (D)	500,000	3.0	2000	184	215	17
Silica (A)	60.1	---	---	97	135	39
Silica (B)	60.1	---	---	190	265	39
Silica (C)	60.1	---	---	438	480	12
Silica (D)	60.1	---	---	947	1010	7
Alum. (A)	27.0	---	---	15	23	53
Alum. (B)	27.0	---	---	50	80	60

Table 6.1. Spin coating parameters of polymer films, and ellipsometrically and acoustically measured thicknesses for all sample films.

Reference [12] assumed that for a very thin film of PMMA, 20-130 nm, the thickness measured with ellipsometry was correct. The authors then used the picosecond ultrasonics technique to find the timing of round-trip acoustic echoes within the film, and calculated the acoustic velocity using the formula,

$$\tau_{RT} = \frac{2d_{PMMA}}{v_s} \tag{6.1}$$

where τ_{RT} is the round trip time and d_{PMMA} is the thickness of the PMMA film. They found that τ_{RT} was much shorter than expected, based on the ellipsometry thickness, especially for the thinner films. This was attributed to a jump in the sound velocity from 2700 m/s in "thick" films thicker than 40 nm, to 8000 m/s for the "thin" films of 20 nm – a nearly 300% change. A perhaps more plausible explanation would be a systematic and growing error in ellipsometry for films thinner than a certain thickness threshold. If τ_{RT} is smaller than expected, then assuming the same acoustic velocity as a thicker film, the film could simply be much thinner than expected. Also using the picosecond ultrasonic technique, Reference 6 reports a smaller velocity discrepancy, on the order of 10-20%, for polymer films thinner than 40 nm, compared to what would be expected based on ellipsometry. This was observed for PMMA as well as others. Based on the round trip echo time, this could again be taken to mean that the film is thinner than ellipsometry indicates. In the case of the Deathstar method, the exact opposite case is found – that the acoustically measured thickness is thicker than that from ellipsometry, by as much as 60% depending on the thickness of the film. Based on the arguments of the authors above, using Equation 6.1 this would result in a *slower* sound velocity than that for the bulk, v_s=1770 m/s for the "20 nm" PMMA film. Taken together, there are very wide discrepancies between the "measured acoustic velocities" for ellipsometrically measured 20 nm thin films of PMMA. Between References 6 and 12, as well as the current measurement, a variation of ~6200 m/s using *similar* acoustic techniques exists. The results suggest, somewhat circumstantially, that very thin films are not measured accurately (or even with a monotonic error) by ellipsometry. The authors of Reference 6 choose to use Equation 6.1 to calculate the thicknesses of thin films, using the "thick film" acoustic velocity and the measured acoustic round trip time. This is also done here for all of the films, due to the dubious reliability of ellipsometry for this purpose. It is possible that complications arise from the combination of thin polymer and metal layers, whose partial reflections give rise to interferences that must be treated with considerable care.

The values of the reflection and transmission coefficients described by Equations 4.12, 4.13, and 4.14 in Section 4.4, are also important parameters for the success of the measurements, because they determine the amount and form of the signal measured after propagation through the multilayer sample. For the silica sample, the difference in acoustic impedance $Z=\rho v$, listed in Table 4.2, between the aluminum and the glass is small: $Z_{Al}=17\times10^6$ kg m^{-2}s^{-1}, $Z_{silica}=13\times10^6$ kg m^{-2}s^{-1}. This leads to a large transmission coefficient from the silica glass into the aluminum film, t=0.87, yielding large signals. After the wave reaches the air-aluminum interface it reflects completely with phase inversion r=-1.0, and travels back towards the aluminum-sapphire interface where it is mostly transmitted, t=1.13, with a small partial reflection back into the aluminum film, r=0.13. In the case of the polymer samples the situation is drastically different, Z_{PMMA}=3.3x10^6 kg m^{-2}s^{-1}, leading to a much-reduced transmission coefficient into the aluminum t=0.32. The only way of addressing this issue is to average the data longer. A less tractable problem than weak signal is a persistent echo inside the aluminum film, due to the large impedance mismatch with the PMMA. The reflection coefficient for the wave traveling from the aluminum back to the PMMA is r=0.67, trapping much of the energy inside the aluminum and resulting in a "ringing" of the film, which smears out the original acoustic response. This is problematic for broadband (i.e. single-pulse) measurements where the shape of the waveform transmitted to the sample is crucial to the analysis. For the narrowband measurements it is somewhat less destructive as the magnitude of the total transmitted amplitude is the important quantity. This problem was addressed by sometimes adding an additional coating of aluminum to the aluminum film, to make the time it took the aluminum reflection longer than the time it took for the original signal inside the PMMA to be recorded. In general, it may be best to seek a more suitable transducer material to optimize transmission into polymer films while retaining good photoacoustic bandwidth.

6.2.3 Acoustic Analysis

The damping coefficient and velocity of a high frequency acoustic wave may be easily determined using the current technique and samples by observing the changes in amplitude and temporal delay accrued by the wave upon propagation through two different thicknesses of the material of interest, in otherwise identical samples. This method allows the measurement of material parameters while making *no assumptions* about any components of the sample, as the only difference experienced by the wave between the two measurements comes from the thickness difference. In this case the damping at a given measurement frequency ω_0 is given by:

$$\alpha(\omega_0) = \frac{1}{d_B - d_A} \ln \left| \frac{I_A(\omega_0)}{I_B(\omega_0)} \right| \qquad 6.2$$

where d_A and d_B indicate the thicknesses of the thinner and thicker films of the material of interest, and I_A and I_B are the amplitudes of the corresponding spectral peaks in the Fourier transform of the time-dependent signal. The acoustic velocity may be determined by:

$$v(\omega_0) = \frac{d_B - d_A}{\left[\tau_B(\omega_0) - \tau_A(\omega_0)\right]} \qquad 6.3$$

where τ_A and τ_B are the temporal delays of the acoustic wave through the two layers. Modest errors in the thickness values of the disordered materials will add a constant offset value via Equations 6.2 and 6.3 to the acoustic spectra discussed in Section 6.3, but will not change the frequency dependence of the result, which is the most important feature of the acoustic spectrum. Error in the aluminum thickness will alter the acoustic bandwidth, as discussed in Section 4.3, but is irrelevant to the current results so long as both the thick and thin samples are coated with identical aluminum films. For thin polymer samples, the properties of the material may be influenced at and near the interface regions of the multilayer sample; the use of thicker samples will minimize this effect.

6.3 Results for Silica Glass

In this section, selected raw and processed data obtained from measurements throughout the 50-300 GHz frequency range will be presented as a way of illustrating the process of constructing the acoustic spectrum and of revealing the behavior of silica glass in different frequency and temperature ranges. The preferred method of data analysis is without assumption of any material parameters or models, using Equations 6.2 and 6.3, and results on this basis are always taken as the most reliable. The acoustic mismatch model for propagation through the multilayer sample can then be useful to confirm whether the experimentally determined damping coefficient describes the behavior of individual data sets from different thickness samples.

6.3.1 Room Temperature Spectrum

As shown earlier in Figure 4.26, the amplitude of an acoustic wave at two different sample thicknesses may be used to determine the damping constant. As shown Figure 6.2 (a) and (b), tuning of the Deathstar pulse shaper allows the acoustic responses at different frequencies to be compared readily as well. As before, the strain is calculated by taking the time-derivative of the displacement data, using Equation 4.3. The values of the displacement and strain are not routinely calibrated on an absolute scale, but they generally lie in the same range that was discussed in Section 4.4, roughly a few tenths of a nanometer displacements and a few percent strain. The transmitted wave at 150 GHz exhibits clear oscillations, however the scan at 300 GHz shows far stronger damping over the propagation length. Determining the frequency dependent damping constants at room temperature is the goal of this section; the results will be compared to the only other spectrum in this frequency and temperature range found in the literature.[5,6] In Section 6.3.2 the frequency dependent damping at 20 K will be presented, and compared to the tunneling model described in Chapter 2, as no other acoustic spectrum in this frequency range, and below 80 K, can be found in the literature.

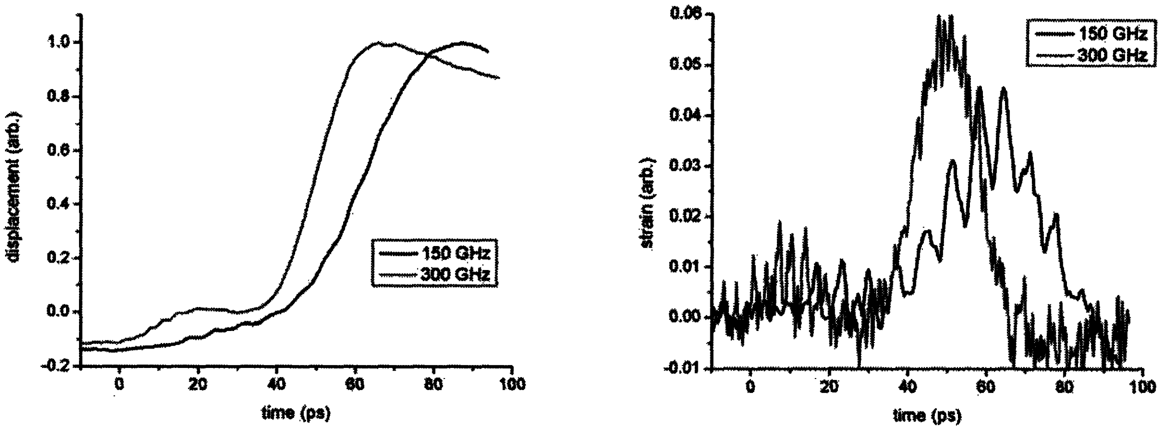

Figure 6.2. Transmitted acoustic waves at 150 and 300 GHz through 210 nm silica glass: (a) displacement, (b) strain.

Determination of the acoustic damping coefficients for multiple frequencies, sample thicknesses, and temperatures requires careful acquisition and processing of the data, in order to ensure that the difference in spectral amplitudes between measurements on different samples or different sample regions may be accurately compared. Because each scan takes a fairly long time to acquire, between 15 minutes to 1 hour depending on the scan length and resolution (with at least 10 time steps required to resolve each acoustic cycle), the determination of the entire spectrum using multiple thicknesses of films can take several days. Over this time the laser power may fluctuate by up to 10%, and even the optical alignment can shift slightly. Therefore the data need to be normalized to a consistent standard. The data presented in Figure 6.3, which are scans with the excitation frequency at 200 GHz and with propagation through three thicknesses of silica glass, were collected over the span of four days. As discussed in Section 4.4, a small amount of probe light leaks through the receiving aluminum film and observes the excitation process of the sample at a time of zero picoseconds. This signal contribution persists while at some later time, starting around 50 ps for the 210 nm sample, around 90 ps for the 480 nm sample, and 170 ps for the 1000 nm sample, the propagating wave arrives at the back of the sample. The displacement corresponding to this initial contribution is subtracted, so that the rise in the displacement caused by the propagating wave begins with an amplitude of zero. Then the signals are normalized, which is accurate assuming that the transmission of the low-frequency envelope which dominates the signal (about which the narrowband wave oscillates) will be the same for excitation at the same frequency through different films. The validity of this procedure is supported by the results of measurements conducted in succession on different SiO_2 layer thicknesses, which consistent give nearly identical signal levels for the acoustic wave envelope. As seen in Figure 2.9, the expected damping rate for waves of frequencies less than 10 GHz is less than $1\text{x}10^4$ m^{-1}, yielding an amplitude reduction of only 1% for propagation through 1 μm of glass. The data shown in Figure 6.3, and all following data, have been processed in this manner.

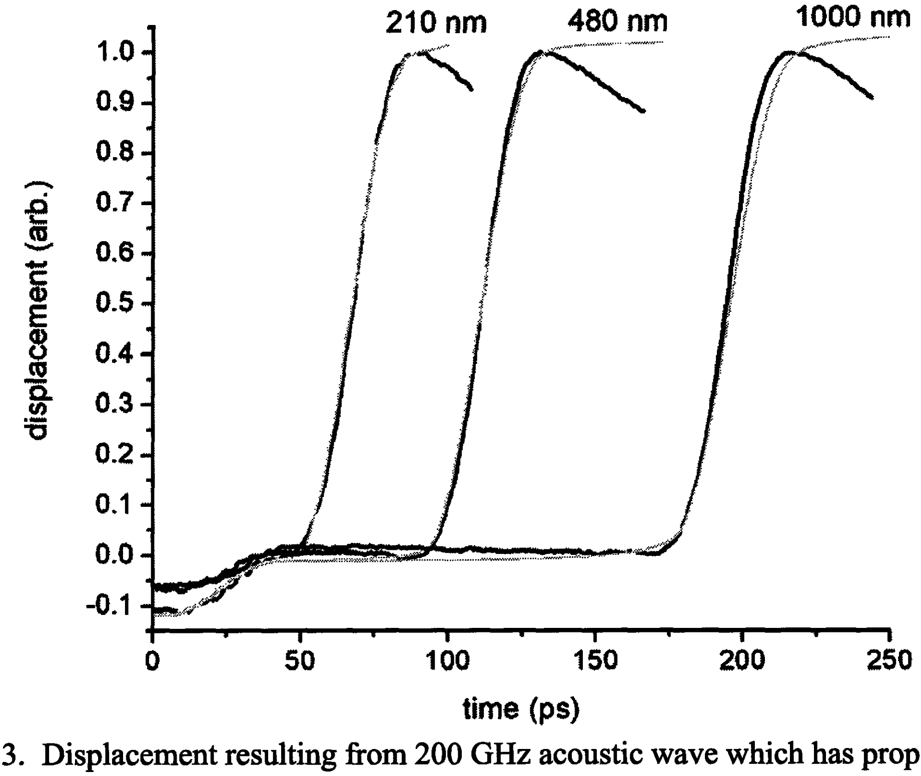

Figure 6.3. Displacement resulting from 200 GHz acoustic wave which has propagated through 210, 480, and 1000 nm of silica glass. Black lines are data with baseline subtraction and normalization as described in the text. Grey lines are simulations using acoustic mismatch model described in Section 4.4, with damping constant of $3.0\text{x}10^6$ m^{-1}.

Also shown in Figure 6.3 are simulations of the data, using the acoustic mismatch model described in Section 4.4, which will be discussed in more detail later in this section.

The acquisition of data from different thickness samples must be performed with identical resolution, and also with the same number of time points. The latter requirement is not always practical, since for the thickest samples the times of propagation may be very long, with little content before the arrival of the transmitted wave. To avoid extended scans, the transformed strain data may be zero-padded in order to match the lengths of the time scans, as shown in Figure 6.4 (a) for scans at 200 GHz through 210 and 480 nm of glass. The time axis of the shorter scan is extended to match that of the longer scan, and assigned a strain value corresponding to that of the final value of the original scan. The presence of a somewhat sharp feature at this time is unimportant, because only a narrow temporal range is eventually selected for Fourier transformation, as shown in Figure 6.4 (b). Only the signal corresponding to the transmitted wave is transformed, in order to minimize contributions of high frequency noise (as can be seen at times after 140 ps in Figure 6.4 (a) to the spectrum.

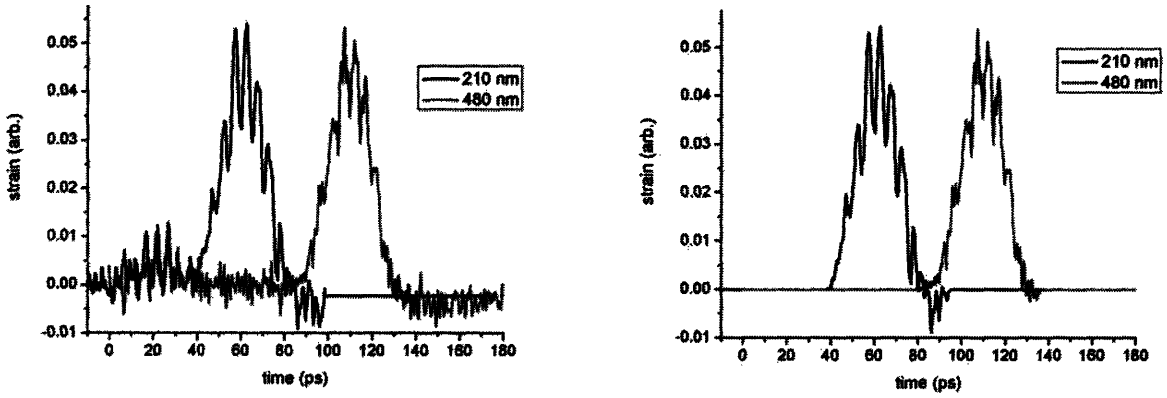

Figure 6.4. (a) Zero-padding of strain data to ensure identical spectral content of Fourier transforms of two data sets. (b) Cropping of extraneous data to minimize noise at frequency of interest. Data sets are 200 GHz through 210 and 480 nm of silica glass

The Fourier transformed spectra from scans through 210 and 480 nm of glass, processed as shown in Figure 6.4 (b), are shown in Figure 6.5. As previously, the spectra contain a comparable amplitude low-frequency component, and here it becomes apparent that this component experiences little if any damping over these propagation lengths. The spectra show a distinct peak at the driving frequency of the scan, and very little noise at other frequencies. From the ratio of the amplitudes of the peaks shown here, $I_{210}(\omega_0)/I_{480}(\omega_0) = 1.67$, using Equation 6.2 a damping rate of α=2.0x10^6 m^{-1} is determined. The spectra resulting from Fourier transformation of 480 and 1000 nm samples, processed identically, are shown in Figure 6.6. It should be noted that in this case the 480 nm scan was zero-padded to match the length of the 1000 nm scan, to yield the same resolution in both scans. All of the data were handled as similarly as possible, so their resulting spectral peak amplitudes could be accurately compared. It is still seen that the low-frequency amplitudes for both spectra are similar, and that there is little other content aside from the response at the driving frequency, though the noise in the 1000 nm spectrum is beginning to approach the level of the peak at 200 GHz. In this case $I_{480}(\omega_0)/I_{1000}(\omega_0) = 2.41$, yielding a damping constant of α=1.7x10^6 m^{-1}, which agrees fairly well (within 20%) with that measured in the thinner pair of samples. These values, along with the results at a few other frequencies where data could be obtained from three different thickness samples, are presented later in this section, Table 6.2. Ideally a large number of different samples would be available, and would allow for extremely accurate determination of the transmitted amplitude as a function of thickness.

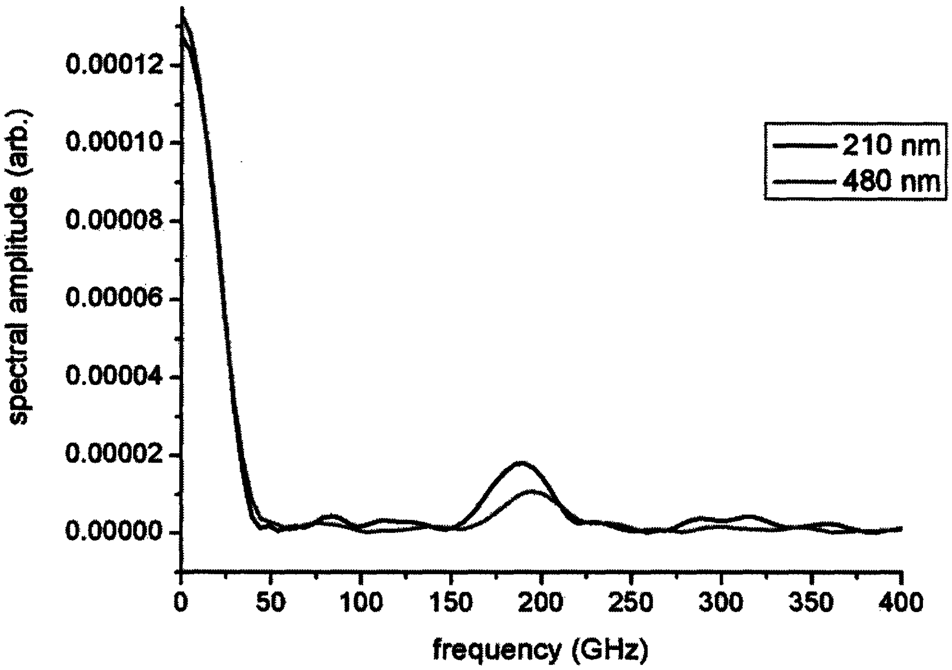

Figure 6.5. Spectra of 200 GHz acoustic waves transmitted through 210 and 480 nm of silica glass, following the processing described in this section. By taking the ratio of the peaks a damping rate of 2.0x10^6 m^{-1} is obtained.

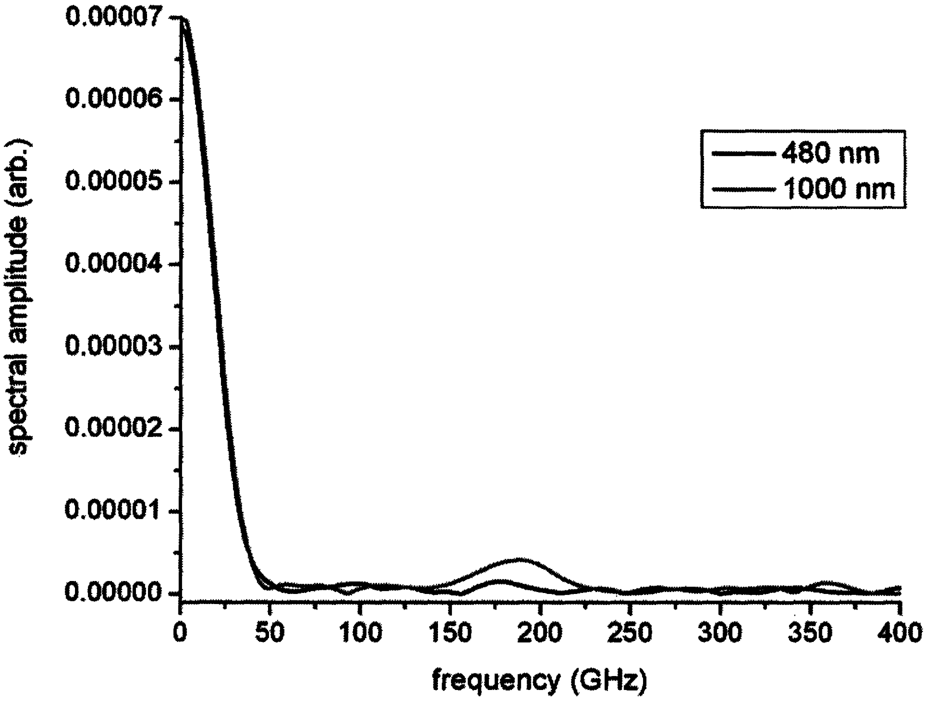

Figure 6.6. Spectra of 200 GHz acoustic waves transmitted through 480 and 1000 nm of silica glass, following the processing described in this section. By taking the ratio of the peaks a damping rate of 1.7x10^6 m^{-1} is obtained.

Using the acoustic mismatch model described in Section 4.4, with the output from the TTM described in Section 4.3 used as the acoustic input to the model, the scans may be simulated using the measured damping rate. Here it was found that a damping rate of 3.0×10^6 m^{-1} fit all of the data scans quite well, which is somewhat larger than that measured via the data itself. This implies some small error in the parameters in the model, which is reduced at lower frequencies. The simulations to the displacement data for the three films were already presented in Figure 6.3, however it can be more illuminating to examine the strain traces which emphasize the oscillations resulting from the narrowband acoustic wave. Figure 6.7 shows the result for propagation through 210 nm of silica glass, Figure 6.8 for propagation through 480 nm, and Figure 6.9 for propagation through 1000 nm. The depth of modulation in the simulations can be seen to be quite similar to the depth of modulation of the data. As shown later in this section, the discrepancies between the measured damping values and the best-fit values using the acoustic mismatch model vary somewhat with both frequency and temperature, suggesting a rather subtle error in one of the adjustable parameters of the two-temperature model, compared to the actual properties of this sample. In all cases the errors were modest, and generally support the support the spectra obtained based on analysis of the raw data.

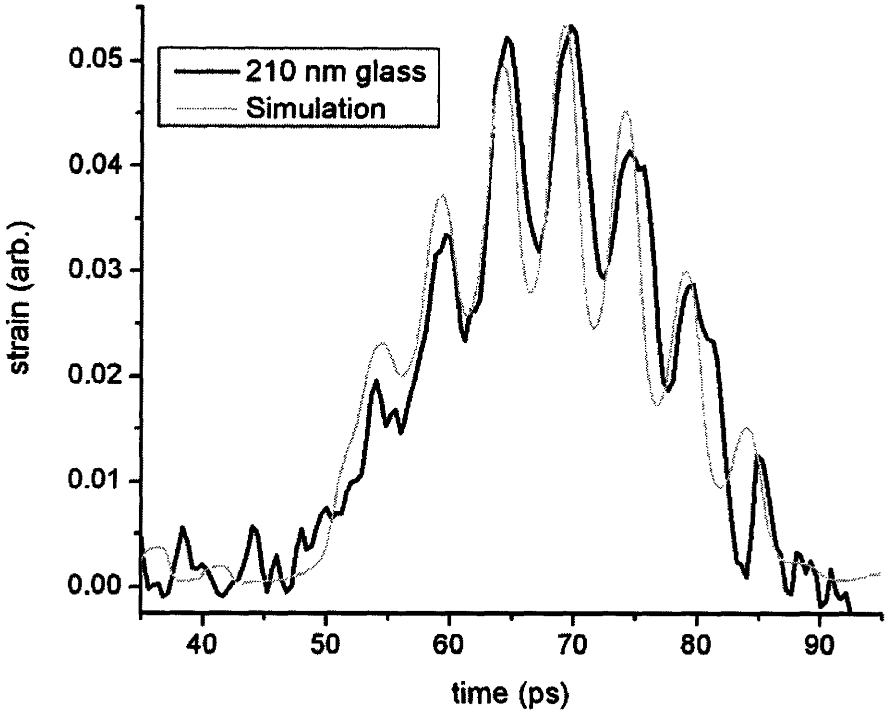

Figure 6.7. Strain resulting from 200 GHz acoustic wave which has propagated through 210 nm of silica glass. Black line is data with processing as described in the text. Grey line is simulation using acoustic mismatch model (Section 4.4) with damping constant of 3.0×10^6 m^{-1}.

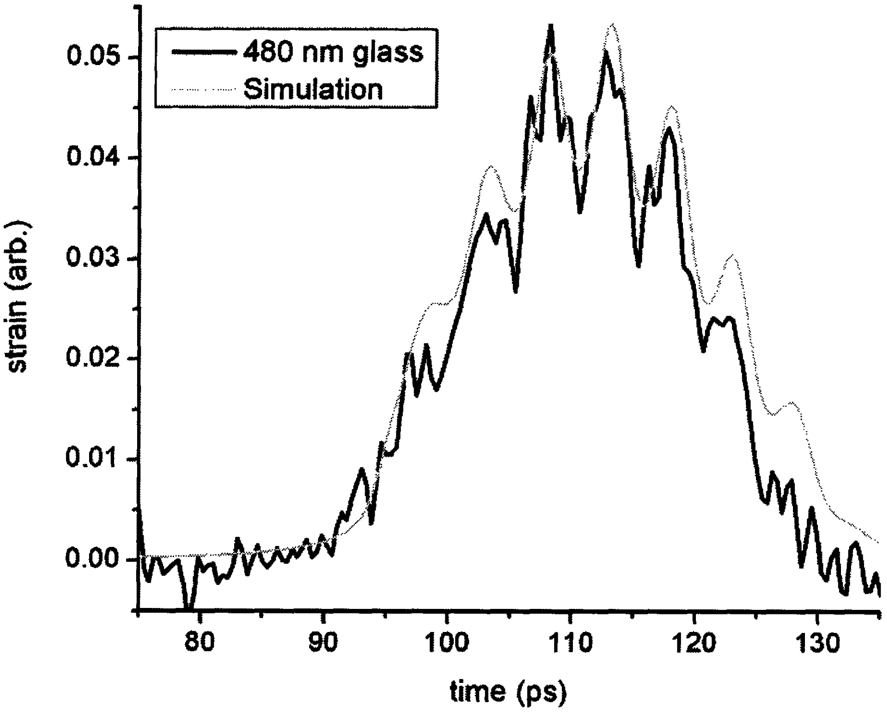

Figure 6.8. Strain resulting from 200 GHz acoustic wave which has propagated through 480 nm of silica glass. Black line is data with processing as described in the text. Grey line is simulation using acoustic mismatch model (Section 4.4) with damping constant of 3.0×10^6 m^{-1}.

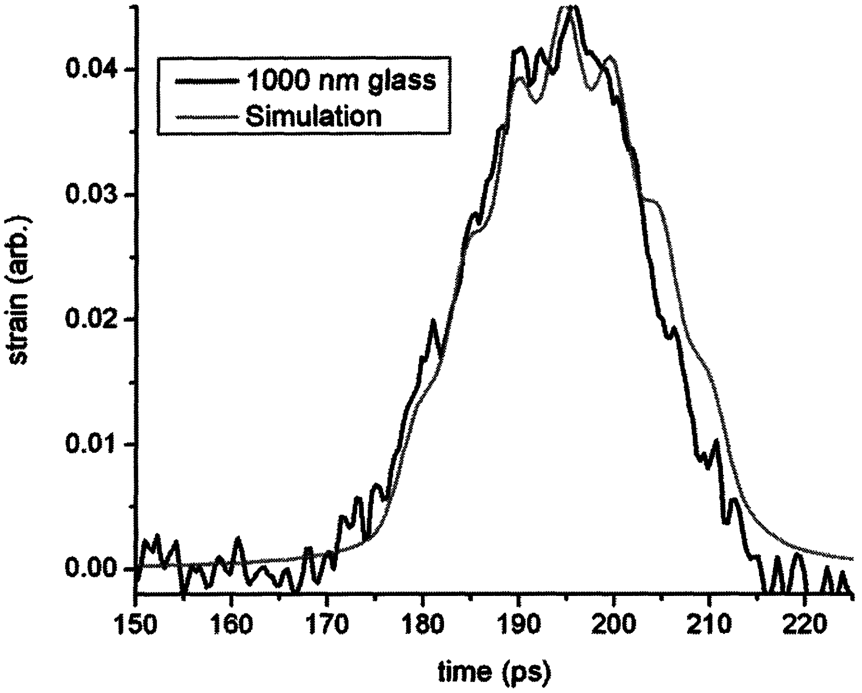

Figure 6.9. Strain resulting from 200 GHz acoustic wave which has propagated through 1000 nm of silica glass. Black line is data with processing as described in the text. Grey line is simulation using acoustic mismatch model (Section 4.4) with damping constant of 1.9x10^6 m^{-1}.

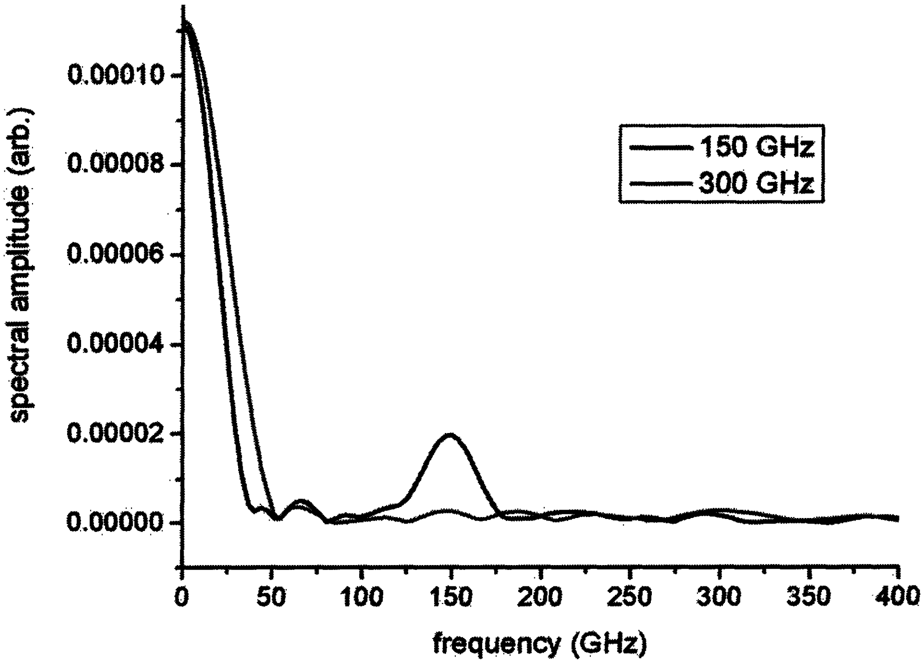

Figure 6.10. Spectra of 150 GHz and 300 GHz acoustic waves transmitted through 210 nm of silica glass. Amplitude of peak at 300 GHz is approaching the noise floor.

To construct the acoustic spectrum, this procedure is repeated for as many frequencies at which it is possible to collect data that can be analyzed. At the highest frequencies, this is limited by the noise floor in the Fourier transforms. As shown in Figure 6.10, the Fourier transformed spectra of the data shown in Figure 6.2 for transmission of 150 GHz and 300 GHz acoustic waves through 210 nm of silica glass, the peak at 300 GHz is very weak compared to that at 150 GHz. The intensity following propagation through 480 nm is yet substantially weaker, and through 1000 nm is non-existent. In order to measure the damping coefficient as accurately as possible for the highest frequencies, only the thinnest samples were considered. Fabrication of much thinner samples than used in this thesis could enable the spectrum to be extended at least up to 440 GHz, and use of a "next generation" excitation transducer such as a quantum well[13] could allow access up to or exceeding 1 THz, where the propagation of an acoustic wave would be expected to fail entirely.

For the measurements at lower frequencies, a different problem presents itself. As shown in Figure 6.11 for the displacement, and Figure 6.12 for the strain, for scans with excitation at 125 GHz in samples of 480 nm and 1000 nm of silica glass, after the optical excitation is complete there is some amount of time during which the acoustic wave propagates before arrival at the back of the sample. However for the scan in the 210 nm sample, the optical excitation is not yet complete before the acoustic wave arrives at the back of the sample. This results in an additional complication to the data analysis. First, the background subtraction of the optical input signal contribution is made more difficult because the final value of the contribution is subsumed by the acoustic signal. This was compensated for by estimating the background level based on scans at slightly higher frequencies, and could result in perhaps a 5% variation from the actual value. Second, the choice of a proper window within which to perform the Fourier

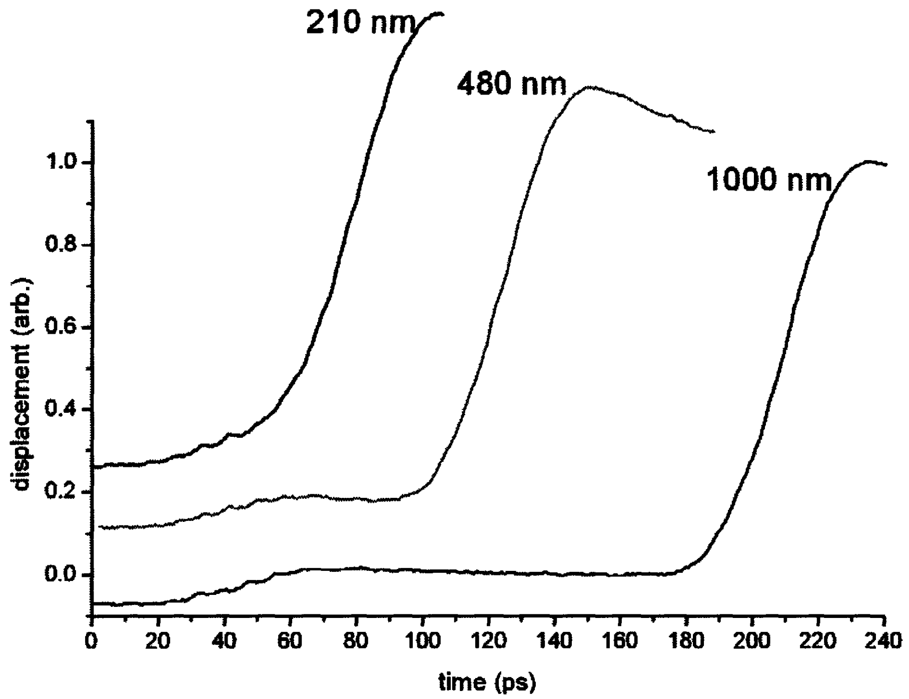

Figure 6.11. Displacements resulting from excitation at 125 GHz through 210, 480, and 1000 nm of silica glass. Through 210 nm silica, the propagating acoustic wave arrives at the back of the sample before optical excitation is complete. Scans are vertically offset as an aid to the eye.

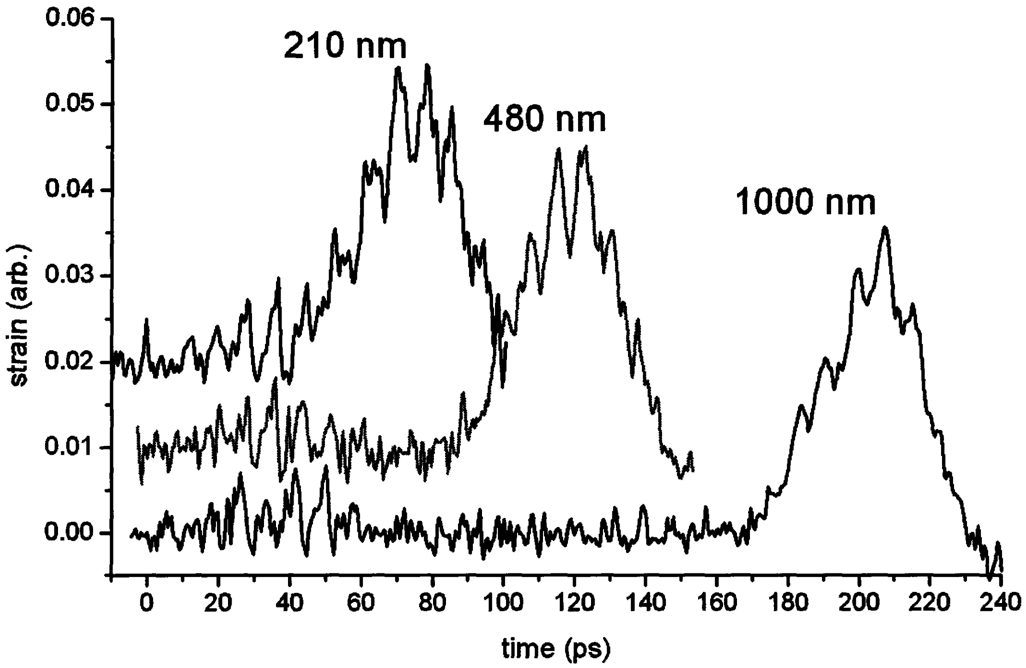

Figure 6.12. Strain resulting from excitation at 125 GHz through 210, 480, and 1000 nm of silica glass. Through 210 nm silica, the propagating acoustic wave arrives at the back of the sample before optical excitation is complete. Scans are vertically offset as an aid to the eye.

transform, as in Figure 6.4 (b) for 200 GHz where optical and acoustic overlap is minimal, is unclear. Here a window excluding any contribution from the first and second acoustic pulses was chosen for *both* the signal from the 210 nm and 480 nm samples, to ensure that the comparison of spectral amplitudes is as reliable as possible.

The Fourier transforms of the 210 and 480 nm signals shown in Figure 6.12 following the processing described in this section, are shown in Figure 6.13 (a) for a transformed window 55 ps long, and in (b) for a window 50 ps long, with the extra time removed from the leading edge of the acoustic waveform. The ratio $I_{210}(\omega_0)/I_{480}(\omega_0)$ at ω_0=125 GHz between the peak amplitudes increases fairly significantly, from 1.02 for the 55 ps window (a), to 1.17 for the 50 ps window (b). It is clear that at relatively low acoustic frequencies and in relatively thin SiO_2 layers, the partial temporal overlap of signal contributions from the front and back aluminum layers leads to an uncertainty in the acoustic Fourier amplitude on the order of 10%. In this case that is prohibitive since the total amount of damping in the thin layer is on the same order. It is plainly apparent in Figure 6.12 that the acoustic amplitude varies very little between the 210 and 480 nm samples. Thus in the present sample, damping rates at low frequencies were determined using data from the thicker layers only. In these data there is no temporal overlap between front and back signal contributions, and there is more damping so the damping constant values are less sensitive to slight changes in the data analysis. Note that the problem of overlap can be eliminated in the future through the use of a slightly thicker aluminum layer as the "receiver" transducer, substantially reducing the transmission of probe light and therefore reducing or eliminating the signal contribution from the "transducer" film at front of the sample. Some regions of the receiver film could be left thin or eliminated entirely so that the arrival times of the excitation pulses could be observed when needed and the proper position of t = 0 on the time axis

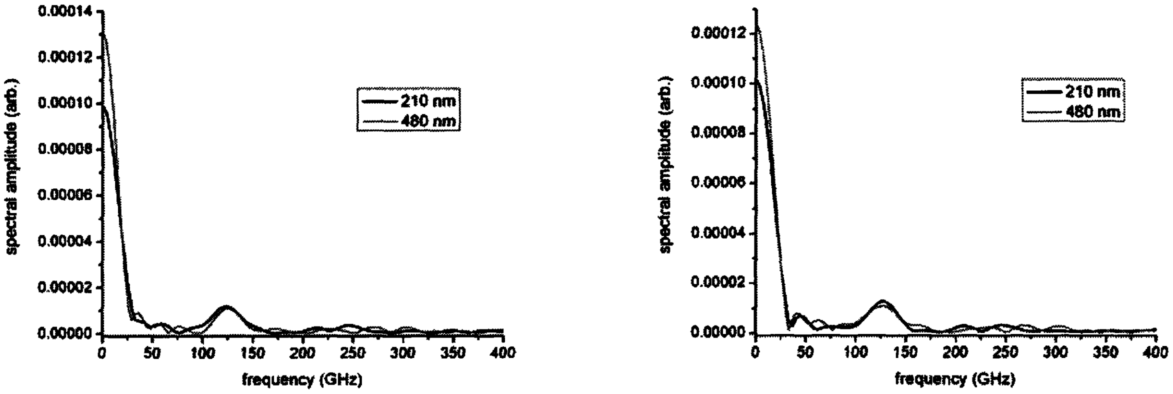

Figure 6.13. Fourier spectra of scans at 125 GHz through 210 nm and 480 nm of silica glass, using temporal windows of (a) 55 ps and (b) 50 ps. The ratio $I_{210}(\omega_0)/I_{480}(\omega_0)$ is (a) 1.02 yielding α=7.3x10^4 m^{-1}; (b) 1.17 yielding α=5.8x10^5 m^{-1}.

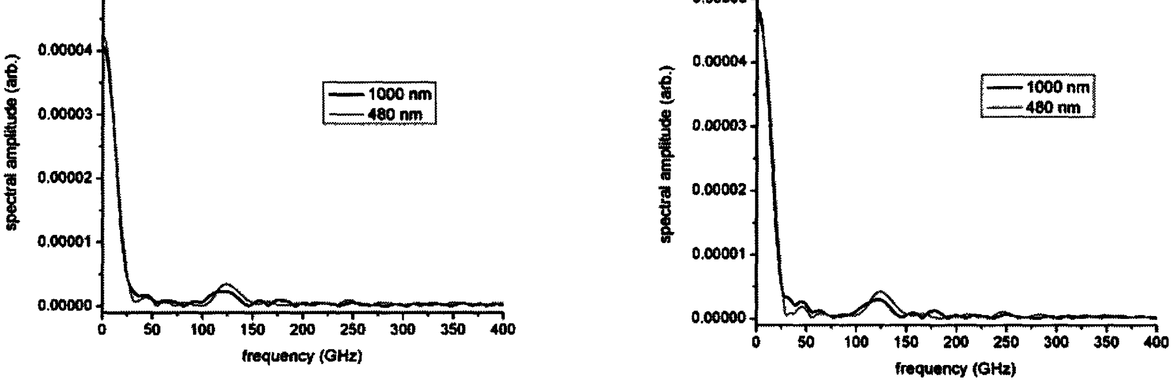

Figure 6.14. Fourier spectra of scans at 125 GHz through 480 nm and 1000 nm of silica glass, using temporal windows of (a) 100 ps and (b) 80 ps. The ratio $I_{480}(\omega_0)/I_{1000}(\omega_0)$ is (a) 1.45 yielding α=7.1x10^5 m^{-1}, and (b) 1.41 yielding α=6.6x10^5 m^{-1}.

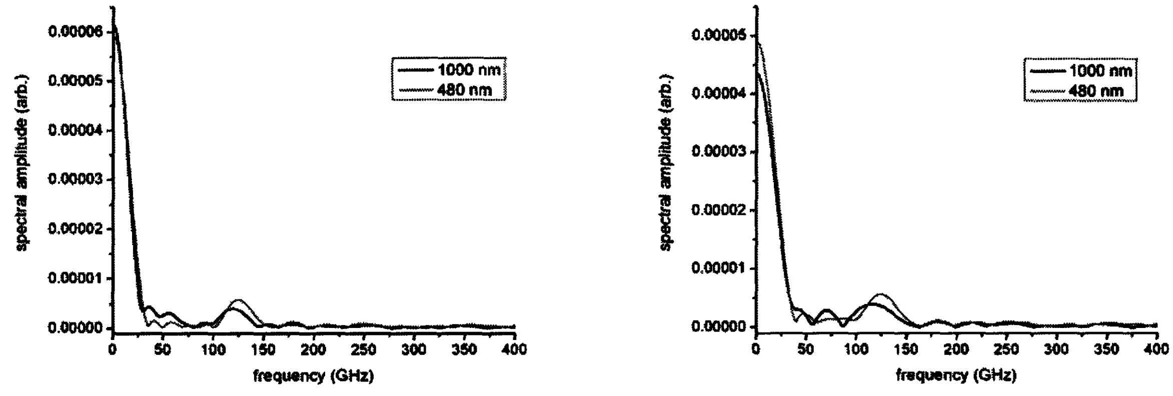

Figure 6.15. Fourier spectra of scans at 125 GHz through 480 nm and 1000 nm of silica glass, using temporal windows of (a) 55 ps and (b) 50 ps. The resulting ratio $I_{480}(\omega_0)/I_{1000}(\omega_0)$ is 1.44 for *both* (a) and (b), resulting in a damping rate α=7.0x10^5 m^{-1}.

could be established as in the present measurements. A slightly thicker "receiver transducer" film layer would also be helpful, since excitation light that passes through this layer and excites the receiver layer also gives rise to signal at short times.

Fourier transforms from the 480 nm and 1000 nm scans shown in Figure 6.12 are shown in Figure 6.14. Because the data scans were much longer and there is no temporal overlap with the data from the front aluminum film, the window size chosen for the Fourier transforms could be widely varied, and the effect on the ratio $I_{480}(\omega_0)/I_{1000}(\omega_0)$ of the signal intensities could be assessed. As the temporal window size is reduced for the scans through the thicker pair of samples, as in Figure 6.14 with 100 ps and (b) with 80 ps windows, the low-frequency spectral amplitudes increase a bit. This makes sense because spectral contributions from the noisy baseline are removed with the shortened window. For these two windows, the ratio $I_{480}(\omega_0)/I_{1000}(\omega_0)$ between the peaks at ω_0=125 GHz is 1.45 for (a) and 1.41 for (b), which are within 3% of each other. This small variation is somewhat exaggerated when the damping rate is calculated from this value with Equation 6.2, to yield damping rates of $7.1\text{x}10^5$ m^{-1} for (a) and $6.6\text{x}10^5$ m^{-1} for (b), which are within 8% of each other. Reducing the window size further, as shown in Figure 6.15 (a) to 55 and (b) to 50 ps, by removing the 1st and 2nd cycles of the acoustic wave as was done for Figure 6.14 (a) and (b), results in a similar discrepancy in the low-frequency part of the spectrum. However the result for the thicker pair of films completely disagrees with what is observed in the thinner pair: there is *no change* in the ratio between the peaks. Both scans for the pair of thicker films yield a ratio of 1.44, and a damping rate of $7.0\text{x}10^5$ m^{-1}, which is within 6% of that measured upon Fourier transformation of drastically larger temporal windows. The main point is that as long as the temporal overlap between signal contributions from front and back films is avoided, and as long as there is significant damping between the two thicknesses, then measurement of the damping constant with reason accuracy is possible. The accuracy will be improved somewhat in future measurements on samples with slightly thicker aluminum films. The results of the measurements are presented in Table 6.2.

To check the damping rates measured from the thinner and thicker films in a different way, the time-domain data were simulated using the acoustic mismatch model employed earlier. This avoids the windowing problem discussed above, because the model accounts for the additional signal contributions resulting from the optical excitation of the sample, and even if the signal contributions are not predicted quantitatively, one can examine the acoustic signal from the receiver film at relatively late times, well after the signal from the front film has finished changing. For this illustration simulations were performed at a frequency of 150 GHz instead of 125 GHz as discussed above. This is because the numerical calculation of the two-temperature model acoustic waveforms that are used as the input into the acoustic mismatch model are very time-consuming, and at the time of this publication had only been generated at 100, 150, 200 GHz, etc. However the 150 GHz scan in the thinnest film also exhibits temporal overlap between the optical input and acoustic output, and the discrepancy between the measured damping in thinner and thicker films is fairly large. By adjusting the apparent damping rate $\alpha(\omega_0)$ for each SiO_2 layer thickness to match strength of the oscillations in Figure 6.16 for the 240 nm sample, Figure 6.17 for the 480 nm sample, and Figure 6.18 for the 1000 nm sample, the damping rates which fit the scans vary somewhat different for the different thicknesses. They also vary somewhat from that determined by the Fourier transform method for either pair of film thicknesses. The Fourier transform gave a result of 5.5×10^5 m^{-1} (not considered highly reliable) for the thinner pair of films, 210 and 480 nm, and 1.1×10^6 m^{-1} for the thicker pair of films, 480 and 1000 nm. Time domain fitting of the strain yielded a damping rate of 4.0×10^6 m^{-1} for the

210 nm film, 3.0x10^{6} m^{-1} for the 480 nm film, and 2.3 x10^{6} m^{-1} for the 1000 nm film. In all cases, the amplitude of the modeled strain was fit to that of the measured strain (which itself is on an arbitrary but consistent scale) by adjusting the damping constant. The fit, especially at 210 nm, requires a value of the damping constant that is quite high. This occurs because the TTM prediction for the high-frequency acoustic amplitude (relative to the low-frequency component) is far too high, and therefore strong damping in just 210 nm is the only way that the high-frequency acoustic amplitude can be reduced sufficiently to allow a good fit to the data. At higher acoustic frequencies than 125 GHz, the problem persists, but it is reduced since there is some significant damping even in 210 nm at those frequencies. Similarly, for thicker films the problem is diminished because of real damping. The values measured based on the FT analysis are presented in Table 6.2.

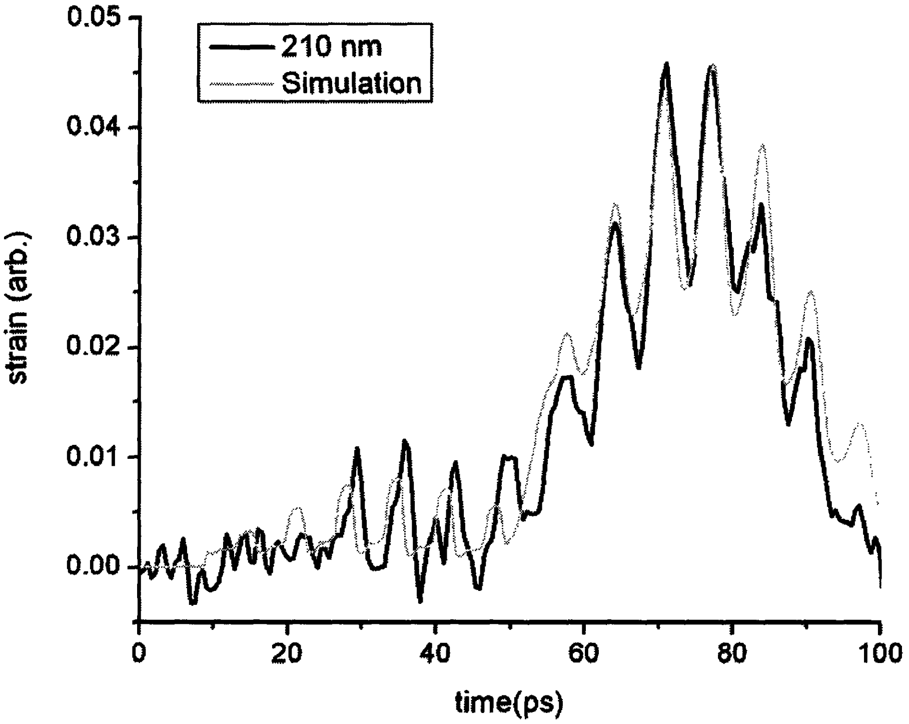

Figure 6.16. Strain resulting from excitation at 150 GHz in 210 nm of silica glass. The overlap between the 6th, and 7th pulses in the optical pulse train with the 1st and 2nd pulses in the acoustic pulse train following propagation to the back side of the sample are apparent. Also included is a fit using the acoustic mismatch model with a damping constant α=4.0x10^{6} m^{-1}.

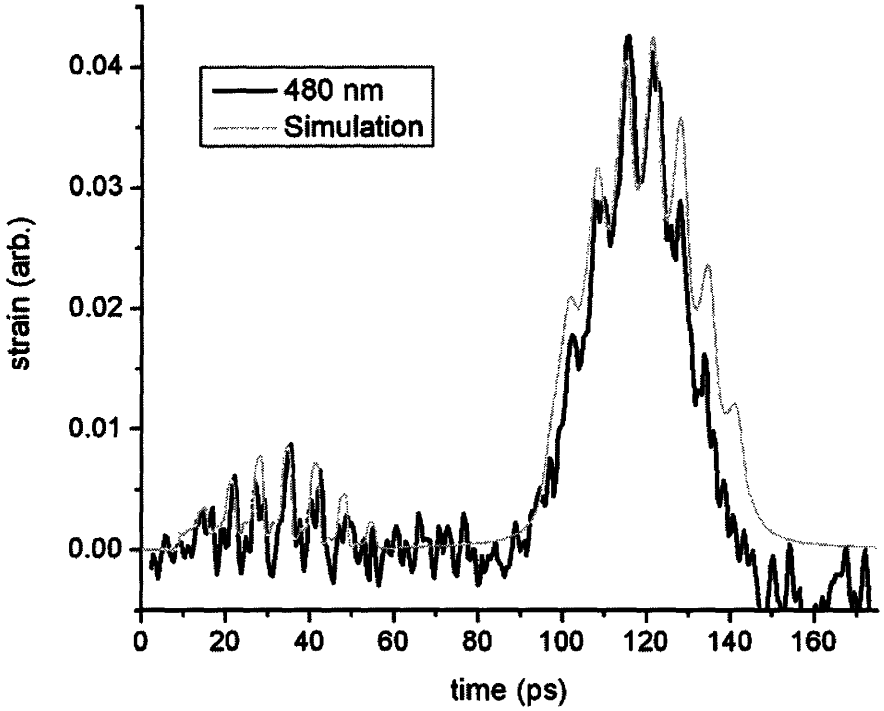

Figure 6.17. Strain resulting from excitation at 150 GHz in 480 nm of silica glass. Also included is a fit using the acoustic mismatch model with a damping constant α=3.0x10^6 m^{-1}.

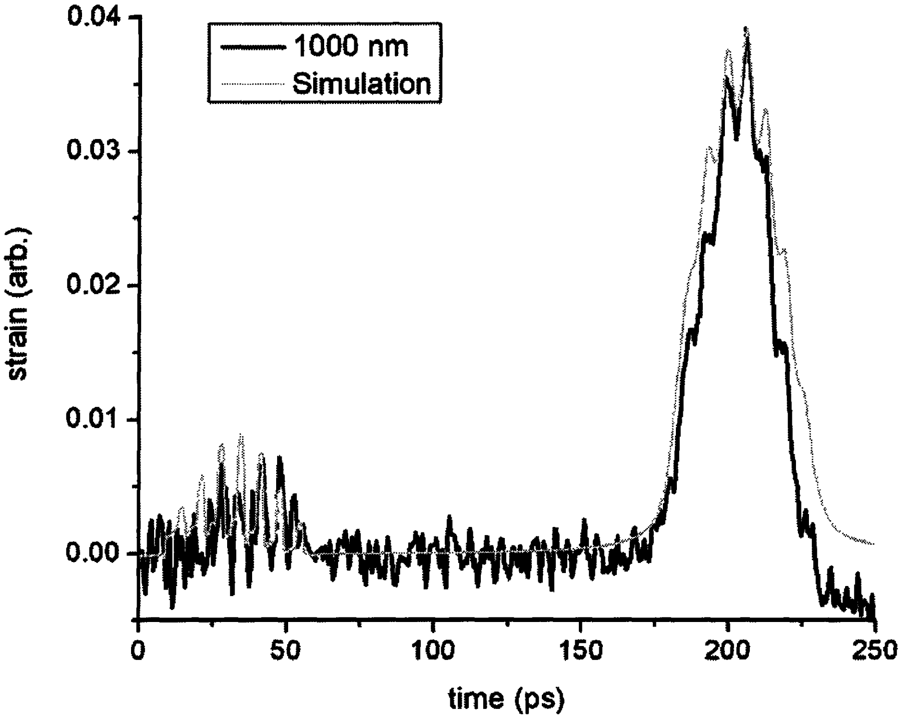

Figure 6.18. Strain resulting from excitation at 150 GHz in 1000 nm of silica glass. The optical excitation is excluded so detail of high frequency oscillations may be easily seen. Also included is a fit using the acoustic mismatch model with a damping constant α=2.3x10^6 m^{-1}.

Method	α(125 GHz), m^{-1}	α(150 GHz), m^{-1}	α(175 GHz), m^{-1}	α(200 GHz), m^{-1}
$\log(I_{210}/I_{480})/\Delta d$	2.9x10^5	5.5x10^5	1.5x10^6	1.9x10^6
$\log(I_{480}/I_{1000})/\Delta d$	6.9x10^5	1.1x10^6	1.7x10^6	1.7x10^6
Ratio	2.3	1.8	1.1	0.89

Table 6.2. Damping constants in silica glass measured at frequencies where information was available for three different thickness films. "Ratio" expresses the damping observed in the thinner film pair relative to the thicker pair

A final item of interest in the spectra is the apparent "shifting" of the peak to lower frequencies, as shown at 200 GHz in Figure 6.6 and at 125 GHz in Figure 6.14 and Figure 6.15. The meaning of this pair of results is unclear. It would certainly be expected that if the damping increases strongly with frequency, then the high frequency contributions to the relatively broad (FWHM ~ 25 GHz) would be damped more than the low frequencies as propagation increases. This would result in a "shift" to lower frequencies, which is indeed observed for the thicker films. However the frequency-dependent damping coefficients that we determine do not support this interpretation.

The acoustic spectrum determined by the techniques described in this section is presented in Figure 6.19, for the Fourier transform analysis of both the thinner and thicker pairs of data in the regimes where they are reliable as described above. The gaps in the spectrum represent frequencies where reliable information was not available due to uninterpretable Fourier transforms of the data. For example, at 75 and 100 GHz, strong echoes were seen following the arrival of the propagating acoustic wave, which may have been due to echoes inside one of the aluminum films that were stronger than expected. The scan at 75 GHz produced an extremely strong Fourier component at 125 GHz. These effects were not observed at other frequencies, and they did not correspond to any expected resonant frequencies of the films as discussed in Section 4.5. The scan at 250 GHz was overwhelmed with noise but no explanation was found. The results in the middle frequency range and overall appear to show a roughly linear increase of the damping constant with frequency, with a slope of $9.2\text{x}10^{-6}$ s/m ($\pm 1.4\text{x}10^{-6}$) using just the middle frequency range. This is a remarkable result when the results are compared to the only other acoustic spectrum for silica glass found in the literature, obtained by Maris, et al. The picosecond ultrasonics techniques they use are described in Reference 5, and the spectrum used in this chapter was taken from Reference 6. As shown in Figure 6.20, Maris, et. al., find a quadratic dependence of the damping rate on the frequency. Also included in the plot is a value at 35 GHz obtained from Brillouin scattering[14] at room temperature which yields a damping constant of $1.1\text{x}10^5$ m^{-1}.

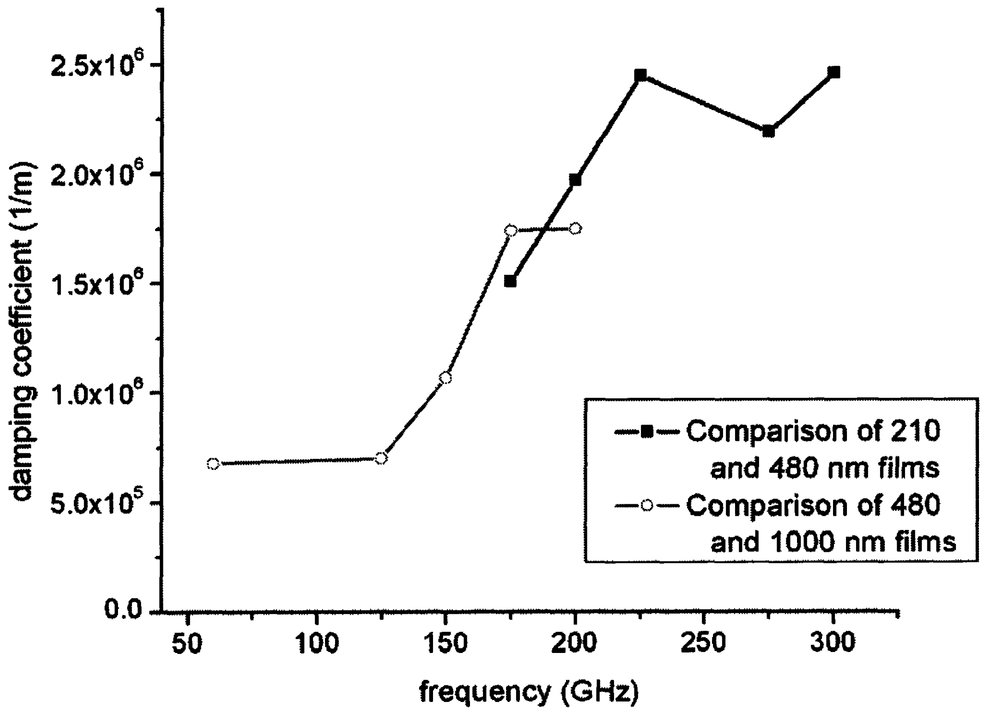

Figure 6.19. Room temperature acoustic spectrum from 50 to 300 GHz in silica glass, based on comparison of Fourier amplitudes of waves transmitted through films of different thickness.

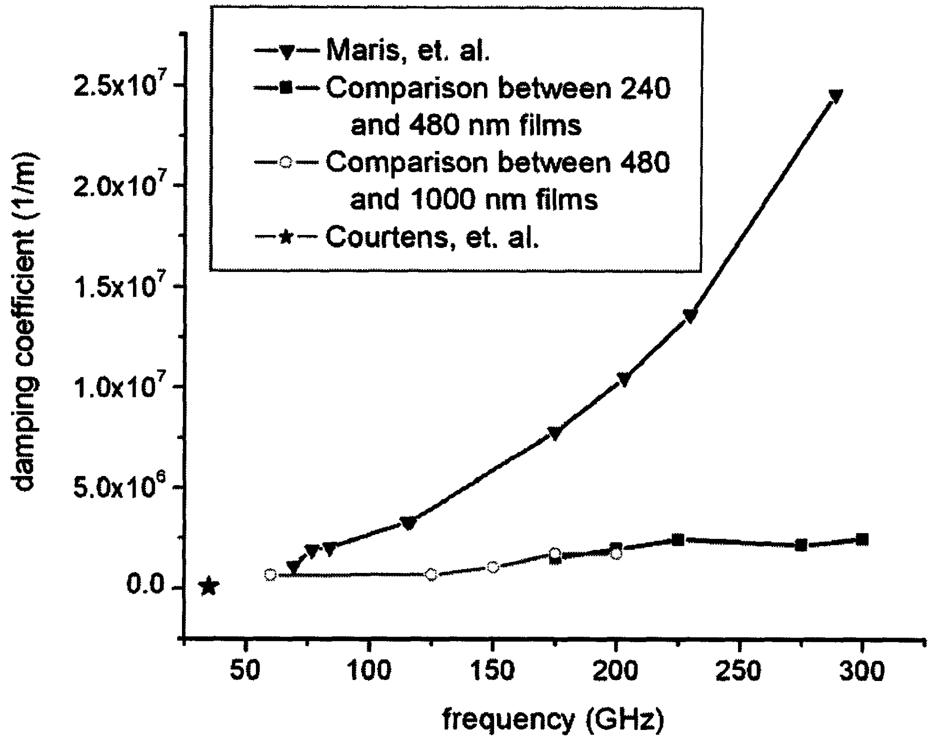

Figure 6.20. Room temperature acoustic spectrum from 50 to 300 GHz in silica glass, based on comparison of Fourier amplitudes of waves transmitted through films of different thickness. Results are plotted along with spectrum obtained by Maris, et. al., References 5 and 6, as well as a point obtained by Brillouin scattering by Courtens, et. al., Reference 14.

The dramatic quantitative difference between the results can be considered by again turning to the raw data obtained via the two techniques. For the data shown from Maris, et. al., the spectrum was measured in a sample consisting of a thin ~13 nm aluminum film, which doubles as both excitation and detection film; a layer of silica glass which was one of a few selected thicknesses between ~25 and 500 nm; and a dense tungsten substrate. The acoustic wave is generated by a single optical excitation pulse via the same processes described in Section 4.3, yielding in this case a single-cycle acoustic wave with frequency components up to ~440 GHz. The sample response is measured directly via a strain-induced change in the aluminum reflectivity of a variably-delayed probe pulse at 800 nm. Because heat generates strain in the aluminum, and detection is made at the excitation spot, a slowly-decaying thermal contribution to the signal is seen for the duration of the measurement, as shown in Figure 6.21. For the signal shown here the silica was 75 nm thick, and the measurement was made at 160 K. After generation at the air-aluminum interface, the acoustic wave propagates through the silica layer, reflects completely at the silica-tungsten interface, and returns to the excitation spot as an "echo" where it is detected as an oscillation. Each echo has two cycles, due to a small partial reflection experienced by the wave inside the aluminum film. By comparing the spectral amplitudes of subsequent echoes of a broadband acoustic wave inside the sample, as shown in Figure 6.22, the damping incurred by the acoustic wave upon propagation through twice the film thickness may be determined. The data analysis is similar to what is done in this chapter, using Equation 6.2 but performing the division of amplitudes across the entire spectrum instead of performing a frequency-by-frequency analysis. With the exception of a) the use of a single-cycle acoustic wave, and b) detection at the excitation spot using a change in reflectivity, the two experiments seem fairly comparable.

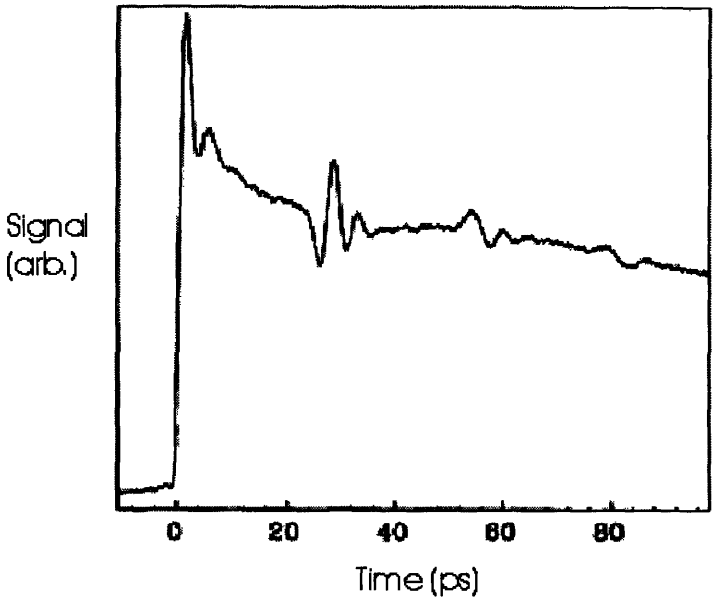

Figure 6.21. Single-pulse excitation of the aluminum-silica-tungsten assembly described in the text. Acoustic echoes return to excitation spot where they are probed via strain-induced change in reflectivity. Four echoes in the sample are apparent. Adapted from Reference 5.

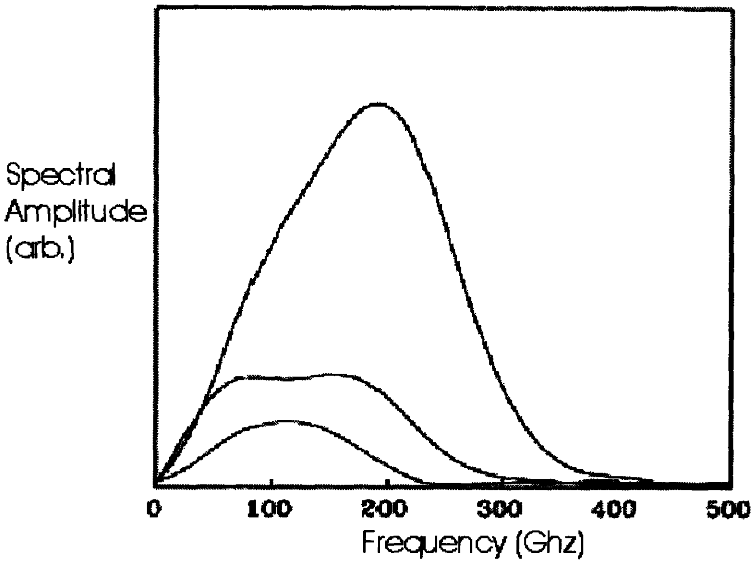

Figure 6.22. Comparison of spectral amplitudes of the three echoes seen in Figure 6.21. Adapted from Reference 5.

At a frequency of 200 GHz, Maris, et. al., determine a damping rate of $1.0\text{x}10^{7}$ m^{-1}. Assuming this damping rate is accurate, upon propagation through 1000 nm of silica glass the total transmitted amplitude would be $4.5\text{x}10^{-5}$ of the initial amplitude. In terms of our available data, the amplitude corresponding to propagation through 210 nm of silica glass may be considered an approximate "initial" amplitude. Then, the amplitude following propagation through 1000 nm of silica may be considered simply to have traveled an additional 790 nm. The expected amplitude measured at the end of the 1000 nm sample should be $3.7\text{x}10^{-4}$ of that measured at the end of the 210 sample. As shown in Figure 6.23, and earlier in Figure 6.9 with simulation, the five strongest acoustic cycles at 200 GHz appear to be resolved following transmission through the additional 790 nm of glass. Using the damping rate of $1.8\text{x}10^{6}$ m^{-1} determined by the Fourier analysis of the narrowband acoustic data presented in this section, Beer's law predicts a transmission of 24% of the initial amplitude, in reasonable agreement with the data presented in Figure 6.23 and Figure 6.24. Certainly more than 10^{-4} transmission is

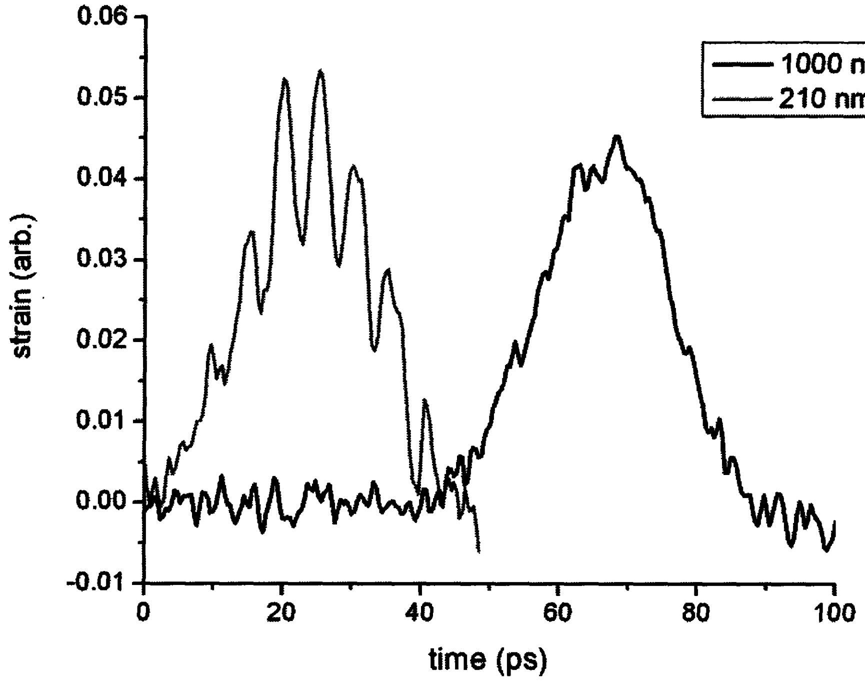

Figure 6.23. Strain in 210 nm and 1000 nm silica glass following excitation at 200 GHz. Time axis of scans have been shifted to facilitate comparison.

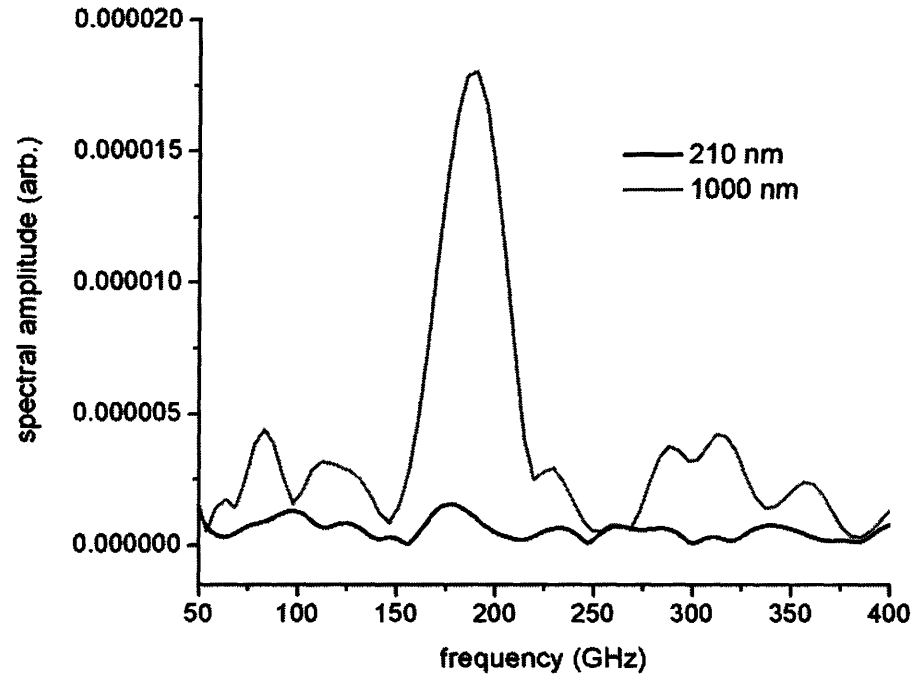

Figure 6.24. Spectra of 200 GHz excitation in 1000 nm and 210 nm films.

can be seen.

The quantity of much interest to the field of disordered materials, as discussed in Chapter 2, is the temperature and frequency dependent phonon mean free path. This may be easily computed from the measured damping rate at frequency ω_0 by:

$$\lambda_{MFP}(\omega_0,T)=\frac{1}{\alpha(\omega_0,T)} \qquad 6.4$$

The result is shown in Figure 6.25. The mean free path is roughly 1.5 μm at 60 GHz. Then it gradually decreases with increasing frequency, to a value which remains near 0.5 μm above 175 GHz.

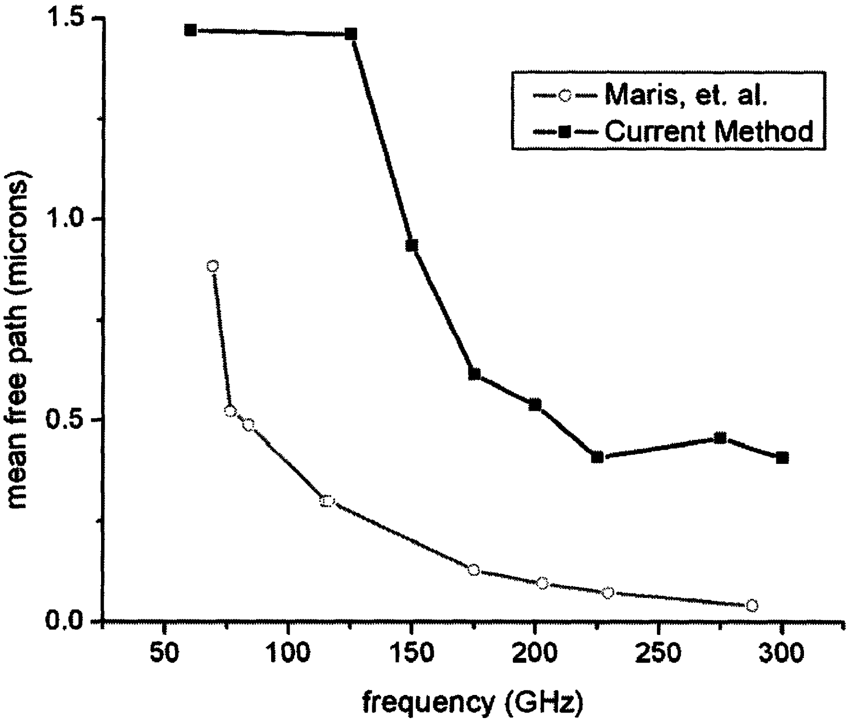

Figure 6.25. Phonon mean free path as a function of frequency. Also included are results from Maris, et. al., References 5 and 6.

The number of cycles that the acoustic wave propagates before damping by 1/*e* can give a qualitative clue to the environment the acoustic wave experiences. This is computed by:

$$\# cycles = \frac{\lambda_{MFP}}{\lambda_s} = \frac{f_s \lambda_{MFP}}{v_s} \qquad 6.5$$

where f_s is the acoustic frequency (determined by the Deathstar) and v_s is the speed of sound, here given by the literature value 5900 m/s.[5] As shown in Figure 6.26, the number of cycles stays around 20 for most of the spectrum measured with the Deathstar technique. Maris, et. al. show a number of cycles lower than 10 in all cases, and decreasing with increasing frequency. This underscores the dramatic difference both quantitatively and qualitatively between the current and previously reported results.

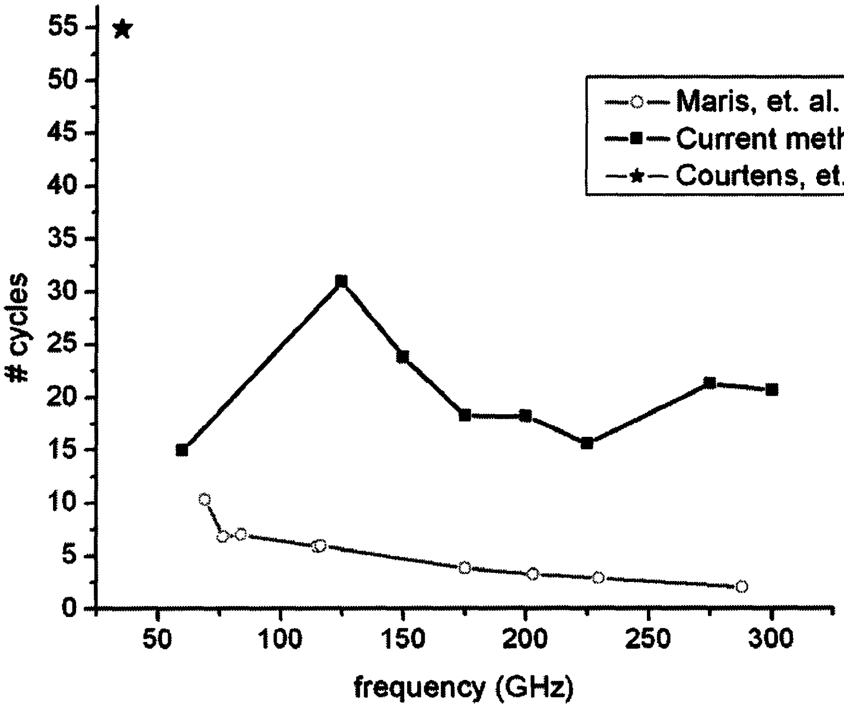

Figure 6.26. Number of cycles the acoustic wave propagates before damping by 1/*e*. Also shown are data from Maris, et. al., References and , and Courtens, et. al. Reference 14.

The surprising frequency-dependent acoustic damping rates that have been measured require a reconsideration of the mechanism for phonon scattering in disordered solids. It is clear that a Rayleigh scattering model, as suggested in Chapter 2, is entirely inadequate since over a rather wide frequency range there is nowhere near a fourth-power dependence (or even second-power dependence) of the damping on rate on the frequency. The Rayleigh scattering result is appropriate for scattering of sunlight in the upper atmosphere, where the distance between scatterers is far longer than the light wavelength. Almost surely more appropriate for scattering of high-frequency phonons in glass is a model derived from the scattering of light in turbid media. This has been an extremely active area in recent years due to applications in biological imaging, and although a simple analytical form for the wavelength dependence may not emerge, experimental and simulation results for media with varying densities of heterogeneity and varying degrees of index contrast have been reported.[15,16] It is hopeful that a model along these lines will permit rationalization of the present results and, going farther, that wavelength-dependent phonon mean free paths will yield reliable estimates for the physical properties of interest including average impedence constrast and correlation length scale.

To conclude this section, the room temperature acoustic spectrum has been determined between the frequencies of 60 and 300 GHz. The robustness of the measurement method has been demonstrated, and at the same time it has been shown to give remarkably different results than observed in the only other measurement reported in the literature – a damping rate which increases pseudo-linearly, rather than quadratically, with frequency, and whose values at the higher frequencies are dramatically lower than those reported earlier. The interpretation of these results will demand substantially revised models of phonon scattering in amorphous materials.

6.3.2 Low Temperature Spectrum

The field of amorphous materials has its origins in the low-temperature thermal anomalies measured in the early 1970's.[17] As described in Chapter 2, by analyzing the shape of the anomalous low-temperature thermal conductivity curve, a host of microscopic properties of a glass can be described – with an undetermined level of uniqueness – via the "tunneling model."[18,19] These properties are modeled to describe interactions involving the acoustic waves which carry heat through the glass, and these interactions yield the measurable bulk thermal anomalies. The microscopic details incorporated by the model include phonon-mediated tunneling between structural two-level systems below ~2 K; relaxation processes above ~2 K; and at all temperatures very strong and frequency-dependent Rayleigh scattering of acoustic waves from static structural heterogeneity. This yields a predicted acoustic spectrum, which is shown in Figure 2.9, which has its most interesting features in the frequency range from 1 GHz to 1 THz. In this frequency range, the Rayleigh scattering from inhomogeneity is predicted to dominate the spectrum at all temperatures, exceeding the strengths of all other acoustic wave-material interactions.

The most notable weakness of the tunneling model and the conventional determination of its parameters is that they rely upon upon bulk measurement of very few macroscopic parameters to characterize the results of several processes, each of which is the result of a weighted average of microscopic parameters and phonon characteristics. Nonetheless, the model has remained heavily used due to its success in reproducing many observed properties of glasses below 50 K, as shown in Figure 2.11. Above this temperature, additional interactions such as multi-phonon scattering events and the thermal saturation of the two-level systems could in some systems alter the propagation of phonons in more complicated temperature and frequency dependent ways.

The direct measurement of ultrahigh frequency acoustic phonons in this low-temperature region has not been reported in the literature. Numerous techniques have been employed to test the predictions of the tunneling model, as described in Section 6.1, but access to the relevant frequency range, in the relevant temperature range, has been exceedingly difficult to achieve. To that end, using the techniques described in the previous section, the measurements between 50 and 300 GHz were repeated in the same silica glass sample at a temperature of 20 K. This is the first acoustic data in this frequency range presented in the temperature range of the thermal conductivity plateau.

Execution of the measurements was somewhat more challenging at lower temperatures, due to a few factors. The sample was placed inside of a sample-in-vapor cryostat (STVP-100, Janis Research Company, Inc., Wilmington MA) which allowed excellent temperature control by immersing the sample in helium gas at a selected temperature. Temperatures down to 1.6 K were accessed in this manner, and originally the experiment was to be performed there. However it was found that at temperatures below 15 K, the presence of increasingly dense and turbulent helium gas created an insurmountable amount of noise in the interferometer which is used to detect the subnanometer acoustic displacements. The static phase of the interferometer, which is related to its sensitivity by Equation 5.3, could not be stabilized below ~10 K. Between 10 and 20 K, the performance improved very much, but it was found that at 20 K and above the times required to average scans to signal-to-noise were more similar to those at room temperature. For this reason the experiment was performed at 20 K; use of a sample-in-vacuum cryostat would likely yield access to measurements at lower temperatures, though access to the lowest temperatures is more challenging with this type of cryostat. For the current purposes the measurement at 20 K overlaps the high temperature end of the plateau in the thermal conductivity, as shown in Figure 2.11, and therefore should still be adequately explained by the tunneling model.

Separately, the magnitude of the acoustic strain generated by multiple-pulse irradiation of thin aluminum films is temperature dependent, as the heat capacity and thermal expansion coefficient of the metal are temperature dependent, which in principle could be problematic. However as discussed in Section 4.6 the use of a clever sample design allows any temperature or frequency dependence of the acoustic generation process to be ignored. By allowing propagation of the acoustic wave through multiple thicknesses of silica glass in an otherwise identical sample, the only relative modification to the acoustic wave occurs from the additional propagation length, as described by Equations 6.2 and 6.3 which include no other material or excitation parameters.

The acoustic spectrum at 20 K was determined by comparison of the Fourier amplitudes of acoustic waves which propagated through samples 210 and 480 nm thick. Signal at 150 GHz in the 480 nm sample is shown in Figure 6.27 along with a simulation using a damping constant of $1.5\text{x}10^6$ m^{-1}, which agrees with that measured at this frequency by the Fourier method. The spectrum is presented in Figure 6.28 along with the results of the room temperature measurements (294 K) described in Section 6.3.1. The reliability of the values at lower frequencies is limited somewhat by the fact that only thinner samples were used, for the reasons discussed in Section 6.3.1. Though there is a substantial amount of variation in the data, it is apparent that the magnitudes and overall trends are roughly similar to those found at room temperature. This would appear to be consistent with expectations that scattering by static heterogeneity is the dominant loss mechanism in SiO_2 for acoustic phonons in the GHz frequency range at essentially all temperatures up to 300 K.

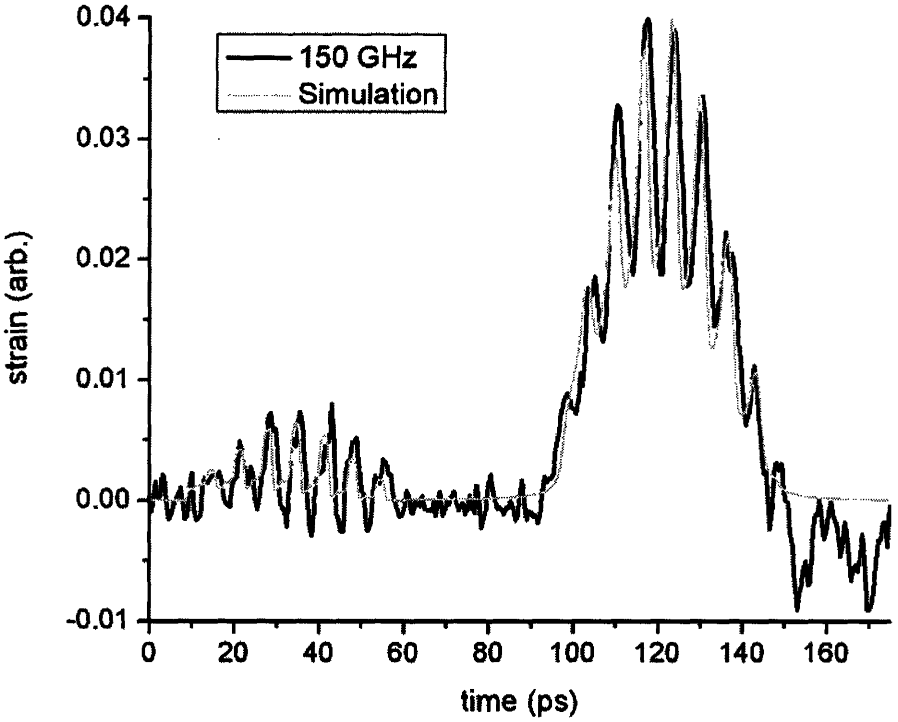

Figure 6.27. Strain at 150 GHz in 480 nm silica sample. Also shown is simulation using acoustic mismatch model, using damping constant of 1.5×10^6 m^{-1}.

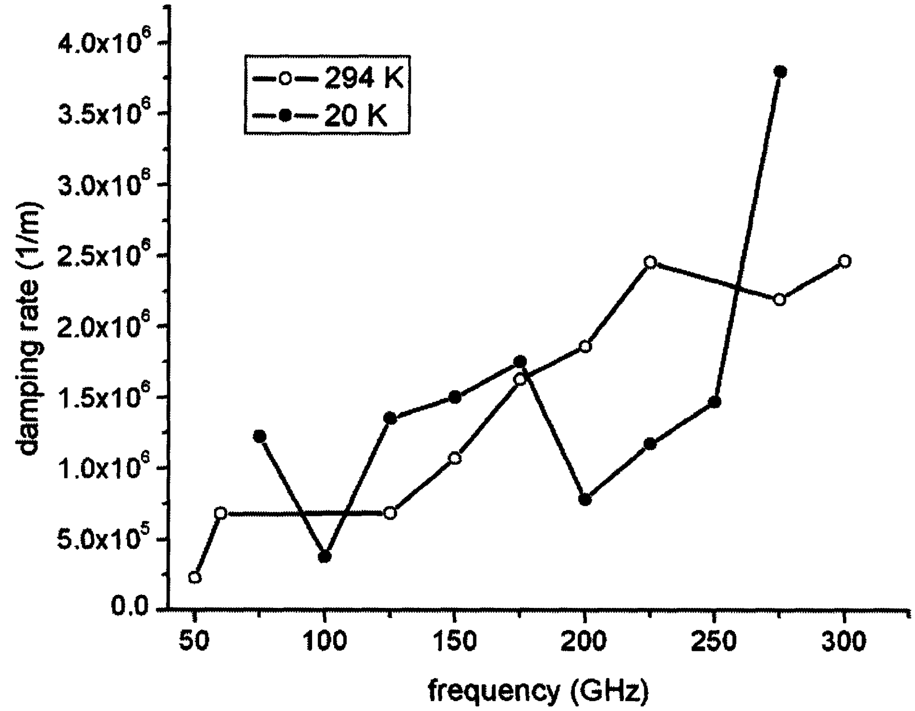

Figure 6.28. Acoustic spectra at 20 K and at 294 K.

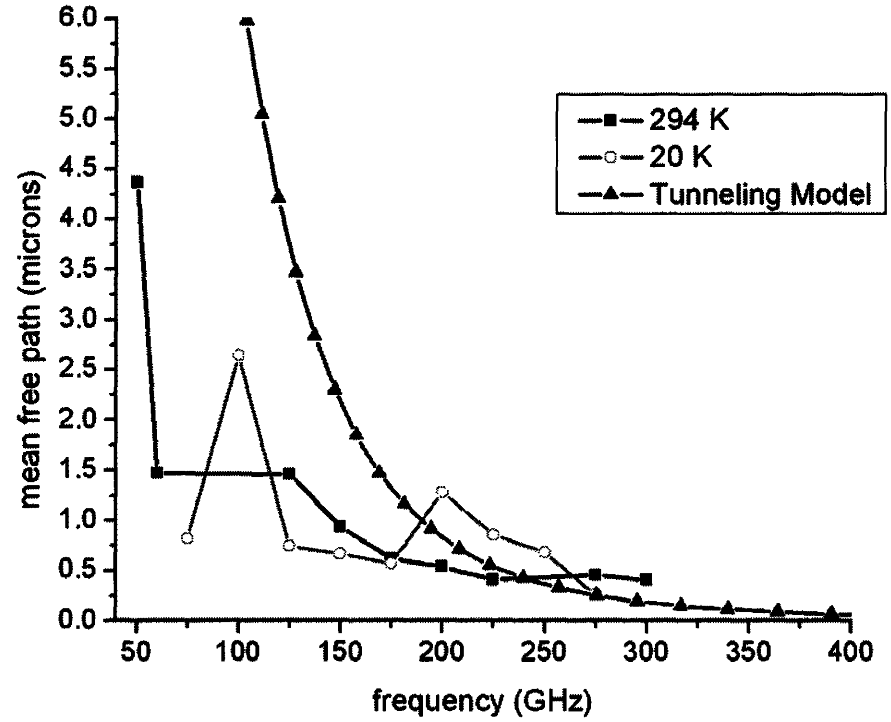

Figure 6.29. Phonon mean free path at 20 K, 294 K, and that predicted by the tunneling model (see Chapter 2).

The phonon mean free paths calculated from the damping coefficients with Equation 6.4 for the spectra at 20 and 294 K, along with those predicted by the tunneling model as described in Chapter 2, are presented in Figure 6.29. At the highest frequencies, the value of the mean free path measured by the experiments approaches that of the predictions, albeit with a much weaker frequency dependence than anticipated. The mean free path in this region is modeled to be dominated by Rayleigh scattering from structural inhomogeneity. While the small measured mean free paths suggest a very strong scattering mechanism, the frequency dependence goes roughly as ω and definitely not as the predicted ω^4 which was used to explain the plateau in the thermal conductivity, as shown in Figure 2.11. However, since the thermal conductivity is dominated by phonons at high wavevectors where the density of states is high, the tunneling model predictions still can be fit adequately to the thermal conductivity even though they do not describe the microscopic behavior well. The fact that the success of the model in fitting macroscopic thermal behavior does not provide an adequate test of its microscopic underpinnings is precisely the reason that more definitive measurements of the detailed wavevector-dependent properties are needed.

6.4 Conclusions on the Properties of Amorphous Materials at the Microscopic Level

The technique for generating ultrahigh frequency acoustic waves that has been developed in this thesis holds great potential for addressing heretofore unanswered questions about the low-temperature dynamical processes and structural features of amorphous materials. The effort to develop the technique is justified by the remarkable and previously unobserved results that it has produced on what is generally believed to be the best understood glass material. The results at room temperature demonstrate that the damping rate is far lower, by an order of magnitude at higher frequencies, than previously shown. The results at 20 K were expected to confirm the predictions of the tunneling model, as described in Chapter 2. However while at high frequencies the values agree fairly well with what is expected, the lower frequencies experience drastically higher damping than expected. Further, the spectra at both 294 and 20 K seem to agree quite closely, which demonstrates that their damping likely has a common origin – structural heterogeneity. Studies at even lower temperatures might be expected to support this conclusion. The very gradual increase in damping with frequency, as opposed to a damping increasing as the fourth power of the frequency, suggests that while the Rayleigh scattering model yields a fairly accurate *magnitude* of the damping of high-wavevector acoustic waves, which duplicates the conductivity results, it is not at all an appropriate model of the true interaction of phonons with the structure. A more physical model could be that of a wave propagating through turbid media. Surely as the acoustic waves they travel they see not a low density of strongly scattering centers, but rather a near continuum of weakly scattering heterogeneities. Further theoretical consideration is in order.

6.5 Future Directions

Currently studies are ongoing to explore the interesting new information which has become available through the development of this technique. For example preliminary data have been obtained in silica glass between the range 300-20 K, with hopes of testing the presence at higher temperatures (~50 K) of two-level system relaxation effects which are not predicted by the tunneling model, but have been seen at much lower frequencies.[20] However the data quality were relatively poor for a combination of reasons which would be addressed by several improvements: 1) the laser system was recently updated, and should give much improved signal-to-noise ratios; 2) use of a cold-finger instead of a sample-in-vapor style cryostat would reduce interferometric noise in the detection system; and 3) access to an increased range of sample thicknesses, some potentially with thicker aluminum films for detection of the acoustic waves with little contribution from other signals. On the whole the preliminary data show similar trends to that shown in this chapter.

The final section of this chapter points toward two important additional prospects for the experimental approach that has been developed. We show in Figure 6.30 and Figure 6.31 data from the polymer PMMA at 425 K. Polymer samples represent an additional level of complexity due to their particularly broad distribution of dynamics over numerous timescales, many of which may be correlated.[11] In addition, at this temperature the sample is well above the

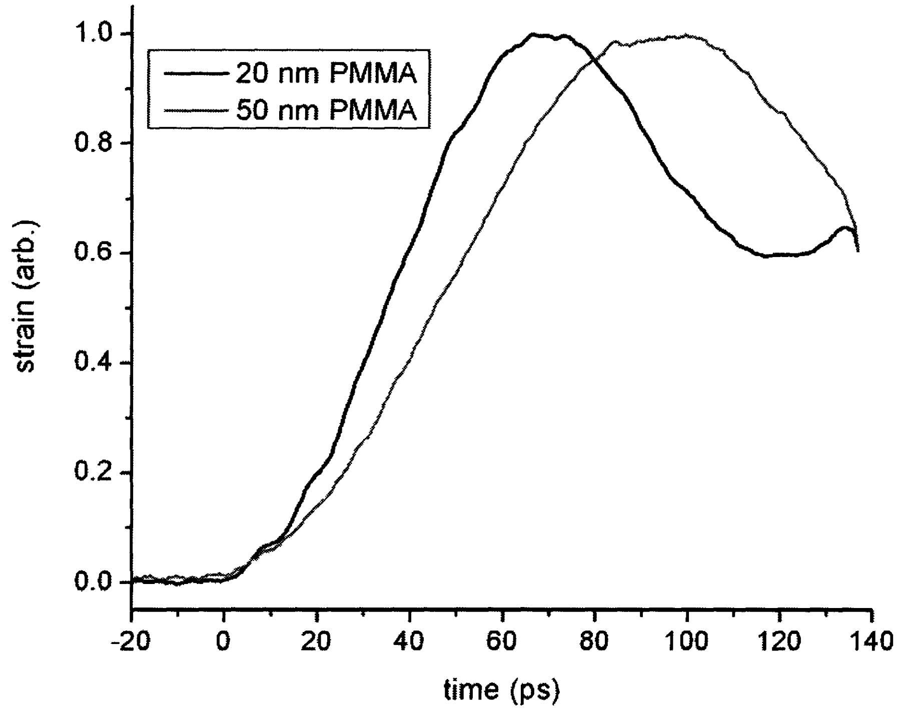

Figure 6.30. Displacement at 100 GHz in 20 and 50 nm of PMMA, at 425 K (above T_g=410 K)

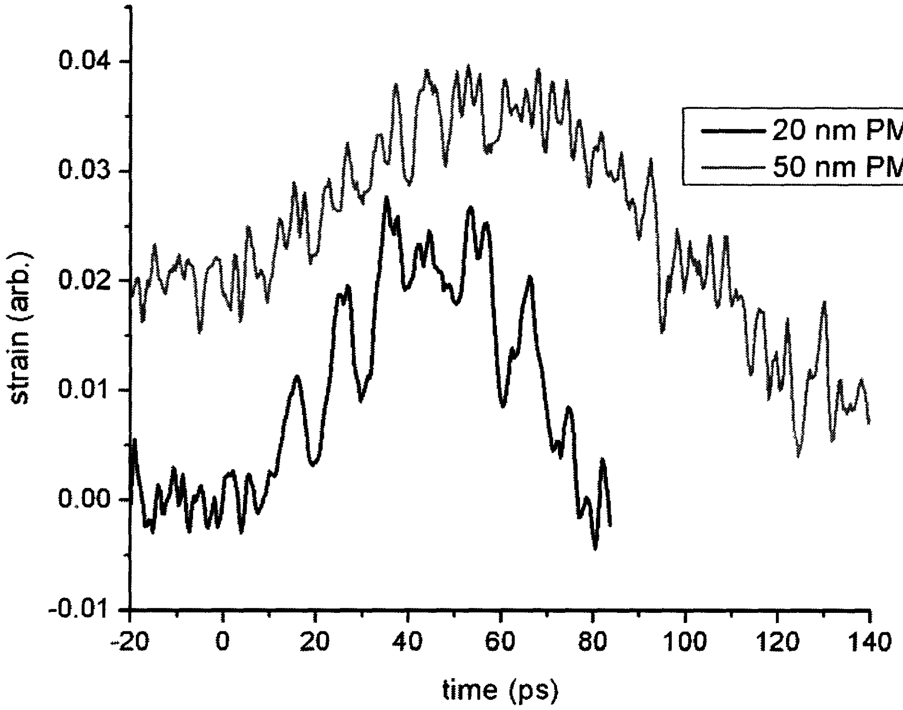

Figure 6.31. Strain at 100 GHz in 20 and 50 nm of PMMA, at 425 K (above T_g=410 K).

glass transition temperature T_g =410 K. The data collected at this temperature illustrate the potential for direct study of high-frequency acoustic waves and the rapid structural relaxation dynamics that mediate their properties in the liquid state, not only in polymers but in glass-forming liquids generally. Currently studies are ongoing to explore the changes in the acoustic spectrum of PMMA that occur with the onset of liquid-like dynamics as the polymer is raised above its glass transition temperature.

6.6 References

---

1. E. Courtens, M. Foret, B. Hehlen, R. Vacher. The vibrational modes of glasses. *Solid State Communications*, 117(3): 187-200, 2001.

2. N.V. Surovtsev, J.A.H Wiedersich, E. Duval, V.N. Novikov, E. Rössler, A.P. Sokolov. Light scattering spectra of fast relaxation in B_2O_3 glass. *Journal of Chemical Physics*, 112(5): 2319-2324, 2000.

3. R. Vacher, J. Pelous, F. Plicque, A. Zarembowitch. Ultrasonic and Brillouin scattering study of the elastic properties of vitreous silica between 10 and 300 K. *Journal of Non-Crystalline Solids*, 45: 397-410, 1981.

4. W. Dietsche, H. Kinder. Spectroscopy of phonon scattering in glass. *Physical Review Letters*, 43(19): 1413-1417, 1979.

5. T.C. Zhu, H.J. Maris, J. Tauc. Attenuation of longitudinal-acoustic phonons in amorphous SiO_2 at frequencies up to 440 GHz. *Physical Review B*, 44(9): 4281-4289, 1991.

6. C.J. Morath, H.J. Maris. Phonon attenuation in amorphous solids studied by picosecond ultrasonics." *Physical Review B*, 54(1): 203-213, 1996.

7. T. Scopigno, R. Di Leonardo, G. Ruocco, A.Q.R. Baron, S. Tsutsui, F. Bossard, S.N. Yannopoulos. High frequency dynamics in a monatomic glass. *Physical Review Letters*, 92(2): 025503, 2004.

8. M. Foret, R. Vacher, E. Courtens, G. Monaco. Merging of the acoustic branch with the boson peak in densified silica glass. *Physical Review B*, 66(2): 024204, 2002.

9. D. Engberg, A. Wischnewski, U. Bucheneau, L. Börjesson, A.J. Dianoux, A.P. Sokolov, L.M. Torrell. Sounds waves and other modes in the strong glass former B_2O_3. *Physical Review B*, 58(14): 9087-9097, 1998.

10. C. Kittel. Interpretation of the thermal conductivity of glasses. *Physical Review*, 75(6): 972-974, 1949.

11. N. Vachhani, *Using Narrowband Pulse-Shaping to Characterize Polymer Dynamics*. Master Thesis, Massachusetts Institute of Technology, Department of Materials Science, January 2005.

12. Y.-C. Lee, K.C. Bretz, F.W. Wise, W. Sachse. Picosecond acoustic measurements of longitudinal wave velocity of submicron polymer films. *Applied Physics Letters*, 69(12): 1692-1694, 1996.

13. Ü. Özgür, C.-W. Lee, H.O. Everitt. Control of coherent acoustic phonons in semiconductor quantum wells. *Physical Review Letters*, 86(24): 5604-5607, 2001.

14. R. Vacher, J. Pelous, E. Courtens. Mean free path of high-frequency acoustic excitations with application to vitreous silica. *Physical Review B*, 56(2): R481-R484, 1997.

15 V. Gopal, S. Mujumdar, H. Ramachandran, A.K. Sood. Imaging in turbid media using quasi-ballistic photons. *Optics Communications*, 170: 331-354, 1999.

16. R. Elaloufi, R. Carminati, J.-J. Greffet. Diffusive-to-ballistic transition in dynamic light transmission through thin scattering slabs: a radiative transfer approach. *Journal of the Optical Society of America A*, 21(8): 1430-1437, 2004.

17. R.C. Zeller, R.O. Pohl. Thermal conductivity and specific heat of noncrystalline solids. *Physical Review B*, 4(6): 2029-2041, 1971.

18. P.W. Anderson, B.I. Halperin, C. Varma. Anomalous low-temperature thermal properties of glasses and spin glasses. *Philosophical Magazine*, 25(8): 1-9, 1972.

19. W.A. Phillips. Tunneling states in amorphous solids. *Journal of Low Temperature Physics*, 7(3-4): 351-360, 1972.

20. S. Rau, C. Enss, S. Hunklinger, P. Neu, A. Würger. Acoustic properties of oxide glasses at low temperatures. *Physical Review B*, 52(10): 7179-7194, 1995.

JAIME D. CHOI

EDUCATION

Massachusetts Institute of Technology **Ph.D. Physical Chemistry, 2005**
Area: Ultrafast optical characterization of complex dynamics and structure in advanced materials. Thesis title: "Generation of ultrahigh frequency acoustic waves for the characterization of complex materials."
GPA: 4.2/5.0

Rice University **B.A. Chemistry, 1999**
GPA: 3.4/4.0

WORK EXPERIENCE

1999-2004
Research Assistant, Massachusetts Institute of Technology
Thesis Advisor: Keith A. Nelson

Developed new spectroscopic technique for the measurement of dynamical intermolecular processes in complex materials: designed and built novel laser pulse shaper for the tunable generation of higher frequency narrowband acoustic waves than ever before possible, and illustrated the benefits of this spectroscopic technique above existing technology.

Demonstrated the use of novel technique for the characterization of molecular-scale heterogeneity and motion in liquids, polymers, and glass, and for high-resolution thickness measurements of films.

Extended the designed use of the pulse shaper to the coherent control of lattice modes in ferroelectric crystals, and the active amplification of terahertz frequency electromagnetic waves.

Related the microscopic features of polymers and glasses to their bulk thermal and elastic properties, through the combined use of two distinct experimental techniques, and with computer modeling of nanoscale structure and ultrafast dynamics. Confirmed a theory that had yet to be conclusively proven for 30 years.

Developed a new interferometer with improved noise characteristics, ease of use, and simplicity of alignment, over existing techniques. Demonstrated its use for both imaging and point-probe of propagating electromagnetic or acoustic waves in crystals, liquids, and at interfaces; for measuring sub-nanometer topological features on surfaces and ionic displacements in crystals; for measuring the value of strain.

Summers 1997, 1998, Spring and Summer 1999
Intern, Los Alamos National Laboratory
Research Advisor: Basil I. Swanson

Created self-assembling hybrid organic/inorganic structures and characterized their phase transitions with near-infrared spectroscopy.

Prepared monolayers on silicon wafers with self-assembly and soft lithography. Fabricated lipid bilayer micelles, and used together with monolayers to create stable bio-mimetic materials "on a chip."

Engineered lateral features of monomolecular layers at the air-water interface; imaged with Brewster Angle Microscopy; transferred to substrates for use as a prototype cholera biosensor.

LEADERSHIP

2001-2003
Co-founder and treasurer of "The Epicurean" club, MIT

Organized and led numerous monthly events centered on teaching cooking skills and food appreciation to undergraduate and graduate students. Total club membership: 100.

Collaborated with club president to formulate direction and constitution of club activities, membership, and budget. Hosted inaugural event, Sushi Night, which became an annual event by popular demand.

Wrote biannual budget requests to the MIT Undergraduate Finance Board.

1996-1997
Photography editor of Rice University student newspaper, the "Thresher"

Worked directly with the Editors-in-Chief to determine form and content of photography in weekly student newspaper. Trained student photographers.

Modernized darkroom, converting from optical photo printing to an all-digital system of photo manipulation.

Documented campus events such as: conference attended by Janet Reno, James A. Baker III, and Jack Kemp; visits by Vanessa and Colin Redgrave, and Hakeem Olajuwon; sports such as college basketball and Beer Bike.

Teaching Assistantships:

MIT 1999-2000 (Head TA, 2000)	Thermodynamics and Kinetics
Rice University 1998	Advanced Organic Chemistry Lab

Awards:

Presented graduate research at Ultrafast Phenomena XIV conference in Niigata, Japan, July 2004
Poster Prize at MIT George Harrison Spectroscopy Lab Annual Meeting, 2004
Poster Prize at MIT George Harrison Spectroscopy Lab Annual Meeting, 2003
Los Alamos National Laboratory Pipeline Initiative Award, 1998
President's List, Rice University, 1997
National Merit Scholar, 1995

SKILLS

Spectroscopic techniques: Experimental design, femtosecond and picosecond ultrafast spectroscopy, pulse shaping, interferometric detection and imaging, four-wave mixing, nonlinear spectroscopy, optical heterodyning, liquid nitrogen and helium cryogenics, infrared spectroscopy, NMR, HPLC.

Lasers: Extensive hands-on experience in use of femtosecond Ti:Sapphire oscillators and amplifiers, homebuilt picosecond Nd:YAG lasers, argon-ion, diode, and diode-pumped solid state lasers.

Material fabrication techniques: Plasma-enhanced chemical vapor deposition of dielectric films, E-beam assisted evaporation of metals and metal oxides, spin-coating, self-assembly of hybrid organic/inorganic materials in liquid phase and at the air-water interface, and soft lithography.

Software: OriginPro 7.0, CorelDraw 11.0, Adobe Photoshop 5.0, Microsoft Office 2003, extensive programming experience in Matlab for modeling and data analysis.

ACTIVITIES

Golf, skiing, dancing, cooking.